Hydrodynamic and cavitation behavior of an innovative pump with independent rotation of inducer and centrifugal impeller

Ehsan Dehnavi

HESAM UNIVERSITÉ

Arts et Métiers Sciences et Technologies

ECOLE DOCTORALE SCIENCES ET METIERS DE L'INGENIEUR

Laboratoire d'Ingénierie des Fluides et des Systèmes Energétiques(**LIFSE**)
Campus de Paris

THÈSE

présentée par : **Ehsan DEHNAVI**
soutenue le : **08 Mars 2024**

pour obtenir le grade de : **Docteur d'HESAM Université**

préparée à : Ecole Nationale Supérieure d'Arts et Métiers
Spécialité : Mécanique des Fluides

Hydrodynamic and cavitation behavior of an innovative pump with independent rotation of inducer and centrifugal impeller

THÈSE dirigée par :
Professeur Farid BAKIR

et co-encadrée par :

Docteur Amélie DANLOS **Docteur Mohamed KEBDANI**

Jury

Mme. Céline MORIN	Professeur, Université Polytechnique Hauts-de-France	Présidente
M. Miguel ASUAJE	Professeur, Universidad Simon Bolivar	Rapporteur
M. Antonio BRASIL JUNIOR	Professeur, University of Brasilia	Rapporteur
Mme. Marie-Christine DULUC	Maître de conférences, Le Cnam,Paris	Examinatrice
M. Nicolas MYON	Directeur technique , FAPMO	Invité

THÈSE

Acknowledgements

I am sincerely grateful to my supervisor, Prof. Farid Bakir, for his expertise, understanding, and patience during my thesis. His guidance was crucial at every stage of my research and the writing of this thesis and I am fortunate to have had such an outstanding advisor and mentor for my Ph.D. studies. I would like to express my deepest gratitude to Dr. Amélie Danlos, my thesis advisor for her unwavering support and invaluable guidance throughout this journey. I am thankful for the support of my colleagues in LIFSE laboratory. Our discussions, collaborative work during experimental parts, and mutual support greatly enhanced my Ph.D. experience. Special acknowledgment is due to Mr. Nicolas Myon, technical manager at FAPMO whose expertise in the field was indispensable during the technical experiments.

I am profoundly grateful to my family for their endless love and support. My mother, father and brother made every possible effort to support me in achieving my aspirations. And, a special thanks to my wife, Nooshin, for her endless love, patience, and encouragement. Their support has been my pillar of strength and has kept me grounded throughout this academic pursuit. Finally, I would like to extend my appreciation to everyone who directly or indirectly contributed to this research, and who has made this journey both possible and memorable.

Résumé

La technologie permettant aux rotors des turbomachines de tourner indépendamment, notamment dans des configurations en contre-rotation, a suscité l'intérêt de nombreux chercheurs et industries. L'étude de l'effet de cette technologie sur la turbine, le compresseur et les pompes axiales a montré son impact significatif sur les caractéristiques des turbomachines. Jusqu'à présent, aucune recherche n'a été menée sur l'effet de la rotation indépendante de l'inducteur et de la roue dans les pompes. Dans cette thèse, l'influence de la rotation indépendante de l'inducteur et de la roue sur les caractéristiques de la pompe a été étudiée pour la première fois, en utilisant à la fois des méthodes expérimentales et numériques. Pour atteindre cet objectif, la roue et l'inducteur en co-rotation et en contre-rotation ont été conçus pour une rotation indépendante. Cette conception permet d'étudier trois paramètres impossibles à évaluer dans la pompe conventionnelle lorsque l'inducteur et la roue sont liés et tournent ensemble. Les paramètres étudiés dans cette recherche sont la vitesse de rotation de l'inducteur, la distance entre l'inducteur et la roue, et la direction de rotation de l'inducteur. Pour examiner ces paramètres, un nouveau banc d'essai expérimental a été conçu. Un arbre séparé et un moteur électrique ont été intégrés pour garantir que la vitesse de l'inducteur puisse être ajustée sans influencer la rotation de la roue, permettant une rotation indépendante de l'inducteur. La direction de rotation de l'inducteur a été modifiée en conservant sa géométrie et en inversant l'orientation des aubes, conduisant à un inducteur en contre-rotation. De plus, pour ajuster la distance entre l'inducteur et la roue, un curseur a été intégré dans la section de l'inducteur, permettant de modifier la distance entre l'inducteur et la roue. L'étude des caractéristiques de la pompe est divisée en deux parties principales : l'analyse des caractéristiques en condition de non-cavitation et l'étude des performances en cavitation. La rotation indépendante de l'inducteur améliore les caractéristiques de la pompe dans les conditions de cavitation et de non-cavitation.

Mots-clés : Inducteur, Roue centrifuge, Rotation indépendante,Pompes contre-rotatives, Cavitation,

Abstract

Over the years, the technology that enables rotors in turbomachines to rotate independently, especially in counter-rotating configurations, has captured the interest of numerous researchers and industries. The study of the effect of this technology on the turbine, compressor and axial pumps has shown its important effect on the characteristics of the turbomachines. Until now, no research has been done on the effect of independent rotation of inducer and impeller in pumps. In this thesis, the influence of the independent rotation of the inducer and impeller on pump characteristics has been investigated for the first time, using both experimental and numerical methods. To meet this aim, the impeller and both co-rotation and counter-rotation inducer were designed for independent rotation. This design permits the investigation of three parameters not possible to evaluate in the conventional pump when the inducer and impeller are linked and rotated together. The parameters studied in this research are the rotational speed of the inducer, the distance between the inducer and the impeller, and the direction of the inducer rotation. To examine these parameters, a new experimental test bench was designed. A separate shaft and electric motor were incorporated to ensure that the speed of the inducer could be adjusted without influencing the rotation of the impeller, enabling independent rotation of the inducer. The direction of rotation for the inducer was changed by keeping its geometry consistent and reversing the blade orientation, leading to a counter-rotating inducer. Furthermore, to adjust the distance between the inducer and the impeller, a slider was incorporated within the inducer section, allowing for modification of the distance between the inducer and the impeller. The investigation into pump characteristics is divided into two main parts : the analysis of characteristics in non-cavitation condition and the study of cavitation performance. The independent rotation of the inducer enhances the pump characteristics in both cavitation and non-cavitation conditions.

Keywords : Inducer, Centrifugal impeller, Independent rotation, Counter-rotating pumps, Pump performance, Cavitation, Numerical simulation.

Table of contents

List of tables

List of figures

Chapitre 1

Introduction

content

1.1 Motivation

A large part of the conversion of mechanical energy into electrical and electrical to mechanical energy is done by turbomachines, and this makes them a special place in the industry. These machines are divided into several categories : fans, turbines, compressors and pumps. Improving the efficiency of turbomachines has always been an important topic among scientists and industries. These improvements can be reached by changes in blade geometry, rotation speed, blade size, etc. In recent decades, the use of turbomachines with the ability to rotate the two rotors simultaneously independently of each other has caused a dramatic change in their efficiency. Using Counter-Rotating Pumps, on one hand, can improve the operating area and efficiency, on the other hand, can reduce the chance of cavitation by giving the fluid more energy thanks to the rotation of the second rotor. By adding a degree of freedom to the turbomachine (rotation of the second rotor independently), more efficiency and smaller volume can be achieved, although the complexity of construction is one of the most important weaknesses of this type of system. Increasing the efficiency of pumps and reducing the cavitation phenomenon are two important considerations in pumps.

While numerous research have explored the independent rotation of rotors in various turbomachines such as the turbines, compressors and axial pumps, no investigations have specifically focused on the

independent rotation of inducers and impellers in centrifugal pumps equipped with inducers. This thesis pioneers the exploration, both numerically and experimentally, of the independent rotation of the impeller and inducer, examining their effects on pump characteristics and cavitation performance.

1.2 Thesis objectives

This research aims to explore the impact of independent rotation of the inducer and impeller on pump characteristics and cavitation performance. For the first time, a novel test bench has been developed that allows for the independent rotation of both the inducer and the impeller. In this thesis, three crucial parameters that only can be examined through the independent rotation system are explored : the rotational speeds of the inducer and impeller, the direction of inducer rotation (co-rotation and counter-rotation), and the gap between the inducer and impeller. Additionally, with the help of a high-speed camera, various cavitation types within the inducer at varying speeds and flow rates were observed. The reasons for their emergence and their correlation with pump cavitation performance were explored. The pump characteristics were further examined using CFD simulation, providing insights into areas that are inaccessible or challenging to measure experimentally.

1.3 Thesis outlines

The progression of this thesis is structured into different sections, as detailed below. Chapter 2 provides a review of the literature : this chapter examines prior research on all turbomachinery, specially the pumps, with an emphasis on the application of independent rotation technology. Furthermore, it examines centrifugal pumps equipped with inducers and looks into how various factors influence the characteristics and cavitation of such pumps.

Chapter 3 outlines the materials and methods utilized in this study. It begins by detailing the design processes for the inducer and impeller. This is followed by an explanation of how the test bench components, such as shafts, ball bearings, and mechanical seals, were designed and produced. The chapter then discusses the design of a rotation system for two closely placed rotors and the uncertainties associated with the sensors. The chapter concludes by describing the data collection methods, cavitation testing procedures, and the preparation of the test bench.

Chapter 4 explores the impact of the independent rotation of the inducer and impeller on pump

efficiency and pressure. The chapter presents the findings concerning the role of inducer speed on pressure and pump efficiency, as well as changes in the direction of inducer rotation and its effects during counter-rotation mode. Additionally, numerical simulations were conducted to explore areas that couldn't be assessed through experiments. The simulation approach, its parameters, and its outcomes are further discussed in the latter part of this chapter.

Chapter 5 focuses on three specific parameters related to pump cavitation that can be analyzed only with the independent rotation of the inducer and impeller. These parameters include the speed of the inducer, its rotation direction, and the distance between the inducer and impeller. Following that, the chapter investigates the impact of these parameters over three distinct flow rates. Through the use of a high-speed camera, different cavitation phenomena are visually analyzed, and the effects of the evaluated parameters on different cavitation types within the pump are detailed.

The last chapter reviews the design and assembly of the inducer and impeller, as well as the development of an innovative test bench for experimentation. Following this, a brief overview is provided on the influence of independent rotation on pump efficiency, pressure, and cavitation. The chapter concludes by suggesting future research works and studies that could be undertaken with this new system.

Chapitre 2

State of the art

content

2.1 Counter-rotating turbomachines

Rotational machines are used to transfer energy between the mechanical part and the working fluid. The rotational machines can be divided into two main groups, the first one which absorbs energy and produces mechanical movement such as pumps, compressors, fans. The second one produces energy (mostly electrical) by absorbing mechanical energy from the working fluid (it could be steam, gas, or water) [1]. The direction of flow can classify the rotational machines into the axial, centrifugal, and mixed-flow machines. Axial machines can work with a higher flow rate with a lower pressure drop which gives this kind of machine the ability to work as high flow rate pumps, turbines, and compressors[2]. During the last decades, the rapid changes in designing turbomachines and the need for more efficient and reliable turbomachines is the reason for the scientists and industries to pass over the conventional single-blade propellers and design counter-rotating turbomachines[3].

Counter-rotating turbomachines have many applications in industries. These machines include two co-axial rotors with the opposite direction of rotation which conclude more energy conversion, lower machine size, and better performance. Part of rotational kinetic energy from the front rotor is converted to the static head by the rear rotor. However, the noise generated by the interaction of two rotors and design complexity is the most disadvantage of counter-rotating turbomachines [4]. The studies on the axial counter-rotating pumps showed using rear-rotor instead of the stator will help to improve flow rate and total efficiency of counter-rotating axial pump, especially in low flow rates[5]. The rotor distance has a major effect on the local and total performances and an increase in relative axial spacing between two rotors reduces the rotor interaction peaks near the front rotor without significantly affecting the overall performance.[6].

Counter-rotating propellers consist of two propellers mounted on dual coaxial shafts, rotating in opposite directions. While they come with challenges such as a more complex design and additional weight due to the propeller's motor, they provide several advantages over single propellers. The main advantage of contra-rotating propellers is their increased efficiency, thanks to the energy reclaimed by the rear propeller. The back propeller captures some of the rotational energy that the front propeller transfers to the water, leading to decreased fuel consumption. Additionally, the second rotor assists in stabilizing the system torque, particularly in situations demanding high stability. The noise output is reduced due to the consistent downstream wake field created by the counter-rotating propellers[7].

2.1.0.1 Counter-rotating fan

The effect of some parameters on the Counter-Rotating Axial Fan (CRAF) is investigated by Wang et al[8]. Three different fans with the same design point were fabricated and the effect of load distribution on the overall performance is evaluated. The load distribution is the ratio of pressure rise of the rear rotor to the Counter-Rotating System (CRS) at the design point. Three different designs are called JW1, JW2, and JW3 respectively. JW2 configuration has the highest load distribution ($L = 52$) which means most of the fluid energy is transferred by the rear rotor. The static pressure rise and performance are investigated for three different rotors in various flow rates (Q_v). For $Q_v \leq 0.38\ \mathrm{m}^3/\mathrm{s}$ the flow rate is low and there is the same trend for the characterization curve of each configuration with or without a rear rotor. For $0.38\ \mathrm{m}^3/\mathrm{s} \leq Q_v \leq 0.6\ \mathrm{m}^3/\mathrm{s}$ there is an obvious difference in the slope of the curves for each configuration and for CRS the slope is approximately two times higher. For $0.6\,\mathrm{m}^3/\mathrm{s} \leq Q_v \leq 1\,\mathrm{m}^3/\mathrm{s}$ the slope is increased compared to only the front rotor system and for the last and high volume rate region $1\ \mathrm{m}^3/\mathrm{s} \leq Q_v \leq 1.3\ \mathrm{m}^3/\mathrm{s}$ the static pressure curves have the highest slope.

The axial distance between two rotors has a significant effect on the performance and static pressure. The results for a fan with blade tip radius ($R_t = 178.5\,\mathrm{mm}$) show by increasing the distance from $0\,\mathrm{mm} \leq S \leq 1.3\,\mathrm{mm}$ both static pressure and performance rise sharply and for the $40\,\mathrm{mm} \leq S \leq 100\,\mathrm{mm}$ slowly decreased before sharply falling for $100\,\mathrm{mm} \leq S \leq 300\,\mathrm{mm}$. For low axial distance, the rear rotor recovers more energy to the fluid whereas the power consumption of the front rotor increased. The static efficiency is about 65% for all configurations which is good and the operating range for the CRS system is more stable. The lower distance is better to achieve higher performance[8]. Ryu et al.[9] studied the effect of tip clearance on the performance of the ducted fan. The tip clearance ratio of the rear rotor to the front rotor varies from 1.80% up to 7.62% and thrust coefficient drops by increasing tip clearance of the front rotor because of higher tip leakage, however, by decreasing the tip clearance of the rear rotor, the thrust coefficient increased. Power coefficient also decreased with larger tip clearance due to the effect of viscous loss and tip leakage loss. The efficiency increased by decreasing the rear rotor tip clearance and it will be decreasing by increasing the front rotor tip clearance.

2.1.1 Counter-rotating turbine

Jung et al[10] studied the aerodynamic performance of 30 KW Counter Rotating Wind Turbine (CRWT) and compare it to conventional turbine and the results indicate that the power increase is affected by flow characteristic and rotation of the first rotor. The velocity of flow at the second rotor is low when the first rotor is the same size as the second rotor so the power will be decreased and the output power is highly related to the rotor distance.

The blade diameter ratio of CRWT is carried out by Koehaun et al.[11] which demonstrated that when the rear rotor is smaller than the front rotor the power and efficiency are low because of the front rotor wake and the rear rotor should rotate in this region, on the other hand when the rear rotor is larger than front rotor the power and efficiency increased, however geometrically, the maximum efficiency can be achieved when the rotors have the same diameter. The diameter ratio of 0.5 has better performance and power because about half of the rear rotor is not affected by the wake of the primary rotor so it faces the free stream and the losses due to wake are reduced. The performance of the counter-rotating pump was influenced by the blade angle of the impellers. It was observed that when the inlet angle stayed constant and the outlet angle reduced, the inlet flow rate decreased, impacting the performance of the rear rotor[12].

2.1.2 Counter-rotating compressor

Aerodynamic instabilities are the main problem in designing the compressor. Using a Counter-Rotating Compressor (CRC) is one of the most interesting ways in recent years to reduce instabilities and the weight of an axial compressor. Studies showed the second rotor can improve the efficiency of compressors and the different speed ratio in CRC has a magnificent role in the performance of the compressor[13]. The study of speed ratio effect in CRC has been investigated by Chen et al.[14] and the results showed that when the speed of the front rotor (R_1) is greater than the rear rotor (R_2), by decreasing the ratio, the pressure ratio peak is reduced and efficiency is increased. On the other side when the speed of the front rotor (R_1) is lower than the rear rotor (R_2) the pressure ratio has a major decrease by increasing the speed ratio. The higher efficiency with lower reduction of pressure ratio (R_1/R_2) will occur at the speed ratio of 1.143 and the flow regime will be different by changing the speed ratio. The CRC can reach a higher pressure ratio rather than the conventional compressor

and this rise relies on the length ratio of the front rotor, in another word the higher length ratio results in a higher pressure ratio, however, a decrease in efficiency appears. By increasing the front rotor speed up to 130% of design point, the pressure ratio moves up about 8.7% while the efficiency remains constant[15]. The performance study of Counter-Rotating Centrifugal Compressor (CRCC) is done by Nguyen et al.[16] Four different geometries (CF1, CF2, CF3 and CF4) based on reference rotor were made and the results indicate that CRCC has a higher pressure ratio in flow rate less than Design Operating Point (DOP) and the pressure ratio rises by increasing the length ratio (length at the hub of first rotor to length of the reference rotor ratio) ; however, the efficiency sharply decreases. By changing the first rotor speed to 130% of DOP the pressure ratio can rise up to 8.7%. The larger diameter of the first rotor outlet results in a higher pressure ratio by producing higher kinetic energy flow in the second rotor. The pressure ratio for the reference is 1.29 whereas the maximum pressure ratio is 1.53.

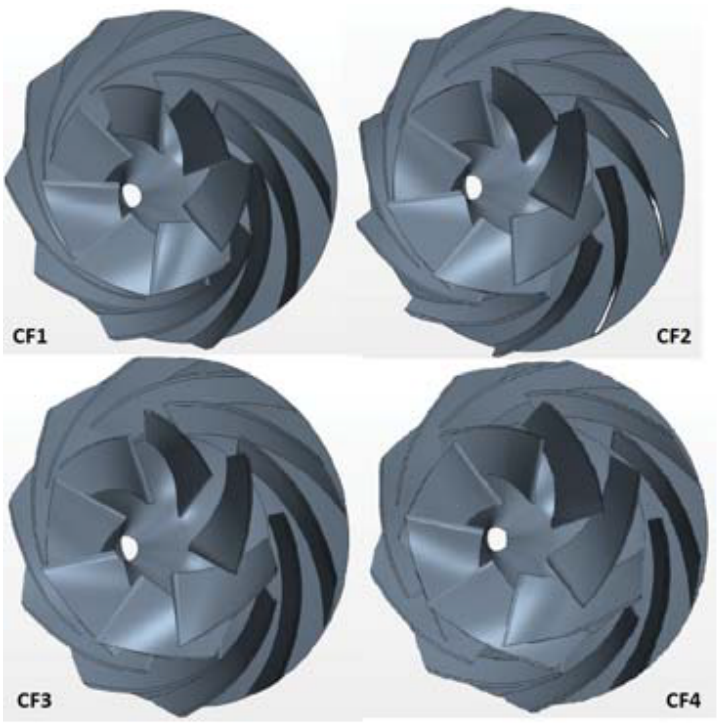

FIGURE 2.1 – Four configurations of CRCC system[16]

2.1.3 Counter-rotating pumps

Unstable performance and high consumption of energy are two major challenges in pump operation. Increasing efficiency and decreasing instability can result in saving more energy. Using Counter-Rotating Pumps (CRP) is recently considered due to its higher specific speed and efficiency. The concept of CRP is to replace a rotating blade in the opposite direction instead of a stator.

The investigation of Furukawa et al.[17] shows the cavitation in counter-rotating pumps will be appearing at the rear rotor tip and this phenomenon results in lower static pressure in the rotors. This study demonstrated the cavitation suppressing due to lower front rotor speed and high discharge so by increasing the front rotor speed, the rear rotor speed will be increased due to constant speed ratio and discharge will be decreased.

Using CRP in the air/water two-phase flow by Shigemitsu et al[5] showed a significant rise in performance and efficiency by controlling rear rotor speed. A more stable head characteristic curve, more operating range with higher performance, and less cavitation are some of the counter-rotating pump advantages however this kind of pump has some disadvantages such as complex two independent driving shaft. The rear rotor designing is important to reach better performance and efficiency.

The main characteristic parameters of the pump will be different by changing the rotors distance.[18] Considering the thickness of impeller L as a reference, by increasing the distance of the rotor from zero $D_L = 0$ until $D_L = 2L$, the maximum head and highest efficiency achieved when the distance of the rotor is equal to the axial width of the impeller $D_L = 1$ (Figure 2.2). By passing this value, the efficiency does not rise and the head will be decreased slowly. The vorticity at the secondary rotor is distributed near the rotor inlet, the high-pressure area on the working face of the secondary blade is smaller rather than the low-pressure area on the back of the blade. As the rotors' distance increases, the low-pressure area on the back of the blade decreased and the high-pressure area on the working surface increased. When the distance of the rotor is low, there is high vorticity on the secondary rotor and a more dynamic interface of counter-rotating rotor which results in lower head and efficiency, however, by increasing the rotors distance more than $D_L = 0$ these parameters will also decrease slowly.

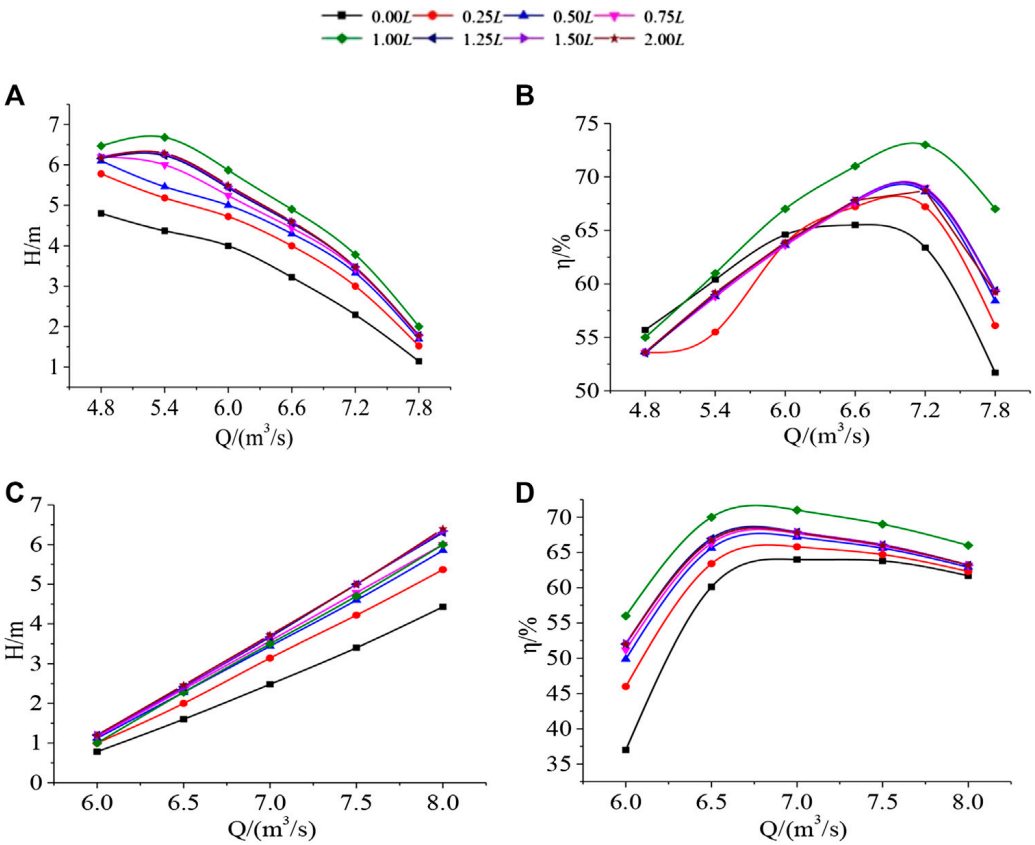

FIGURE 2.2 – Performance curves of pumps and turbines with different inter-stage clearances. (A) the pump head. (B) the pump efficiency. (C) the head curves of the turbine. (D) the efficiency curves of the turbine.[18]

Pavlenko et al.[19] studied the impact of impeller trimming on the energy efficiency of the rotating counter pump. The study revealed that the counter-rotating mechanism affects both the pressure and energy of the pump. Additionally, using the counter rotation pump can lead to reduced size and weight of the centrifugal pump.

An et al.[20] has researched the dynamics of axial counter rotation pump-turbine rotors operating in pump mode. The findings indicate that when both rotors move at the same speed, the rear rotor uses significantly more power. However, as the speed of the rear rotor declines, its power consumption drops in a linear trend. Notably, changing the speed of the rear rotor did not affect the vorticity of the front rotor.

The tip clearance effect of counter-rotating axial pump is numerically studied by Han et al.[21] Three-dimensional Navier-Stockes equation with RNG $k-\epsilon$ turbulence model is applied and Multiple

Reference Frame (MRF) method is used for the rotating fluid region. The minimum tip clearance value is 0.2 mm and the clearance coefficient σ is the ratio of tip clearance to the minimum value. The tip clearance has a small effect on the efficiency when the flow rate is less than 0.7 design flow rate, whereas by increasing flow rate the efficiency is changed remarkably by changing the tip clearance and it decreases by increasing the tip clearance and highest thrust coefficient is achieved when $\sigma = 4$.

Three CRP models with a different specific speed and two loss evaluation methods have been numerically investigated by Zhang et al.[22] The speed of the front rotor is 1500 and for the rear rotor, three different speeds are considered (1200 rpm, 1300 rpm, and 1400 rpm). The simulation was carried out by Ansys CFX and the results showed the total efficiency is maximum with the medium specific speed of the rear rotor. Although the high loss area occurred at the triangle edge because of corner separation but larger dissipation and loss are observed near the wall especially in the tip region. Loss near the tip leading edge is caused by the interaction of casing boundary layer, blade rows and other phenomena however loss near the tip leakage vortex may be the result of the blockage effect caused by the higher specific speed of the rear rotor.

A novel pumping system with a counter-rotating mechanism was suggested by Kanemoto et al.[23] It comprises two-stage axial flow impellers and a unique motor equipped with double rotors. Because of their smart control system, as the discharge decreases, the front impeller speed increases and then slows down to keep the relative speed steady. Meanwhile, the rear impeller speed slows and then rises with a drop at discharge. The head curve shows no upward trend, and the proposed counter-rotating design is expected to significantly improve stability. Additionally, it is anticipated that cavitation might be reduced at high discharge levels because of the decreased speed of the front impeller.

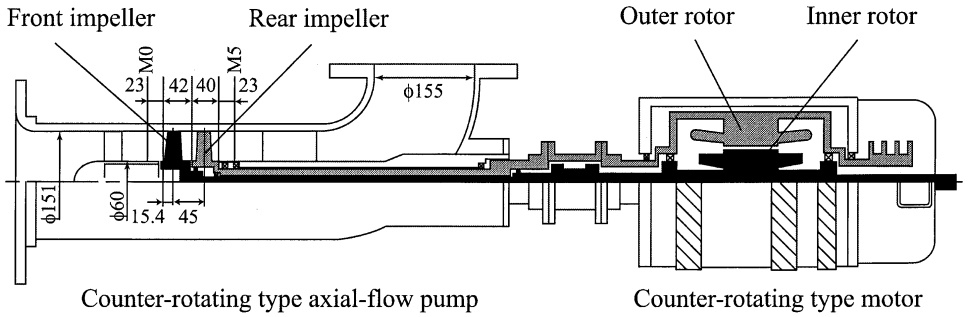

FIGURE 2.3 – Trial model of the counter-rotating type pumping system by Kanemoto et al.[23]

Cao et al.[24] studied the flow dynamics within an axial counter-rotative pump with a newly

optimized rear rotor design (Figure 2.3). Their findings indicate that while the new rear rotor performed well at the designated flow rate, there is a sharp upward trend in head rise performance within a particular range of low flow rates. The counter-rotation of the rear rotor significantly affects the flow leaving the front rotor, especially at low flow rates. Key characteristics of the internal flow within the rear rotor include the tip leakage vortex flow from the blade leading edge and the corner separation that forms at the base of the blade suction side.

Brizzolara et al.[25] investigated a comprehensive approach rooted in lifting line/lifting surface theory for creating modern high-speed counter rotating propellers. The influence of primary design elements in the novel design approach has been explored using application examples. Specifically, they examined the impact of strength and cavitation margins and the effect of applying an unloading function to the ideal circulation distribution. Min et al.[26] investigated the design and performance prediction techniques for the CRP system. Their findings indicate that a CRP system considerably enhance propulsion efficiency, leading to potential fuel savings.

Danlos et al.[27] carried out numerical simulations to evaluate a standard mono-rotor pump with two axial contra-rotating pumps. These pumps had identical specifications, but one system had a rotation speed reduced by 35% and the other had its size reduced by 25%. Their findings indicate that contra-rotating systems can enhance static efficiency by at least 18%. Numerical investigations of the flow dynamics inside contra-rotating axial flow pump rotors, with an emphasis on the rear rotor and its impact on pump performance show that there is not a significant flow recirculation near the hub exit of the rear rotor at partial flow rates. The tip leakage vortex displayed unsteady characteristics, causing a flow blockage in that zone. The interaction between the rotors was less pronounced at the design flow rate, but became more evident at partial flow rates[28].

Counter-rotating mix flow pump was investigated experimentally by Tosin et al[29] (Figure 2.4). Two prototypes of counter-rotating pump have been developed to improve the cavitation behavior and this aim is reached by redesigning the front rotor whereas the rest of the system is kept constant. Another research presented by Tosin et al[30] investigate a new counter-rotating approach with mixed and radial flow pumps for the first and second rotor respectively. Both rotors are developed by streamline curvature analysis and the optimization method is the Response Surface Method (RSM). An auto-adaptive approach that can vary the speed of each rotor independently to achieve the highest performance is presented. The front rotor of the system had a speed range between 1200 and 1450

rpm, while the rear rotor operated in counter-rotation mode with a speed range from 0 to 1048 rpm. Using RSM results in optimum design by combining the design speeds and pressure ratio for both rotors.

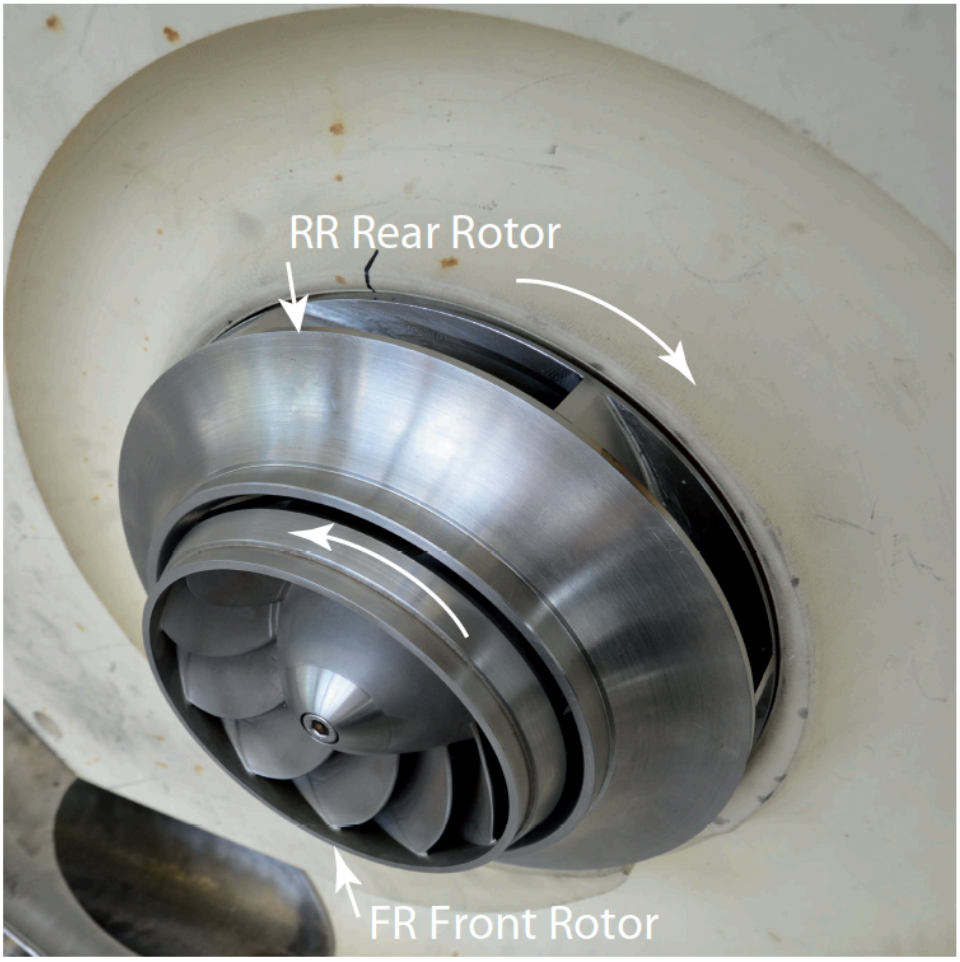

FIGURE 2.4 – Picture of the impellers in the test rig by Tosin et al.[29]

2.2 Centrifugal pumps with inducer

To improve the Net Positive Suction Head (NPSH) and prevent performance degradation, an axial impeller, known as an inducer, is positioned ahead of the primary centrifugal impeller. The inducer can either be a built-in component of the pump rotor or separately positioned on the pump shaft before the impeller. The primary aim when designing an inducer is to optimize suction capabilities. However, reaching its utmost efficiency is restricted by aspects of its structural design. This configura-

tion effectively increases the inlet pressure of the impeller. The main objective of inducer design is to ensure a sufficient cavitation margin rather than aiming for peak efficiency. The head rise of an inducer needs to be just sufficient to prevent cavitation in the main pump impeller[31], thereby maintaining and optimizing performance at the nominal operating point. Centrifugal impellers equipped with inducers are utilized in various industries, including the nuclear[32], aircraft, and marine industries and in cryogenic propellant pumping[33].

Centrifugal pumps are widely chosen in both domestic and industrial settings because of their simple design, compactness, and adaptability. They operate at high speeds and can be modified easily to match specific needs. They are often preferred over positive displacement pumps as they deliver a smooth and steady flow with little to no variations[34]. In liquid rocket propulsion systems, the turbopump can create cavitation at the inlet due to its high rotational speed. To enhance its suction capability, an inducer is added ahead of the impeller. However, cavitation issues like cavitation surge, rotating cavitation, and uneven cavitation can result in shaft vibrations and noise. Such disturbances might even damage the impeller. So, it is crucial to effectively manage suction performance and control these instabilities[35].

The inducer and centrifugal pump combination are widely used across various industries. This is largely because the inducer effectively boosts the pump suction performance, maintaining high head-rise even under challenging cavitation situations. Due to this effectiveness, there is an increased interest in understanding the performance limitation of the inducer when working under conditions set by the downstream centrifugal pump. Often in real-world application, the conditions are not aligned with the inducer nominal flow rate or rotational speed. This means the inducer might function at its standard flow rate, or it could be under conditions of overload or reduced load[36]. To select an appropriate inducer to pair with the impeller, it is essential to consider the efficiency of both components. The inducer should have optimal efficiency to ensure that when it is incorporated, the centrifugal pump also operates at its highest efficiency[37]. The study into the impact of the shunt blade inducer tip clearance on the centrifugal pump at low flow rates highlights the significant influence of this parameter on cavitation. The presence of tip clearance often leads to tip leakage cavitation, and cavitation is mainly observed at the inlet of the long blades[38]. The tip clearance of the inducer significantly impacts the efficiency and pressure of the centrifugal pump equipped with an inducer. At low flow rates, an increase in tip clearance leads to increased backflow and clearance leakage, resulting in a decrease in

both pressure and pump efficiency. However, at high flow rates, a larger tip clearance can eliminate blocked flow, leading to improvements in pump efficiency and pressure[39]. Aboelnil et al.[40] studied the influence of the helical inducer on a centrifugal pump performance and NPSH. Their findings indicate that while there is not a noticeable improvement in performance at higher speeds, at lower rotational speeds like 2000 rpm, efficiency increases by up to 20%. Additionally, the NPSH sees an improvement of up to 3%. Investigation the impact of the screw inducer on the vortex pump, suitable for transporting two-phase fluids with long fibers, reveals that adopting the screw inducer increases the pump head and enhance the internal flow of impeller. However, there is a slight decline in pump efficiency[41].

The interaction or clocking effect between the inducer and impeller on pump efficiency is examined by Yang et al.[42] A method that evaluates entropy production, while also correcting for wall effects, was employed to determine energy losses in a liquid rocket engine's oxygen turbopump. This approach aims to understand the origin of the clocking effect in terms of energy dissipation. Their results show that when the leading edge of the impeller blade aligns with the trailing edge of the inducer blade at a 0° relative angle, the best performance is achieved. On the other hand, the least efficient condition occurs when the inducer blade trailing edge is positioned midway between two consecutive impeller blades. Investigation on the entropy production across different pump components indicates that the main influence of the clocking effect on pump performance comes from turbulent dissipation within the impeller and diffuser. Direct dissipation and wall friction have a relatively lesser impact on this effect.

Understanding the pump characteristic curves is essential for designing the system for a liquid rocket engine. This information ensures that the pump inducer is designed to achieve the desired performance, even under non-ideal conditions. The cavitation can affect both the thermal and rotational efficiency of the pump, leading to vibrations. Proper design measures are essential to resolve these challenges[43]. Shamsuddeen et al[44] researched the impact of Inducer-Type Guide Vane (ITGV) on the hydraulic loss in the multistage centrifugal pump and noted an increase in the pump power consumption by 1.78%. However, there was an increase in the head by 5.78%, resulting in an overall efficiency gain of 3.94%. The second stage efficiency rose by 47.17%, with the pressure in this stage increasing by 63.28%. Flow analysis revealed changes in flow velocity in the interaction area between the volute and impeller due to ITGV. At off-design conditions, pump performance and pressure both

increased by 3.58% and 13.7%, respectively. For higher flow rates, pump performance and head showed increases of 17.87% and 18.45%. Implementing ITGV appears to have had a positive effect on pump efficiency by reducing losses in the second stage. Cui et al.[45] investigated the impact of the axial position inducer on energy loss in a centrifugal pump. Their findings suggest that this parameter has a minimal influence on the pump's performance.

2.3 Cavitation in turbomachines

R. E. Froude was the pioneer in introducing the term "cavitation" to highlight the phase transformation in a liquid, brought about by localized pressure drops due to dynamic movements. From a physical perspective, cavitation presents complexity as it combines both dynamic and thermodynamic interactions between two phases[46]. The evolution of cavitation in turbomachines typically begins with inception, characterized by a laminar separation cavity at the leading edges of blade tips or as tip vortex cavitation, then progresses to blade cavitation, a more expansive form which may appear on every other blade in certain moments, followed by developed cavitation marked by larger, periodically oscillating cavities, and concludes with cavitation breakdown where cavities greatly impact the flow and reduce the turbomachine efficiency[47].

In the blade inlet region, due to low suction pressure head combined with high flow velocity, there can be a significant drop in local pressure, sometimes falling below the liquid vapor pressure. This condition leads to the liquid vaporizing and the subsequent formation and growth of vapor cavities. The cavities then move downstream or towards the impeller walls in regions where the static pressure is higher than the fluid vapor pressure. These cavities quickly collapse, their volume disappears, and the void left behind is immediately filled by the surrounding liquid, which creates high-speed microjets. This process generates high localized pressure rises, which are the main causes of cavitation damage on the impeller and blade surfaces[48].

In pumps, cavitation can appear in different forms (Figure 2.5), primarily determined by the pump flow rate and the angle of the flow inlet velocity at the blade leading edge. These elements significantly influence the pressure distribution on the blade surfaces at the entrance. Cavitation first appears at the blade leading edge and its tip, leading to "tip vortex cavitation". With a slighter reduction in the cavitation number, traveling bubble cavitation develops on the blade suction sides. This is also

known as “bubble cavitation”. These cavities relate to a small angle of incoming flow and, based on the impeller design, they align with the area of lowest pressure at the impeller inlet[49]. Reducing further leads to the merging of bubbles, resulting in attached cavitation on the blade suction side. This is commonly called “blade cavitation” in pumps[50].

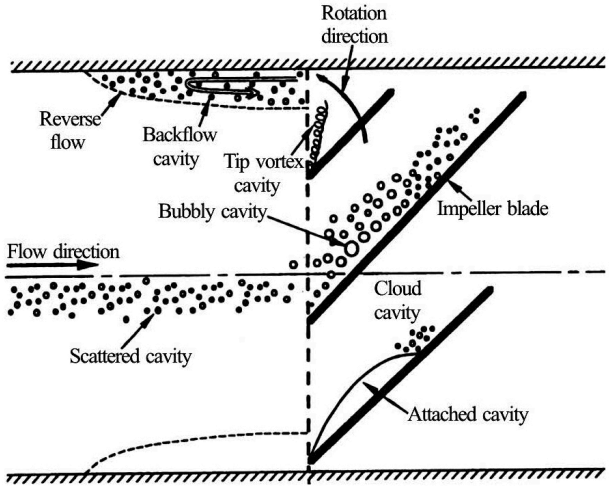

FIGURE 2.5 – Different type of cavitation in pumps[51]

Cavitation can cause damage to material surfaces near where the bubbles collapse as they move into areas of higher pressure. The consequences of cavitation can be costly and challenging to fix. Another negative outcome of cavitation is the notable reduction in the efficiency of pumps or other hydraulic mechanisms. Specifically, with pumps, there is a certain inlet pressure where the functionality drops sharply, known as cavitation breakdown. This issue has led to modifications in pump design to lessen the performance drop. In other words, designs have been optimized to function better even when cavitation occurs. The third negative consequence of cavitation is not as commonly understood. It affects not just the steady state of fluid flow but also its dynamic response. This change in flow dynamics can lead to instabilities that wouldn’t exist without cavitation. Examples include “rotating cavitation” which is similar to the rotating stall found in compressors, and “auto-oscillation,” comparable to compressor surge[51]. Analyzing three-dimensional unsteady cavitation flows in turbomachines is a complex challenge. No method has succeeded in capturing all of these effects completely[46].

The analyze of propeller cavitation using compressible Large Eddy Simulations (LES) is studied by bhatt et al.[52] and Wetted flow conditions were tested at a Reynolds number (Re) of 894,000 and an advance coefficient (J) of 0.89. The impact of shock capturing was evaluated by modifying the corrector

fluxes to align with the non-dissipative predictor step. A detailed examination of thrust/torque revealed extensive cavitation covering the full radial length of the blade's suction side and extending into the wake with areas of minimal void fraction.

2.3.1 Cavitation in centrifugal pump and inducer

During the last decades various experimental methods have been used for identifying cavitation in centrifugal pumps and inducers[48] like static pressure measurements[53, 54, 55, 56], acoustic and noise detection [57, 58, 59], vibration acceleration methods[60, 61, 62] and image visualization of cavitation[63, 64, 65].

The investigation of cavitation near the splitter-blade inducer as well as around the impeller in the centrifugal pump shows that as the rotational speed increases, the cavitation area increases and asymmetric cavitation is observed. The traid of inducer and the normal position of the tongue of the volute are two main area with higher chance of cavitation[66]. Huan et al.[67] researched the progression of cavitation in a centrifugal pump equipped with an inducer. Their findings suggest that cavitation begins at the tip of the inducer leading edge and extends to its hub as cavitation advances. As the cavity expands, the affected area extends downstream, influencing the pump pressure. While the intensity of backflow cavitation grows as cavitation progresses, no correlation between tip leakage cavitation and backflow cavitation was observed.

Coutier-Delgosha et al.[68] conducted a numerical analysis to investigate the characteristics of a four-blade inducer under both cavitating and non-cavitating conditions. Guo et al.[69] demonstrated that the number of blades on the inducer significantly influences the pump head and its resistance to cavitation. According to their experimental findings, a three-blade inducer outperforms two-blade or four-blade inducers in terms of efficiency, pressure, and cavitation resistance. Additionally, Guo et al.[70] studied the performance of a centrifugal pump with variable-pitch inducer at different rotational speed. They found that when the inducer speed is increased, there is a rise in the static pressure within both the inducer and the impeller, and this pressure is not symmetrical. On the other hand, accelerating the impeller speed results in a reduction of the lowest pressure in the impeller, subsequently diminishing the pump cavitation performance. Magne et al.[71] conducted experimental investigations on a three-bladed inducer, focusing on the effects of dissolved CO_2 and jet fuel on its performance. The study showed that the concentration of CO_2 had minimal impact on the inducer efficiency under

non-cavitating conditions but had a significant effect in the presence of cavitation. Through the use of a high-speed camera, they demonstrated that as pressure drops, vortex patterns emerge. The vortex rotates slower than the rotation speed of the inducer. Moreover, alterations in the inducer's inlet geometry don't influence the structure or creation of these vortices. Moreover, changes in the inducer inlet nozzle shape have no impact on the structure or development of these vortex structures. Bakir et al.[72] successfully developed a two-phase cavitation model for inducers and validated it through experimental tests. Their model demonstrated good agreement and correlation with the experimental findings in terms of pressure drop and identification of cavitation pockets. The inducer was designed with three blades, with an outer diameter of 235 mm, a 0.4 mm tip clearance, and a rotational speed of 1450 rpm, demonstrated strong performance under cavitation conditions by the experimental results. Due to the favorable characteristics of the inducer, a smaller version of it has been utilized in this thesis.

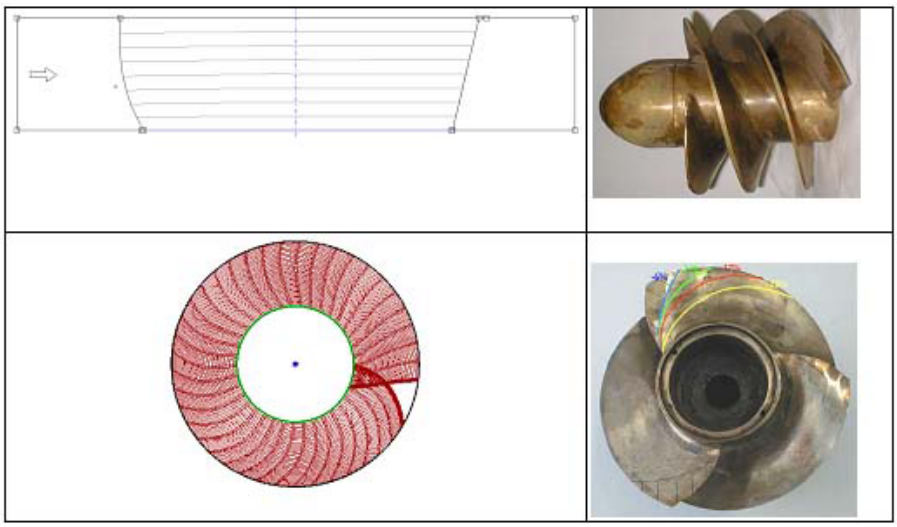

FIGURE 2.6 – Inducer designed by Bakir et al.[72]

Although the addition of an inducer to the centrifugal impeller enhances the hydraulic performance of the pump, it results in a 20% decrease in total pressure generated by the pump at a flow rate of 60% of the nominal flow rate due to the generation of pre-rotation[73]. Research on the impact of the radial height of a helical static blade on inducer cavitation performance has shown that the efficiency of the inducer decreases as the radial height of the helical static blade increases within specific ranges. They found that there is an optimal radial height range to improve the cavitation performance. Backflow and

vortex are consistently present in the channel of the helical static blade, intensifying with increasing radial height. This backflow results in the fluid having a reduced attack angle due to the blades reverse turning direction[74]. A visual experimental investigation conducted by Xu et al.[75] on a high-speed inducer revealed the development of a vortex at the inducer inlet rotating at half the inducer speed. The volume of the backflow vortex decreases with the flow rate and disappears completely at flow rates greater than 30% of the design flow rate. Campos-Amezcua et al.[76] investigated the cavitating flow through an axial two-bladed inducer, considering the effect of tip clearance. Based on the performance analysis of a centrifugal pump with variable pitch inducers operating at different speeds [39], it was observed that the static head increases with rotation speed. However, higher rotation speeds also lead to an increase in the NPSH, indicating a higher risk of cavitation in the pump. Kim et al.[77] examined the impact of existing inducers on centrifugal impellers. They found that under non-cavitating conditions, inducers enhance the head and efficiency at low flow rates. However, at high flow rates, they decrease both the head and efficiency. Numerical investigations on the matching between the inducer and the impeller indicate that as the distance between them increases, the distribution of bubbles becomes more uniform, improving the pump's cavitation performance. However, it is important to note that at high angles of attack, there is a decrease in pressure due to circumferential deflection[78].

2.4 Originality and novelty of this research

This chapter started by reviewing previous research on turbomachines that can rotate two rotors independently. It then covers the details of centrifugal pumps that used the impeller and the inducer. Numerous studies have looked into parameters that influence centrifugal pump with inducer efficiency and cavitation, such as blade angle, number of blades, tip clearance, rotational speed, etc. While there has been a lot of research on turbomachines with independent rotation of rotors like fan, turbine, compressors and axial pump, there is almost no researches on centrifugal pumps with both inducers and impellers that rotates independently. In all previously studied pumps that feature both inducers and impellers, the two components have shared the same shaft. This means they have consistently had identical rotation speeds and directions. This thesis presents a novel approach by examining a centrifugal pump in which the inducer and impeller operate on individual shafts, allowing them to rotate independently. This unique configuration provides a chance to investigate varied parameters,

such as the rotational speed ratio between the inducer and impeller and the rotational direction of inducer. Additionally, with the innovative incorporation of a slider in the experimental test bench, the research further explores the distance between the inducer and the impeller.

Chapitre 3

Materials and methods

content

3.1 Introduction

To research a pump with the ability for the inducer and impeller to rotate independently, the first step involves designing an appropriate inducer and impeller. Once the inducer and impeller designs are finalized, the next step is to design and construct a novel experimental test bench that can accommodate the independent rotation of these two rotors. This section explores the design procedures for the impellers, inducers, and the experimental test bench. Next, the procedures for conducting both non-cavitation and cavitation tests are described. Following that, the accuracy and repeatability of the experimental test bench outcomes are detailed. Lastly, the validation process for the pump similarity test is provided.

3.2 Impeller and inducer design

3.2.1 Centrifugal impeller

The design process for a pump begins with creating the impeller based on certain requirements. This section presents the design methodology for the impeller, highlighting its hydrodynamic and physical characteristics. In this research, a closed-type centrifugal impeller with 6 blades was developed. The preliminary design of the impeller employed the MFT and 3D Turbo software tools, products of the *Laboratoire d'Ingénierie des Fluides et des Systèmes Energétiques (LIFSE)*. The final design of the impeller was developed using CATIA software, which also helped in producing its blueprint. Using this software, the disk and shroud were designed to ensure compatibility with the impeller.

In the initial part of the thesis, a 6-blade aluminum impeller was utilized, designed with the assistance of MFT and 3D Turbo software. Upon designing, a cavitation test was conducted on the impeller. The results indicated that the impeller experienced cavitation at a speed of 2000 rpm under very low NPSH conditions. This means the effect of the inducer on the impeller could not be assessed since the impeller was not experiencing cavitation. Figure 3.1 displays the primary aluminum impeller.

The specific speed of an impeller in a pump is a dimensionless number used to describe the hydraulic performance of the impeller based on its shape, flow rate, and head. The equation for the specific speed N_s of an impeller is typically given by :

$$N_s = \frac{n\sqrt{Q}}{H^{3/4}}$$

Where N_s is the specific speed, n is the rotational speed of the impeller in revolutions per minute (RPM), Q is the flow rate through the pump or turbine in cubic meters per second (m^3/s), and H is the developed head in meters (m). The value of specific speed for this primary impeller is 51.

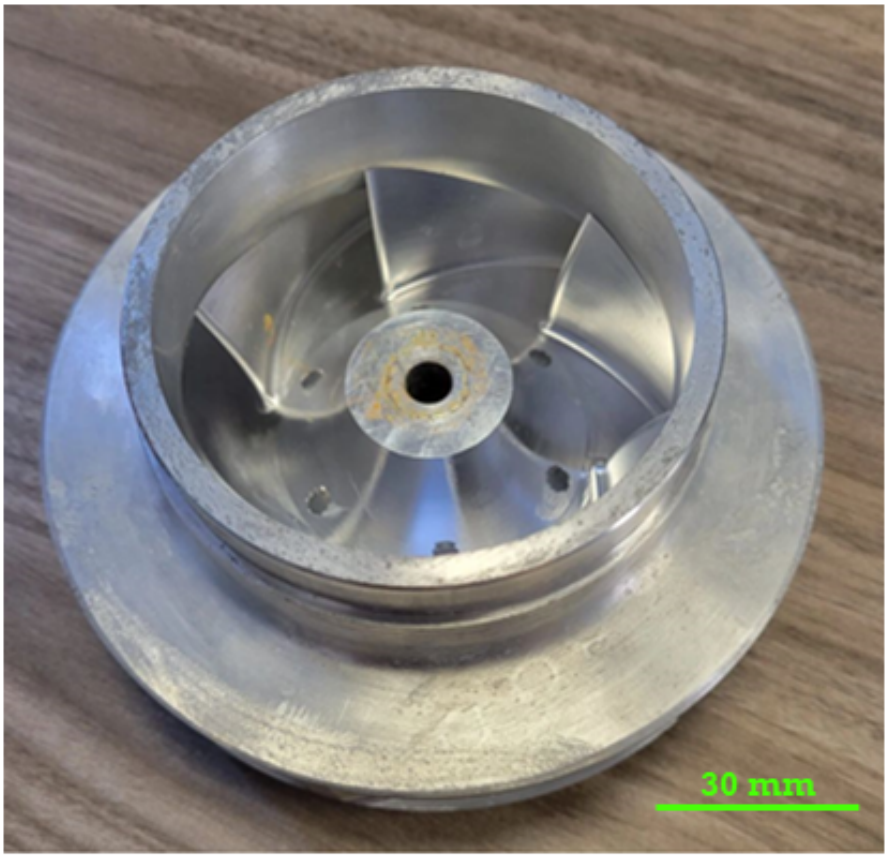

FIGURE 3.1 – Primary aluminium centrifugal impeller

The experimental results of the cavitation test on the primary designed impeller at 2000 rpm are shown in Figure 3.2. The data suggests that at this speed, cavitation happens in $NPSH$ lower than 0.5, even with high flow rates, making it challenging to analyze the inducer effect on the cavitation performance of the pump. There are two potential solutions : either increasing the impeller rotation speed, which was complicated due to experimental constraints, or adjusting the blade thickness to enhance the fluid velocity within the blade to apply cavitation in blades.

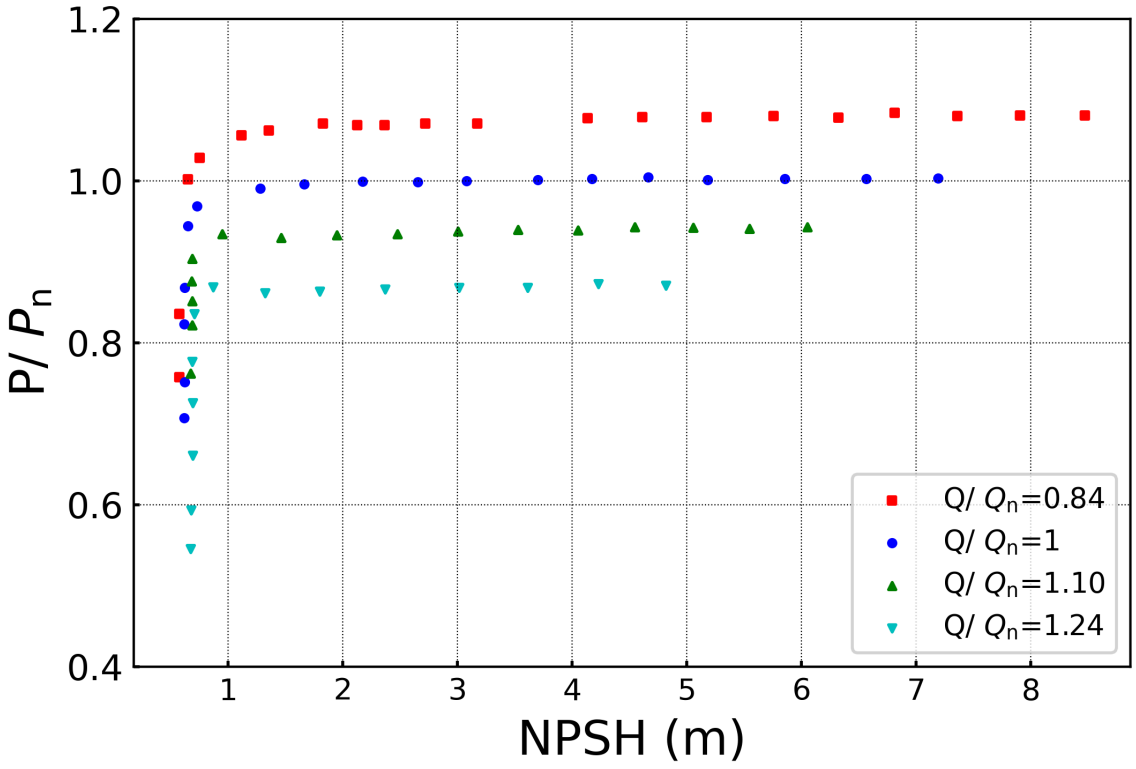

FIGURE 3.2 – Cavitation performance of the primary designed aluminium impeller at 2000 rpm for normalized pressure ($\frac{P}{P_n}$) and flow rate ($\frac{Q}{Q_n}$)

To increase the chance of cavitation in the impeller, the geometry of the primary impeller was modified. By reducing the cross-section between two blades and increasing the fluid speed in that area, there will be more chance of cavitation in the impeller. The design was further refined using the ANSYS BladeGen software, as shown in Figure 3.3. The impeller design is configured for a flow rate of 40 m^3/h (Q_n) and pressure of 560 mbar (P_n) at its Best Efficiency Point (BEP), with a rotational speed of 2000 rpm.

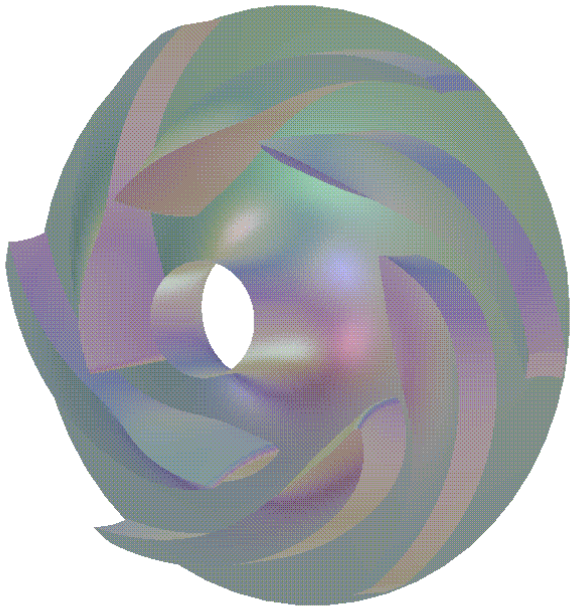

FIGURE 3.3 – Centrifugal impeller designed by ANSYS BladeGen

Table 3.1 presents the blade specifications for the centrifugal impeller. The parameters D_1, b_1, and β_1 correspond to the blade inlet diameter, blade inlet width, and blade angle at the inlet, respectively. Similarly, D_2, b_2, and β_2 correspond to the blade outlet diameter, blade outlet width, and blade angle at the outlet, respectively.

TABLE 3.1 – Geometrical characteristics of the impeller.

Parameters	Number of blades	D_1	b_1	β_1	D_2	b_2	β_2
Value	6	67.6 mm	23.3 mm	68.9°	134.2 mm	17.6 mm	70°

Figure 3.4 shows the six-blade closed centrifugal impeller manufactured using a stereolithography printer (SLA printer). A SLA printer is a specific type of 3D printer that utilizes the stereolithography technique to create three-dimensional objects from liquid resin. In this case, the printing process utilized black standard resin, known for its excellent mechanical properties and high-quality surface finish, both of which are crucial for ensuring the impeller functionality. The 3D printing method has the ability to produce objects with complex geometry such as impellers with precision and high strength

in a short time.

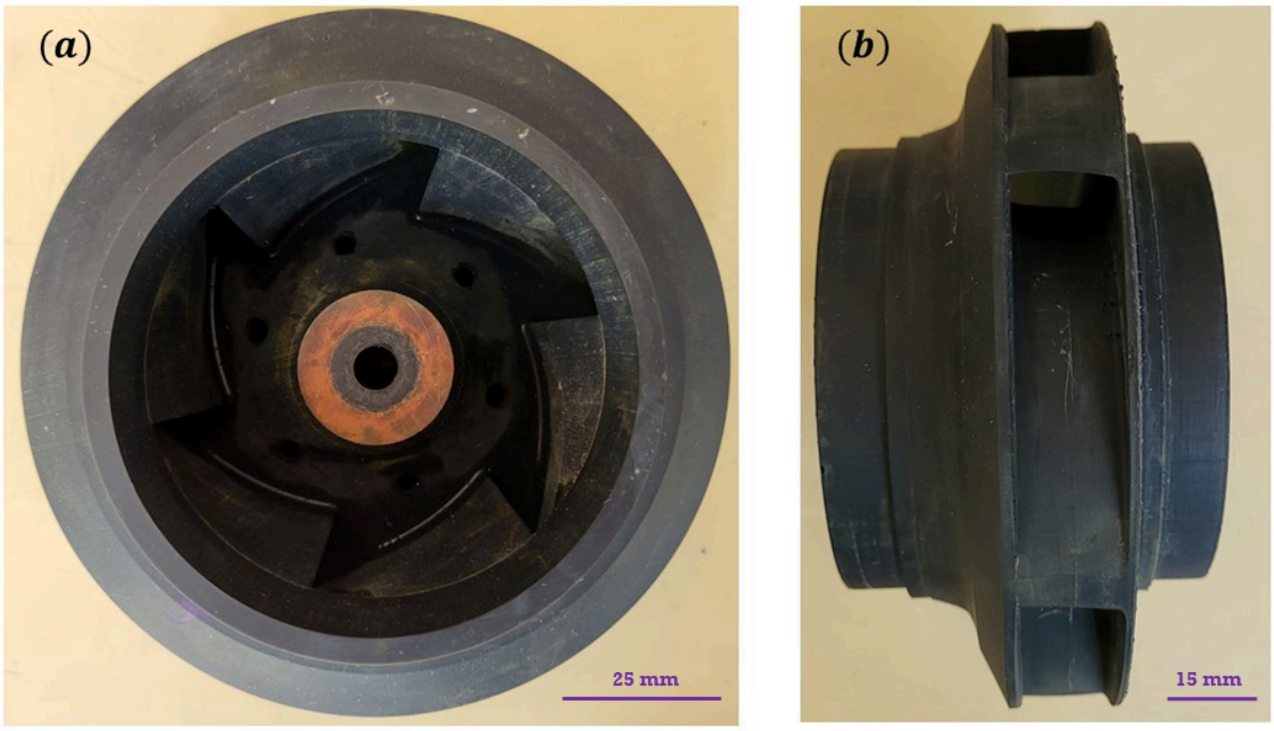

FIGURE 3.4 – (a) Front and (b) side views of the centrifugal impeller made by SLA method.

A comprehensive explanation of the impeller characteristic diagram and details can be found in the subsequent chapter.

3.2.2 Co-rotative inducer

After completing the design of the impeller, the inducer needs to be designed to align with the specifications of the impeller. The design of the inducer derived from modifications made to the inducer discussed in the article by Bakir et al[72]. Given that the original inducer demonstrated good cavitation performance, a scaled-down version of it was utilized for this thesis. For this objective, the 3D Turbo and MFT software are used to design a 3-blade inducer, as shown in Figure 3.5. Given the 80 mm diameter of the impeller inlet, it is neccessary for the outer diameter of the inducer to match it. Therefore, the inducer has an external radius of 39 mm, with an added 1 mm considered for tip clearance. The inner radius of the inducer is chosen based on a required shaft diameter of 12 mm.

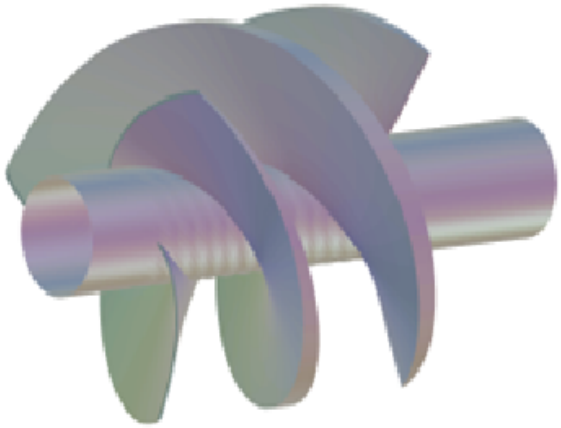

FIGURE 3.5 – Inducer designed by ANSYS BladeGen

Table 3.2 presents the specific characteristics of the inducer where R_1, R_2, θ, S_h, and S_t represent the internal radius, external radius, sweep angle, hub solidity, and tip solidity of the inducer, respectively.

TABLE 3.2 – Geometrical characteristics of the inducer.

Parameters	Number of blades	R_1	R_2	θ	S_h	S_t
Value	3	12 mm	39 mm	62°	3.8	2.15

The CATIA software was employed to develop and complete the construction blueprints for both the inducer and impeller. To reduce weight and prevent shaft bending and vibration at high speeds, the inducer is made of aluminum 6062, given the long shaft used in the inducer section. To align the characteristics of the inducer with those of the impeller, the inducer is designed to reach its optimal efficiency at a flow rate of $40\,\mathrm{m}^3/\mathrm{h}$ (Q_n) when rotating at a speed of 2500 rpm. This matches the best efficiency point of the impeller. The characteristic diagram for the inducer, along with details about its pressure and efficiency, will be discussed in the following chapter.

3.2.3 Counter-rotative inducer

To achieve reverse rotation of the inducer while maintaining its characteristics, only the angles of the blades were reversed. As a result, the co-rotative and counter-rotative inducers exhibit identical performance characteristics. A comparison of these two types of inducers, which operate in opposite directions but with the same performance characteristics, can be seen in Figure 3.6.

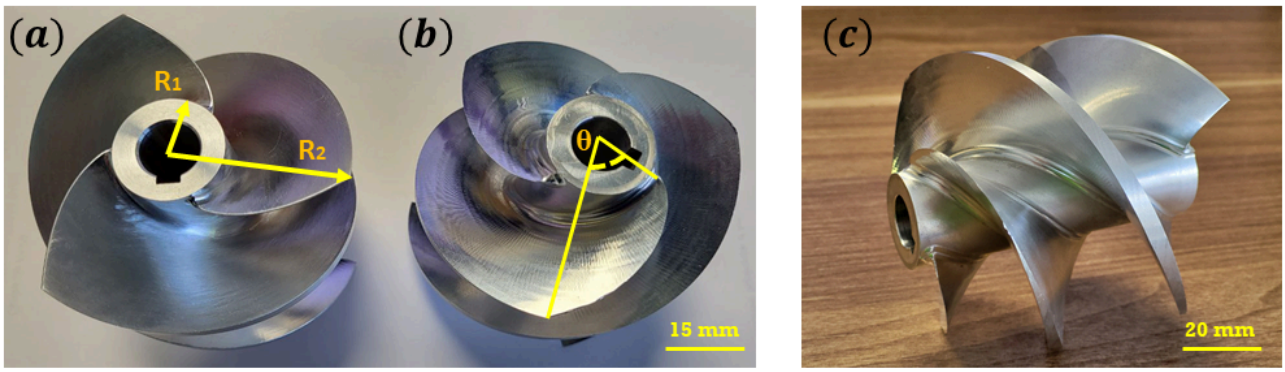

FIGURE 3.6 – Front view of the (a) counter-rotative and (b) co-rotative inducers and (c) side view of the co-rotative inducer.

3.2.4 Diffuser

As shown in Figure 3.7, the diffuser is manufactured with Fused Deposition Modeling (FDM) printing methods. Using this printing approach offers a cost-effective and quick way to produce diverse geometries like diffusers and impellers. To produce a three-dimensional product using the FDM printing method, a thermoplastic filament is melted and extruded layer by layer, fusing to the one below it.

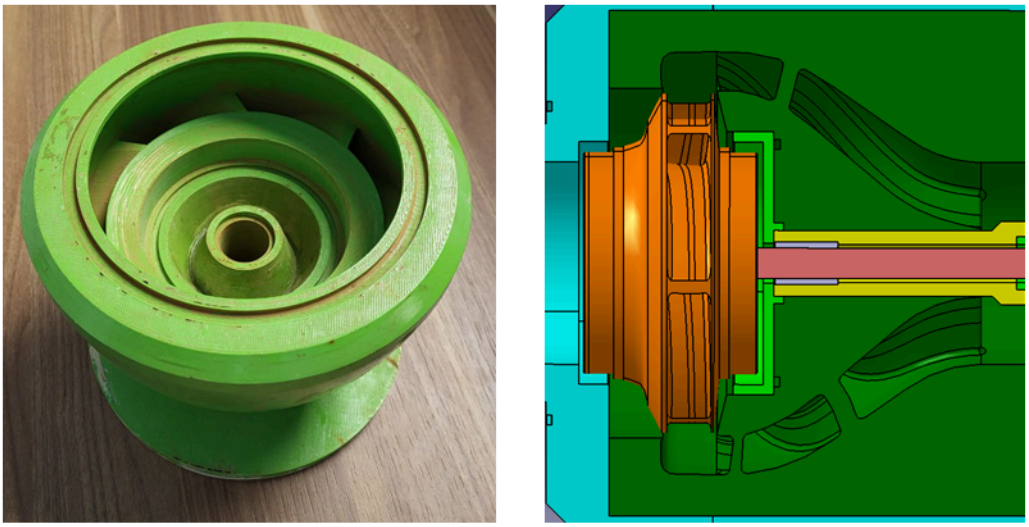

FIGURE 3.7 – Left) Diffuser made by FDM method and right) schematic of diffuser assembled in test bench

The FDM method is appropriate for generating complex and rapid geometric parts, much like SLA, but with a notable difference : the strength of parts produced by SLA is higher due to the difference in materials used and how the parts are printed. In this study, the SLA method was selected for impeller fabrication because it is a moving part and is subjected to pressure and radial and axial forces. However, due to the larger dimensions of the diffuser, it was not feasible to produce it with the SLA printer, and since the diffuser is a stationary part and does not rotate, the strength of the part printed by FDM is sufficient to conduct the tests.

3.3 Description of test bench

3.3.1 Test bench components design

After finalizing the design of the impeller and inducer, a novel experimental test bench was developed for the pump system. This test bench incorporates unique characteristics that enable the two rotors to be operated individually and to be positioned at varying distances from each other. The entire test bench is divided into two main sections : the impeller section and the inducer section. Each of these was designed separately before being combined to form the complete test bench (Figure 3.8).

The impeller section is an integral part of the overall system. This section is powered by a Dietz 30-kW electric motor, which propels the impeller to rotate up to 20000 rpm. The motor, as the primary

driver, ensures consistent and efficient performance. The shaft is designed to connect directly to the impeller, purposefully designed to hold the impeller in place and ensure its seamless operation. This shaft is held in position and supported by two bearings. Each bearing plays a unique role : one has the ability to support both radial and axial loads, ensuring the shaft remains stable during operations. The other bearing, made of self-lubricating bronze, is adept at operating in water, reducing the need for constant maintenance and ensuring the lifetime of the bearing.

In contrast, the inducer section, which is slightly smaller in scale, is powered by an ABB 4-kW motor. This motor is used to rotate the inducer up to 3000 rpm. Just like the impeller section, a shaft is used here to mount the inducer. This shaft is also supported by two bearings. These bearings mirror the specifications of those in the impeller section, ensuring uniformity in design and functionality. Ensuring the fine sealing and connections between the static components is achieved using O-rings sealer. These O-rings are customized and calculated to the exact dimensions of each fixed part to ensure the sealing of the system. For rotating parts, both in the inducer and impeller sections, mechanical seals come into play on the shafts. Generally, with increased fluid pressure, these seals offer better sealing. However, in this system, the inducer is placed in front of the impeller, exposing it to the low-pressure side of the system. This unique position makes sealing during inducer rotation a challenge. To solve this problem, an innovative design has been incorporated : the mechanical seal remains slightly pressurized. This design provides superior sealing and ensures that there is no leakage from the mechanical sealing part of the inducer but causes the inducer motor to consume more power, slightly reducing its efficiency. The rotational force of the motors is transmitted to the shafts by spring couplings, which have the ability to neutralize a slight misalignment and angular deviation.

Figure 3.9 shows the crop view of the test bench with different parts and details. As can be seen, the test bench consists of various complex parts that are designed and assembled in the CATIA to evaluate the accuracy of the design and prepare the construction drawings.

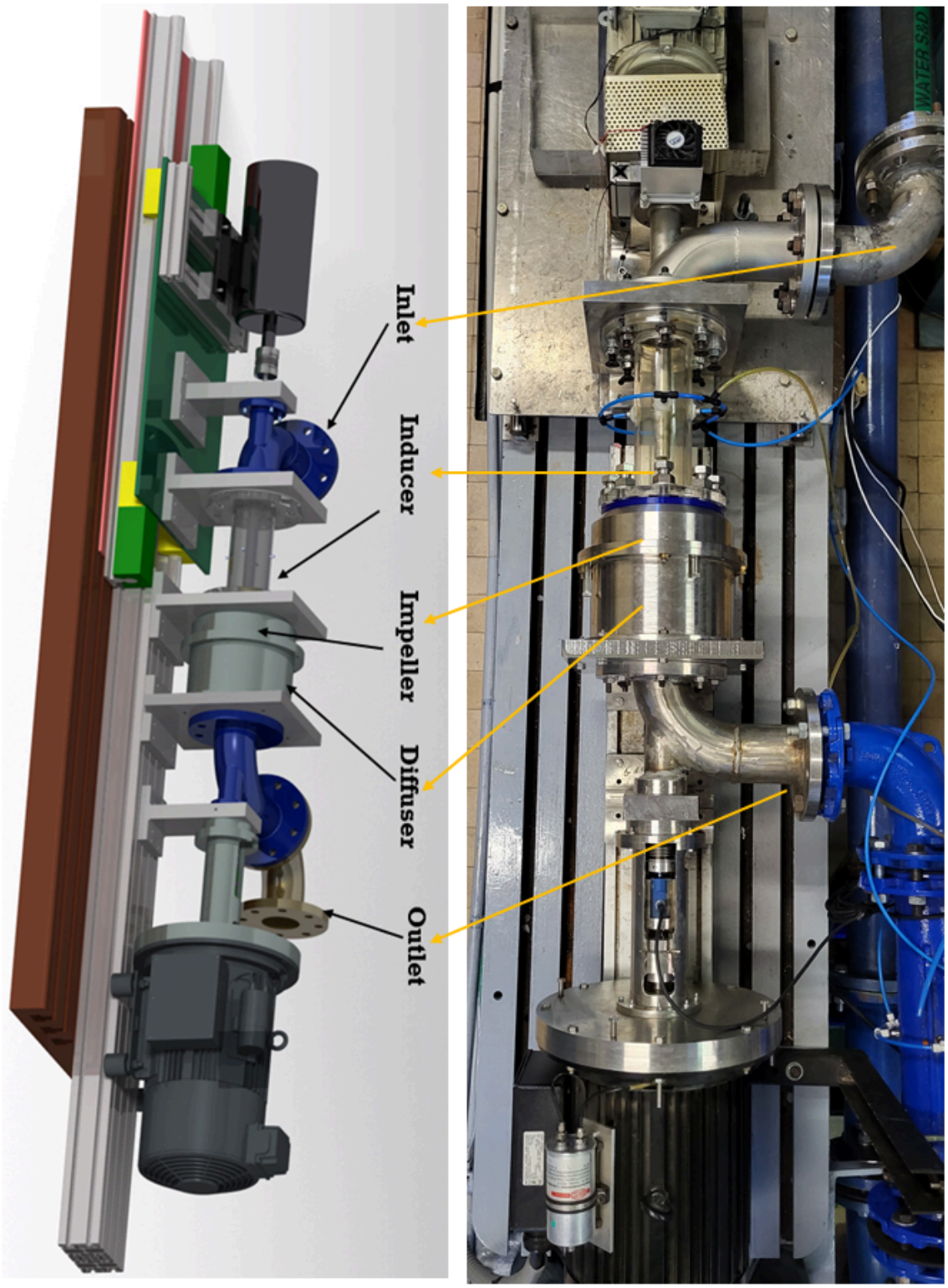

FIGURE 3.8 – Schematic and constructed experimental test bench

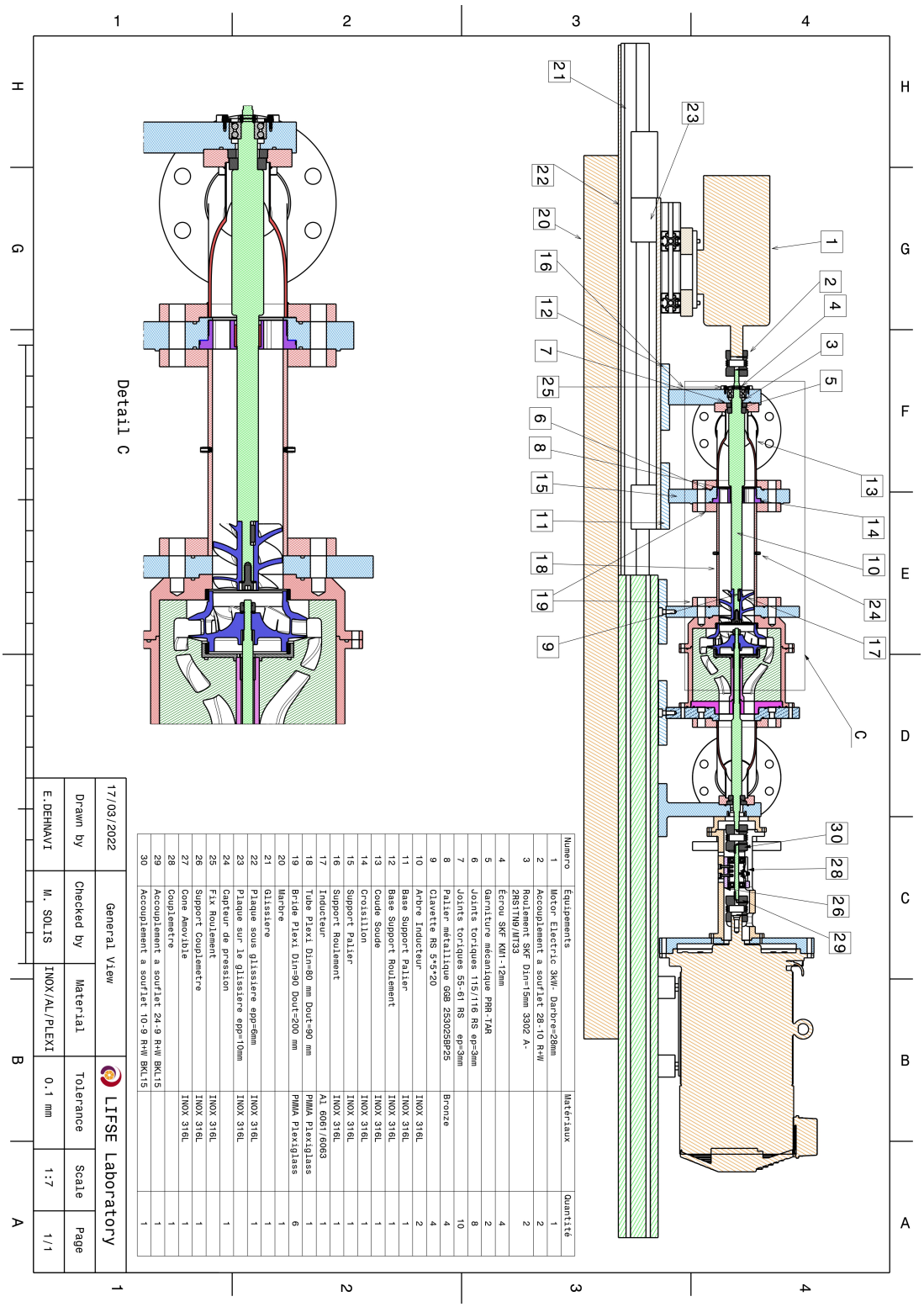

FIGURE 3.9 – Schematic crop view of designed test bench with detailed parts.

3.3.1.1 Shaft

The inducer shaft was designed to be compatible with the other components on the test bench. To determine its durability and compatibility, it was subjected to both stress and frequency simulatedevaluations. In Figure 3.10, it is demonstrated that the maximum displacement of the shaft is almost negligible. Moreover, a stress of about 10 MPa was recorded on the shaft, which, when compared to its maximum allowable limit of 345 MPa, is quite low. This indicates that the shaft met the necessary strength criteria. Another essential factor that was assessed is the natural frequency of the shaft, as it has potential implications on system vibrations. Upon assessment, it was revealed that the shaft first natural frequency stands at 341 Hz. This value is significantly higher than the rotational speed that the shaft is intended to operate at, ensuring stability in its functioning.

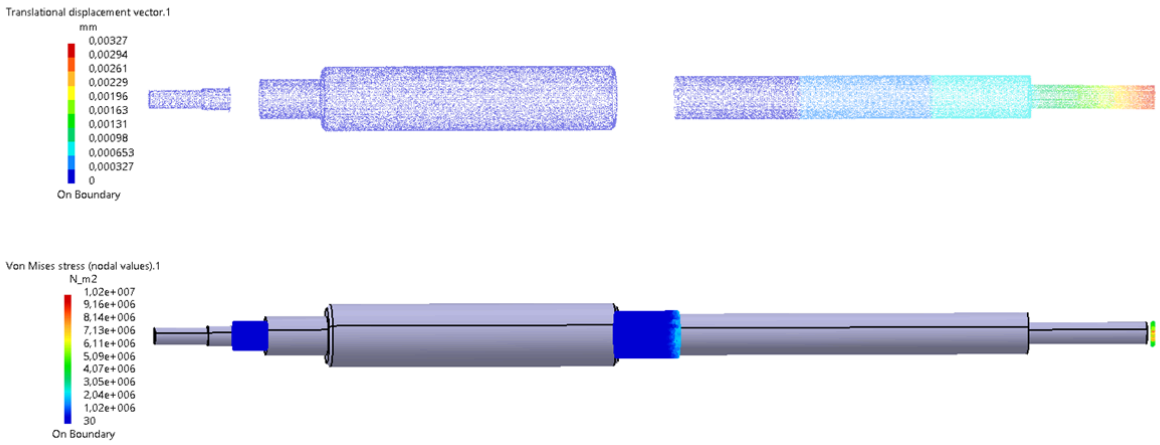

FIGURE 3.10 – Inducer shaft stress and displacement analysis

3.3.1.2 Ball bearing support

The design of the supports for the shaft rotation is particularly important in the independent rotation setup because of the long length of the inducer shaft. To ensure stability and reduce vibration, two supports have been integrated into the design to assist the shaft. As depicted in Figure 3.11, the

primary support is a structure that houses the bearing. For enhanced reliability and to ensure optimal performance, a double row angular contact ball bearing has been selected. This bearing has a dynamic load capacity of 15 kN and a static load capacity of 8 kN, along with the ability to operate at rotational speeds up to 12000 rpm. Notably, these specifications exceed the basic requirements of the design, ensuring added safety and longevity for the test bench.

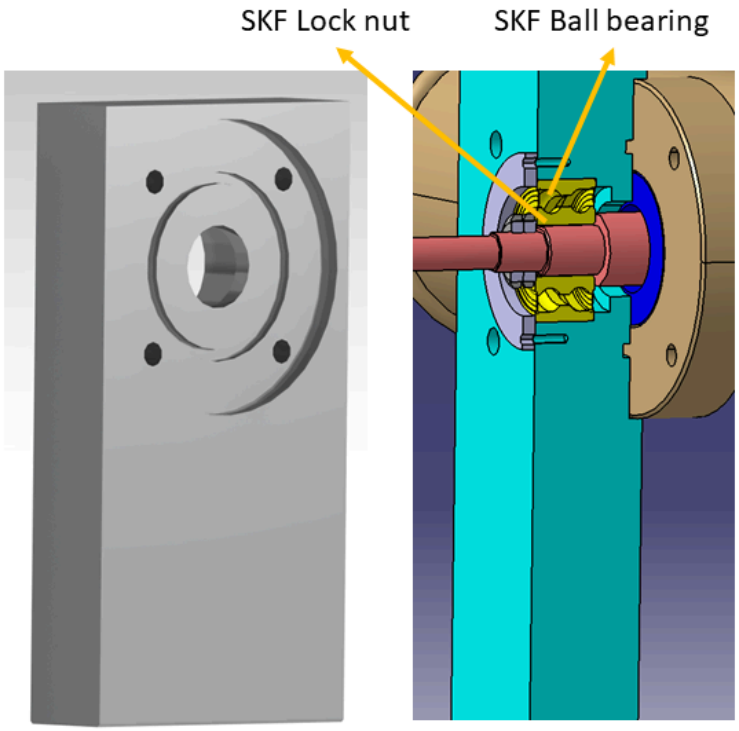

FIGURE 3.11 – Ball bearing support

3.3.1.3 Inlet elbow

Since the two rotors are mounted on separate shafts in the independent rotation mode, the input flow must approach the blades through an elbow. This is accomplished by designing a 90-degree elbow that allows the input flow to come from one side of the inducer shaft and from the other side. Additionally, the rigid portion of the mechanical seal is held in place by this component. As seen in Figure 3.12, this component serves as a holder for the mechanical seal fixed part as well.

In the independent rotation system with two separate electric motors and shafts, using a continuous straight pipe to direct fluid to the inducer inlet becomes a challenge. As a solution to this challenge,

a 90-degree elbow was incorporated into the system in this study. Water is directed into the system through one end of this elbow, while the inducer shaft is introduced into the system from the other sides. Beyond its primary function of directing the fluid, the elbow is also tasked with maintaining the stationary part of the mechanical seal of the shaft. Figure 3.12 shows the elbow designed for the input of the system.

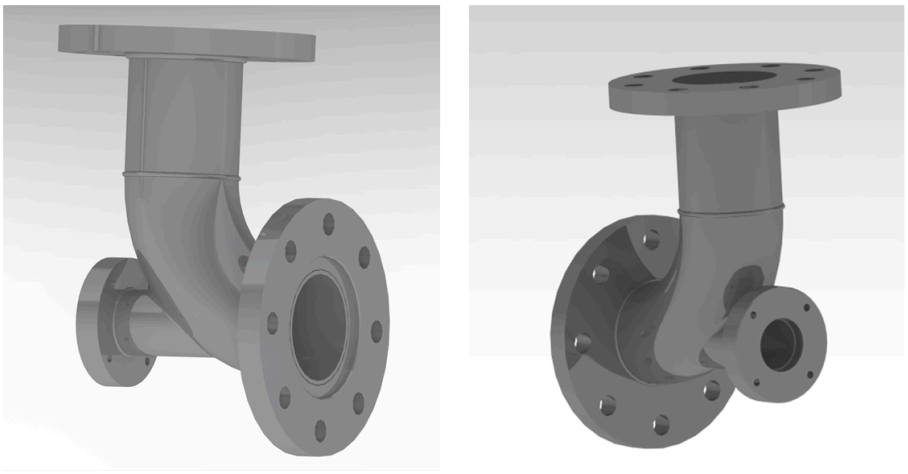

FIGURE 3.12 – Inlet elbow

3.3.1.4 Support of second bearing

To prevent vibration, two supports have been employed in the inducer part due to the use of a long shaft. The second support is situated in the water, making it impossible to use conventional bearings. Instead, self-lubricating bronze bearing that can function in a water environment have been utilized. The location of this support is shown in Figure 3.13, which comprises two distinct internal and external components to facilitate assembly. In the design, the fluid is channeled to the inducer inlet using a 90-degree elbow. Due to this setup, it is essential to figure out the correct distance between the elbow and the inducer inlet, ensuring the flow is unaffected by the elbow at the inlet of inducer. Using this configuration design results in the inducer shaft being extended compared to what is commonly observed in standard setups. A longer shaft, however, can lead to two main concerns : potential bending and increased vibrations, especially when operating at higher speeds. To prevent the inducer shaft from vibrating or bending, particularly at high speeds, an additional support is added

after the elbow. Since this section of the shaft is submerged in water, standard supports like ball bearing that are used in the initial part of the shaft aren't suitable. Therefore, a water-compatible, self-lubricating bronze bearing is employed here.

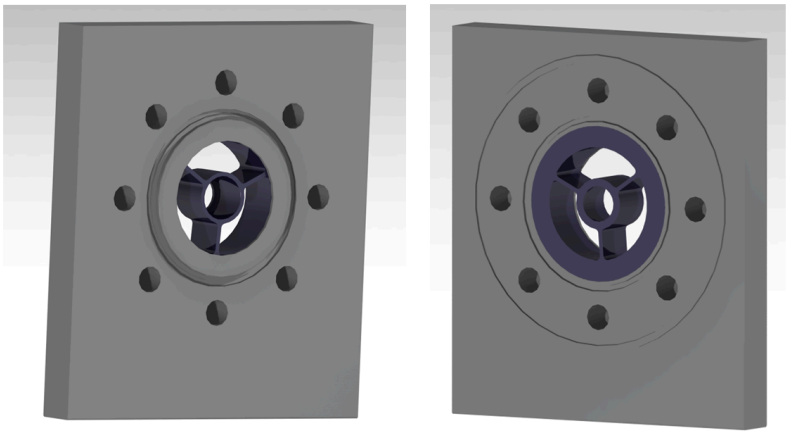

FIGURE 3.13 – Support of second bearing

3.3.2 Inducer shaft cooling system

In this novel test bench, the inducer is positioned in front of the impeller with its shaft coming from the opposite side. The end of the inducer shaft, linked to the motor and the mechanical seal, is at the inlet of the system. Here, as water flows, it is not under pressure and even experiences a drop in pressure. This makes the inducer mechanical seal ineffective at sealing the system because its operation relies on pressure. To solve this challenge, the design ensures that the mechanical seal always has pressure, which maintains the sealing during cavitation tests. However, this design introduces more mechanical losses in the inducer section and causes the mechanical seal to heat up. To manage the rising temperature of the mechanical seal, a cooling mechanism, as shown in Figure 3.14, is used. This system includes two heat exchangers with fans on both sides of the support to dissipate heat into the surrounding air.

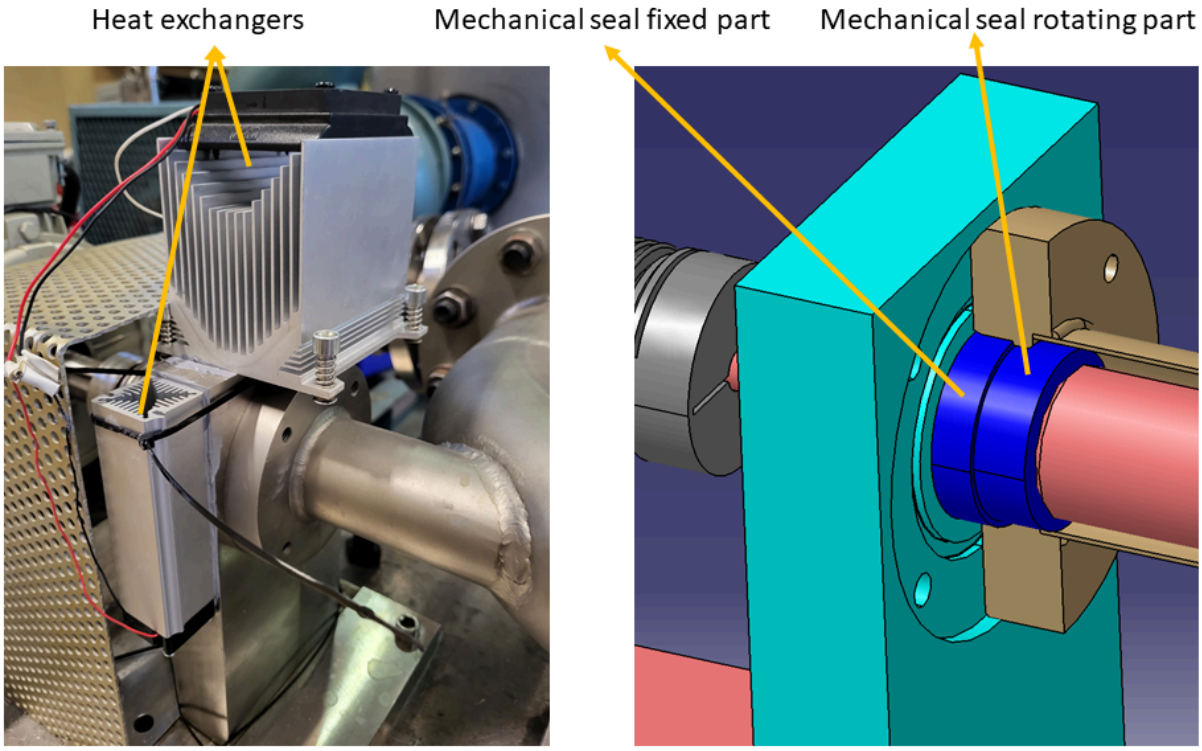

FIGURE 3.14 – Inducer shaft cooling system

3.3.3 Interaction of inducer and impeller section

The inducer section in the test bench is mounted on a slider that is connected to the plate below it with a screw, allowing for easy replacement and adjustment of the distance between the inducer and the impeller, which is an important parameter in this study. The use of a slider offers two key advantages : it simplifies the process of separating the inducer section from the impeller section for maintenance or replacement, and it enables the adjustment of the distance between the two components. To facilitate the observation of the inducer and cavitation phenomenon, a transparent plexiglass tube with a 90 mm external diameter and 5 mm thickness is used to enclose the inducer. By adjusting the length of the tubes, the distance between the inducer and the impeller can be changed. In this thesis, to adjust the distance between the inducer and the impeller, two plexiglass tubes of 270 mm and 330 mm in length are utilized, corresponding to inducer distances of 20 mm and 80 mm, respectively.

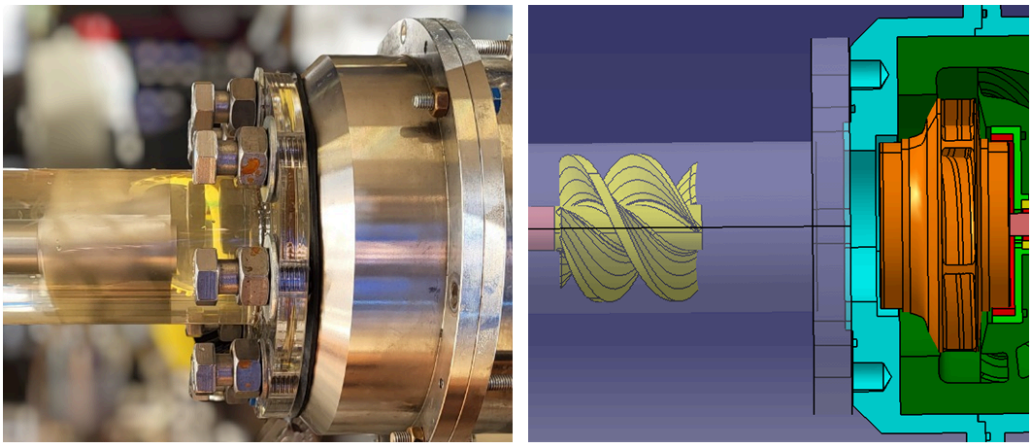

FIGURE 3.15 – Photography and schematic of the test section including inducer and impeller in the test bench

Figure 3.15 illustrates the interaction between the impeller and the inducer. Despite efforts to minimize the gap between the two rotors, design constraints result in a consistent gap between them. Even at the closest point of the inducer to the impeller, there remains a gap to ensure the independent rotation of each rotor and enable high-speed rotation. This gap ranges from 20mm to 80mm depending on the case. Following the interaction between the impeller and inducer, the water flow passes through a diffuser and exits through an elbow. As shown in Figure 3.16, the test bench is designed to operate within a closed circulation that includes a water tank, a vacuum pump, and a flow meter. The tank has a volume of 1000 liters and is fitted with two pressure gauges for measuring positive and negative pressure. In addition, there is an inlet valve for filling the tank, a valve connected to atmospheric air for regulating system pressure, and a valve for connecting the vacuum pump. An Edward vacuum pump with a pumping capacity of 17.1 m^3/h has been utilized to reduce the system pressure, capable of reducing it to as low as 0.007 mbar. Figure 3.16 indicates the direction of flow in the system. Two valves are situated at both the inlet and outlet to regulate the flow rate and a flow meter is installed before the outlet valve to measure the flow rate.

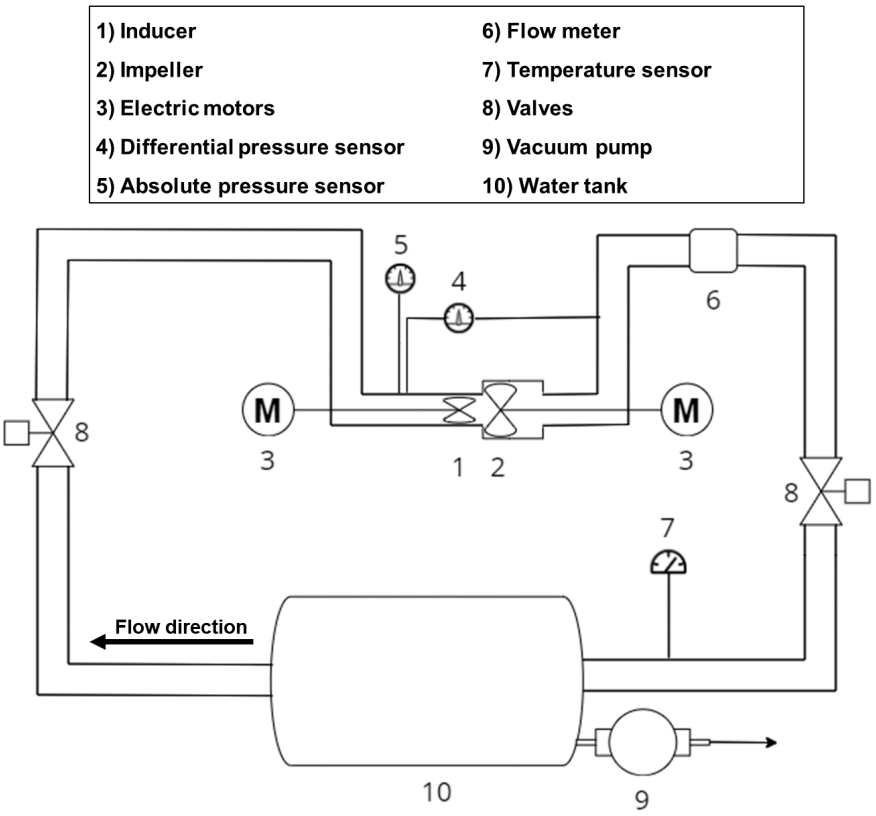

FIGURE 3.16 – Test bench and circulation system

3.3.4 Inducer section and slider mechanism

The space between the inducer and the impeller can be varied by using plexiglass tubes of various sizes. To change this distance or to replace the inducer, the inducer and impeller sections must be separated. For this, a slider is integrated into the inducer section, as shown in Figure 3.17. This slider allows for adjusting the inducer's position without changing the placement of the shaft or its supports. After setting the inducer and the desired distance, a locking screw is used to secure the setup. This screw attaches the inducer and slider to a base made of cast iron. Also, a thick plexiglass block is positioned under the motor, ensuring vibrations from the motor are transferred to the ground and avoiding system vibration and resonance.

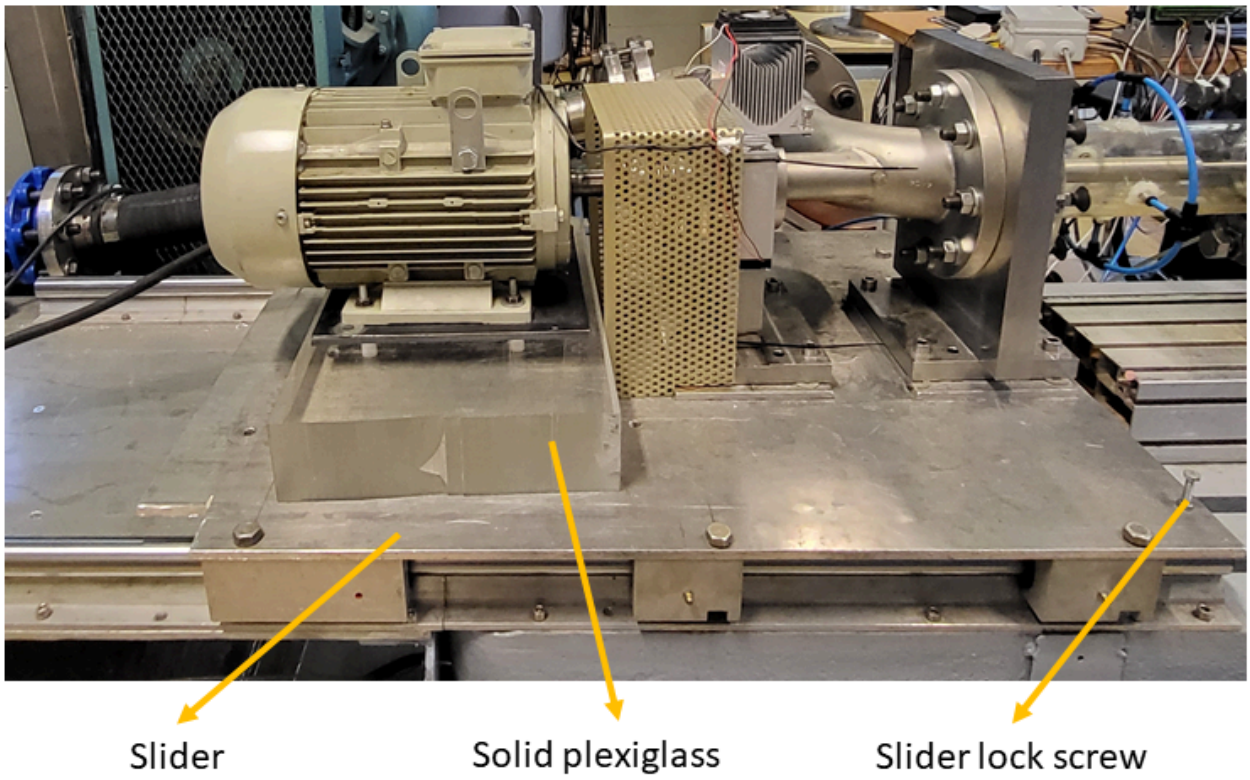

FIGURE 3.17 – Slider parts and mechanism

3.4 Uncertainty and measuring instruments

This section provides an overview of the measuring equipment used in the setup. The measured value and its true value usually define the difference as the error in a measurement. A possible value that an error may have is referred to as uncertainty[79]. The uncertainty in a measurement is often derived from the limitations of the instruments used or to statistical variations in the value observed. No matter its origin, the importance of recognizing and evaluating this uncertainty cannot be overstated. Based on this knowledge, the level of trust given to the recorded value can be determined.

In this study, based on the properties of the sensors utilized for measurement, the uncertainties of the existing sensors can be categorized into two groups : absolute and relative uncertainties. Absolute uncertainty is defined by specific numerical values that indicate the precision of the sensor. In this context, the flow meter sensor has an absolute uncertainty of 0.6 m^3/h. On the other hand, relative uncertainty is determined using the given formula :

$$\frac{\delta x}{x} = \frac{\text{Absolute Uncertainty } (\delta x)}{\text{Measured Value } (x)} \tag{3.1}$$

By applying the given formula and using the range and absolute uncertainty values of the flow meter sensor, the flow meter relative uncertainty is 0.2%. For the other sensors used in this study, the manufacturer provides the relative uncertainty of the sensor. An absolute pressure transducer with a range of 0 to 2.5 bar and an uncertainty of 0.1% is positioned at the inlet of the inducer to measure the absolute pressure. A differential pressure transmitter with a measurement range of 0 to 3 bar and an uncertainty of 0.1% is connected to the inlet and outlet of the pump to measure the pressure produced by the pump. A torque sensor, with a measurement range of 0 to 20 Nm and an uncertainty of 0.5%, is placed between the electric motor and the impeller shaft to calculate the torque transmitted to the centrifuge impeller. The impeller rotational speed is controlled by a DANFOSS variable-frequency drive, which is capable of adjusting the impeller rotational speed and calculating the power consumption of the impeller. Similarly, in the inducer section, a 4-kW motor is rotated by an ABB variable-frequency drive, which also measures the power consumption of the inducer. The flow rate is measured by an Endress+Hauser flowmeter with a measurement accuracy of 0.6 m^3/h and measuring capacity of 282 m^3/h, located at the outlet of the pump. In experimental measurements, two primary errors are typically existed : random error and systematic error. The random errors are described as errors that change during the measurement period and systematic errors are defined as errors that remain constant throughout the measurement period[80].

3.4.1 Gaussian distribution

When measurement variations come from numerous small errors of the same magnitude, with each error having an equal probability of being positive or negative, the distribution of an infinite sequence of these measurements aligns with the Gaussian or normal distribution. The equation for the Gaussian distribution is :

$$f(X) = \frac{1}{\sigma\sqrt{2\pi}} e^{-\frac{(X-\mu)^2}{2\sigma^2}} \tag{3.2}$$

where $f(X)$ is the probability that a single measurement of X will lie between X and $X + \mathrm{d}X$, μ is the distribution mean defined as :

$$\mu = \lim_{N\to\infty} \frac{1}{N} \sum_{i=1}^{N} X_i \tag{3.3}$$

and σ is the distribution standard deviation defined as :

$$\sigma = \lim_{N\to\infty}\left[\frac{1}{N}\sum_{i=1}^{N}(X_i-\mu)^2\right]^{1/2} \tag{3.4}$$

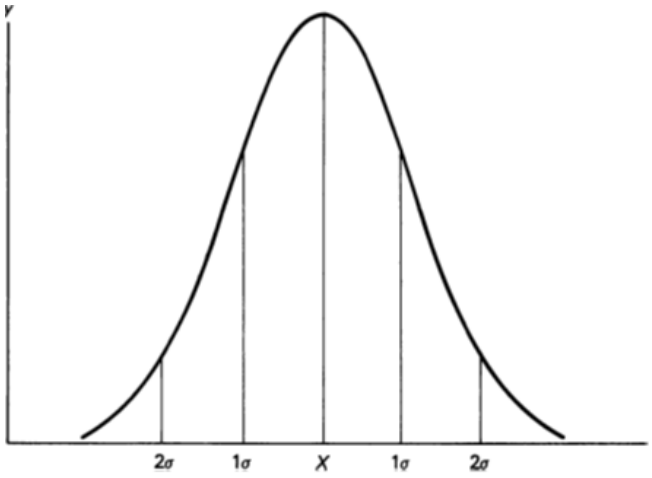

FIGURE 3.18 – Plot of the Gaussian distribution showing the different values of standard deviation[81].

In a Gaussian distribution, the area enclosed within the range $X \pm \sigma$ is 68% of the total area under the curve, while the area within the range $X \pm 2\sigma$ covers 95%.

3.4.2 Output uncertainty

Now, after determining the uncertainty for each of the measured values, the uncertainty must also be calculated for the values derived from the equations. If the equation is an addition or substraction equation, like the equation below :

$$q = x + \cdots + z - (u + \cdots + w) \tag{3.5}$$

uncertainty will be calculated from the following equation :

$$\delta q = \sqrt{(\delta x)^2 + \cdots + (\delta z)^2 + (\delta u)^2 + \cdots + (\delta w)^2} \tag{3.6}$$

If the calculated value is according to the following equation :

$$q = \frac{x \times \cdots \times z}{u \times \cdots \times w} \tag{3.7}$$

uncertainty will be calculated from the following equation[82] :

$$\frac{\delta q}{|q|} = \sqrt{\left(\frac{\delta x}{x}\right)^2 + \cdots + \left(\frac{\delta z}{z}\right)^2 + \left(\frac{\delta u}{u}\right)^2 + \cdots + \left(\frac{\delta w}{w}\right)^2} \tag{3.8}$$

In this research, derived values that rely on multiple measured values include pump efficiency, determined using the subsequent equation :

$$\text{Efficiency} = \frac{\Delta P \times Q}{T\omega} \tag{3.9}$$

where ΔP represents the pressure difference measured by the differential pressure gauge, Q shows the flow rate measured by the flowmeter, T is the torque as measured by the torque meter, and ω indicates the shaft rotation speed. The uncertainty in the efficiency calculation, determined by the following equation :

$$\frac{\delta \text{Eff}}{|\text{Eff}|} = \sqrt{\left(\frac{\delta \Delta P}{\Delta P}\right)^2 + \left(\frac{\delta Q}{Q}\right)^2 + \left(\frac{\delta T}{T}\right)^2} = \sqrt{(0.1)^2 + (0.2)^2 + (0.5)^2} = 0.5\% \tag{3.10}$$

3.4.3 Data acquisition system

The process of data collection is done automatically and all the sensors are connected to a NI instruments Data Acquisition module (DAQ) and the output signals are read by this card and transferred to the computer. All the data can be viewed and saved in real time using the graphic coding by LabView software. The NI Instruments 9207 module was utilized for data collection. Its capability to offer 8 voltage inputs and 8 current inputs eliminates the need for an additional module when handling sensors with varying voltage and current outputs. However, given the unique output of temperature sensors, the 9217 NI Instrument temperature module is employed to collect the water temperature in the system. This module automatically recognizes the temperature sensor type and directly displays the temperature output.

The differential pressure gauge sensor operates within a range of 0 to 3 bar and produces an output current ranging from 4 to 20 mA. Given the sensor specifications and the linear relationship between the current output and pressure, a linear equation is employed in the LabView software to translate from current to pressure. Moreover, a Gaussian filter is applied to eliminate any potential noise arising from the sensor wire pathways. Similarly, both the absolute pressure sensor and the flow meter generate outputs between 4 to 20 mA. The linear nature of their relationships enables the use

of a linear equation to convert the current outputs of these sensors into absolute pressure and flow values. To collect the power consumption in the impeller section, a torque meter with a capacity of up to 20 nm is positioned between the motor and the shaft. This torque meter outputs a range from 0 to 10 volts. Once the blade torque is recorded, its power is determined using the blade rotational speed. For the inducer section, the power consumption is directly determined using the output from the ABB drive. The drive output, which ranges from 4 to 20 mA, is translated into power consumption via a linear equation. Table 3.3 show the sensor specifications.

TABLE 3.3 – Sensor Specifications

Sensor	**Range**	**Accuracy**
Absolute Pressure	0-2.5 bar	0.1%
Differential Pressure	0-3 bar	0.1%
Flow Meter	0-282 m^3/h	0.2%
Torque Meter	0-20 Nm	0.5%

3.4.4 Mechanical loss

Due to high mechanical losses in the inducer section from the compression of the mechanical seal, mechanical loss measurements were taken in both the inducer and impeller sections to improve pump efficiency accuracy results. The results show negligible mechanical losses in the impeller section. To measure the mechanical losses in the inducer section, the inducer was removed from the shaft. With the system filled with water, the shaft was rotated at speeds ranging from 1200 rpm to 2900 rpm. The power consumption of the motor is measured at each speed. It can be said that this power consumption of the motor is only used to overcome the mechanical losses of the system, for this reason, in the efficiency calculations, according to the rotation speed of the inducer, the measured mechanical losses are reduced from the power consumption of the motor. Although in real, the power consumption of the motor to overcome the mechanical losses when the inducer is on the shaft is more than the calculated value, but it is not possible to calculate it accurately, and the calculated mechanical losses add good accuracy to the experimental results.

3.5 Experimental test procedure

3.5.1 Characteristics test procedure

In the previous section, it was indicated that all data are collected by DAQ and organized using LabView software. This section explains how to carry out a test procedure to examine the characteristics of the pump. To perform the characteristic test following steps should be taken :

1. The test bench is placed in the circuit by ensuring that both the inlet and outlet valves are opened.
2. The valve connected to atmospheric air at the top of the tank is opened to allow the system to vent.
3. The inlet valve of the tanker is opened so that trapped air can escape, preventing the tank from becoming pressurized.
4. Once the system is completely filled with water, the tank water inlet valve is closed.
5. The impeller and inducer speeds are adjusted to the desired setting using the frequency drive.
6. Water is allowed to flow throughout the system, and during this process, any remaining air is vented out via the atmospheric valve.
7. This flow is maintained for 10 minutes to ensure that all trapped air in the system is removed.
8. Once a steady state in the system is observed, the data collection phase is begun.
9. Both the inlet and outlet valves of the test bench are fully opened to achieve the maximum possible flow rate and at this point, the system data is recorded.
10. The test bench's outlet valve is gradually closed, resulting in a reduced flow rate.
11. After each adjustment, the system is allowed approximately one minute to stabilize before further data collection.
12. Data recording is continued for every change in flow rate and the process is repeated until the outlet valve of the test bench is fully closed.

3.5.2 Removing trapped air and degassing

To perform the cavitation test, the tank is filled using the same method as previously described, and the air is also removed in the same way. However, during the cavitation test, the system must be

checked from two additional perspectives due to the reduction of pressure to nearly absolute zero.

First, it should be ensured the system is completely sealed. This is critical to prevent air from entering during the cavitation test, especially at very low pressures. Next, the system should be eliminated from dissolved gas in the water. This process is necessary after each filling and emptying of the tank because water contains various gases that are dissolved in it under normal conditions. When the water pressure decreases, these gases begin to come out of the water, and if they are not removed before performing the cavitation test, the test results will be inaccurate. There are different methods for removing dissolved gas from water, such as heating the tank to remove the gases and slowly cooling it again. However, this method is effective only for small tanks, and it is not feasible for large tanks like the one in this system. The degassing process is performed by reducing the system pressure using a vacuum pump.

Before starting the cavitation test, the following steps should be done after filling the system for Removal of air and dissolved gases in water :

1. Using a vacuum pump to reduce the pressure of the system, aiming for a level close to absolute zero pressure.
2. The system is to be maintained in this low-pressure state for a specific duration (about 30 mintues).
3. The pressure of the system should be monitored. If it remains consistent and does not rise, it confirms that the system is properly sealed.
4. After verification of the system sealing, the water degassing process is starting. This step is crucial after each time the tank is filled or emptied.
5. The impeller and inducer are to be rotated at desired speeds.
6. The system pressure should continue to be reduced until gases are seen releasing from the water.
7. The system should operate under this reduced pressure for an amount of time (about 30 minutes).
8. The atmospheric valve is to be opened, allowing the system to equalize with external atmospheric pressure and exiting air in the process.
9. A period of interaction with atmospheric air is needed for the system to finalize the degassing process.

3.5.3 Cavitation test procedure

After it is been confirmed that the system is devoid of trapped air and most part of dissolved gases have been effectively removed, the cavitation test can be initiated.

1. Both the inducer and impeller are initially rotated at 2000 rpm. The test is conducted at three chosen flow rates that have been studied in this research, with each flow rate being associated with a specific working pressure.

2. For various rotational speeds, the inducer is first set to the desired speed. The speed of the impeller and the flow rate are then adjusted so that the same pressure as the previous setting is achieved. By doing this, the effects of variation in inducer speed or rotation direction can be observed and compared.

3. When the inducer and impeller have reached the desired speed, multiple data points are taken using LabView.

4. The process of system pressure reduction is started using the vacuum pump.

5. After allowing some time for the system pressure and $NPSH$ to decrease, the vacuum pump was turned off and sufficient time has been given for the system to stabilize (about 2 minutes), the pressure for the next point is recorded.

6. Steps 4 and 5 are then repeated for every point throughout the cavitation process.

7. It is observed that near cavitation and during the pump pressure drop, fluctuation in the flow rate might occur due to cavitation phenomena, which are regulated by the outlet valve.

Given the highly unstable nature of cavitation, the test is conducted multiple times to verify the precision of the results for every cavitation graph. Subsequently, the gathered data is processed using Python software to filter data with flow rate fluctuations, ensuring the cavitation process maintains a constant flow rate. Using a temperature sensor, the temperature of the water in circulation is accurately measured, and using the water temperature and vapor pressure tables, the vapor pressure of the water at the desired temperature is calculated and before performing any cavitation test, the value of vapor pressure in the NPSH formula is updated in the Labview software.

3.5.4 Image visualization with high speed camera

An IDT motion studio Y4 camera with a maximum resolution of 5100 frames per second (fps) is used to capture images. Two LED screens are placed on both sides of the high-speed camera to avoid reflections from the plexiglass tube during acquiring images. In addition, a white digital screen is positioned behind the inducer and Plexiglas tube. This configuration reflects light and creates a white background, which makes different cavitation forms more visible.

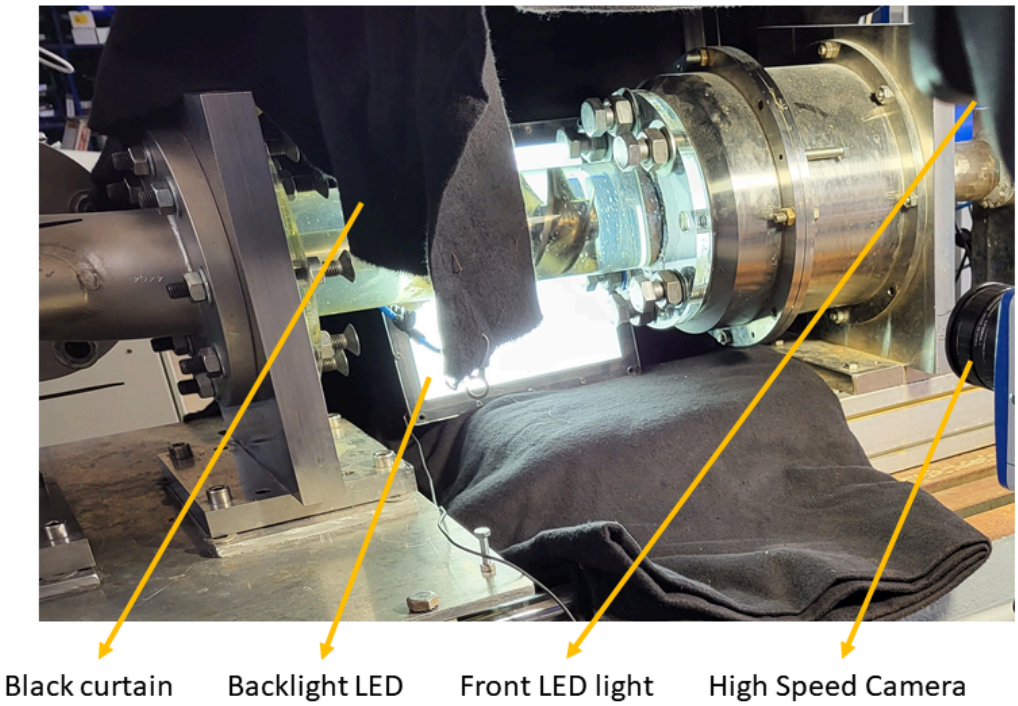

FIGURE 3.19 – The different equipment of visualization.

Figure 3.19 show the different equipment such as LED backlight and high speed camera that is used to take the cavitaiton images. For more transparency of the images, an LED backlight is used behind the inducer, and two LED light screens are used in front of the inducer to make the cavitation images more bright and clear. A black curtain has been used to prevent noise from ambient lights.

3.5.5 Test bench validation and results repeatability

After finalizing the earlier steps, it is necessary to validate the experimental test bench and ensure the results can be reproduced. To achieve this, the system was tested at multiple intervals and on

various days. Figure 3.20 illustrates the results from four different tests carried out on separate days in co-rotation mode wit hte same rotational speed and condition. These findings suggest that the system is highly reproducible. The test bench consistently provides the same results, demonstrating that the outcomes remain unaffected by the specific timing or conditions of the test.

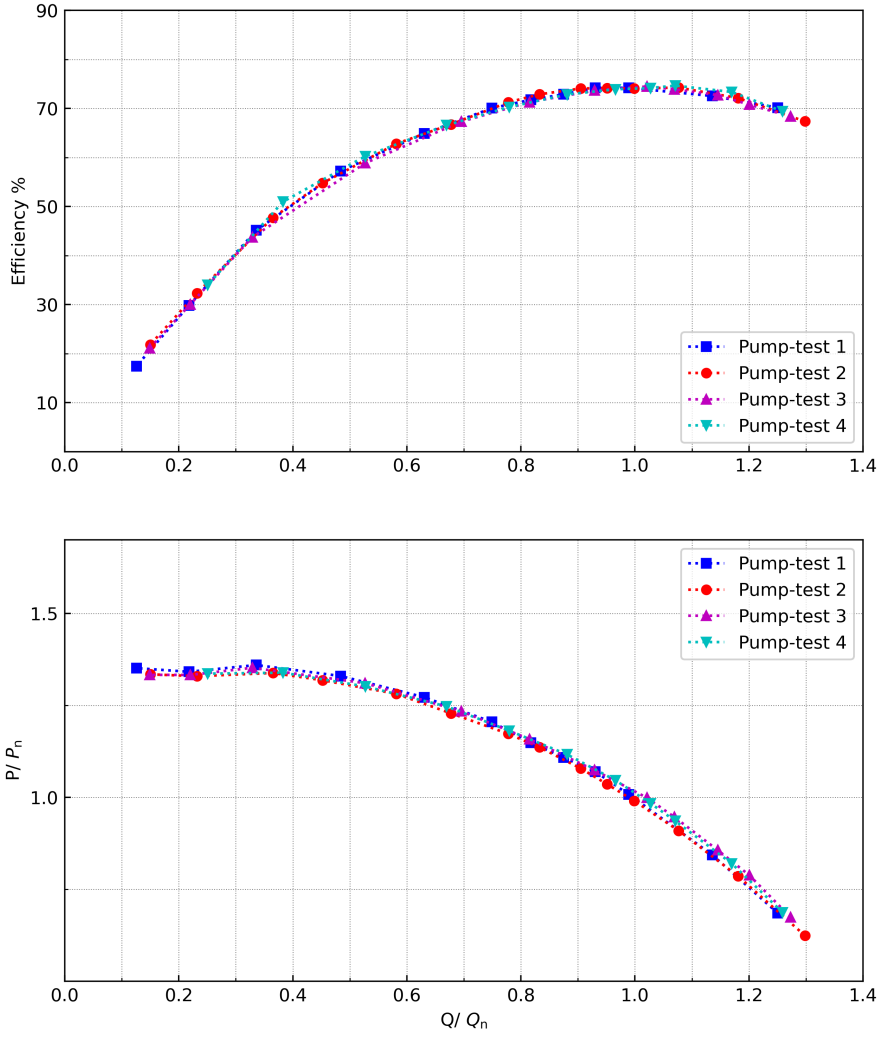

FIGURE 3.20 – Reproducibility of experimental test results

Similarity laws for pumps offer a method to estimate changes in pump pressure and flow rate when either the speed or diameter changes, or both. These laws provide a framework for approximating new operational conditions. In industrial applications involving large pumps, these laws prove to be particularly useful. By using smaller or slower pumps in lab tests and applying similarity laws, one can save both time and cost. Additionally, these laws make it possible to compare characteristics between the lab-tested pump and the original full-scale version. The similarity laws equations are as below :

$$\frac{H_{p2}}{H_{p1}} = \left(\frac{N_{p2}}{N_{p1}}\right)^2 \left(\frac{D_{p2}}{D_{p1}}\right)^2 \tag{3.11}$$

$$\frac{Q_{p2}}{Q_{p1}} = \left(\frac{N_{p2}}{N_{p1}}\right) \left(\frac{D_{p2}}{D_{p1}}\right)^3 \tag{3.12}$$

where H_{p} is pump pressure, N_{p} is pump rotational speed, and D_{p} is impeller diameter. Indexes 1 and 2 show the condition of the pump in mode 1 and 2, respectively and the similarity coefficient is defined as $K = \frac{N_{\mathrm{p2}}}{N_{\mathrm{p1}}}$. The similarity law of the pump has been studied in this section to evaluate the hydrodynamic behavior of the pump. For this reason, the inducer and impeller are considered as one integrated pump with the same rotational direction and speed. According to the similarity law, the pump rotates at 1000, 1600, 2000, and 2500 rpm, which correspond to $K = 1$, $K = 1.6$, $K = 2$, and $K = 2.4$, respectively. These coefficients are then applied to the flow rate and pressure. From the perspective of hydrodynamics, it can be concluded from Figure 3.21 that the pump satisfies the similarity laws well.

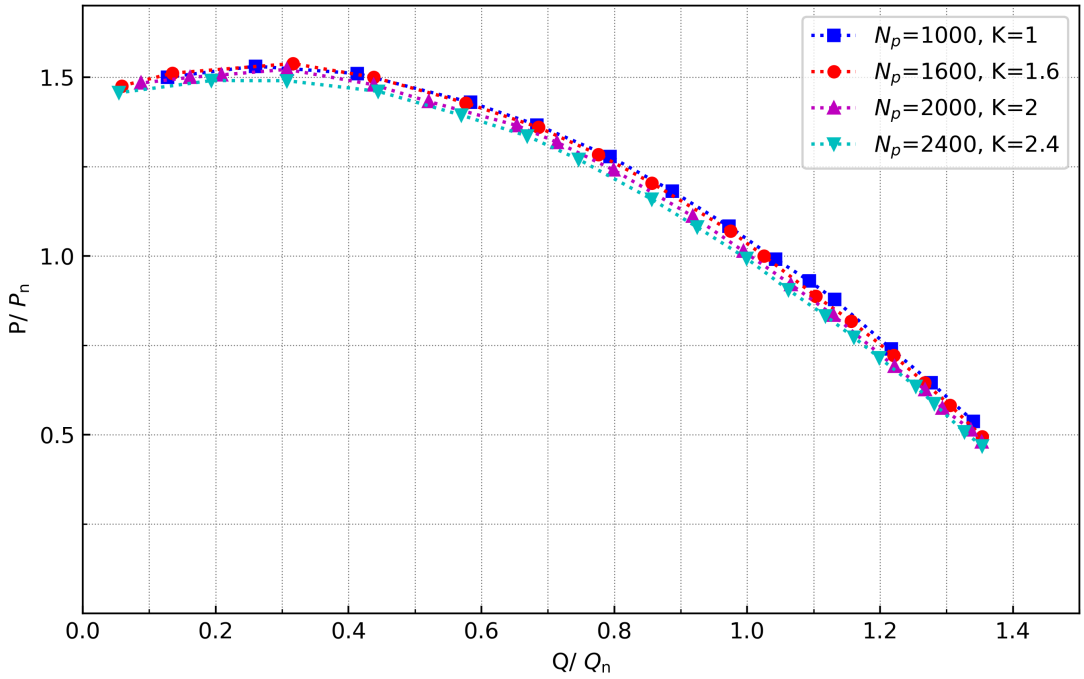

FIGURE 3.21 – Pump pressure with different similarity coefficient for N_p = 1000, 1600, 2000 and 2500 rpm

Chapitre 4

Pump characteristics in non-cavitation condition

content

4.1 Introduction

The characteristics of the impeller and inducer will be examined separately for the first step. This examination will focus on understanding their individual characteristics. Subsequently, the investigation will be conducted to determine the influence of the inducer on the impeller in both co-rotation and counter-rotation modes. The aim here is to understand how the impeller is affected by the inducer when they are operated together. Pump characteristics refer to the performance parameters and properties of a pump, which determine its efficiency, capacity, and pressure capabilities. These characteristics are crucial in understanding how a pump operates and whether it is suitable for a specific application. In the following, the pump characteristics will be described in terms of the effect of different speed ratios. The variations in speed ratios will be analyzed to determine their impact on the pump behavior, including its efficiency and pressure generation. Furthermore, the advantage of independent rotation to increase the pressure and efficiency of the pump will be explained. This approach involves taking advantage of the capability of independent rotation of the impeller and inducer, thereby optimizing the pump performance.

Table 4.1 shows the study parameters examined in the thesis. Three important parameters that can be studied thanks to the independent rotation system of two rotors include the rotation speed of each rotor, the direction of rotation of the inducer and the distance between the two rotors are investigated.

TABLE 4.1 – Study Parameters

Study Parameter	**Value**
Rotational Speed of Inducer	2000, 2500, 2900 RPM
Rotational Direction	+1 (Co-rotation), -1 (Counter-rotation)
Distance Between Rotors	20 mm, 80 mm

4.2 Impeller characteristics

Figure 4.1 shows the characteristics of a centrifugal impeller rotating at 2000 rpm (N_2 = 2000 rpm). The flow rate at which the impeller provides the highest efficiency is referred as the nominal flow rate (Q_n). To normalize the results, the pressure corresponds to the Q_n is also known as the nominal pressure (P_n), and all flow rates are normalized by dividing them by the nominal flow rate,

while all pressures are divided by the nominal pressure. The $Q_n = 40$ m$^3/h$ and the $P_n = 560$ mbar. Additionally, the highest achievable pump efficiency is 74%.

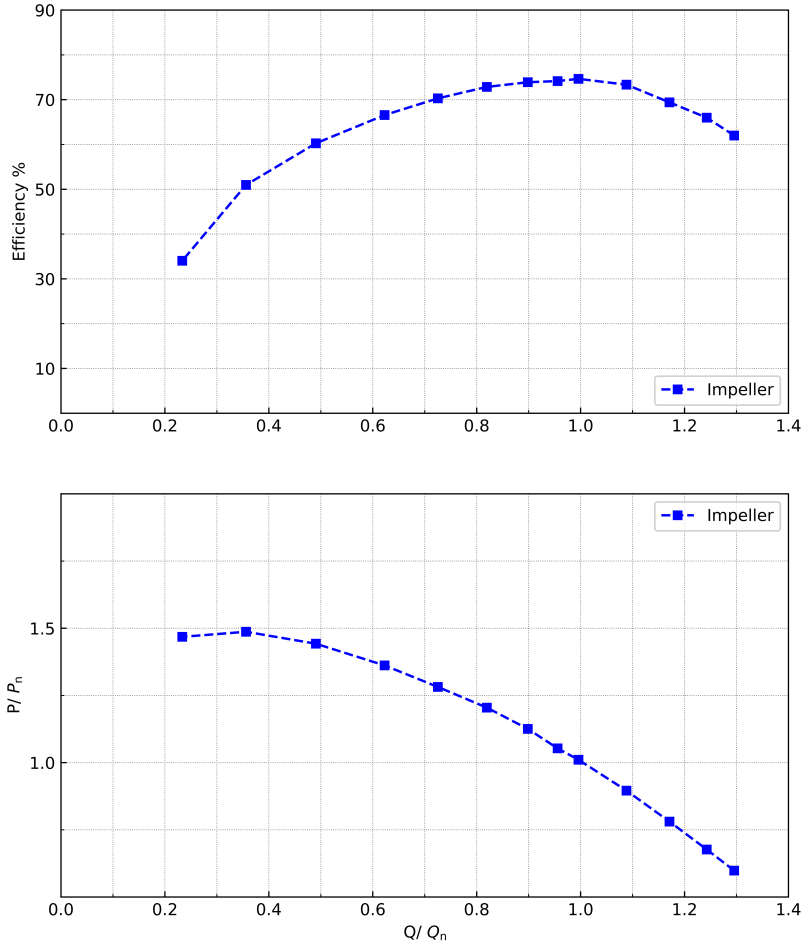

FIGURE 4.1 – Experimental results of impeller characteristics ($N_2 = 2000$ rpm)

4.3 Inducer characteristics

Figure 4.2 shows the characteristics of the inducer operating at a speed of 2500 rpm ($N_1 = 2500$ rpm). The maximum efficiency of the inducer, which is significantly lower compared to the impeller, is 34%. The primary reason behind this decrease in efficiency is the design of the inducer, which aims to prevent cavitation in the impeller. Additionally, the high compression of the mechanical seal in the inducer section contributes to the reduced efficiency. Typically, mechanical seals used to seal the shaft are positioned after the rotor and are compressed by water pressure. However, in this particular system,

due to the placement of the inducer in front of the main impeller, the mechanical seal experiences default pressure. Consequently, this arrangement ensures system sealing but decreases efficiency.

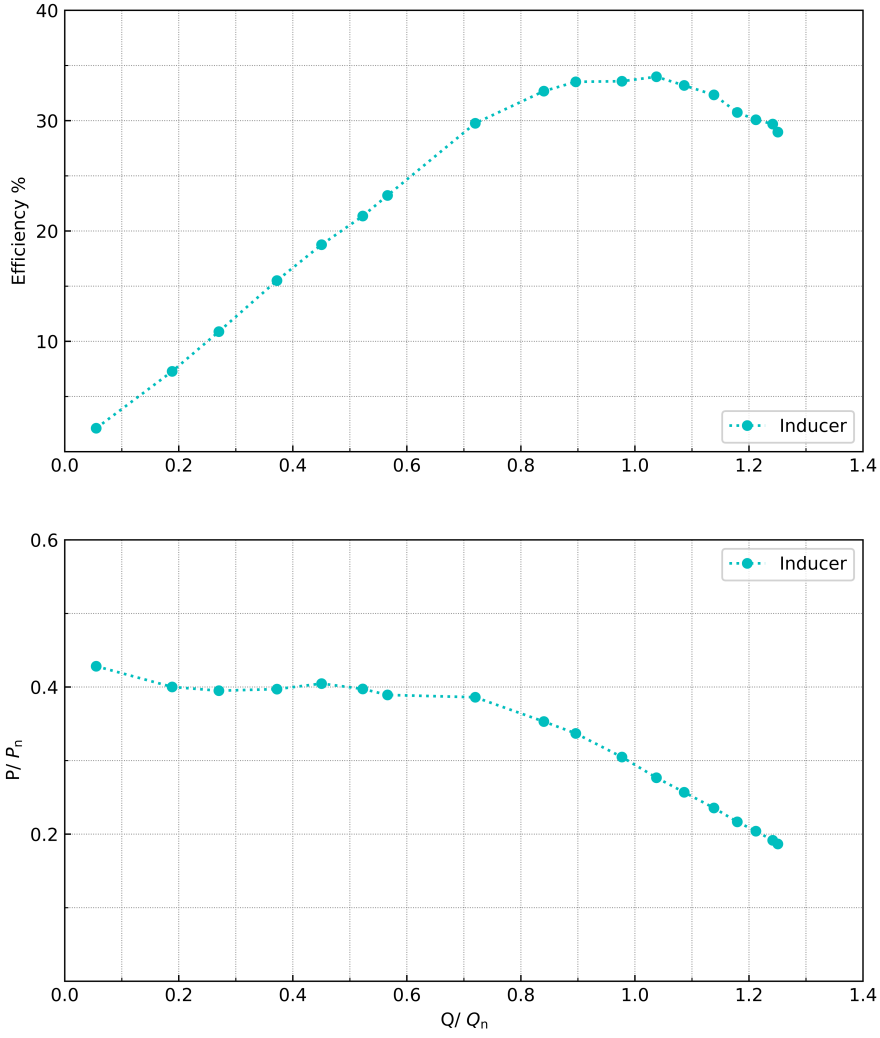

FIGURE 4.2 – Experimental results of inducer characteristics ($N_1 = 2500$ rpm)

4.4 Effect of speed ratio

4.4.1 Co-rotative pump characteristics

Figure 4.3 illustrates the performance characteristics of a pump equipped with both an inducer and an impeller, operating at the same rotational speed and direction ($N_1 = N_2 = 2000$ rpm) in comparison to a pump that only has the impeller without the inducer. The diagram demonstrates a good coupling between the inducer and impeller, as the characteristic curve of the pump with both components aligns well with the curve of the pump featuring only the impeller. Based on the details discussed in the preceding chapter regarding mechanical loss, all findings presented in this section take into account the mechanical loss of the system.

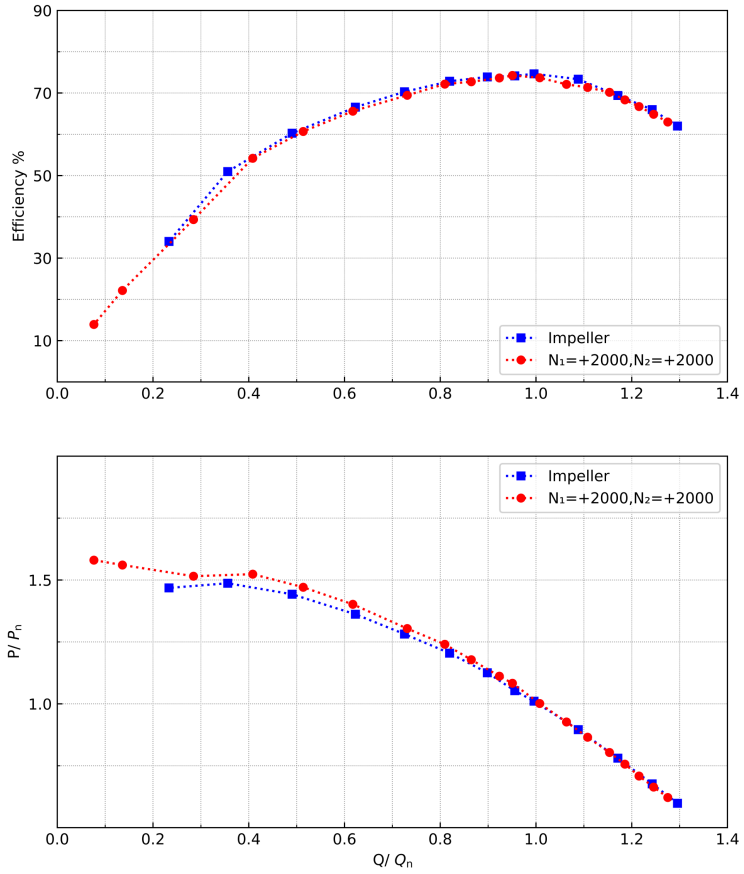

FIGURE 4.3 – Comparison of impeller and co-rotative pump characteristics ($N_1 = N_2 = 2000$ rpm)

Figure 4.4 illustrates the experimental results of the pump when operated in co-rotation mode at

different inducer speeds. The operational range of the pump can be categorized into three primary areas : firstly, the nominal point where the pump achieves its maximum efficiency, secondly, the area where the flow rate is below the nominal flow rate, known as the low flow rate region (LFR) and lastly, the high flow rate area (HFR) corresponds to the region where the flow rate exceeds the nominal flow rate.

The influence of inducer speed on pump pressure is noticeable in all three areas. Increasing the inducer speed enhances the pump ability to generate pressure. This is primarily due to the higher rotational speed of the inducer, which leads to increased pressure production. However, it is important to note that as the inducer speed increases, it also introduces pre-whirl in the fluid as it enters the impeller. This pre-whirl reduces the impeller pressure generation. Despite this, the overall pressure continues to rise because the pressure generated by the inducer exceeds the pressure drop within the impeller caused by the pre-whirl at the inlet. As the flow rate increases, the pressure drop in the impeller caused by the pre-whirl at the inlet also increases. Figure 4.4 illustrates that the pressure difference between $N_1 = 2900$ rpm and $N_1 = 2000$ rpm decreases with higher flow rates. Nevertheless, it is worth noting that regardless of this observation, an increase in the inducer speed consistently has a positive impact on overall pressure. The relationship between efficiency and inducer speed indicates that while increasing the inducer speed raises the pressure, it can have a contradictory effect on efficiency. In the low flow rate (LFR) region, the efficiency is nearly the same for $N_1 = 2000$ rpm and $N_1 = 2500$ rpm, but it decreases for $N_1 = 2900$ rpm. As the flow rate approaches the nominal point, the efficiency of $N_1 = 2000$ rpm and $N_1 = 2900$ rpm becomes similar, while $N_1 = 2500$ rpm remains slightly higher. In the high flow rate (HFR) region, it is clear that the efficiency of $N_1 = 2900$ rpm and $N_1 = 2500$ rpm is superior to $N_1 = 2000$ rpm [83].

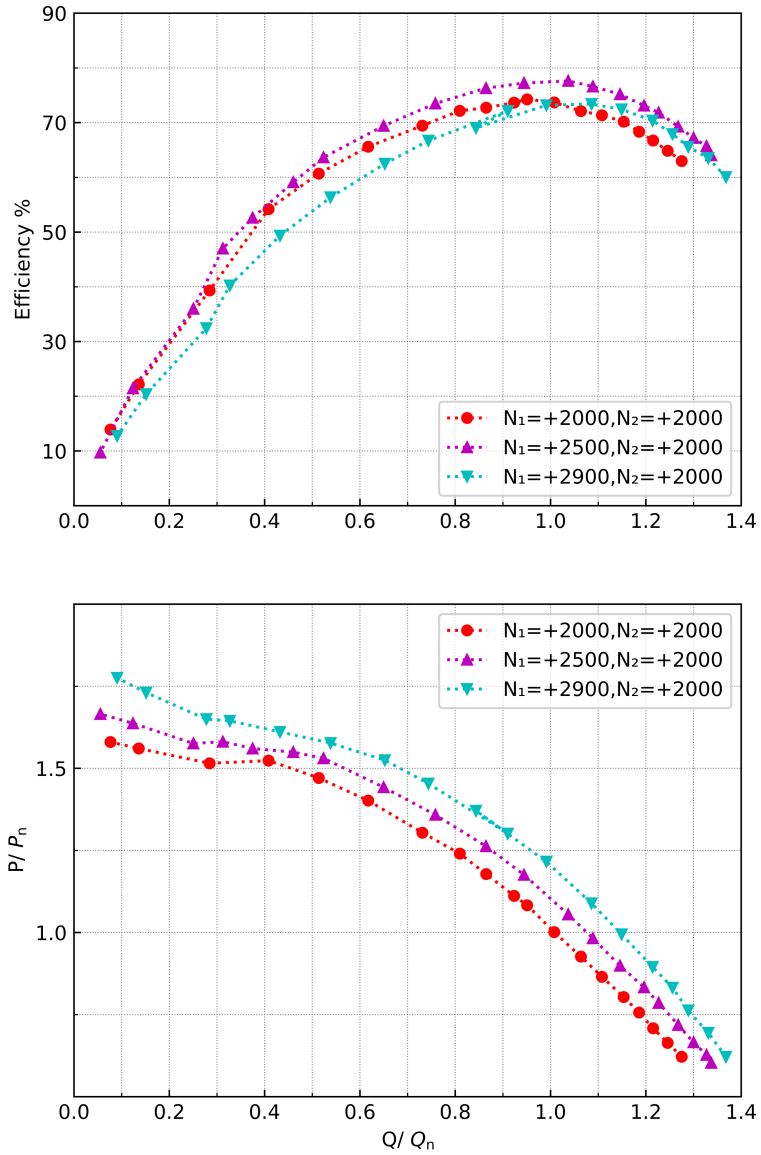

FIGURE 4.4 – Pump characteristics with different rotational speeds of inducer (N_1) in co-rotation mode with a fixed value of impeller rotational speed ($N_2 = 2000$ rpm)

4.4.2 Counter-rotative pump characteristics

Figure 4.5 provides insights into how the rotation direction of the inducer affects the efficiency and pressure of the pump when the rotational speed of both the inducer and impeller remains the same. The results indicate that the rotation direction plays a significant role in determining the pump pressure output. It is observed that when the inducer rotates in the counter-rotation mode, the pump

generates higher pressure compared to the co-rotation mode, while the efficiency is not substantially affected. In the LFR region, the efficiency is slightly lower in the counter-rotation mode compared to the co-rotation mode. However, at the nominal point, the counter-rotation mode achieves higher pressure with the same level of efficiency. This trend continues in the HFR region, where the counter-rotation mode not only achieves higher efficiency but also generates higher pressure compared to the co-rotation mode. This suggests that the rotation direction of the inducer has a significant influence on the pump's performance in terms of both efficiency and pressure output. Because of the increased pressure in the counter-rotation mode, it is possible to reduce the impeller's rotational speed and yet produce the same amount of pressure. As a result, it is possible to decrease the chance of cavitation, which will be discussed in more detail in the following sections.

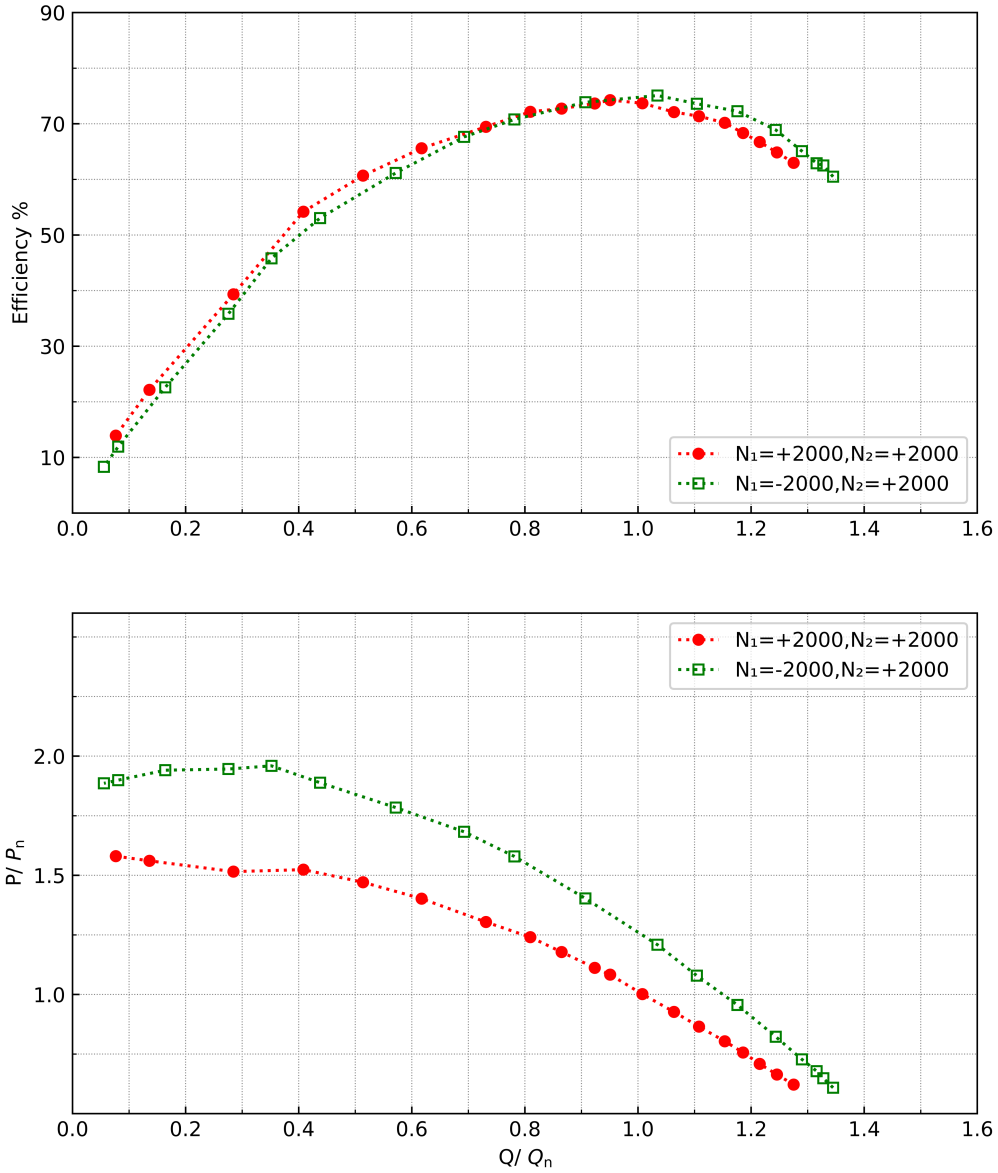

FIGURE 4.5 – Comparison of pump characteristics in co-rotation and counter-rotation mode with $N_2 = +2000$ rpm and $N_1 = \pm 2000$ rpm

Figure 4.6 shows the influence of the speed of the inducer on the characteristics of the pump when operating in the counter-rotation mode. The patterns observed in terms of efficiency and pressure variations with changes in flow rate are similar to those seen in the co-rotation mode. However, it is evident that the impact of inducer speed on pump pressure is more pronounced in the counter-rotation mode compared to the co-rotation mode. This effect can be found from the significant difference in the pressure diagrams. For example, at nominal point and for $N_1 = -2900$ rpm, the counter-rotation

mode generates significantly higher pressure than co-rotation, while maintaining the same efficiency. In the HFR region, the pressure in the counter-rotation mode is still affected by the speed of the inducer, unlike in the co-rotation mode. This difference comes from the reverse pre-rotation of the fluid caused by the inducer's reverse rotation in the counter-rotation mode.

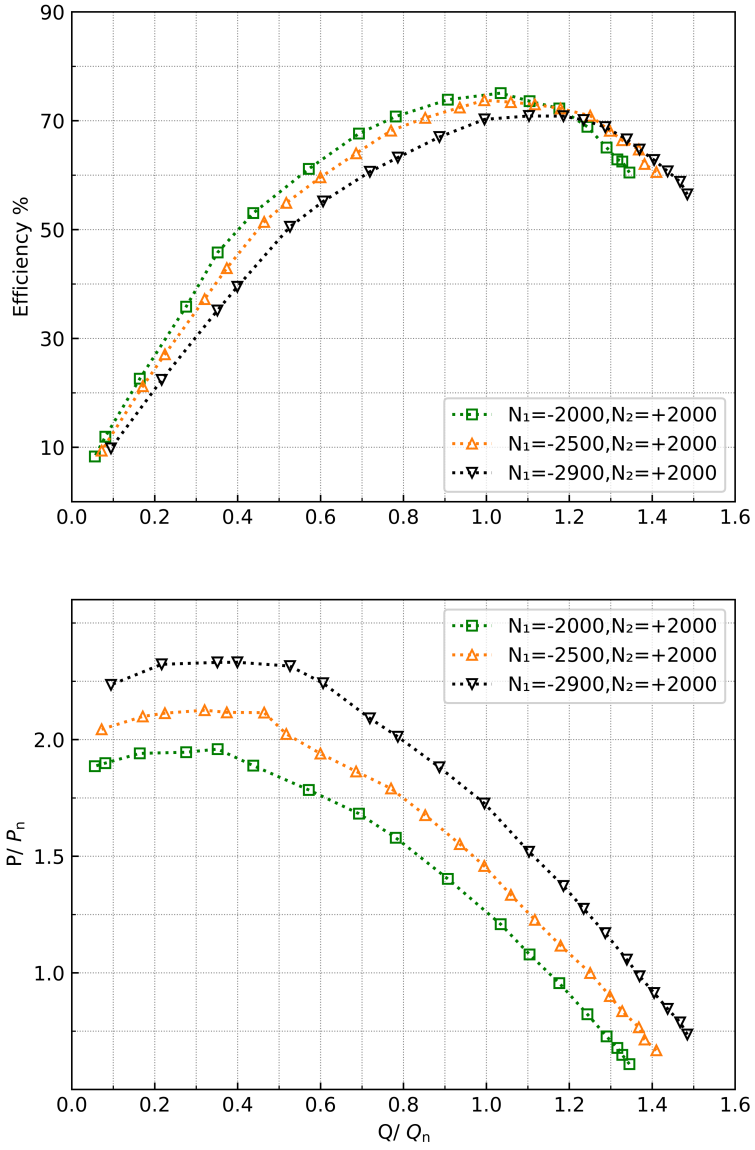

FIGURE 4.6 – Experimental pump characteristics with different rotational speed of inducer in counter-rotation mode with $N_2 = +2000$ rpm

4.5 Effect of distance between rotors in non-cavitation condition

The analysis of how variations in the distance (L) between the inducer and the impeller affect pump characteristics indicates a minimal impact on both pump pressure and efficiency. Figure 4.7 illustrates this by showing the outcomes for the pump operating in counter-rotation mode at a speed of 2000 rpm, for distances of 20 mm and 80 mm between the rotors.

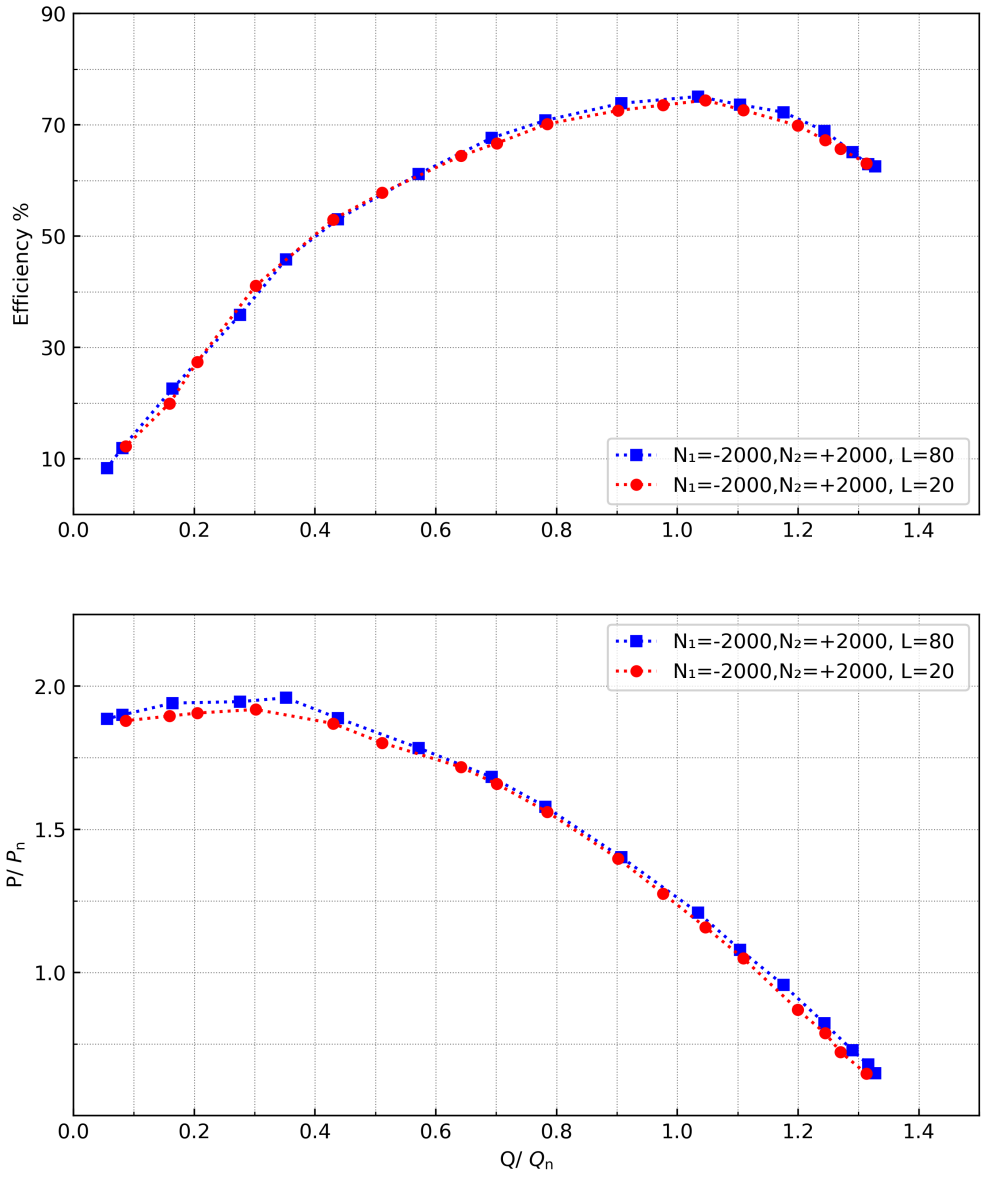

FIGURE 4.7 – Effect of distance between inducer and impeller ($L = 20$ mm, $L = 80$ mm) on pump characteristics in counter-rotation mode ($N_1 = -2000$ rpm, $N_2 = +2000$ rpm)

At extremely low flow rates, a slight influence on the pressure generated by the pump is observed due to variation in distance between rotors ; however, for other flow rates, no impact on pressure is noted. Similarly, changes in the distance between the inducer and the impeller do not affect pump efficiency, as similar efficiency levels are observed for both distances across all data points.

4.6 CFD analysis of pump characteristics

4.6.1 Geometry and calculation domain

Numerical simulation is used to study the interaction between the inducer and impeller, as well as the individual effects of each rotor on the characteristics of the pump like the pressure produced by each rotor independently which is not accessible experimentally due to the experimental limitation. The CFD simulation is carried out using StarCCM+ 16.06 software. The steady state Reynolds Average Navier-Stokes (RANS) equations are solved using the $k - \varepsilon$ standard model as the turbulence model. To achieve the highest level of accuracy for the new independent rotating arrangement, complete geometry must be simulated. Table 4.2 displays the various geometry components with mesh applied. An inlet, inducer (co-rotative and counter-rotative), centrifugal impeller, diffuser, and outlet represent the components of the simulated geometry. According to the new system of independent rotation, each of the rotors is defined as a separate rotating part, which includes the two parts called the inducer and the impeller. This makes it possible to apply different rotational speeds, as well as to change the direction of rotation of the inducers. Although the geometry to be simulated is more complicated and as a result the simulation time and cost are higher. The water is used as the working fluid during the simulations, similar to the conditions of experimental tests. The three-dimensional steady-state flow with constant density is considered as the flow model during the simulation.

Table 4.2 – Details of different applied meshes

	Inlet	Inducer	Impeller	Diffuser	Outlet	Total
Mesh 1	6612	14240	50609	101798	5808	179067
Mesh 2	11796	31136	67573	190945	11004	312454
Mesh 3	59112	46230	86195	231429	30468	453434
Mesh 4	38868	186259	206119	713587	23088	1167921
Mesh 5	59424	435571	1470949	1678222	30084	3674250
Mesh 6	87648	585207	2779696	2531844	69492	6053887
Mesh 7	99792	683961	3231424	2951026	85404	7051607

Figure 4.8 illustrates the variations in pressure for counter-rotation mode with $N_1 = -2500\text{rpm}, N_2 = 2000\,\text{rpm}$ at $\frac{Q}{Q_n} = 1$ across different meshes. Based on the mesh geometry, mesh number 5 has been identified as the optimal choice for this study. In this study, an unstructured polyhedral mesh was employed. The mesh base size was set at 20 mm. To enhance accuracy, 4 prism layers with a size of 2% of the base were added to the tip of the inducer, while 6 prism layers with the same size were applied to the impeller. Surface controls were considered in various parts of the mesh to optimize computational costs and improve accuracy. The minimum and maximum mesh sizes within these surface controls ranged between 1% and 5% of the base size. This approach ensured that unnecessary small meshes were not generated in non-critical areas, preventing an increase in the overall number of meshes and computational costs. Simultaneously, it increased the accuracy of calculations to the desired levels. The y^+ values range from 0.22 to 4.49, demonstrating precise velocity gradient within the walls. To be able to simulate rotating objects, due to the complex geometry, the Multiple Reference Frame (MRF) method was used. Three main interfaces between the inducer inlet and the inlet area, the inducer outlet and the impeller inlet, and the impeller outlet and the diffuser inlet were defined. A segregated flow with upwind convection scheme of second-order accuracy was used.

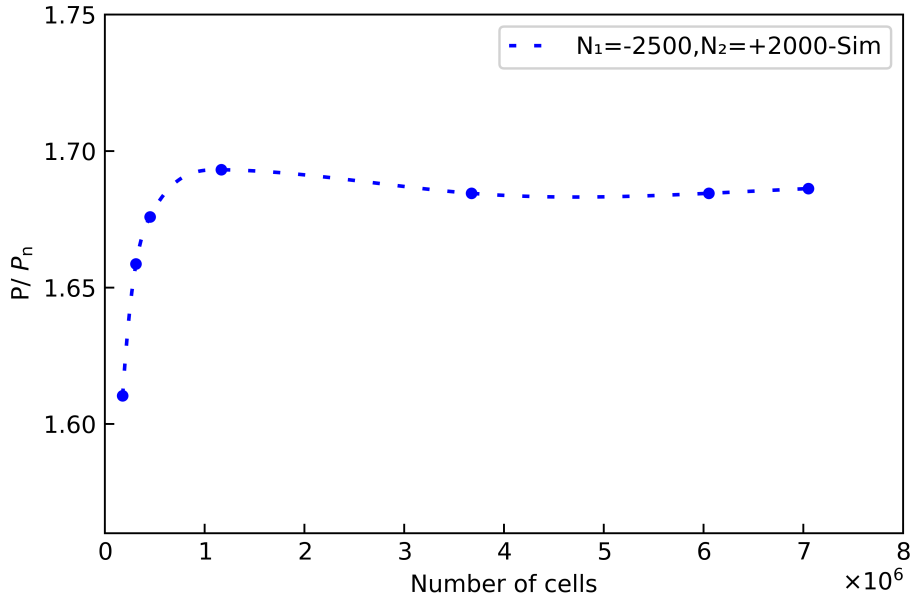

FIGURE 4.8 – Pressure coefficient obtained for the counter-rotating mode with different total numbers of mesh cells

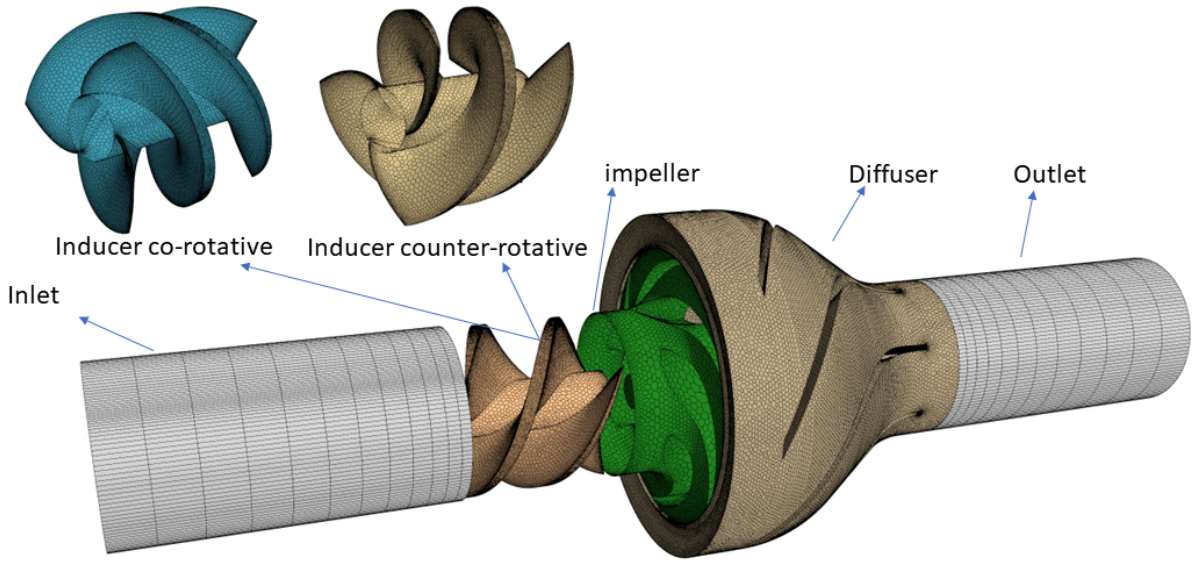

FIGURE 4.9 – Schematic of the simulated pump with co-rotating and counter-rotating inducers

Figure 4.9 displays the various components of the simulated geometry. To conserve both time and cost in the simulation process, and given that the focus was to explore areas not reachable through experimental methods as well as the interaction between the inducer and the impeller, the simulation does not include the elbows at the inlet and outlet of the system. The simulated geometry includes five components. The inducer and impeller are described as moving elements, while the remaining three components including the inlet, diffuser, and outlet are considered as fixed or stationary parts.

4.6.2 Numerical results of co-rotative pump characteristics

The results of numerical simulations of pump pressure and efficiency in the co-rotation mode at various inducer speeds are illustrated in Figure 4.10.

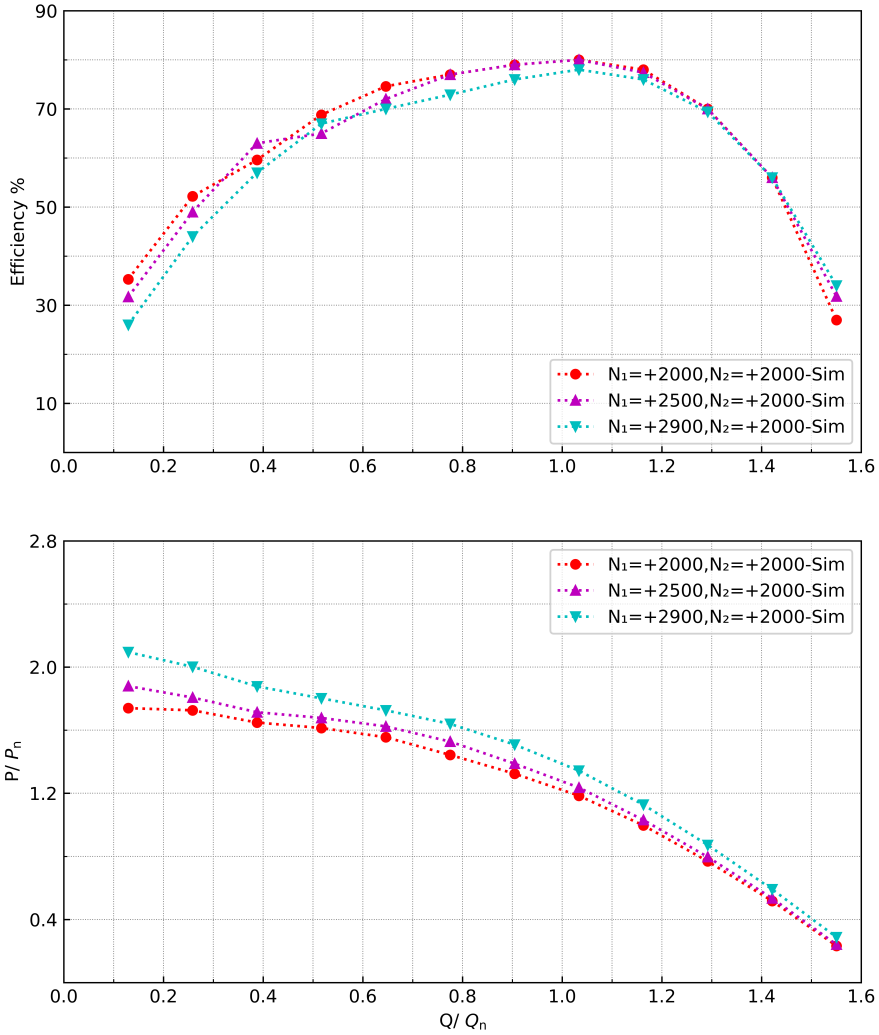

FIGURE 4.10 – Numerical pump characteristics with different rotational speed of inducer in co-rotation mode

The data indicates that when the inducer speed is raised to 2500 rpm, a slight increase in pressure is observed. Further increasing the speed to 2900 rpm results in a more pronounced increase in pressure. This pressure rise is particularly notable in low flow rate regions with pressure enhancements of up to 30%. However, at this flow rate, there is also a 10% decrease in efficiency. At the nominal flow rate, increasing the inducer speed leads to a rise in pump pressure, accompanied by only a slight drop in efficiency. At high flow rates, increasing the inducer speed results in more pressure and efficiency together.

4.6.3 Numerical results of counter-rotative pump characteristics

Figure 4.11 displays the results of the simulation regarding the impact of raising inducer speed on pump characteristics in the counter-rotation mode [84].

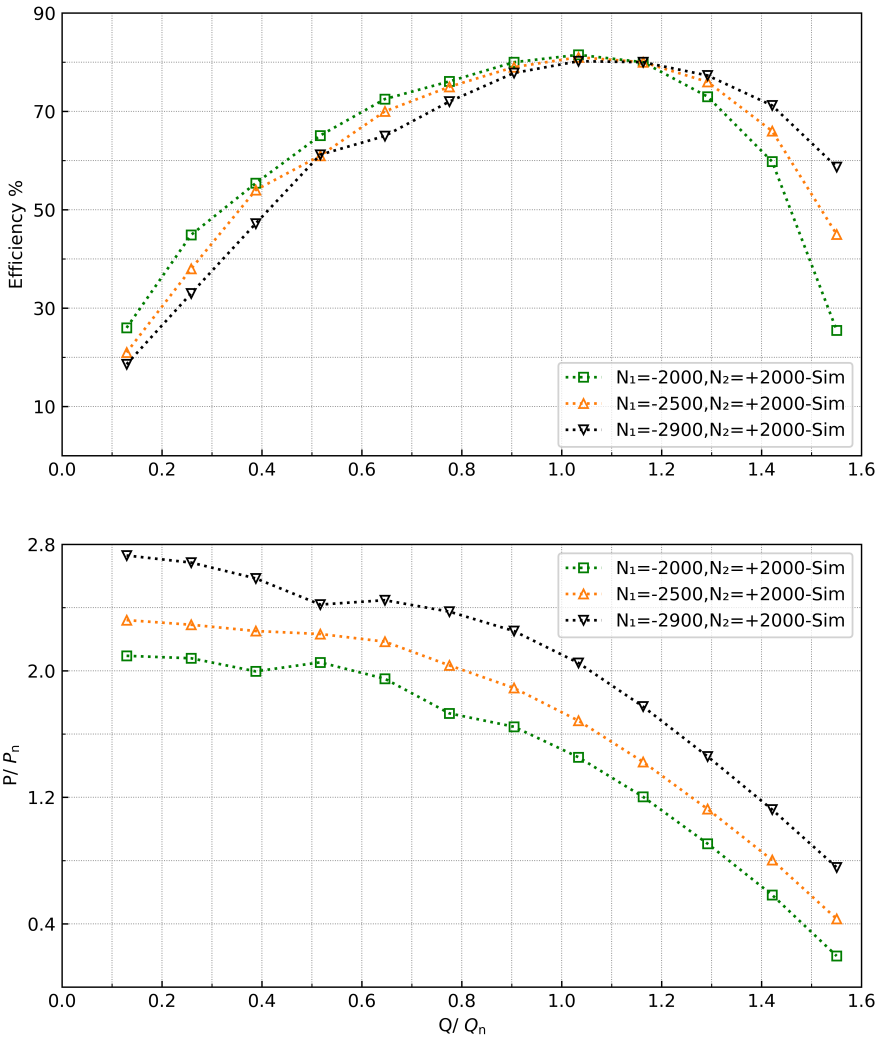

FIGURE 4.11 – Numerical pump characterises with different rotational speed of inducer in counter-rotation mode

It is evident that increasing the inducer speed in this mode has a significant influence on the pump characteristics compared to the co-rotation mode. As a result, by raising the inducer speed to 2900 rpm, the pressure ratio in $\frac{Q}{Q_n} = 1$ rises from $\frac{P}{P_n} = 1.5$ to over $\frac{P}{P_n} = 2.1$, which is significantly greater than the co-rotative mode value of about $\frac{P}{P_n} = 1.2$.

4.6.4 Comparison of numerical and experimental results

Figure 4.12 illustrates the comparison between the experimental and numerical results for the counter-rotation mode at $N_1 = -2500$ rpm, $N_2 = +2000$ rpm. The experimental results include both the test outcomes and the mechanical loss of the system.

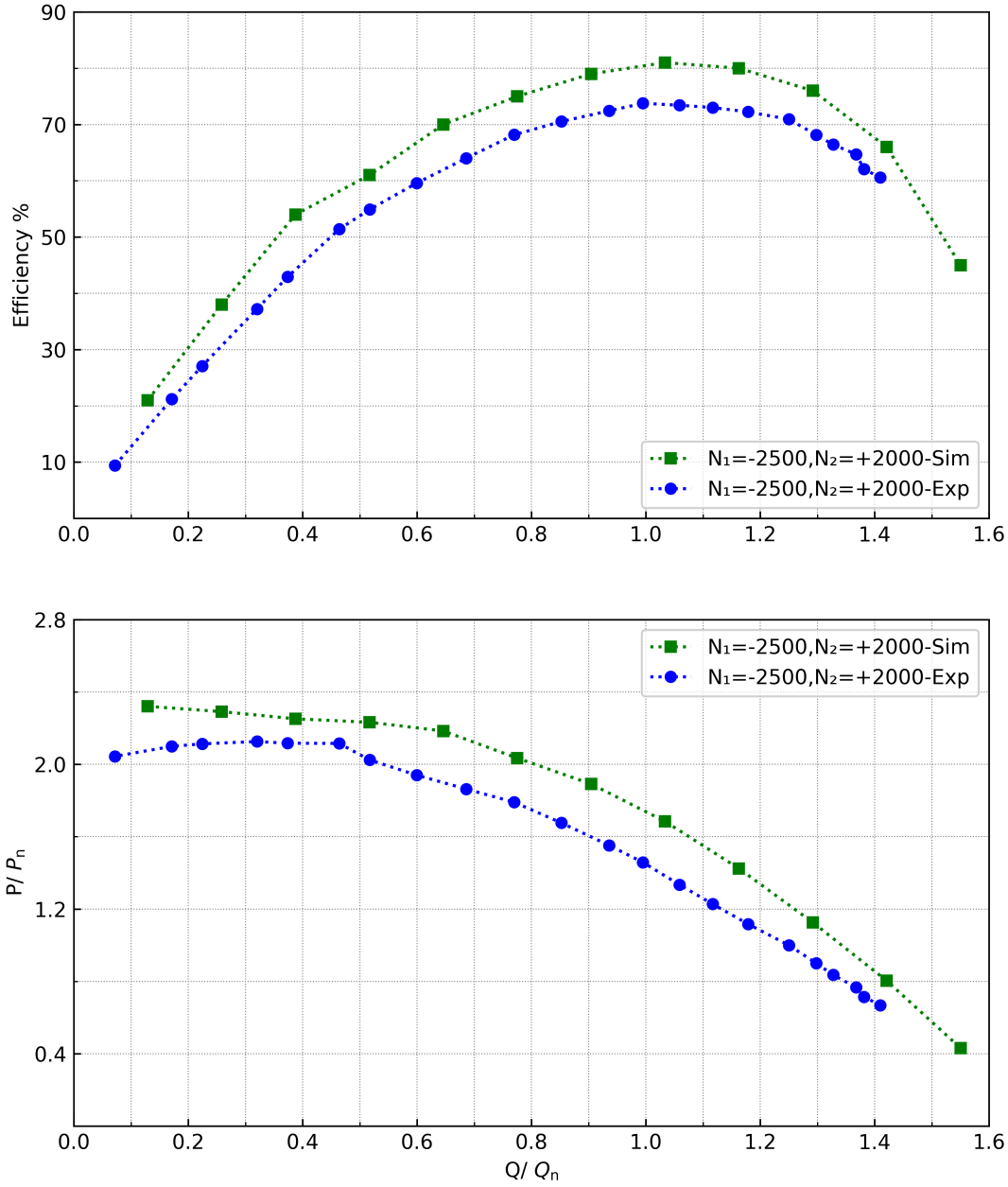

FIGURE 4.12 – Numerical and experimental results of characteristics of pump in counter-rotation mode at $N_1 = -2500$ rpm, $N_2 = +2000$ rpm

To determine the mechanical loss resulting from components like bearings and mechanical seals, the impeller and inducer were removed from the shafts. The shafts were then rotated without these components, and the power consumption of each section (inducer and impeller) was measured. This allowed for the calculation of the mechanical loss caused by the bearings and mechanical seals in the system. The experimental and simulation results demonstrate a good correlation, with a difference of approximately 5%. This difference can be the result of additional losses within the experimental system, primarily the hydraulic loss. The hydraulic loss is notable due to the presence of two elbows at the pump's inlet and outlet, as well as a support for the inducer shaft upstream. Due to the high computational cost involved, the simulation does not consider these elbows and supports that are part of the system. Consequently, a slight variation between the experimental results and the simulation results is observed.

4.6.5 Numerical analysis of internal flow between inducer and impeller

Figure 4.13 provides a visual representation of the pressure distribution within the inducer for both co-rotation and counter-rotation modes for $N_1 = \pm 2000$ rpm, $N_2 = +2000$ rpm. The pressure contour reveals that the pressure distribution is relatively similar in both cases, with a noticeable localized pressure drop at the tip of the inducer. The pressure drop observed at the tip of the inducer increases the potential for cavitation, specifically tip vortex cavitation at high speeds of rotation.

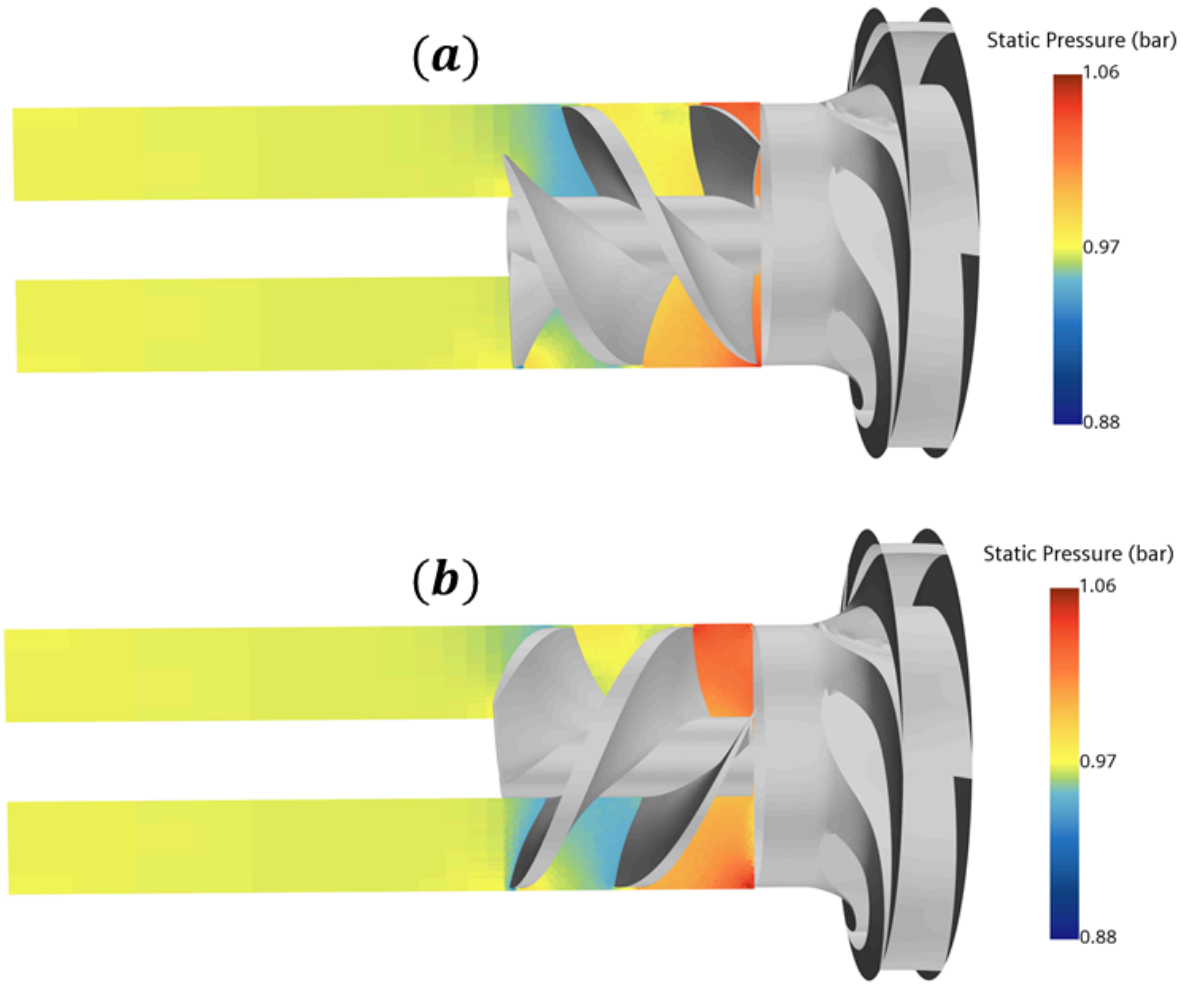

FIGURE 4.13 – Pressure distribution in inducer obtained via numerical simulation for (a) co-rotation and (b) counter-rotation modes at $N_1 = \pm 2000$ rpm, $N_2 = +2000$ rpm

When observing the fluid velocity as it traverses the inducer in both co-rotation and counter-rotation modes at the same rotational speed, as illustrated in Figure 4.14, it can be seen that the fluid velocity direction in counter-rotation is the reverse of that in co-rotation. Additionally, by studying the velocity triangle at both the impeller's inlet and its entrance, and employing Euler equation, the reason behind the higher pressure generation in the counter-rotation mode can be understood.

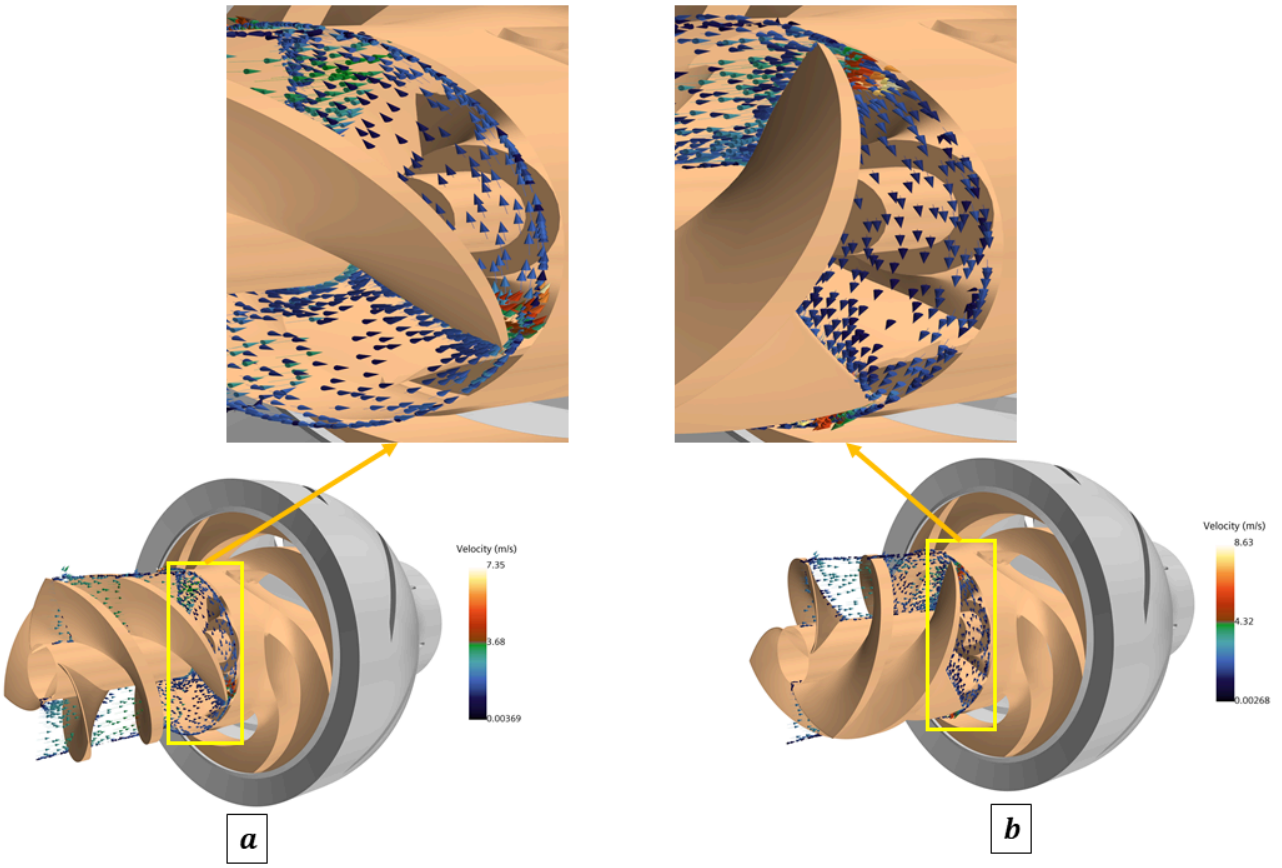

FIGURE 4.14 – Velocity of fluid in inducer at a) co-rotation and b) counter-rotation modes at $N_1 = \pm 2000$ rpm, $N_2 = +2000$ rpm

Investigation of the pressure distribution between the inducer and impeller at speeds for $N_1 = \pm 2000$ rpm, $N_2 = +2000$ rpm, in both co-rotation and counter-rotation mode is shown in Figure 4.15. The pressure between the two rotors exhibits minor variations in the co-rotation mode while maintaining uniformity in the counter-rotation mode. A significant local pressure decrease is observable near the impeller blade, making this area vulnerable to cavitation when the system pressure is reduced so cavitation initiation between the inducer and impeller can originate from this region, which will be further clarified in upcoming sections.

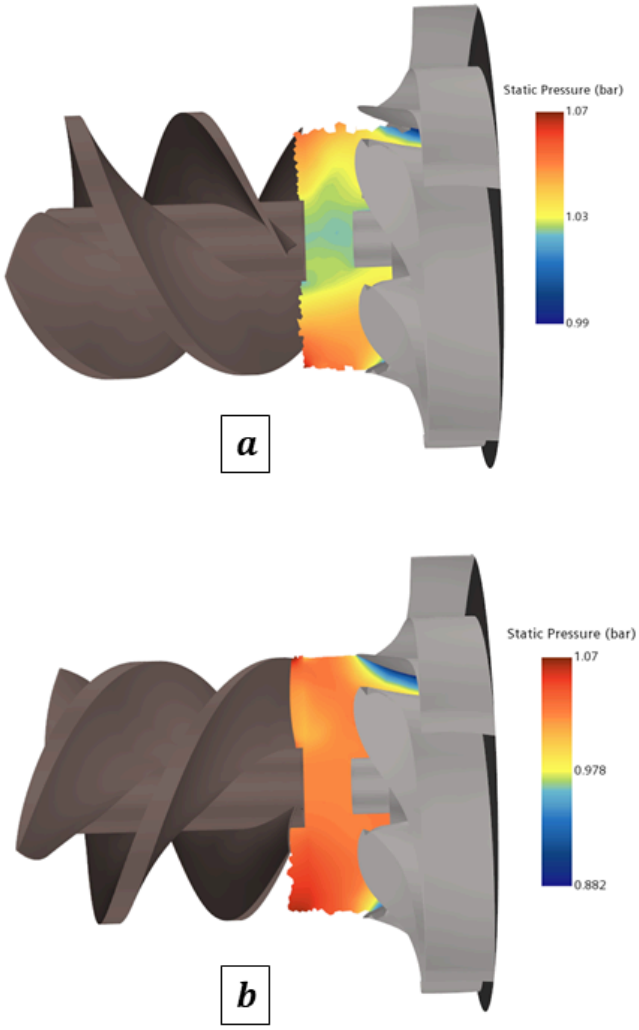

FIGURE 4.15 – Pressure distribution between inducer and impeller obtained via numerical simulation for (a) co-rotation and (b) counter-rotation modes at $N_1 = \pm 2000$ rpm, $N_2 = +2000$ rpm

Figure 4.16 displays the numerical results of the pressure generated by the inducer in both co-rotation and counter-rotation modes at $N_1 = \pm 2900$ rpm at the nominal point. The primary purpose of utilizing the inducer is to enhance the pressure at the impeller inlet. According to Figure 4.16, it can be observed that changing the direction of rotation of the inducer does not have an impact on the pressure produced by the inducer itself. However, the pressure generated by the impeller experiences an increase, resulting in an overall augmentation of the pump total pressure. However, the impeller pressure increases, resulting in an overall increase of the pump total pressure. This indicates that only the inducer affects the impeller, while the impeller does not impact the inducer.

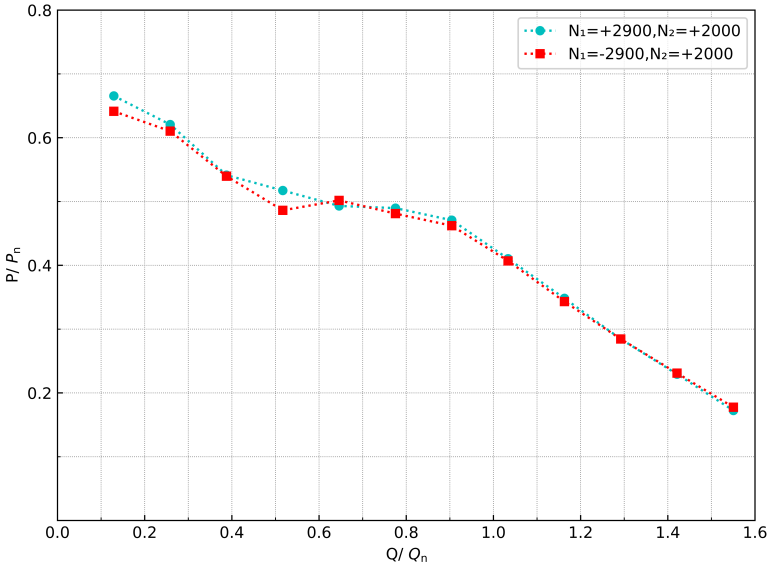

FIGURE 4.16 – Inducer pressure obtained via numerical simulation for co-rotation and counter-rotation modes

In Figure 4.17 the velocity triangles for both co-rotation and counter-rotation modes are presented. The diagram represents various parameters : U represents the speed of the rotor (either the impeller or the inducer) and is defined as $U = r\omega$ where r is the distance to the center of rotation and ω is the rotational speed of the rotor, V represents the absolute velocity of the flow and W represents the relative velocity of the flow.

According to Euler turbomachinery equations[85], the theoretical head H_{th} generated by the impeller can be determined using the following equation :

$$H_{th} = \frac{U_4 V_{t4} - U_3 V_{t3}}{g} \tag{4.1}$$

where V_t represents the tangential velocity of the flow. The flow leaving the inducer is equal to the flow entering the impeller so $V_{t2} = V_{t3}$ and based on the velocity triangle (Figure 4.17), it is apparent that in the co-rotation mode, U_3 and V_{t3} are in the same direction, resulting in a positive value for $U_3 V_{t3}$, but in the counter-rotation mode, the direction of V_{t3} is opposite to the direction of U_3 and the above equation becomes the following equation for counter-rotation mode :

$$H_{th-CR} = \frac{U_4 V_{t4} + U_3 V_{t3}}{g} \tag{4.2}$$

Where H_{th-CR} presented the theoretical head of the pump in counter-rotation mode. The total pressure is higher in the counter-rotation mode compared to the co-rotation mode [86].

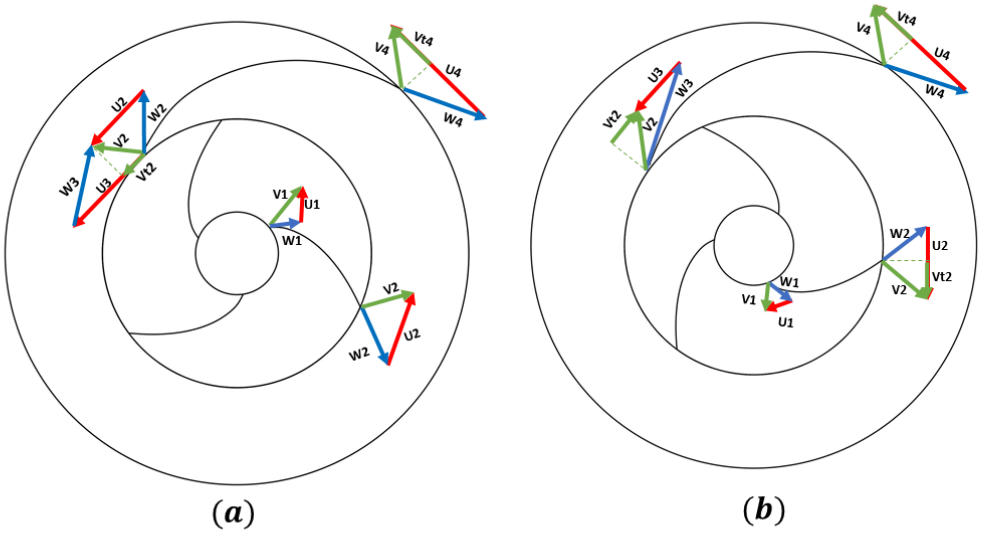

FIGURE 4.17 – Velocity triangle for (a) co-rotation and (b) counter-rotation modes.

Chapitre 5

Pump cavitation performance

content

5.1 Introduction

In this section, the investigation of the pump in cavitation conditions is presented. First, the cavitation performance of the pump in co-rotation mode is analyzed. Then, the impact of modifying the speed of the inducer on the cavitation performance of the pump at different flow rates is explored. Following this, by changing the direction of inducer rotation, the effect of inducer speed on pump cavitation performance in counter-rotation mode at various flow rates is examined. In this part, the effect of the distance between the inducer and the impeller in counter-rotation mode on pump cavitation performance is also analyzed. Subsequently, a comparison between the co-rotation and counter-rotation pumps at different flow rates and rotation speeds of the inducer is presented. Finally, the instabilities of cavitation with time in the inducer and between the inducer and the impeller have been studied using high speed camera.

5.2 Cavitation of inducer and impeller in co-rotation mode

Figure 5.1 presents the cavitation performance of the pump in terms of $NPSH$ at three specified operating points. It can be observed that as the flow rate increases and the pump output pressure decreases, cavitation occurs more rapidly. According to Figure 5.1, $\frac{P}{P_n} = 0.7$, $\frac{P}{P_n} = 1$ and $\frac{P}{P_n} = 1.16$ corresponding to $\frac{Q}{Q_n} = 1.2$, $\frac{Q}{Q_n} = 1$ (nominal flow rate) and $\frac{Q}{Q_n} = 0.87$ respectively.

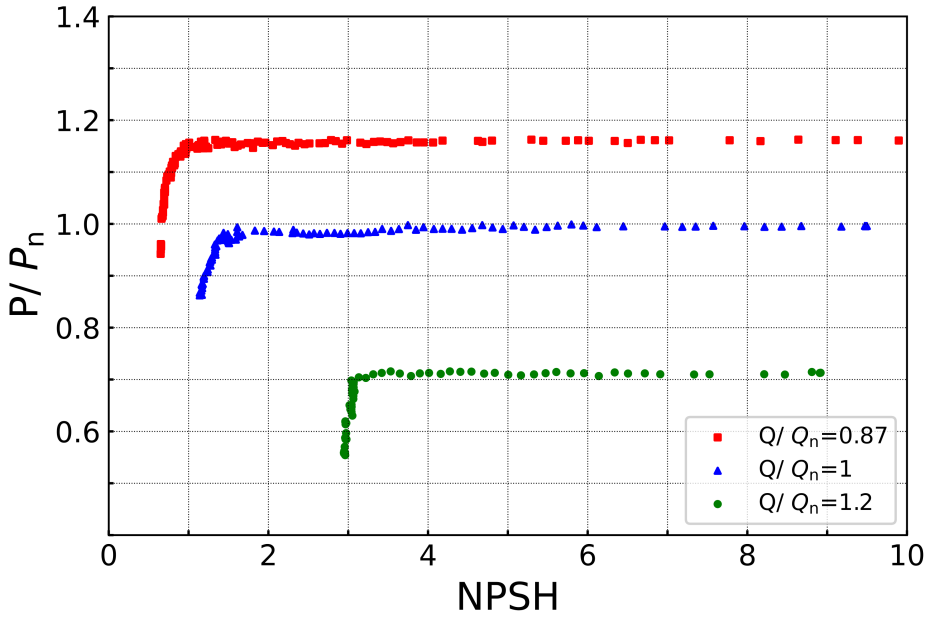

FIGURE 5.1 – Cavitation performance of pump for different flow rates in co-rotation mode

The following investigation will be focused on the examination of how variation in the speed of the inducer, whether increased or decreased, will impact the cavitation characteristics of the pump while operating in the co-rotating mode.

5.2.1 Effect of speed ratio at $\frac{Q}{Q_n} = 0.87$

Figure 5.2 illustrates the cavitation characteristics of the pump when operating in co-rotation mode, showcasing various inducer speeds. As can be seen, the inducer change in speed significantly affects the pump's cavitation. It is evident that the pump faces a 5% pressure drop at $NPSH = 0.7\,\text{m}$ in the case when $N_1 = N_2 = 2000\,\text{rpm}$ (red dots). Increasing the speed of the inducer to 2500 rpm (blue triangles) and reducing the speed of the impeller to 1994 rpm to produce a pressure similar to the state of $N_1 = N_2$ reduces the pump cavitation efficiency, so that at $NPSH = 1.22\,\text{m}$, the pump experiences a 5% drop in pressure.

As inducer speed is increased to 2900 rpm (green squares), the pump cavitation efficiency continues to decline, resulting in a 5% loss in pump pressure at $NPSH = 1.78\,\text{m}$. Figure 5.2 demonstrates that when inducer speed increases, the pressure drop of the pump occurs with a shallower slope and is more

gradual than at lower speeds. The pump pressure drop starts at $NPSH = 5\,\text{m}$, while the pressure drop is 5% at $NPSH = 1.78\,\text{m}$, and the complete breakdown of the pump occurs at $NPSH = 1\,\text{m}$. For an inducer speed of 2500 rpm, pump pressure begins to decrease at $NPSH = 3\,\text{m}$, but a 5% pressure drop occurs at $NPSH = 1.22\,\text{m}$.

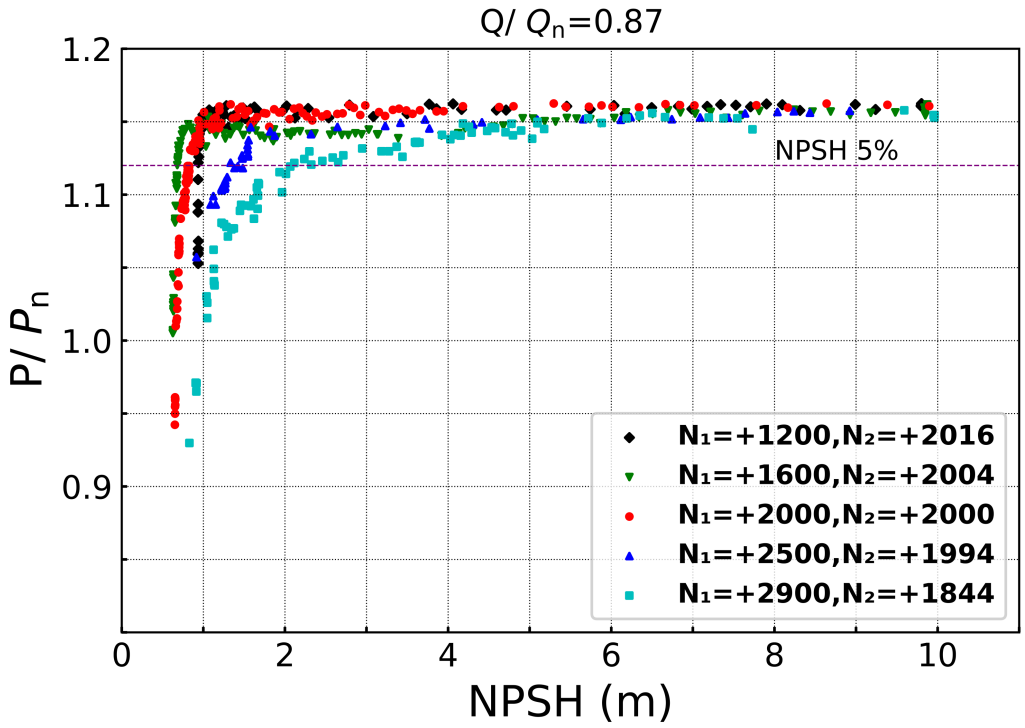

FIGURE 5.2 – Cavitation performance of pump by variation of inducer speed in co-rotation mode for $\frac{Q}{Q_n} = 0.87$

Decreasing the inducer speed to 1600 rpm (green triangles) slightly improves the pump cavitation efficiency, leading to a 5% pressure drop at $NPSH = 0.64\,\text{m}$. However, further decreasing the inducer speed to 1200 rpm (blue diamonds) has an adverse effect, and the pump cavitation efficiency decreases, resulting in a 5% pressure loss at $NPSH = 0.93\,\text{m}$. Generally, it can be said that at $\frac{Q}{Q_n} = 0.87$, reducing the inducer speed from 2900 rpm to 1600 rpm enhances the pump cavitation efficiency in the co-rotation mode. For inducer speeds below 2500 rpm, the pump pressure drops suddenly, while between 2500 and 2900 rpm, there is initially a localized pressure decline followed by a sharp pressure drop.

5.2.2 Effect of speed ratio at nominal flow rate

By increasing the $\frac{Q}{Q_n}$ from 0.87 to the nominal flow rate, it can be seen that variations in inducer speed have a greater effect on the cavitation efficiency of the pump. As can be seen, when the inducer rotates at its highest speed ($N_1 = 2900$ rpm), the pump local pressure drop begins at $NPSH = 3.5\,\text{m}$ and 5% pressure appears at $NPSH = 2.65\,\text{m}$. At this speed, the pump pressure drop continues with a slope and there is no effect of a sudden pressure drop. Lowering the inducer rotation speed to 2500 rpm results in an enhancement of the pump cavitation efficiency. Consequently, a 5% pressure decrease is seen at $NPSH = 2.18\,\text{m}$, which is more than 0.5 meters lower than the 2900 rpm speed. According to Figure 5.2, continuing to reduce the inducer speed to 2000 rpm can smoothly improve the cavitation efficiency of the pump, causing a 5% pressure drop to occur at $NPSH = 1.25\,\text{m}$, but with further lowering the inducer speed and bringing it down to a speed lower than the speed of the impeller, this process is reversed, causing a 5% pressure drop to occur at $NPSH = 1.35\,\text{m}$ for the speed of 1600 rpm. In the co-rotation mode, at nominal and high flow rates, a speed of 1200 rpm for the inducer has resulted in a substantial decline in pump cavitation performance. Consequently, this condition has not been subjected to further investigation and analysis.

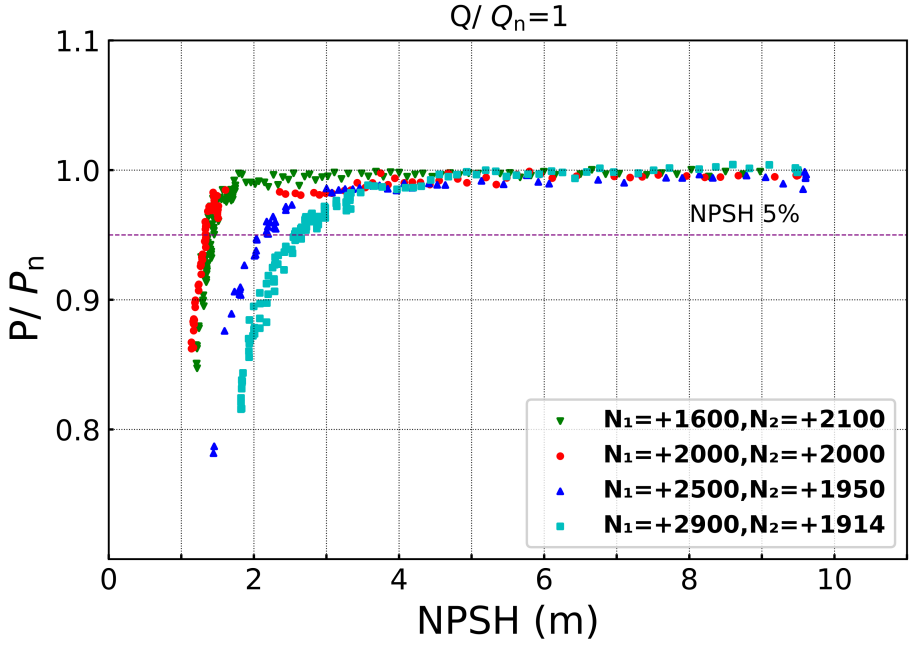

FIGURE 5.3 – Cavitation performance of pump by variation of inducer speed in co-rotation mode for $\frac{Q}{Q_n} = 1$

5.2.3 Effect of speed ratio at $\frac{Q}{Q_n} = 1.2$

Compared to the previous two flow rates, the impact of inducer speed variations on pump cavitation efficiency is significantly stronger for $\frac{Q}{Q_n} = 1.2$. As can be observed, the pressure drop for the inducer at 1600 rpm is rapid, and the pump faces a 5% pressure drop at $NPSH = 3.4\,\text{m}$. However, the cavitation efficiency is enhanced by increasing the inducer's speed to 2000 rpm in the situation where the inducer and impeller are rotating in the same direction and at the same speed. Consequently, the 5% pressure drop within the pump occurs at $NPSH = 2.96\,\text{m}$. Raising the inducer speed to 2500 rpm, similar to the two previous flow rates, leads to a decline in the pump cavitation performance. This results in a 5% pressure drop when $NPSH$ reaches 4.1 m. If the inducer speed is further increased to 2900 rpm, there is a more pronounced deterioration in the pump cavitation performance. This is evident as a 5% pressure drop happens at an $NPSH = 4.9\,\text{m}$.

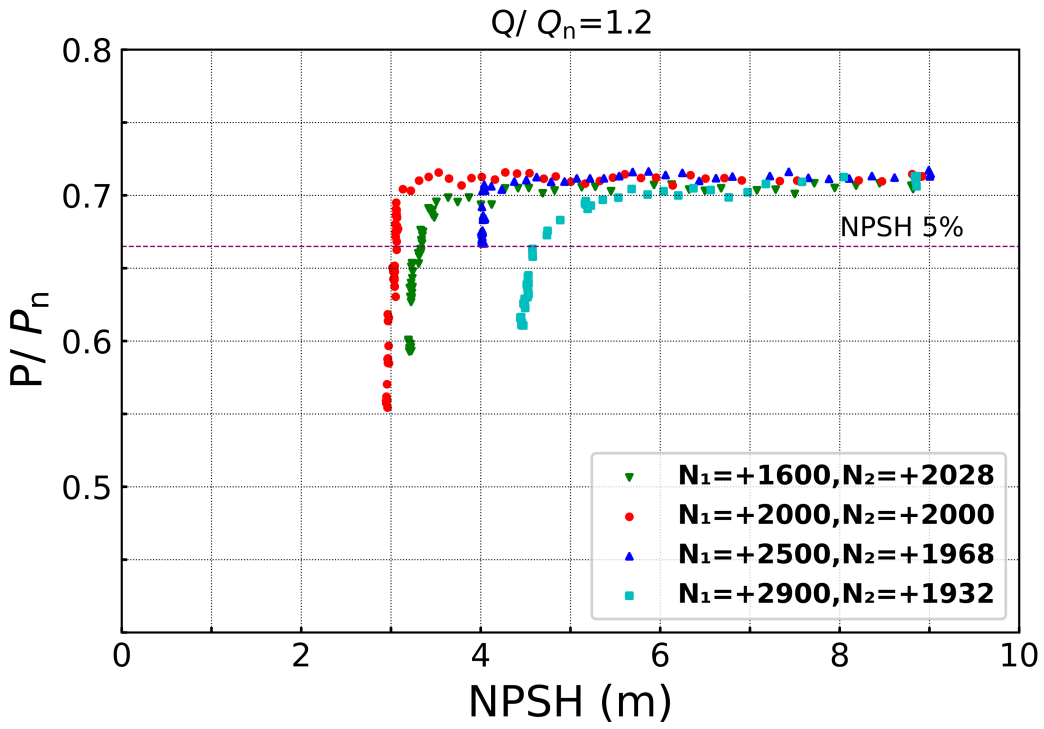

FIGURE 5.4 – Cavitation performance of pump by variation of inducer speed in co-rotation mode for $\frac{Q}{Q_n} = 1.2$

The cavitation efficiency graph of the pump was demonstrated considering the separate rotations

of the inducer and impeller in a co-rotation configuration. In general, it can be said that changing the inducer rotation speed has a significant impact on pump cavitation efficiency. However, this impact gets smaller as the flow rate decreases, resulting in more compression in the pump cavitation diagrams at $\frac{Q}{Q_n} = 0.87$. Moreover, as the flow rate increases, the gap between the points where a 5% pressure drop occurs expands for different rotation speeds. Observations show that when the inducer's speed surpasses that of the impeller, increasing the inducer speed results in a decline in cavitation efficiency. For all other flow rates, the best cavitation efficiency is for when the inducer and the impeller rotate at the same speed, with the exception of $\frac{Q}{Q_n} = 0.87$ and inducer speed of 1600 rpm, when some improvements can be observed. The impact of inducer speed on the cavitation efficiency of the pump in the counter-rotation mode is investigated in the following section.

5.2.4 Effect of inducer speed on the co-rotative pump cavitation performance at different flow rates

Figure 5.5 presents the study of $NPSH5\%$ variations in the co-rotating pump at various flow rates and inducer speeds. As the flow rate increases, the pump's cavitation performance becomes more sensitive to the speed of the inducer. Generally, the optimum speed for the inducer regarding pump cavitation performance is found to be 2000 rpm, representing the optimum point of the co-rotative pump cavitation performance. At the nominal flow rate and $\frac{Q}{Q_n} = 1.2$, an increase or decrease in the inducer speed from 2000 rpm results in an increase in $NPSH5\%$. When $\frac{Q}{Q_n} = 0.87$, increasing the speed of the inducer above 2000 rpm leads to a rise in $NPSH5\%$, while decreasing the speed does not significantly affect the $NPSH5\%$. This can be explained by the interaction between the fluid speed at the inducer outlet and the impeller inlet. When the inducer speed is increased, the speed of the fluid entering the impeller also goes up, increasing the potential for cavitation. On the other hand, for inducer speeds below 2000 rpm, the inducer does not generate enough pressure, effectively not affecting the pump cavitation performance.

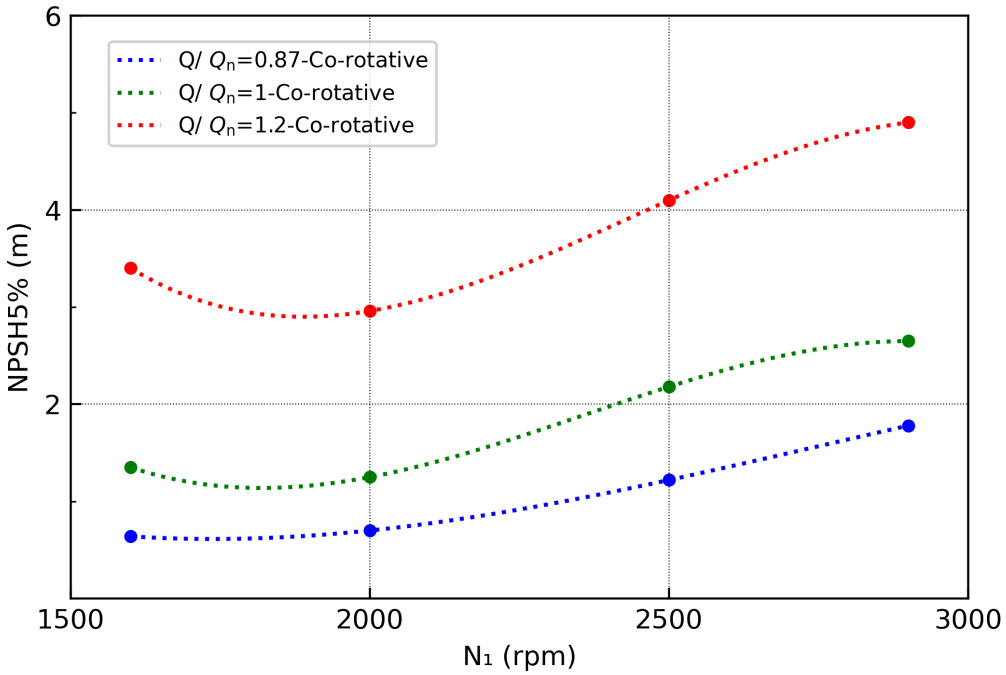

FIGURE 5.5 – $NPSH5\%$ (m) with inducer speed N_1 (rpm) for different flow rates in co-rotation mode

5.3 Cavitation of inducer and impeller in counter-rotation mode

5.3.1 Effect of speed ratio at $\frac{Q}{Q_n} = 0.87$

Figure 5.6 illustrates the cavitation performance of the pump at $Q/(Q_n = 0.87)$ when operating in the counter-rotation mode at various inducer speeds. The impeller must rotate at a slower speed in the counter-rotation mode to achieve the same pressure as in the co-rotation mode because the pump produces more pressure in the counter-rotation mode than in the co-rotation mode as was discussed in the previous section.

Observing Figure 5.6, it becomes evident that at an inducer rotation speed of 1200 rpm, the pump experiences a 5% decline with $NPSH = 0.83\,\text{m}$. Similarly, at the maximum inducer speed of 2900 rpm, there is a 5% pressure decrease at $NPSH = 0.5\,\text{m}$. Based on Figure 5.6, both the inducer low and high speeds enhance the pump cavitation efficiency. Meanwhile, at speeds like 1600, 2000, and 2500 rpm, the 5% pressure drop takes place around $NPSH = 0.35\,\text{m}$. Additionally, the local pressure

drop at speeds of 1200 and 2900 rpm begins from $NPSH = 3\,\text{m}$.

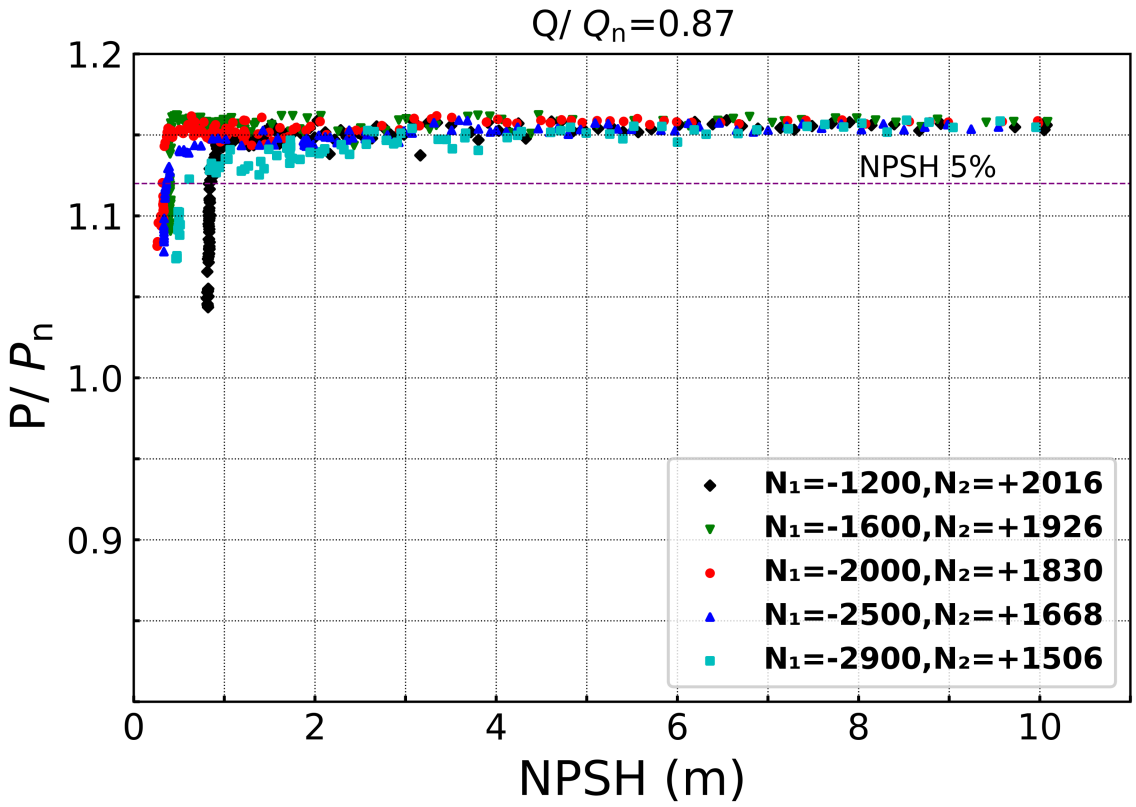

FIGURE 5.6 – Cavitation performance of pump by variation of inducer speed in counter-rotation mode for $\frac{Q}{Q_n} = 0.87$

5.3.2 Effect of speed ratio at nominal flow rate

As the flow rate increases to the nominal rate, the impact of inducer speed variations on cavitation performance shifts, especially at higher speeds. At an inducer speed of 2000 rpm, there is a 5% drop in pressure at $NPSH = 0.62\,\text{m}$. When the inducer speed is raised to 2500 rpm, this 5% pressure decrease is seen at $NPSH = 0.52\,\text{m}$. Operating the inducer in counter-rotation mode at increased speeds improves the pump cavitation efficiency. When the inducer speed is further increased up to 2900 rpm, its cavitation efficiency remains superior to that at 2000 rpm. In contrast, slowing down the inducer to 1600 rpm degrades the pump cavitation performance, with a 5% pressure drop recorded at $NPSH = 1.2\,\text{m}$. A decline in inducer speed consistently diminishes the pump cavitation efficacy. For example, at 1200 rpm, a 5% pressure drop corresponds to $NPSH = 1.8\,\text{m}$.

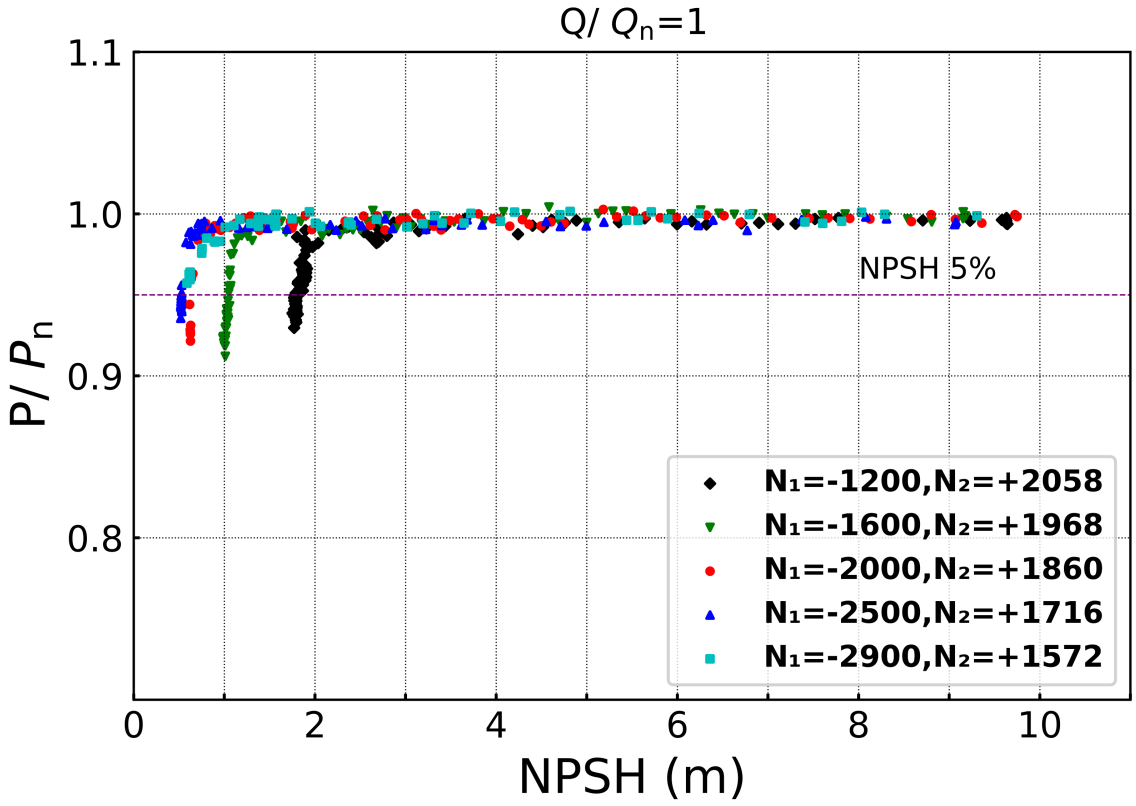

FIGURE 5.7 – Cavitation performance of pump by variation of inducer speed in counter-rotation mode for $\frac{Q}{Q_n} = 1$

5.3.3 Effect of speed ratio at $\frac{Q}{Q_n} = 1.2$

Figure 5.8 illustrates how variations in the inducer rotational speed impact pump cavitation performance when operating in counter-rotation mode at high flow rates. Unlike the co-rotation setting, increasing the inducer's speed notably enhances the pump's cavitation performance. When the inducer rotates at 1200 rpm, a 5% pressure drop is observed at an $NPSH = 4.46\,\text{m}$. However, when the speed rises up to 1600 rpm, this value drops to 3.48. There is a noticeable positive correlation between inducer speed and cavitation performance : at 2000 rpm, the $NPSH = 2.65\,\text{m}$, at 2500 rpm, it stands at 2.15, and remarkably, at 2900 rpm, the 5% pressure drop corresponds to an $NPSH = 1.53\,\text{m}$. The findings from the cavitation experiments on the counter-rotation pump reveal that counter-rotation considerably impacts the pump cavitation behavior. In contrast to the co-rotation pump, increasing up the inducer's speed beyond that of the impeller enhances the pump cavitation efficiency. Thus, at

$\frac{Q}{Q_n} = 1.2$, the $NPSH5\% = 1.53\,\text{m}$ at 2900 rpm, compared to $NPSH5\% = 2.65\,\text{m}$ at 2000 rpm.

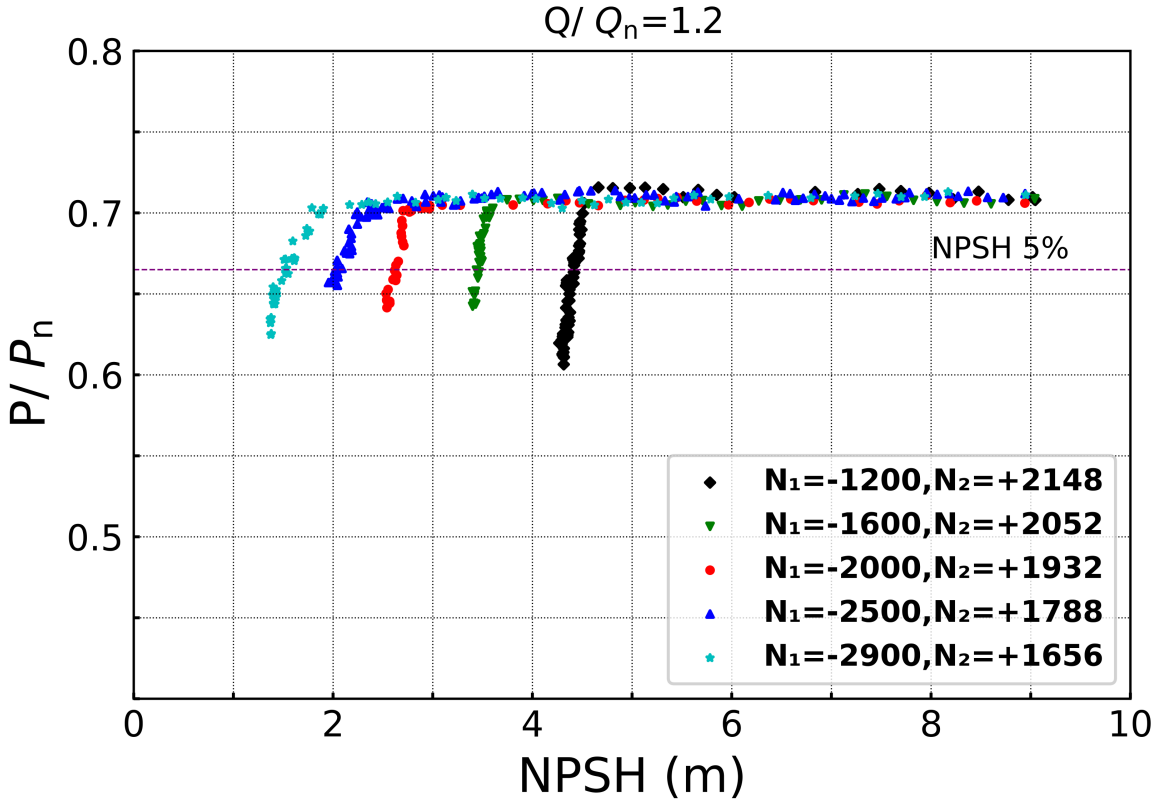

FIGURE 5.8 – Cavitation performance of pump by variation of inducer speed in counter-rotation mode for $\frac{Q}{Q_n} = 1.2$

5.3.4 Effect of inducer speed on the counter-rotative pump cavitation performance at different flow rates

Figure 5.9 shows the changes in $NPSH5\%$ of the pump in counter-rotation mode, with adjustments to the inducer speed across different flow rates. In contrast to the co-rotation mode, increasing the inducer speed in the counter-rotation mode notably enhances the pump cavitation performance. At low flow rates, given that the $NPSH5\%$ of the pump is low even at low inducer speeds, the pump's sensitivity to speed changes is lower than at high flow rates. At $\frac{Q}{Q_n} = 1.2$, increasing the inducer speed from 1200 rpm to 2900 rpm leads to a significant decrease in $NPSH5\%$. For $\frac{Q}{Q_n} = 1$ and $\frac{Q}{Q_n} = 0.87$, it can be observed that while increasing the speed above 2000 rpm slightly improves the $NPSH5\%$ of the pump, further reduction of $NPSH5\%$ is practically difficult due to the already low value of

$NPSH5\%$ (less than 0.4). Because of experimental limitations, the inducer speed cannot be increased above 2900 rpm. However, it can be suggested that enhancing the inducer speed beyond 2900 rpm might still offer opportunities to improve the $NPSH5\%$ of the pump at $\frac{Q}{Q_n} = 1.2$, as indicated in Figure 5.9. The change in $NPSH5\%$ trend with inducer speed in the counter-rotation mode compared to the co-rotation mode can be explained by analyzing the speed triangle at the inducer outlet and impeller inlet. In the counter-rotation mode, increasing the inducer speed not only reduces the flow inlet speed in the impeller but also, due to the increased pressure in the pump as per Euler's law (mentioned in previous sections), leads to a decrease in the impeller speed. This results in a significant drop in the $NPSH5\%$ of the pump in the counter-rotation mode.

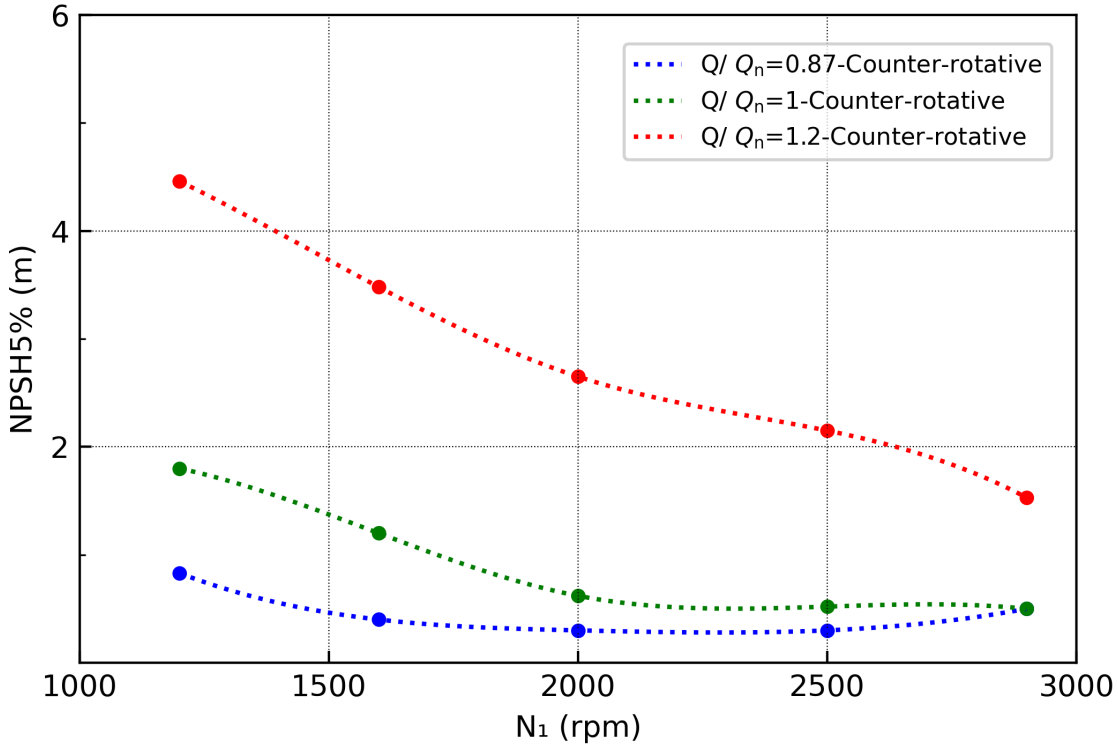

FIGURE 5.9 – $NPSH5\%$ (m) with inducer speed N_1 (rpm) for different flow rates in counter-rotation mode

5.3.5 Effect of distance between rotors at low flow rate

An inducer with the ability to rotate independently allows it to rotate at varying speeds relative to the impeller and even rotate in the opposite direction, utilizing the counter-rotation method. The cavitation efficiency of the pump in both co-rotation and counter-rotation modes was found to be seriously impacted by changing the inducer rotation speed in the previous section. In the newly designed test bench, owing to the independent rotation capability of the inducer, not only can the speed and direction of the inducer rotation be modified, but the distance between the inducer and the impeller can also be adjusted. In the present section, the impact of the spacing between the inducer and the impeller on the pump's cavitation efficiency in counter-rotation mode is explored. Consequently, this spacing is denoted by L, and is assessed at two specific distances : 20 mm and 80 mm.

5.3.5.1 $N_1 = \pm 2000$ rpm

Figure 5.10 displays the cavitation characteristics of the pump in counter mode when the inducer is positioned 20 mm and 80 mm away from the impeller. Three specific points are highlighted for both co-rotation and counter-rotation curves : points a and b indicating pump pressure instability, points c and d indicate the 5% pressure drop, and points e and f representing the breakdown point. Figure 5.10 indicates that the pump's cavitation performance is superior when the inducer is positioned 80 mm from the impeller compared to a 20 mm distance. At the 20 mm spacing, there is a 5% pressure drop in $NPSH = 0.55\,\text{m}$. However, when the gap between the inducer and impeller is extended to 80 mm, this value drops to 0.3.

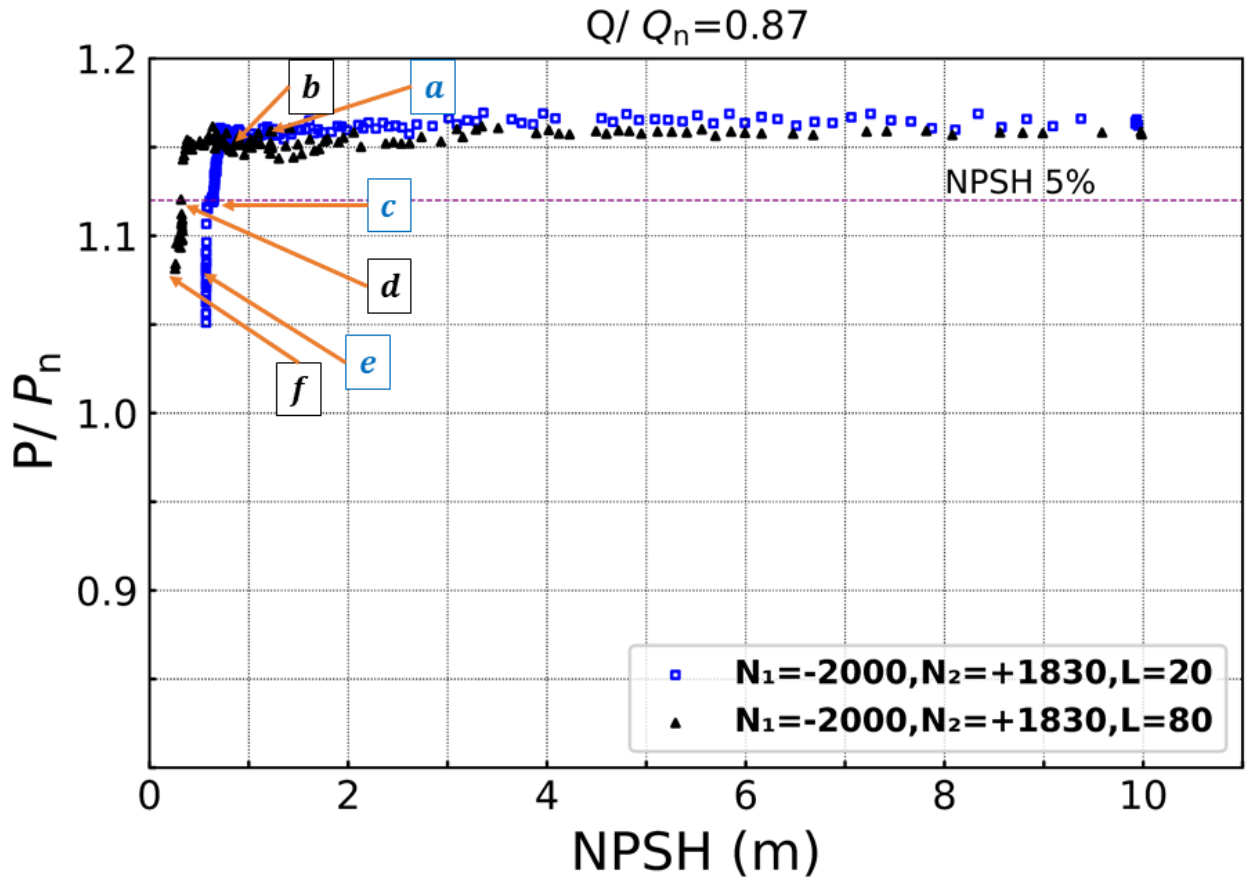

FIGURE 5.10 – Cavitation performance of pump for $L = 20$ mm and $L = 80$ mm in counter-rotation mode for $\frac{Q}{Q_n} = 0.87$ and $N_1 = -2000$ rpm

Cavitation in the inducer and between the inducer and the impeller has been studied using a high-speed camera. The camera's characteristics have been explained earlier, and two LED light screens were used on both sides of the system to generate the required exposure. To reflect light, a white LED screen is also employed behind the inducer. In Figure 5.11, cavitation within the inducer is visually analyzed for $L = 20$ mm and $L = 80$ mm, with the inducer rotating at 2000 rpm. When the inlet pressure of the pump is decreased, a long and narrow tip vortex is observed at the inducer edge for $L = 20$ mm (figure 5.11a). However, when the L is increased to 80 mm, the vortex becomes shorter and a bit wider. Additionally, a hub vortex is detected between the inducer and the impeller (figure 5.11b). This hub vortex exhibits dual rotational patterns : it aligns with the inducer rotation and

simultaneously revolves around its own axis.

In Figure 5.11c, with the pump undergoing a 5% pressure drop, the expansion of cavitation in the inducer is illustrated. Here, not only the first blade but also the second blade display signs of cavitation. A type of cavitation known as cavitation leakage is noted, a phenomenon resulting from the pressure differential across the blade's two surfaces.

Figure 5.11d shows the inducer when subjected to a 5% pressure drop, but with the inducer positioned 80 mm away. In this representation, the cavitation appears to have proliferated across the inducer blade surface. The 'cavitation leakage' type is again observed. Additionally, the vortex hub located between the impeller and inducer is discernibly more pronounced in its thickness.

When the pump inlet pressure is further decreased to the break-down point, the inducer is fully cavitated. Figure 5.11e and figure 5.11f show the various forms of cavitation present in the inducer when it is positioned 20 mm and 80 mm away from the impeller, respectively. From the illustrations, it is evident that with $L = 80$ mm, the hub vortex, which forms between the inducer and the impeller, has expanded. However, as it expands, its intensity appears to diminish.

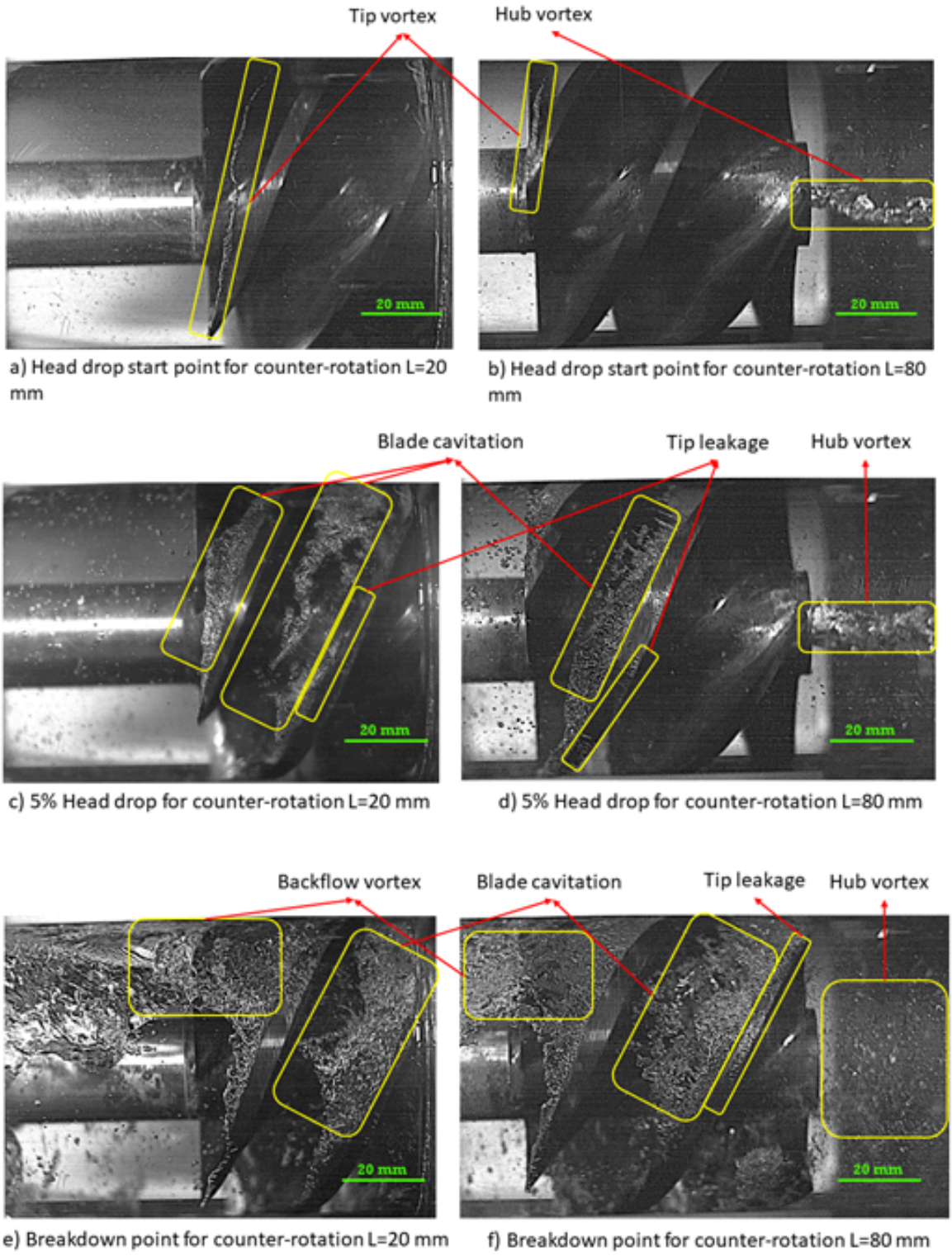

FIGURE 5.11 – Development of cavitation for $\frac{Q}{Q_n} = 0.87$ and $N_1 = -2000$ rpm for $L = 20$ mm and $L = 80$ mm

5.3.5.2 $N_1 = \pm 2500$ rpm

Analyzing the cavitation performance of the pump with the inducer operating at a speed of 2500 rpm at distances of 20 mm and 80 mm, it appears that the distance between the inducer and the impeller at this speed has a smaller impact on the pump cavitation performance than at a speed of 2000 rpm. For $L = 20$ mm, a 5% pressure drop is observed at $NPSH = 0.4$ m. In contrast, this value is 0.3 when the $L = 80$ mm. This suggests that the impact of variation of the inducer speed from 2000 rpm to 2500 rpm on cavitation efficiency is less pronounced when the inducer is 80 mm away. However, as the space between the inducer and impeller decreases, there is an enhancement in efficiency with the increase in speed. This explains why, at 2500 rpm, the difference between 80mm and 20mm distance has decreased.

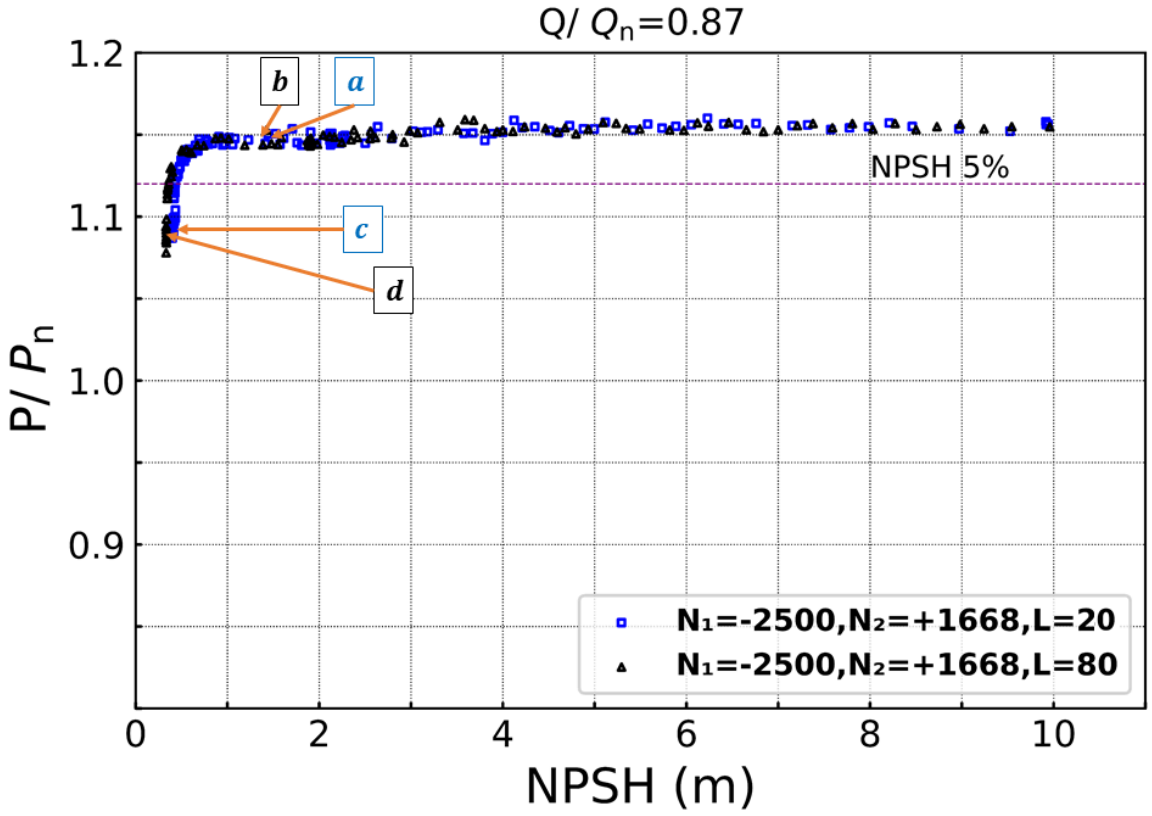

FIGURE 5.12 – Cavitation performance of pump for $L = 20$ mm and $L = 80$ mm in counter-rotation mode for $\frac{Q}{Q_n} = 0.87$ and $N_1 = -2500$ rpm

Figure 5.13a illustrates the initial signs of cavitation in the inducer when it is near the impeller.

At the inducer tip, both leakage and tip vortex cavitation are noticeable. The tip vortex cavitation in this case is shorter than in the previous case and looks like a rope touching the inducer edge. There is also a slight presence of backflow cavitation in this image, which appears to impact the tip vortex cavitation.

When the $L = 80$ mm, besides the tip vortex cavitation and tip leakage cavitation, the hub vortex between the inducer and the impeller is also noted. This hub vortex manifests as a rope-like structure that rotates around its own axis. At the break point, the cavitation patterns in the inducer are similar for both distances. The cavitation is extensive, covering almost the entire surface of the inducer blade. An enhanced tip leakage cavitation is also observed. When the $L = 80$ mm, the hub vortex, located between the inducer and the impeller, still exists. However, its oscillation becomes more pronounced. This results in a steeper angle between the hub vortex and the axis of the inducer.

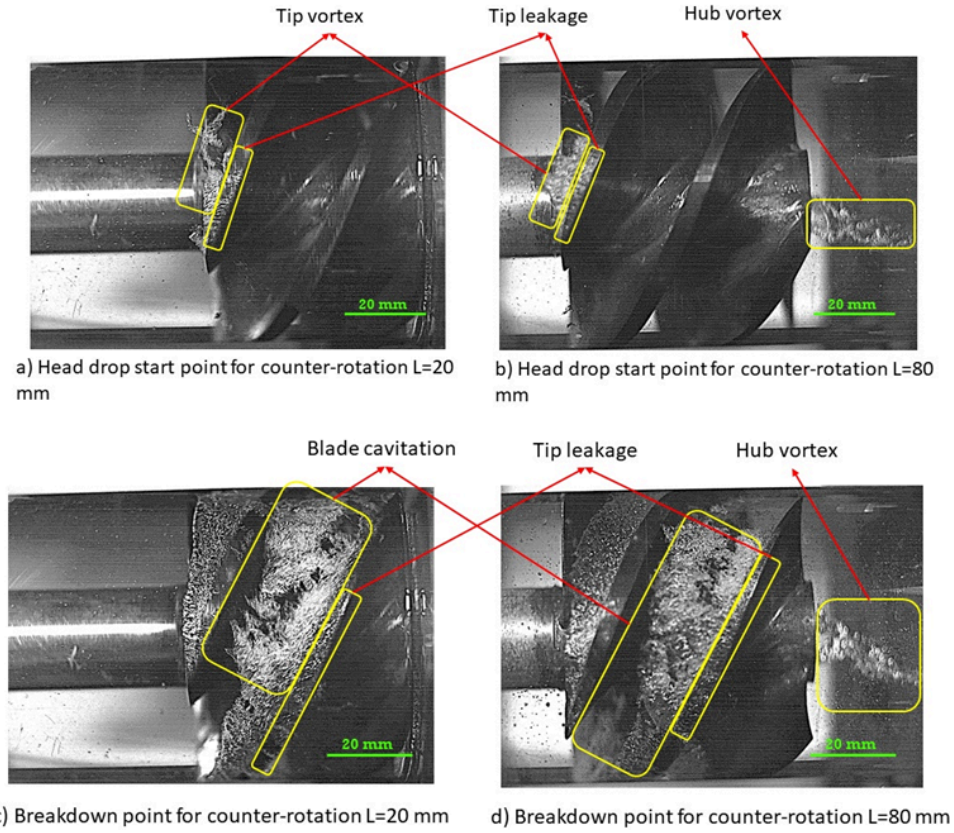

FIGURE 5.13 – Development of cavitation for $\frac{Q}{Q_n} = 0.87$ and $N_1 = -2500$ rpm for $L = 20$ mm and $L = 80$ mm

5.3.5.3 $N_1 = \pm 2900$ rpm

When the inducer speed is raised to 2900 rpm, as shown in Figure 5.14, the impact of the gap between the inducer and the impeller on the pump cavitation performance becomes more pronounced. With a 20 mm distance between the inducer and impeller, the $NPSH = 0.85$ m. However, when this distance is expanded to 80 mm, the $NPSH$ drops to 0.5 m, highlighting an enhancement in the pump's resistance to cavitation.

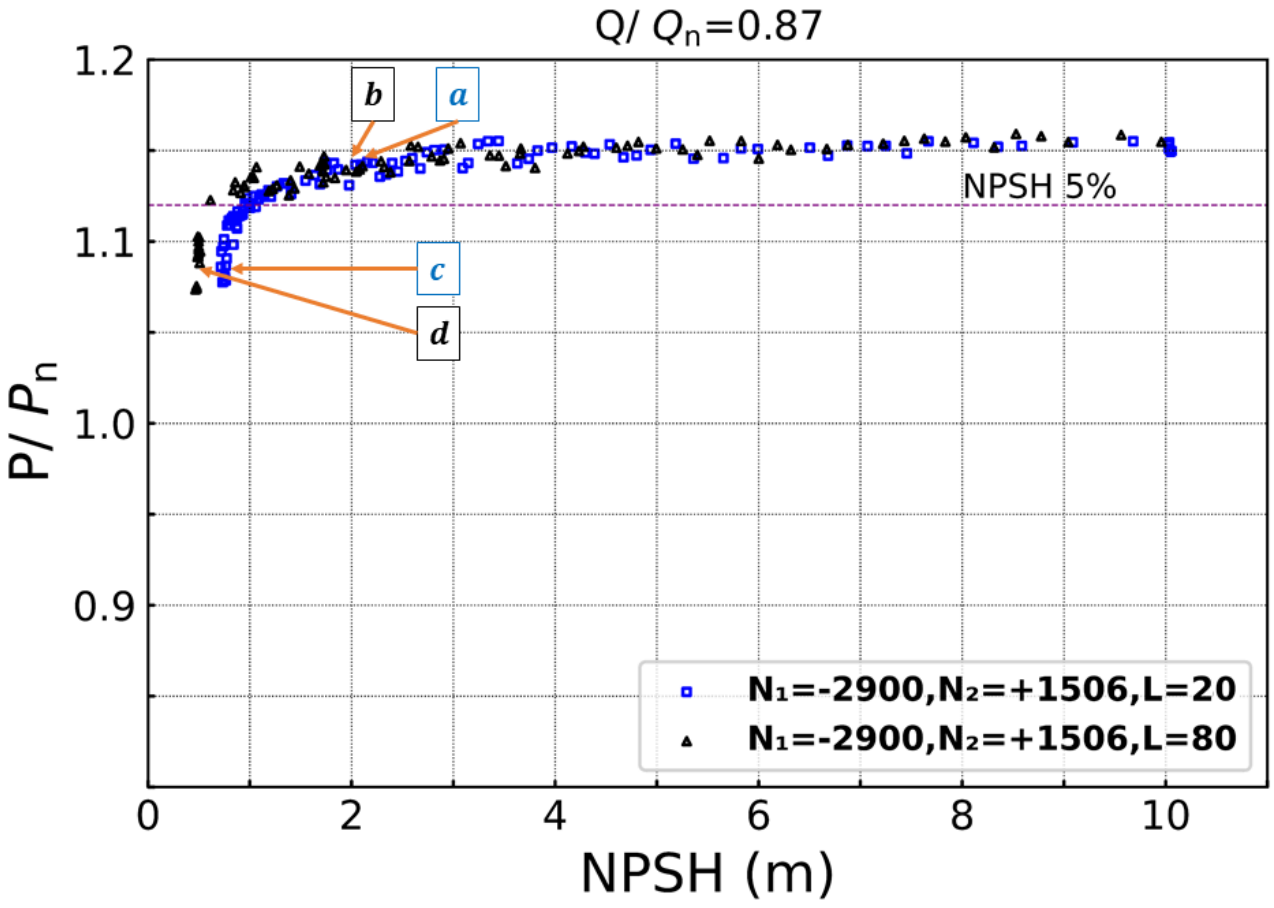

FIGURE 5.14 – Cavitation performance of pump for $L = 20$ mm and $L = 80$ mm in counter-rotation mode for $\frac{Q}{Q_n} = 0.87$ and $N_1 = -2900$ rpm

The patterns of cavitation remain relatively consistent regardless of the changes in distance, meaning the cavitation curves are quite similar whether the distance increases or decreases. For example, at a speed of 2900 rpm, a local pressure drop is observed in both distances and the pressure drop rea-

ched at 5% is steep. Then, with a further reduction of the input pressure, the pressure drops suddenly. However, the value of the $NPSH$ number for a 5% pressure drop is different. By increasing the inducer speed to 2900 rpm, it can be seen that the cavitation backflow phenomena is exhibited in front of the inducer blade in the case where the inducer is close to the impeller (figure 5.15a), where it is close to the 5% pressure drop, and with the start of instability. At this rotational speed, unlike lower speeds where only tip vortex cavitation was observed, both backflow and tip vortex cavitation are seen.

Additionally, cavitation of this kind has been seen over a distance of 80 mm, demonstrating that it is influenced by the inducer speed and flow rate and that it only happens at low flow rates as a result of blockage in front of the inducer. Additionally, hub vortex cavitation may occur when the distance between them is 80 mm. However, it appears to be less intense than what is observed at lower speeds. This particular hub vortex looks like a twined rope with two bound vortices, rotating similar to the inducer but counter to the rotation of the impeller.

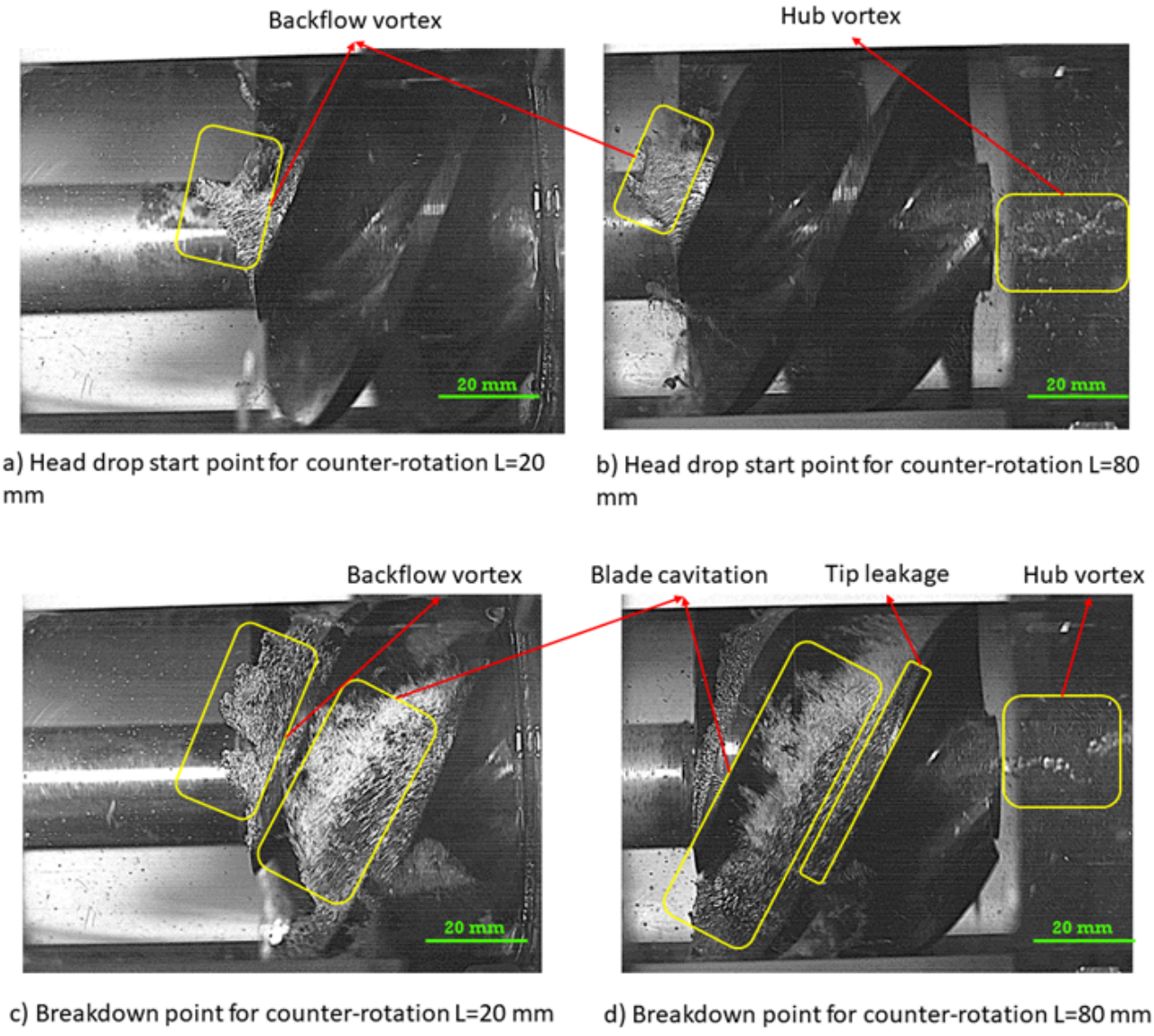

FIGURE 5.15 – Development of cavitation for $\frac{Q}{Q_n} = 0.87$ and $N_1 = -2900$ rpm for $L = 20$ mm and $L = 80$ mm

5.3.6 Effect of distance between rotors at nominal flow rate

Figure 5.16 illustrates how variation in the distance between the inducer and impeller influences pump cavitation at nominal flow rate across three varied inducer speeds. Based on Figure 5.16, one can observe that for the nominal flow rate, variations in the gap between the inducer and impeller do not significantly impact the pump cavitation behavior. Observations indicate that variations in the inducer speed influence the pump cavitation performance. However, regardless of the inducer speed,

adjustments in the gap between the inducer and impeller have no impact on cavitation.

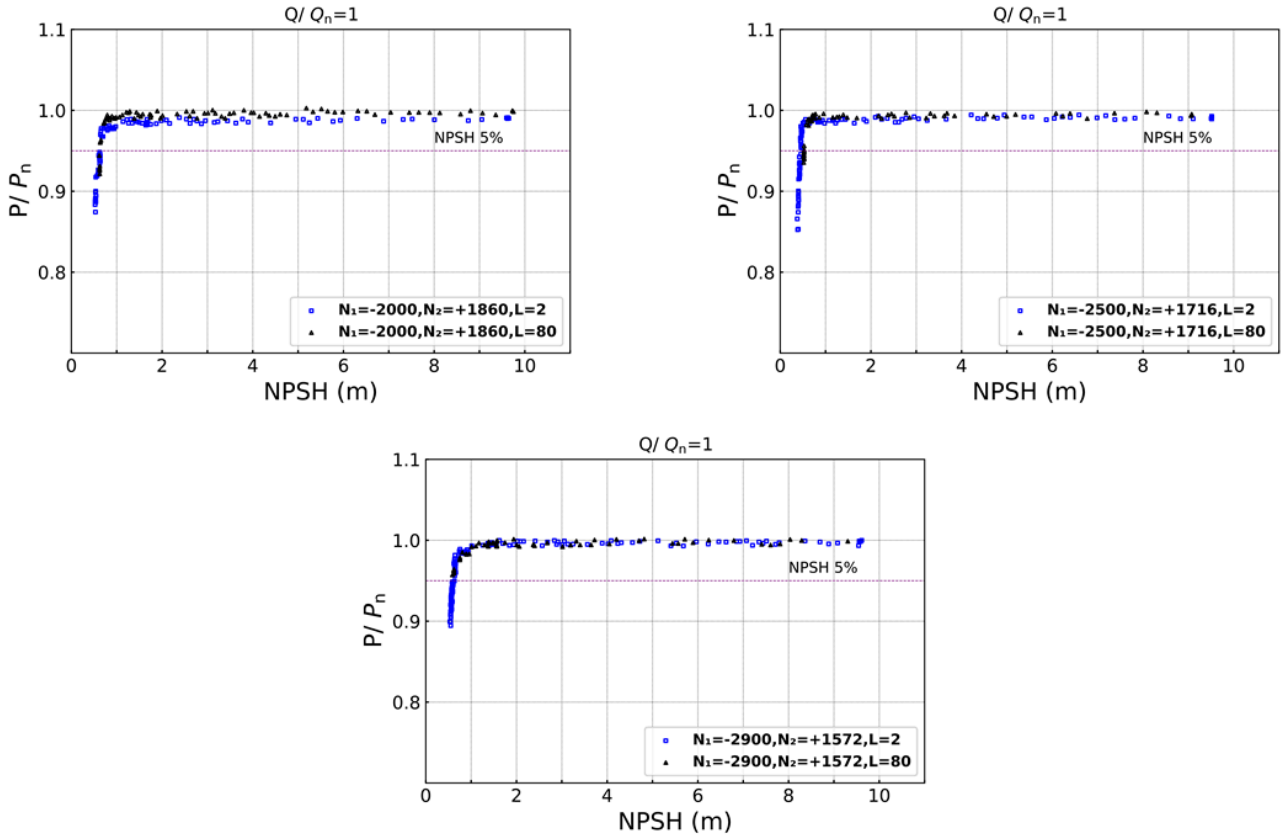

FIGURE 5.16 – Cavitation performance of pump for $L = 20$ mm and $L = 80$ mm in counter-rotation mode for $\frac{Q}{Q_n} = 1$ and different inducer speeds (N_1)

5.3.7 Effect of distance between rotors at high flow rate

When $\frac{Q}{Q_n} = 1.2$, the effect of varying the distance between the inducer and the impeller on pump cavitation becomes evident, which differs from observations at the nominal flow rate. Figure 5.17 demonstrates that at an inducer speed of 2000 rpm, the changes in distance have no significant impact on pump cavitation. However, when the inducer speed is raised to 2500 rpm, there is a noticeable difference in the graphs. Specifically, the pump exhibits superior cavitation efficiency when the gap between the inducer and the impeller is 80 mm. The influence of the distance on the pump cavitation performance becomes more pronounced as the inducer speed increased. For example, at 2900 rpm, a 5% pressure drop corresponds to $NPSH = 1.93$ m at a 20 mm distance, whereas it stands at $NPSH = 1.58$ m for an 80 mm distance.

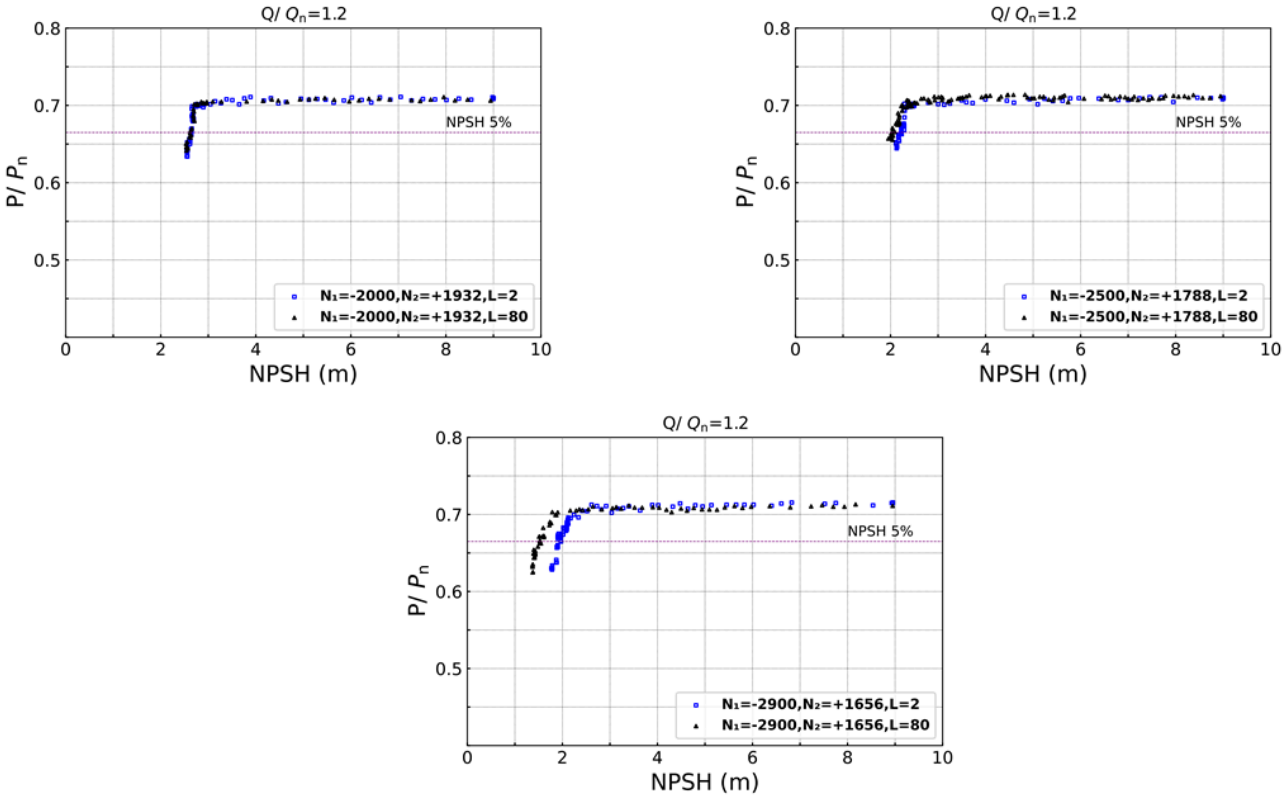

FIGURE 5.17 – Cavitation performance of pump for $L = 20$ mm and $L = 80$ mm in counter-rotation mode for $\frac{Q}{Q_n} = 1.2$ and different inducer speeds (N_1)

5.4 Comparison of co-rotation and counter-rotation cavitation performance

5.4.1 Pump cavitation performance for $N_1 = \pm 2000$ rpm

5.4.1.1 Low flow rate

Figure 5.18 shows that for $\frac{Q}{Q_n} = 0.87$, as the system pressure decreases and the $NPSH$ reaches 3 m, the pump maintains a constant pressure. However, if the pressure continues to decrease, a slight decline in pump pressure is observed in both co-rotation and counter-rotation modes. When the system pressure is reduced to $NPSH = 1\,\text{m}$, the pump operating in co-rotation mode experiences a significant pressure drop, with a 5% decrease observed at $NPSH = 0.7\,\text{m}$. Conversely, in counter-rotation mode, this pressure drop occurs at $NPSH = 0.4\,\text{m}$, and a 5% pressure drop is observed at $NPSH = 0.3\,\text{m}$. A primary factor enhancing cavitation performance in counter-rotation mode is the reduced speed of the impeller. Essentially, by decreasing the impeller speed, the fluid velocity in the suction blade of

the impeller is reduced, leading to a delay in cavitation phenomena.

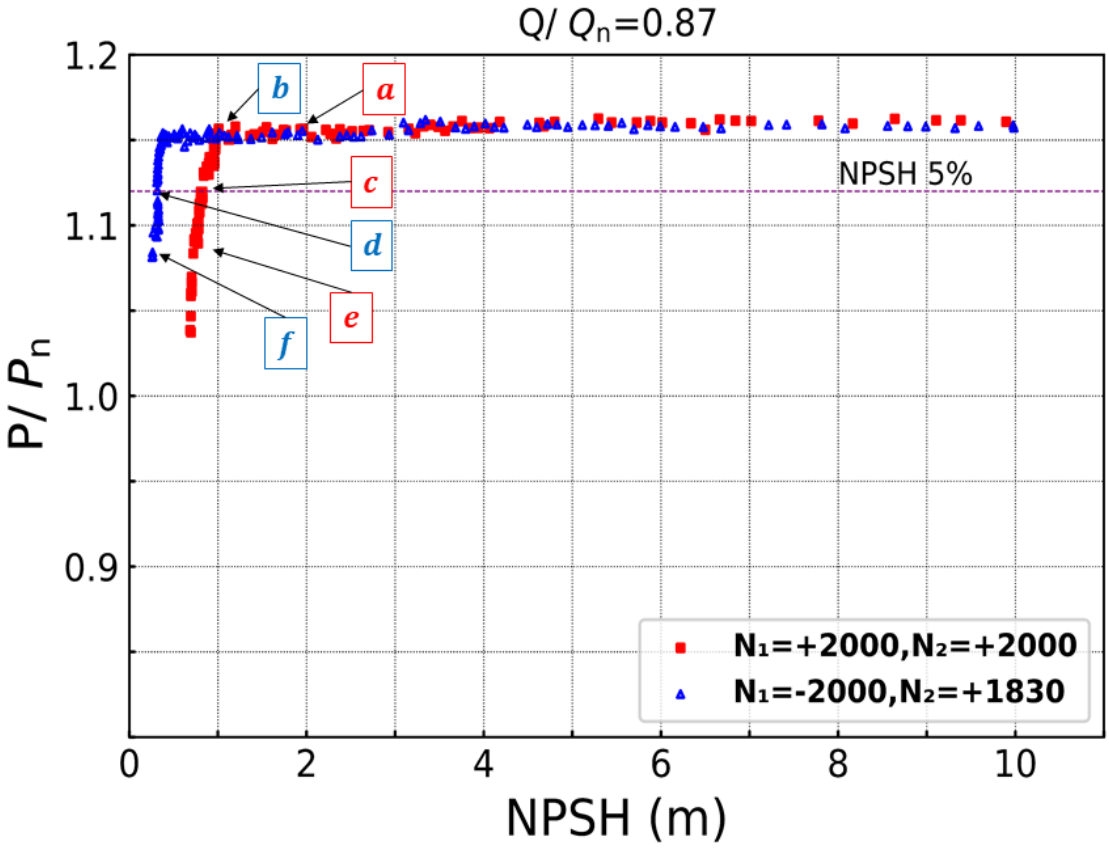

FIGURE 5.18 – Comparison of cavitation performance of pump for $\frac{Q}{Q_n} = 0.87$ and $N_1 = \pm 2000$ rpm

To visually analyze the different types of cavitation occurring in the inducer (Figure 5.19), a high-speed camera is employed. Figure 5.19a shows the presence of tip vortex cavitation at $NPSH = 2\,\text{m}$, which occurs at the tip of the inducer and is observed in both co-rotation and counter-rotation modes. The slight pressure reduction in co-rotation mode at $NPSH = 2\,\text{m}$ can be attributed to the formation of hub vortex cavitation between the impeller and the inducer, as shown in Figure 5.19a. Figure 5.19c demonstrates that in co-rotation mode and at a 5% pressure drop, the strength of the hub vortex cavitation intensifies, leading to an enlargement of its diameter. This hub vortex exhibits two types of rotation : rotational motion around the rotation axis of the impeller and the inducer, and rotation around its own formed axis. The formation of this cavitation is partly caused by the pre-swirl of the fluid induced by the rotation of the inducer. Figure 5.19c also illustrates the growth of tip vortex

cavitation in the co-rotation mode. Figure 5.19e illustrates an increase in the size of the cavitation vortex at the tip and the occurrence of blade cavitation as the $NPSH$ decreases, approaching the breakdown point in co-rotation mode. Notably, significant hub vortex cavitation is still observed at this point. The hub vortex created between the two rotors is due to the low pressure between the inducer hub and the impeller, like what happens in Francis turbines. This area experiences a pressure drop under the influence of the impeller rotation, but because it is not affected by the inducer blades and is in the hub, it is not affected by the pressure increase by the inducer. It can be seen that with the decrease of $NPSH$, this vortex becomes thicker, but it does not reach the area behind the inducer blades and always remains between the inducer hub and the blade, except in the case of break down in counter-rotation, which is due to the very low number of $NPSH$ and complete inducer cavitation, there is no more pressure increase by the inducer blades and the hub vortex is widened. The reason for tip leakage cavitation is the pressure difference between the suction surface and the high pressure surface of the inducer blade. In other words, by reducing the pressure of the system, the high pressure flow in the inducer blade has the ability to return to the suction level of the blade due to the existence of a 1mm clearance between the inducer tip and the tube [87].

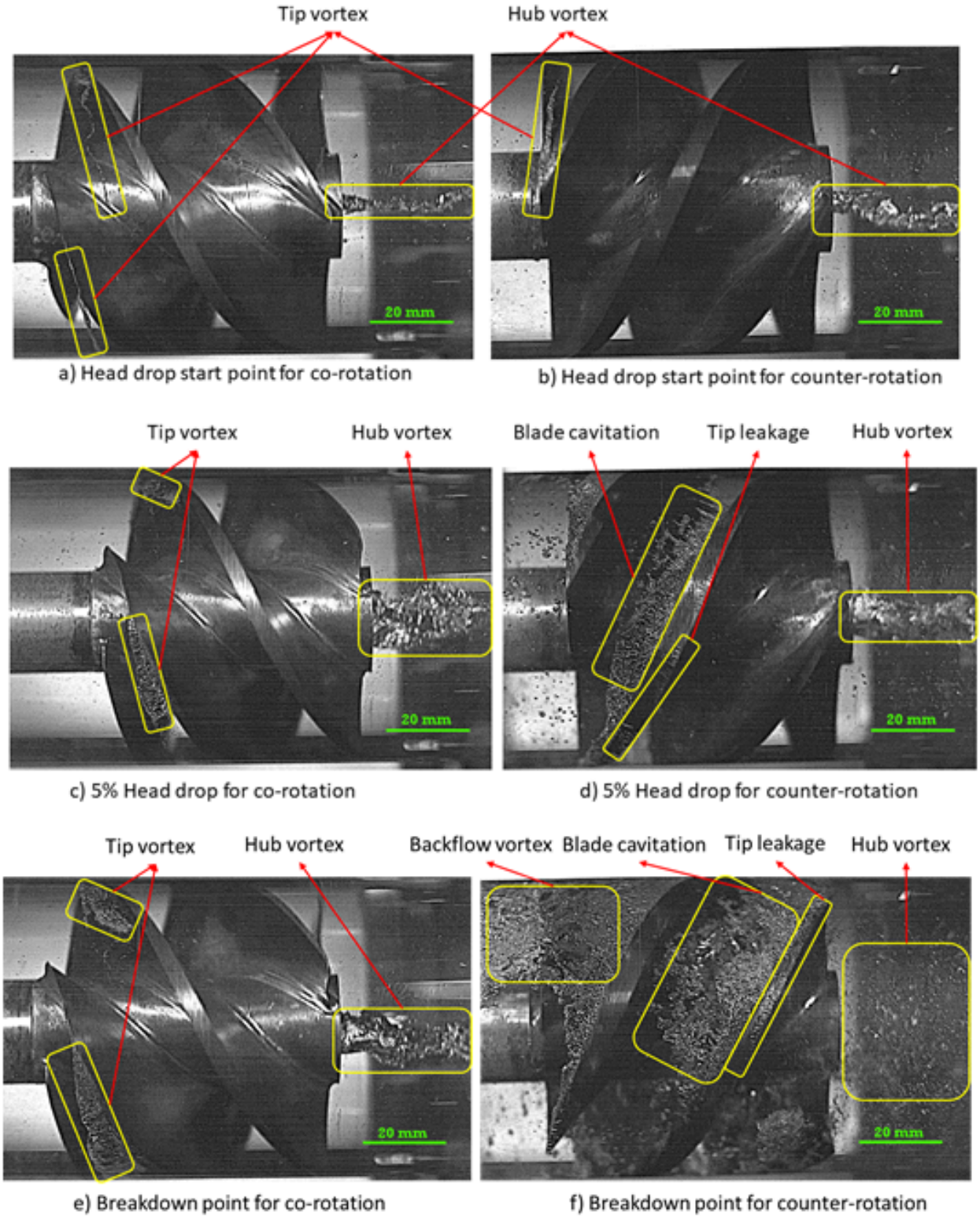

FIGURE 5.19 – Development of cavitation for $\frac{Q}{Q_n} = 0.87$ and $N_1 = \pm 2000$ rpm

Based on Figure 5.19b, in the counter-rotation mode, when the $NPSH = 1\,\mathrm{m}$, tip vortex cavitation becomes evident at the tip of the inducer. Additionally, the presence of hub vortex cavitation between the inducer and the impeller is noticeable. Similar to the co-rotation mode, this hub vortex cavitation rotates around its own axis and the rotational axis of the inducer and impeller. However, its rotational direction aligns with the inducer's rotation and differs from the co-rotation mode.

The hub vortex cavitation between the impeller and the inducer becomes stronger and wider when the head drop point is 5% in the counter-rotation mode at $NPSH = 0.3\,\mathrm{m}$ (Figure 5.19d). Additionally, blade cavitation is observed between the two inducer blades, indicating the spread of cavitation from the blade surface to the inducer hub. The pressure difference between the two sides of the inducer blades also contributes to the occurrence of tip leakage cavitation, as shown in Figure 5.19d.

At the breakdown point for the counter-rotation mode (Figure 5.19f), there is a significant increase in cavitation within the inducer. This cavitation is observed as backflow at the inlet of the inducer, typically caused by low flow rates and flow blockage at the inducer inlet. Moreover, the extent of cavitation on the inducer blades and its progression towards the inducer hub can be observed. Furthermore, there are changes in the hub vortex cavitation at the hub between the inducer and the impeller. The hub vortex expands outward, covering nearly the entire space between the inducer and the impeller. However, this expansion results in a decrease in the intensity and concentration of the cavitation.

5.4.1.2 Nominal flow rate

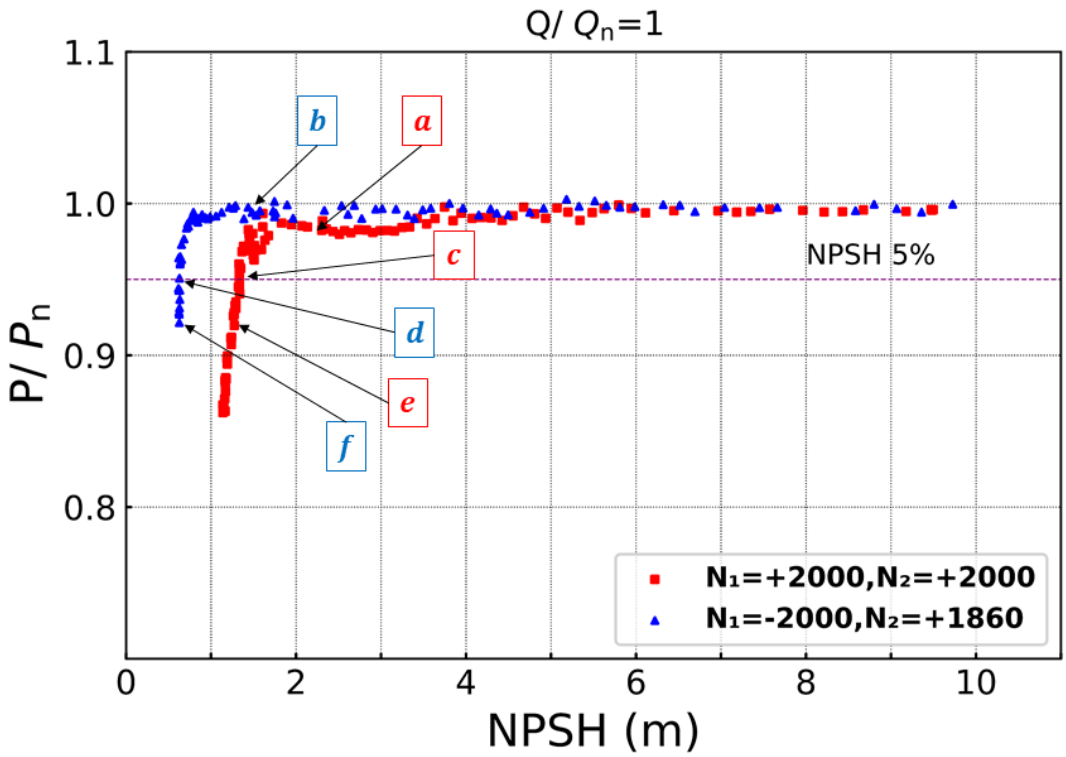

FIGURE 5.20 – Comparison of cavitation performance of pump for $\frac{Q}{Q_n} = 1$ and $N_1 = \pm 2000$ rpm

Figure 5.20 compares the cavitation performance of co-rotation and counter-rotation modes at a nominal flow rate. When $NPSH = 3.5\,\text{m}$, there is a slight decrease in pressure, followed by an increase at $NPSH = 2.5\,\text{m}$, causing pressure fluctuations in the co-rotation mode. The hub vortex cavitation between the inducer and the impeller does not occur due to the high flow rate (Figure 5.21a). As the $NPSH$ decreases and reaches 1.6 m, the pressure experiences a rapid decline, and at $NPSH = 1.25\,\text{m}$, a 5% pressure drop is observed. On the other hand, in the counter-rotation mode, there are no noticeable pressure fluctuations until the $NPSH = 1.2\,\text{m}$. However, beyond this point, pressure drops begin to occur, and at $NPSH = 0.8\,\text{m}$, there is a sudden decrease in pump pressure, resulting in a 5% pressure drop at $NPSH = 0.62\,\text{m}$. The counter-rotation inducer continues to positively impact the cavitation performance of the pump as the flow rate increases, resulting in an improvement in cavitation performance for the 5% pressure drop ($NPSH5\%$) pump from 1.25 m to 0.62 m.

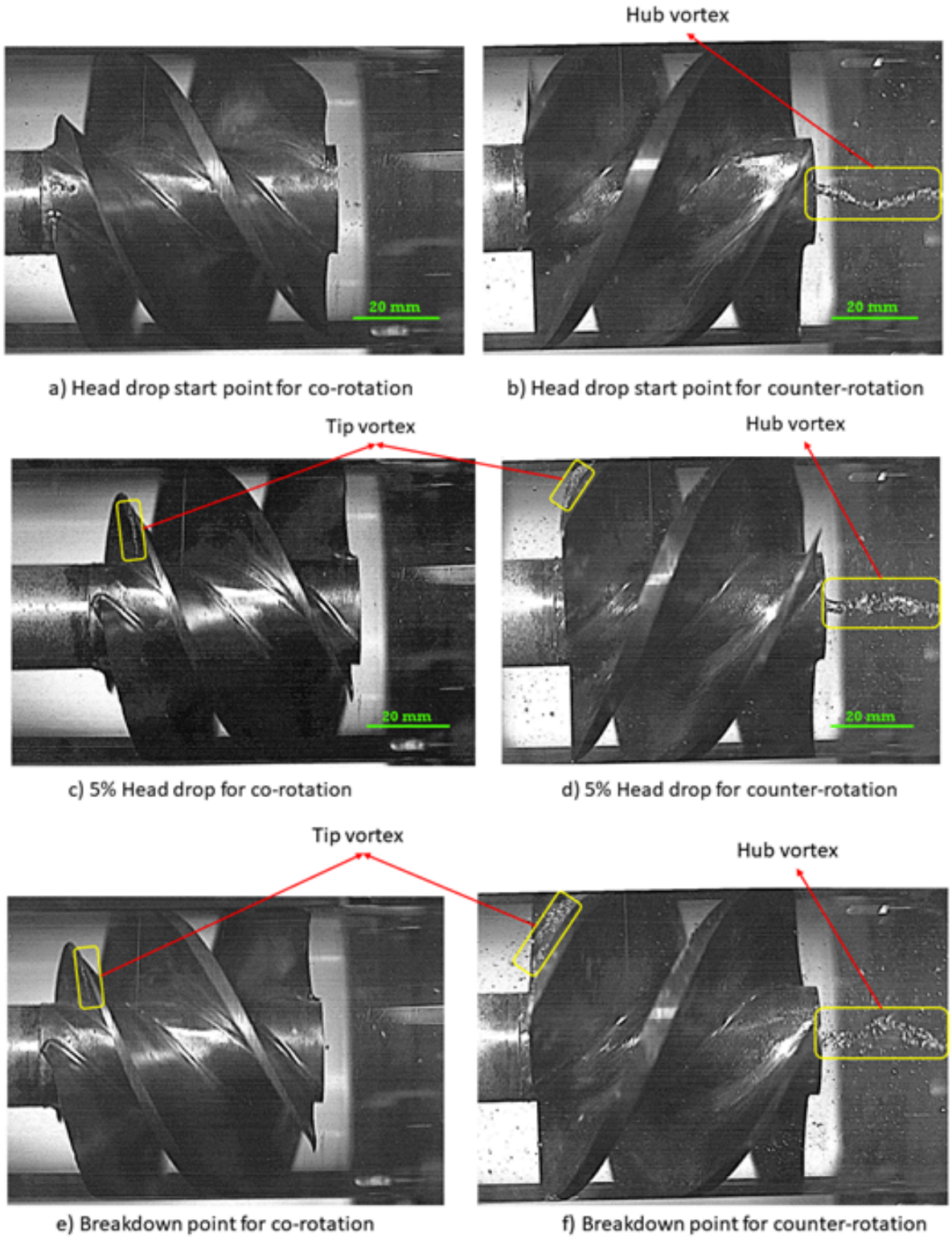

FIGURE 5.21 – Development of cavitation for $\frac{Q}{Q_n} = 1$ and $N_1 = \pm 2000$ rpm

Figure 5.21a shows that for co-rotation mode at an $NPSH = 2.5\,\text{m}$, pressure fluctuations occur in the pump, but they do not result in cavitation in the inducer. Furthermore, there is no observation of hub vortex cavitation between the inducer and impeller. As the $NPSH$ decreases and a 5% pressure drop is observed, tip vortex cavitation becomes visible in the inducer, as shown in Figure 5.21c. While the $NPSH$ continues to decrease, reaching the point of breakdown, there is no change in the cavitation observation in the inducer, and hub vortex cavitation remains absent. This indicates that cavitation occurs in the impeller at this flow rate, leading to a decrease in pump pressure.

In the counter-rotation mode, pressure fluctuations do not cause cavitation in the inducer, but hub vortex cavitation is observed between the inducer and impeller (Figure 5.21b). Figure 5.21d demonstrates that as the $NPSH$ decreases and a 5% pressure drop occurs in the pump, the hub vortex cavitation remains visible. Additionally, the inducer also exhibits tip vortex cavitation. Even with a decrease in the pressure drop in the pump during the counter-rotation mode, the presence of hub vortex cavitation and tip vortex cavitation can still be observed when reaching the breakdown point (Figure 5.21f). As shown in Figure 5.21, it can be said that at $\frac{Q}{Q_n} = 1$ and $N_1 = \pm 2000$ rpm in both co-rotation and counter-rotation modes, the cavitation in the impeller is much stronger than in the inducer, so that the pump experienced the pressure drop in the absence of notable cavitation in the inducer.

5.4.1.3 High flow rate

Figure 5.22 illustrates a comparison of pump cavitation performance between co-rotation and counter-rotation modes at $\frac{Q}{Q_n} = 1.2$. More pressure fluctuation is seen at high flow rates; however, the beneficial impact of the counter-rotation inducer in comparison to the co-rotation inducer is still observed. In the co-rotation mode, the 5% pressure drop is observed at $NPSH = 2.96\,\text{m}$, whereas in the counter-rotation mode, this pressure drop occurs at $NPSH = 2.65\,\text{m}$. No significant impact of cavitation was observed in the inducer at high flow rates.

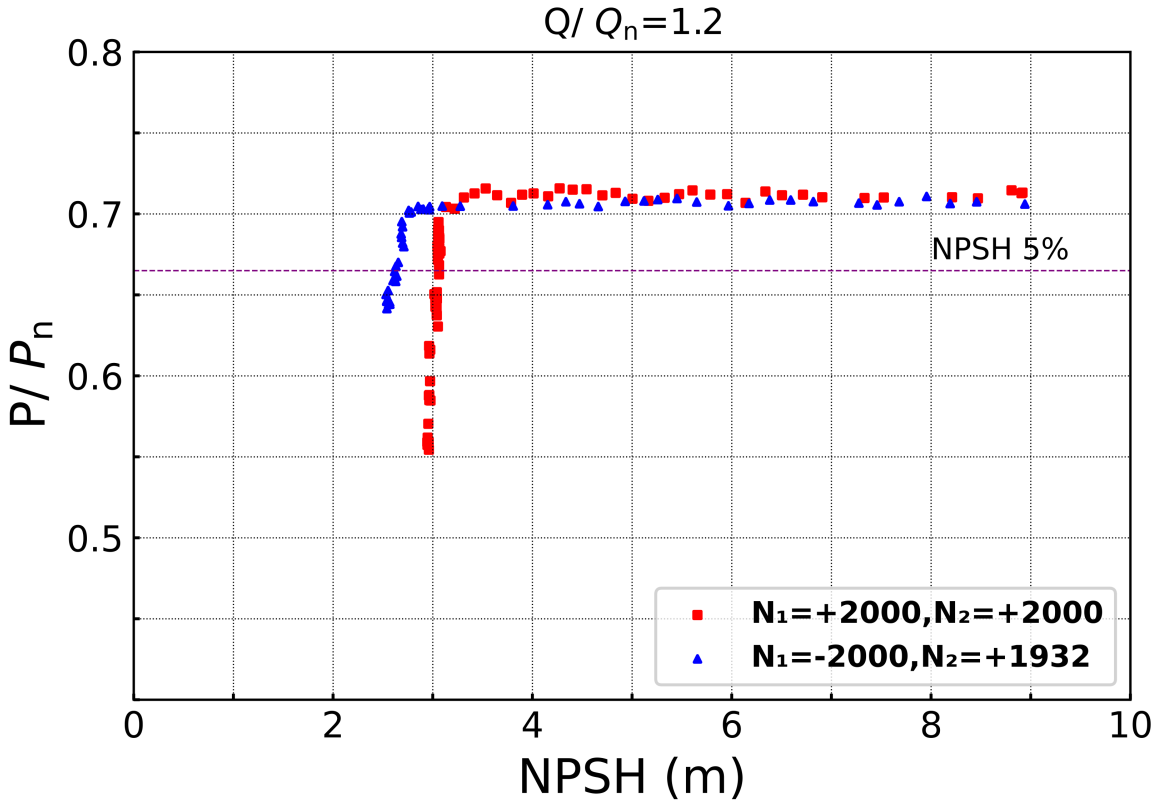

FIGURE 5.22 – Comparison of cavitation performance of pump for $\frac{Q}{Q_n} = 1.2$ and $N_1 = \pm 2000$ rpm

5.4.1.4 NPSH5% for $N_1 = \pm 2000$ rpm

Figure 5.23 demonstrates the variations in $NPSH5\%$ at three different flow rates and their corresponding changes. This figure indicates that the counter-rotation mode exhibits better cavitation performance compared to the co-rotation mode at all flow rates. At $\frac{Q}{Q_n} = 1.2$, the counter-rotation mode successfully reduces the $NPSH5\%$ from 2.96 m to 2.65 m. Furthermore, as the flow rate decreases, this effect becomes more pronounced. For the nominal flow rate $\frac{Q}{Q_n} = 1$, the $NPSH5\%$ decreases from 1.25m to 0.62 m. In the case of the lowest flow rate tested in this research $\frac{Q}{Q_n} = 0.87$, the $NPSH5\%$ decreases by more than half, dropping from 0.7 m to 0.3 m. The improved cavitation performance in the counter-rotation pump can be attributed to its ability to achieve the same pressure as the co-rotation mode while operating at a lower impeller rotational speed. This is primarily due to two factors : reduced pre-swirl of the fluid in the counter-rotation mode and a decrease in the tangential velocity of the flow at the inlet of the impeller. These factors result in higher pressure generation

in the counter-rotation mode.

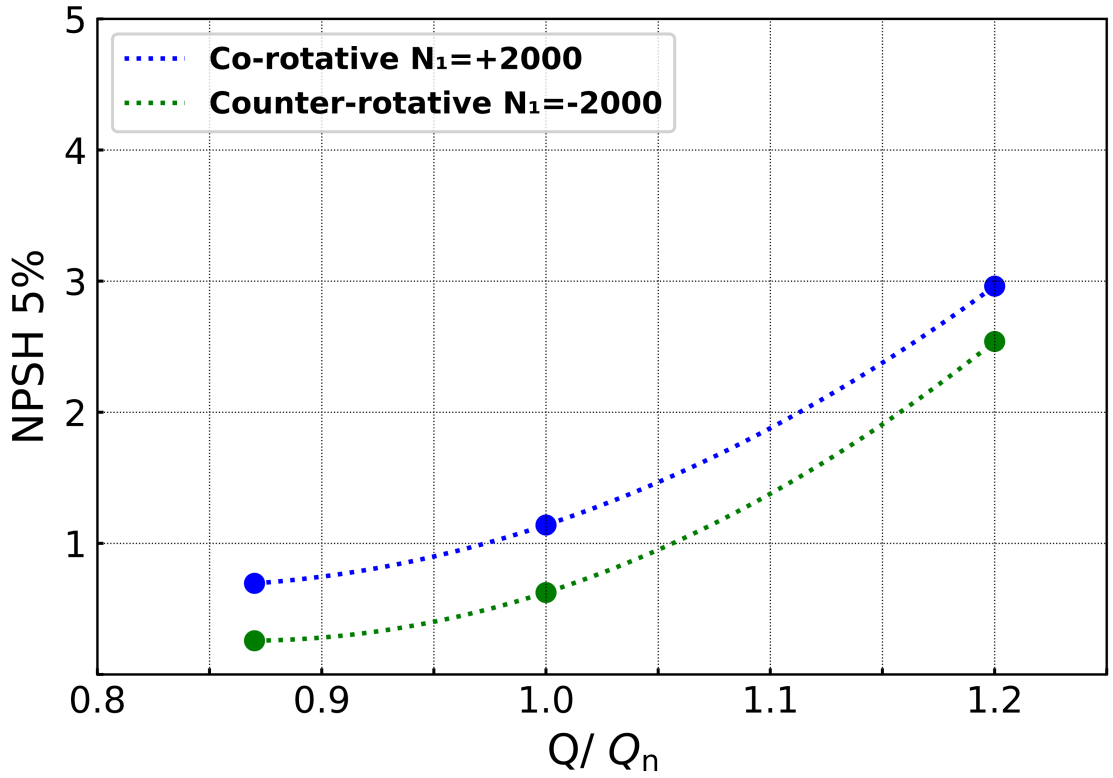

FIGURE 5.23 – NPSH5% for different flow rates and $N_1 = \pm 2000$ rpm

5.4.2 Pump cavitation performance for $N_1 = \pm 2500$ rpm

5.4.2.1 Low flow rate

At a speed of 2500 rpm, there is an observable influence of the counter-rotating inducer on the cavitation performance of the pump at $\frac{Q}{Q_n} = 0.87$, as shown in Figure 5.24. When the inducer operates in the co-rotation mode, a 5% decrease in pressure is observed at $NPSH = 1.22\,\text{m}$. However, when the inducer is in the counter-rotation mode, the same 5% decrease in pressure is noticed at a lower $NPSH$ value of 0.3 m. This indicates the noticeable effect of counter-rotation on the pump's cavitation performance. A primary reason for this difference in performance is the reduced speed of the impeller during counter-rotation. By employing the counter-rotation system, the impeller can operate at a slower speed and still achieve the same pressure as it does in the co-rotation mode. This slower speed is beneficial for delaying cavitation.

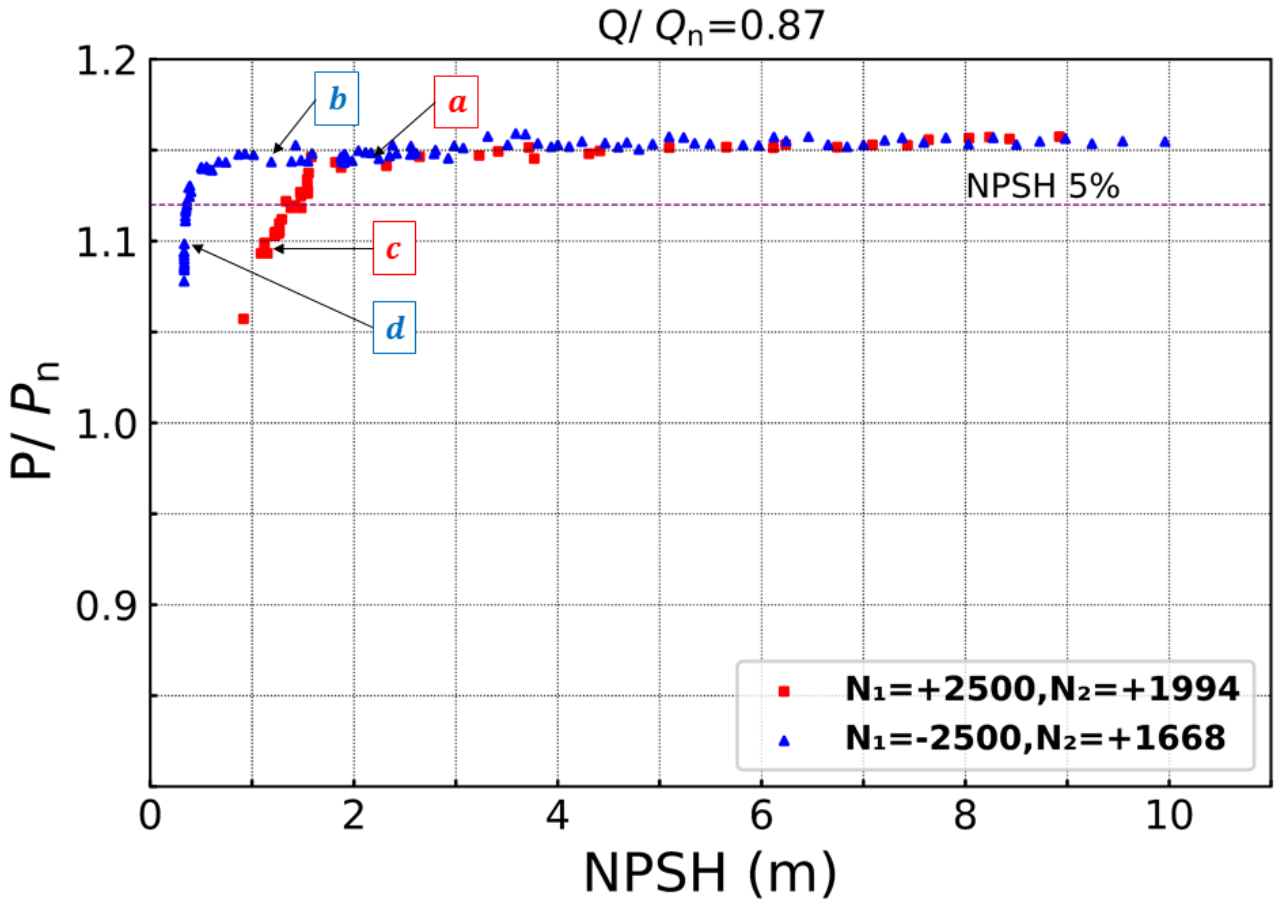

FIGURE 5.24 – Comparison of cavitation performance of pump for $\frac{Q}{Q_n} = 0.87$ and $N_1 = \pm 2500$ rpm

Figure 5.25a and 5.25c illustrate points a and c from Figure 5.24, showcasing the effects for the co-rotation inducer. In contrast, Figure 5.25b and 5.25d represent the effects for the counter-rotation inducer, highlighting points taken from Figure 5.24.

In the co-rotation mode, as the pump pressure begins to drop, a long and wavy tip vortex forms on the first blade. Notably, there is an absence of other cavitation types, like the hub vortex that might form between the inducer and the impeller. On the other hand, the counter-rotation mode presents different characteristics. There is the presence of tip vortex cavitation at the blade edge. However, unlike co-rotation mode, this vortex is broader and seems to blend with the backflow cavitation. There is also visible tip leakage cavitation. Additionally, between the impeller and inducer, a hub vortex emerges. This vortex comprises two intertwined vortices and is slightly misaligned from the central axis of both the inducer and the impeller.

When the pump undergoes a pressure drop leading to more than a 5% loss in its output pressure, changes in cavitation patterns can be noted. In the co-rotation mode, as illustrated in Figure 5.25c, the length of the tip vortex decreases, and backflow cavitation becomes visible. Additionally, a hub vortex emerges between the inducer and the impeller, a phenomenon that was not observable before complete cavitation.

In the case of the counter-rotation inducer, the cavitation effects are more pronounced, attributed to the lower $NPSH$ value. Observations show that the surfaces of both the first and second inducer blades are fully cavitated. The tip leakage cavitation becomes especially pronounced at the inducer's edge. The hub vortex, positioned between the inducer and impeller, remains consistent in intensity. However, its orientation relative to the axis of both the inducer and the impeller is more angled. This change results in a broader span of movements or oscillations around the inducer axis. This angle arises from the expansion of cavitation in the impeller. The vortex hub, which originates in the impeller, moves towards the interior of the blades. However, as it nears the inducer, the pressure produced by the inducer blades causes it to move towards the inducer hub.

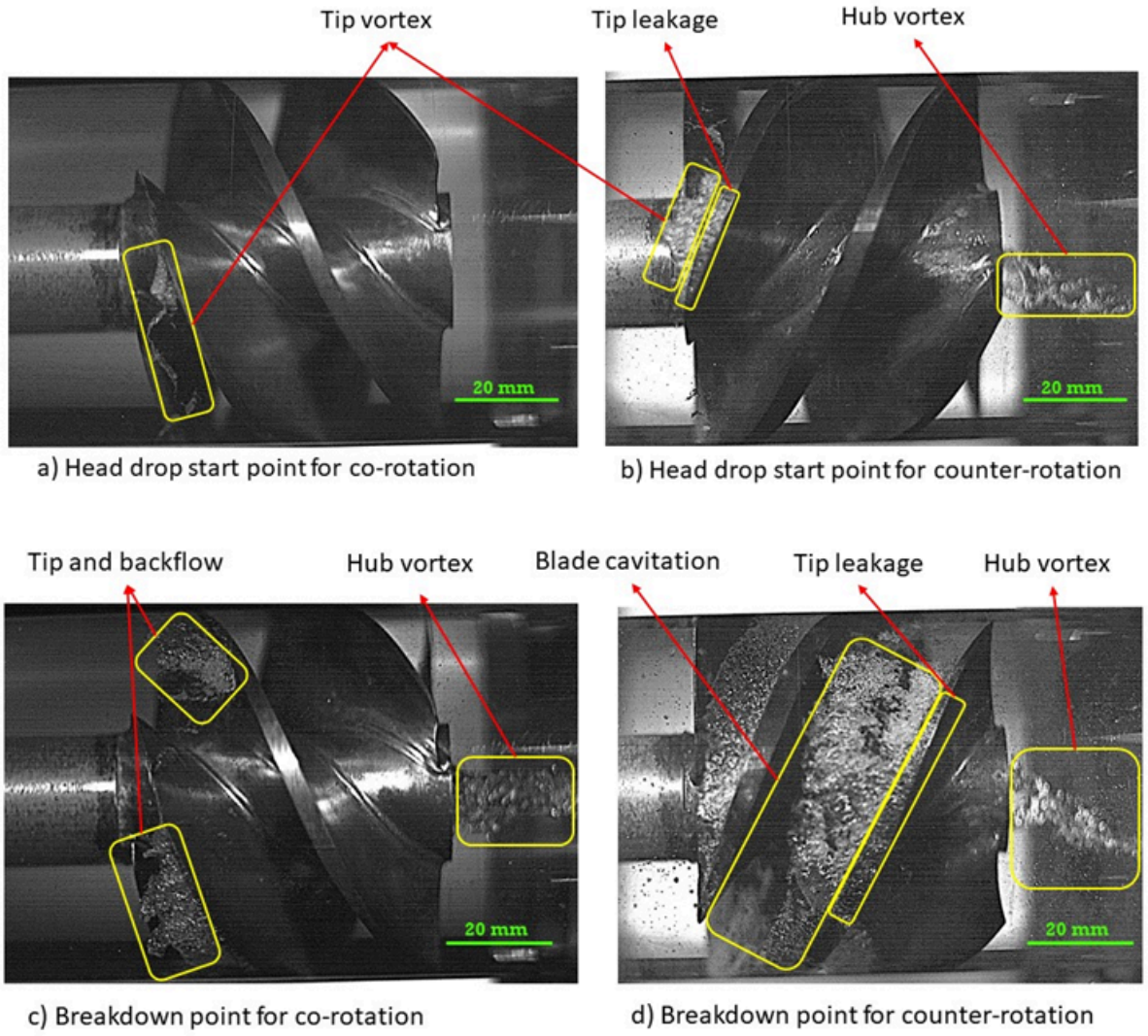

FIGURE 5.25 – Development of cavitation for $\frac{Q}{Q_n} = 0.87$ and $N_1 = \pm 2500$ rpm

5.4.2.2 Nominal flow rate

As the flow rate increases and approaches the nominal flow rate, a notable difference in pump cavitation efficiency emerges when the inducer rotates at 2500 rpm in both the co-rotation and counter-rotation modes. Specifically, in the counter-rotation mode, a 5% pressure drop is observed at $NPSH = 0.52$ m. In contrast, this same pressure drop in the co-rotation mode happens at a higher $NPSH = 2.18$ m.

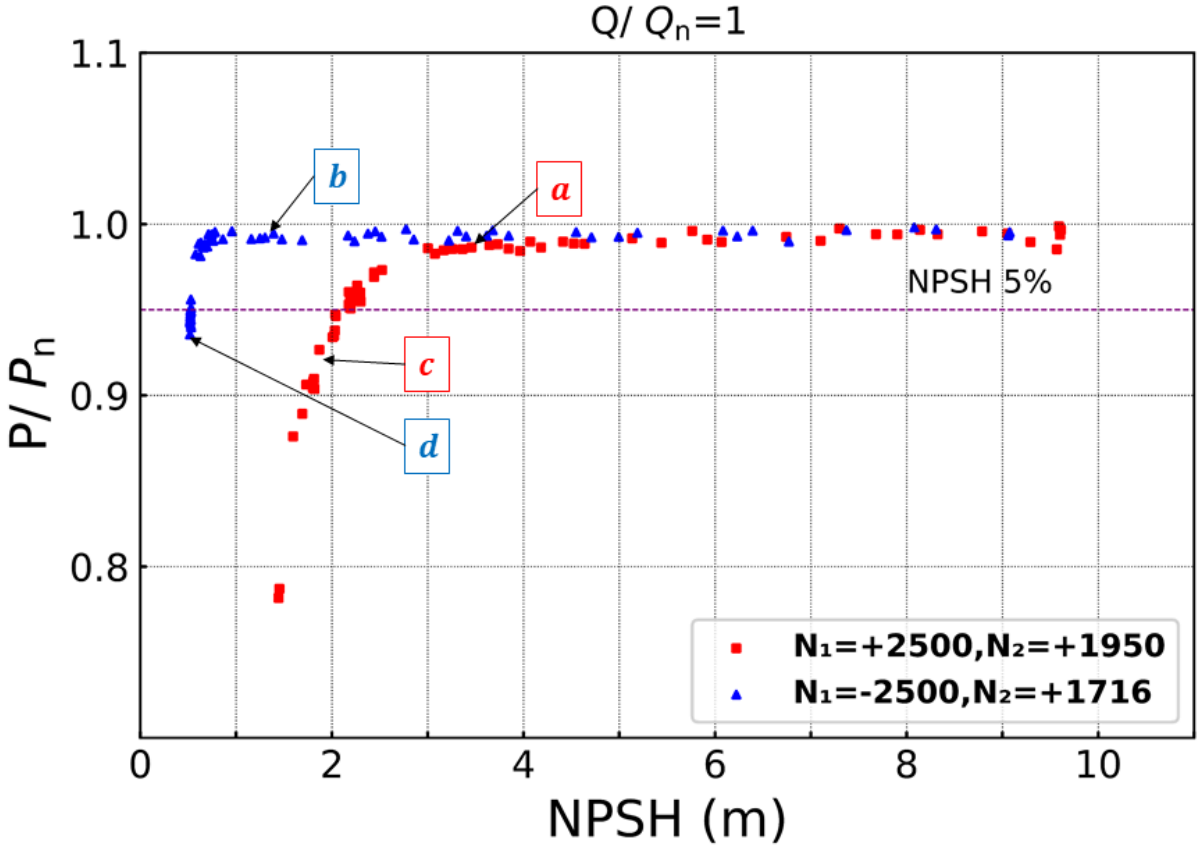

FIGURE 5.26 – Comparison of cavitation performance of pump for $\frac{Q}{Q_n} = 1$ and $N_1 = \pm 2500$ rpm

In the co-rotation mode, there is also evidence of a local pressure drop. This decline in pressure does not happen suddenly but decreases with a slight slope. According to Figure 5.26, at this flow rate and with the inducer speed maintained at 2500 rpm, the impeller rotates at 1950 rpm in co-rotation and slows down to 1716 rpm in the counter-rotation mode. In counter-rotation mode, increasing the speed of the inducer while decreasing the speed of the impeller improves the pump cavitation performance. In contrast, in co-rotation mode, when the speed of the inducer increases, because it rotates in the same direction as the impeller, it results in a higher fluid velocity at the entrance of the impeller blade. This increased velocity leads to a decline in the pump cavitation performance.

In Figure 5.27, as the pump pressure begins to drop in co-rotation mode, a faint tip vortex is noticed at the inducer edge. This contrasts with the thin, yet highly fluctuating, hub vortex observed between the inducer and impeller at low flow rates. When the inlet pressure drops to below 5% of the

pump's pressure, the inducer's edge tip vortex becomes more pronounced and widens, while the hub vortex grows in thickness. However, its angular relationship with the inducer axis lessens, leading to fewer fluctuations.

In Figure 5.27b, at the start of the counter-rotation mode pressure drop, a more pronounced tip vortex emerges, accompanied by tip leakage at the first inducer blade edge. A thick hub vortex appears between the inducer and impeller, its size comparable to the inducer hub. However, its fluctuation is low, and its angle to the inducer and impeller axis remains relatively low. As pressure decreases (as seen in Figure 5.27d), the inducer experiences full cavitation, extending to its third blade and covering all blade surfaces. The hub vortex between the inducer and impeller becomes thinner, but its fluctuation and its angle relative to the inducer increase, meaning it moves closer to the impeller blades, moving away from the impeller center. As the flow rate increases and the speed of the inducer remains constant, the speed of the impeller increases slightly to increase the flow rate. This increase in the speed of the impeller leads to stronger suction in front of the impeller and after the inducer. This low pressure area, especially between the inducer hub and the impeller, which is not affected by the inducer blade pressure, leads to the creation of a stronger hub vortex compared to the lower flow rate5.27b. In the following sections, the dynamic changes and fluctuations of cavitation within the inducer and between the inducer and impeller will be explained.

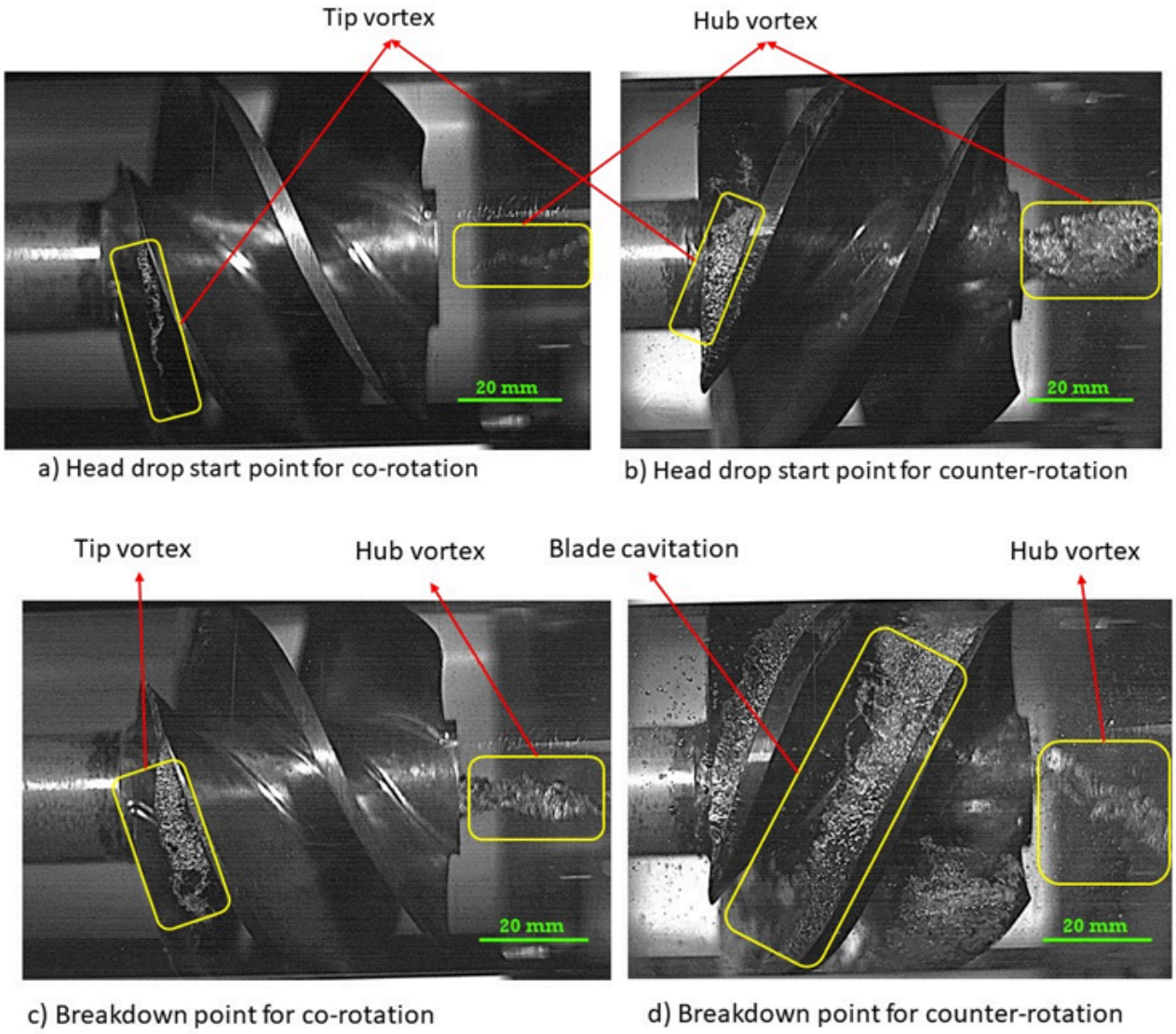

FIGURE 5.27 – Development of cavitation for $\frac{Q}{Q_n} = 1$ and $N_1 = \pm 2500$ rpm

5.4.2.3 High flow rate

Based on Figure 5.28, at the high flow rate, the $NPSH5\%$ for counter rotation mode stands at 2.15. This is approximately double when compared to the co-rotation value of 4.1 m. This observation shows the considerable impact of counter-rotation technology on the pump cavitation performance, effectively halving the $NPSH5\%$ at this flow rate. For both rotation modes, increased flow rates result

in greater pressure fluctuations and there is an almost immediate 5% pressure drop. However, a minor gradient is evident in the counter-rotation mode.

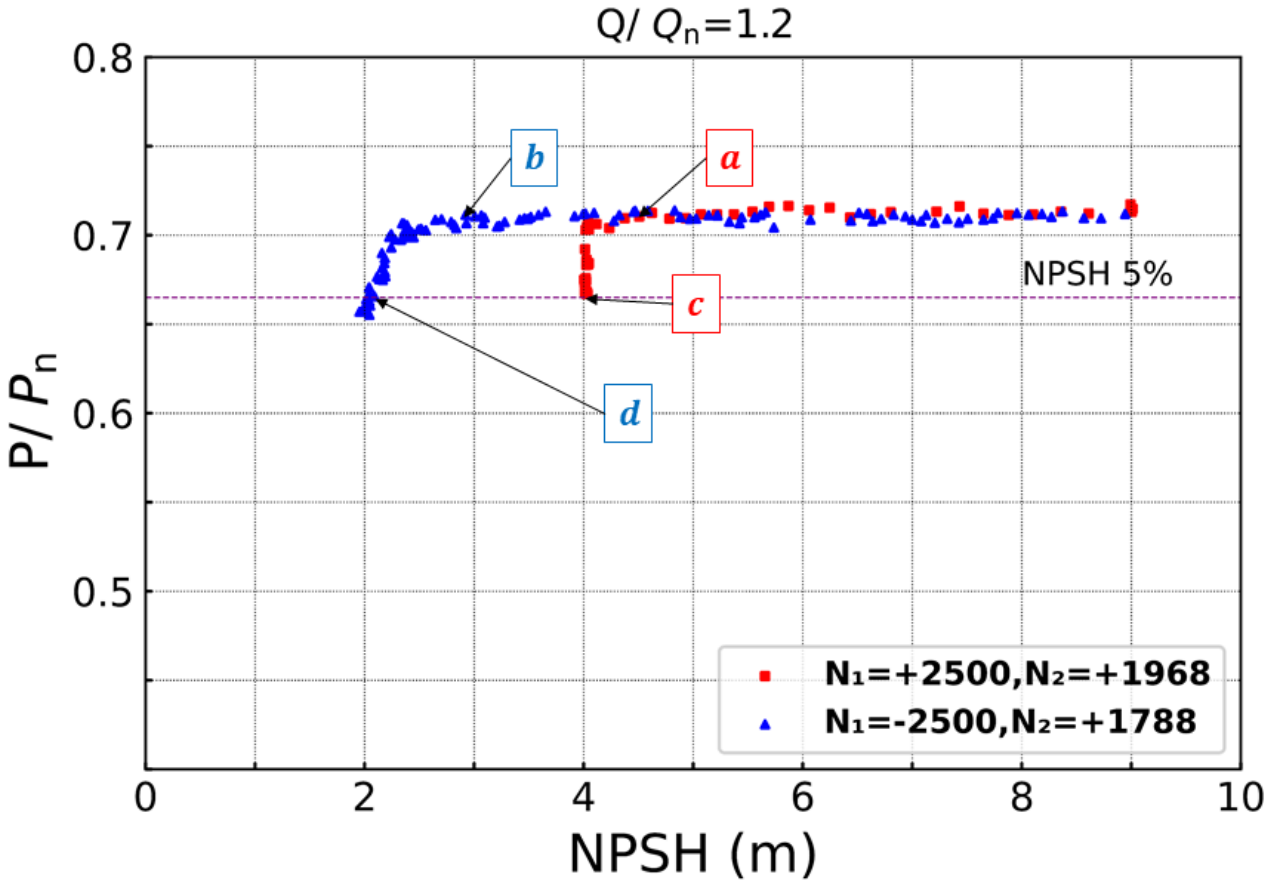

FIGURE 5.28 – Comparison of cavitation performance of pump for $\frac{Q}{Q_n} = 1.2$ and $N_1 = \pm 2500$ rpm

Figure 5.29 illustrates the start of cavitation (as shown in Figure 5.29a and 5.29b) and a pressure drop exceeding 5% (seen in Figure 5.29c and 5.29d). From the figure, it is observed that during high flow rates, the inducer does not exhibit cavitation. Instead, only the hub vortex cavitation emerges between the inducer and the impeller, remaining relatively consistent even as pressure decreases. This suggests that at high flow rates, the impeller undergoes cavitation before the inducer. Consequently, even without noticeable cavitation in the inducer, the pump experienced a 5% pressure drop.

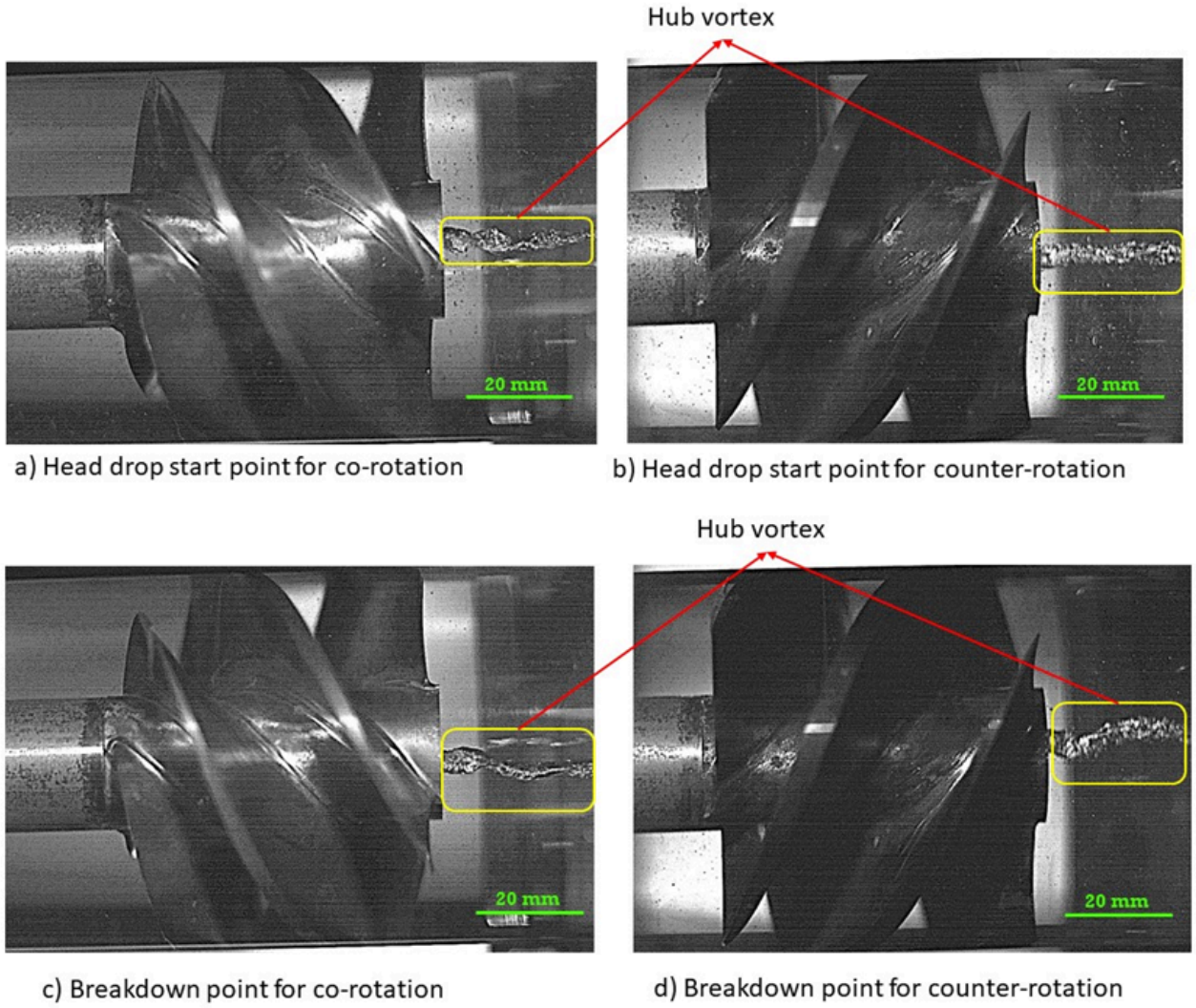

FIGURE 5.29 – Development of cavitation for $\frac{Q}{Q_n} = 1.2$ and $N_1 = \pm 2500$ rpm

5.4.2.4 NPSH5% for $N_1 = \pm 2500$ rpm

Figure 5.30 illustrates the variation in $NPSH5\%$ for three different flow rates at an inducer speed of 2500 rpm in both co-rotation and counter-rotation modes. Notably, the counter-rotation mode consistently displays a lower $NPSH5\%$ across all flow rates when compared to the co-rotation mode. Specifically, the counter-rotation inducer can reduce $NPSH5\%$ by a quarter relative to the co-rotation mode. At $\frac{Q}{Q_n} = 0.87$, the $NPSH5\%$ is reduced from 1.22 m in co-rotation mode to 0.3 m in counter-rotation mode, showcasing a clear enhancement in pump cavitation. At the nominal flow

rate, the $NPSH5\%$ is cut from 2.18 m in the co-rotation mode to 0.52 m in the counter-rotation mode, indicating a notable reduction in $NPSH5\%$ to about one-fourth. Increasing the flow rate $\frac{Q}{Q_n} = 0.87$, the counter-rotation mode still outperforms by enhancing cavitation performance by reducing $NPSH5\%$ to half, with $NPSH5\%$ values transitioning from 4.1 m in co-rotation mode to 2.15 m in counter-rotation mode.

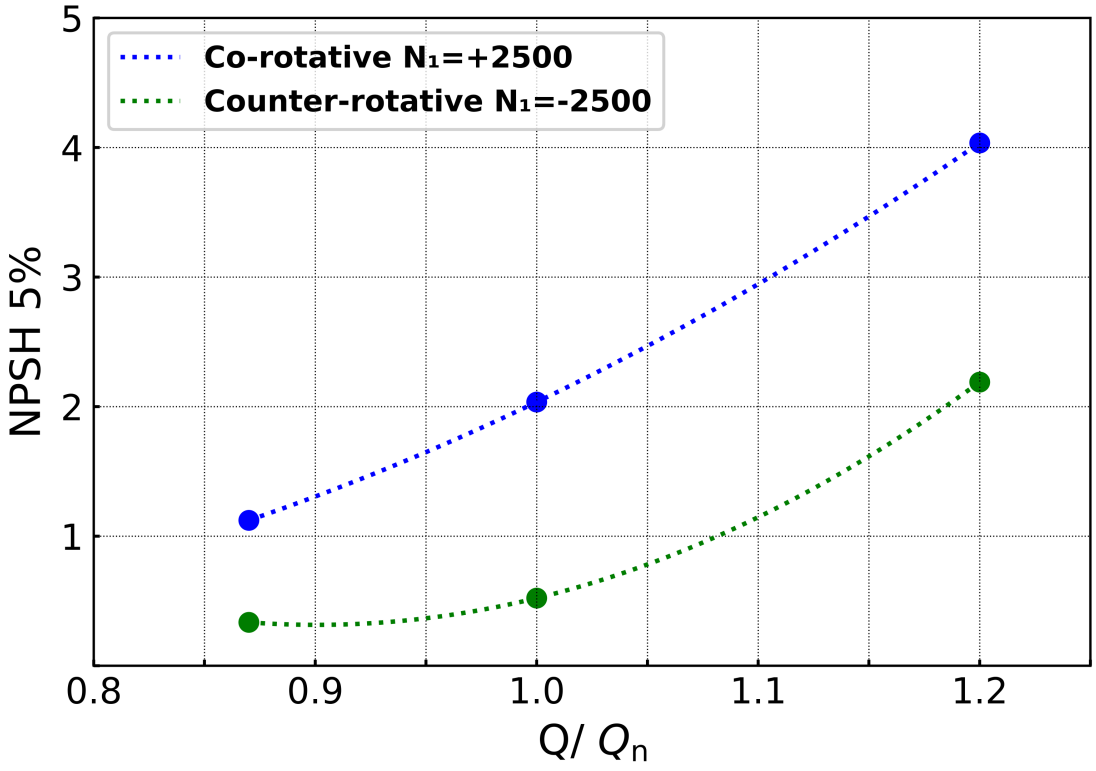

FIGURE 5.30 – NPSH5% for different flow rates and $N_1 = \pm 2500$ rpm

5.4.3 Pump cavitation performance for $N_1 = \pm 2900$ rpm

5.4.3.1 Low flow rate

The pump cavitation diagram for both co-rotation and counter-rotation modes is shown in Figure 5.31 when the inducer speed is raised to 2900 rpm at $\frac{Q}{Q_n} = 0.87$. The chart reveals that the counter-rotation inducer outperforms the co-rotation inducer in terms of cavitation. For the co-rotation inducer at 2900 rpm, there is a gradual increase in the pump pressure drop starting above $NPSH5\%$. This

gradual drop is evident until the $NPSH = 1.78\,\text{m}$, where there is a 5% decline in pump pressure. Beyond this point, the drop in pressure becomes more pronounced. Compared to the co-rotation mode, the counter-rotation mode demonstrates a lower decline in pressure. This pattern persists until there is a 5% pressure reduction at an $NPSH = 0.5\,\text{m}$. After reaching this threshold, the pressure fall becomes notably sharp. By increasing the inducer speed to 2900 rpm, it can be seen that the fluctuations in the pump cavitation diagram have increased in both cases, and this is due to the greater influence of the inducer on the pump cavitation(Figure5.31).

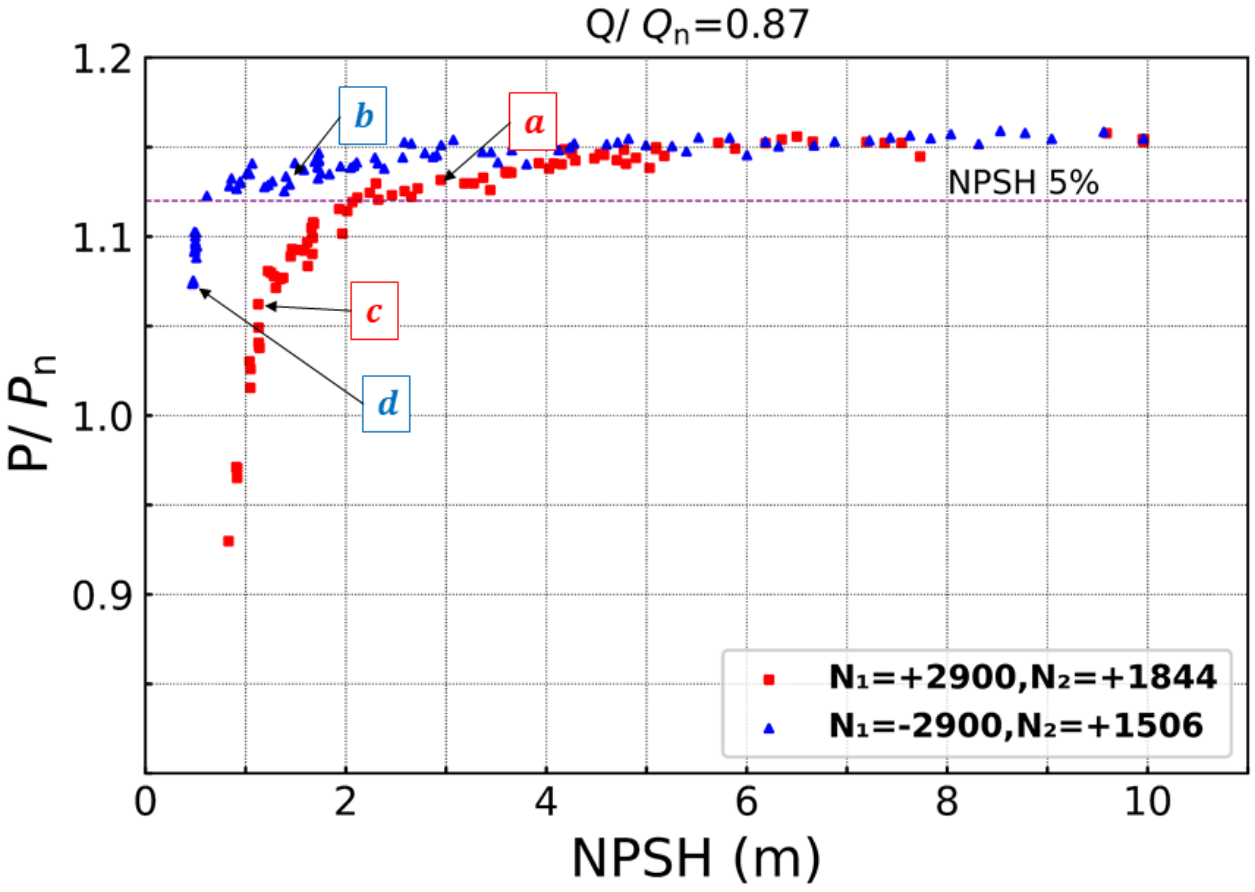

FIGURE 5.31 – Comparison of cavitation performance of pump for $\frac{Q}{Q_n} = 0.87$ and $N_1 = \pm 2900$ rpm

Figure 5.32a demonstrates that there is some evidence of the hub vortex cavitation between the inducer and the impeller at the speed of 2900 rpm, for the co-rotation mode, and at low flow rate at point a. However, a more intense tip vortex is visible compared to what is seen at lower speeds. Signs of backflow cavitation are also apparent at this point. As the system inlet pressure decreases,

surpassing the 5% pressure drop at point c, the backflow intensity visibly increases, and the tip vortex appears to be broader. Yet, there is no evidence of blade cavitation, so it is not conclusive that the entire inducer has been affected by cavitation. In the counter-rotation configuration at point b, the first blade exhibits backflow cavitation, a tip vortex cavitation and tip leakage cavitation. In this mode, a weak hub vortex, which consists of two intertwined vortices, is present between the inducer and the impeller. When the $NPSH$ level decreases and experiences a 5% pressure reduction, the intensity of the cavitation in the inducer rises. Consequently, cavitation fully covers the blade surface between blades 1 and 2, and this cavitation influence progresses to blade 3. When the inducer speed increases and the impeller speed decreases, the low-pressure region in front of the impeller is reduced. Concurrently, the pressure generated by the inducer impacts the area between the inducer and the impeller. Consequently, referencing Figure 5.32, one can observe that compared to the lower speeds of the inducer, the hub vortex that forms is much weaker.

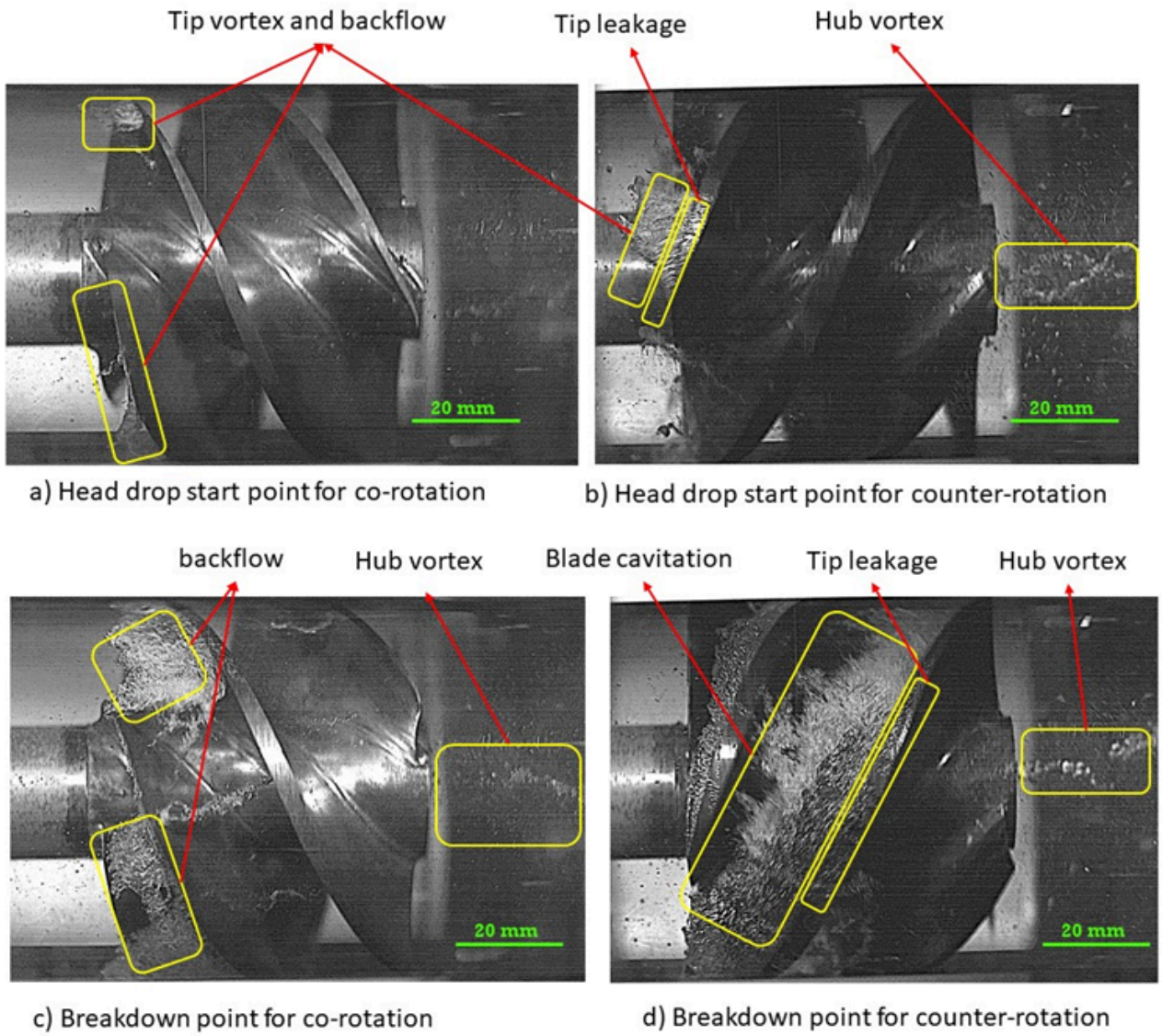

FIGURE 5.32 – Development of cavitation for $\frac{Q}{Q_n} = 0.87$ and $N_1 = \pm 2900$ rpm

5.4.3.2 Nominal flow rate

When the flow rate is adjusted to its nominal value, a difference in the cavitation performance between co-rotation and counter-rotation inducers is noted. In the case of the co-rotation inducer, a local pressure drop is first detected. As the process continues, this pressure drop is seen to steepen until a 5% reduction is reached. Beyond that point, the decrease in pressure is observed to intensify, with

the slope becoming more pronounced. In contrast, for the counter-rotation inducer, no local pressure drop is observed. Only minor pressure fluctuations are observed when the $NPSH$ is less than 4 m. At $NPSH = 0.5\,\text{m}$, a 5% decrease in pressure occurred, whereas for the co-rotation mode, this value is 2.65m From these observations, it is deduced that the counter-rotation mode enhances the $NPSH$ of the pump by over 2 meters for the given rotational speed and flow rate.

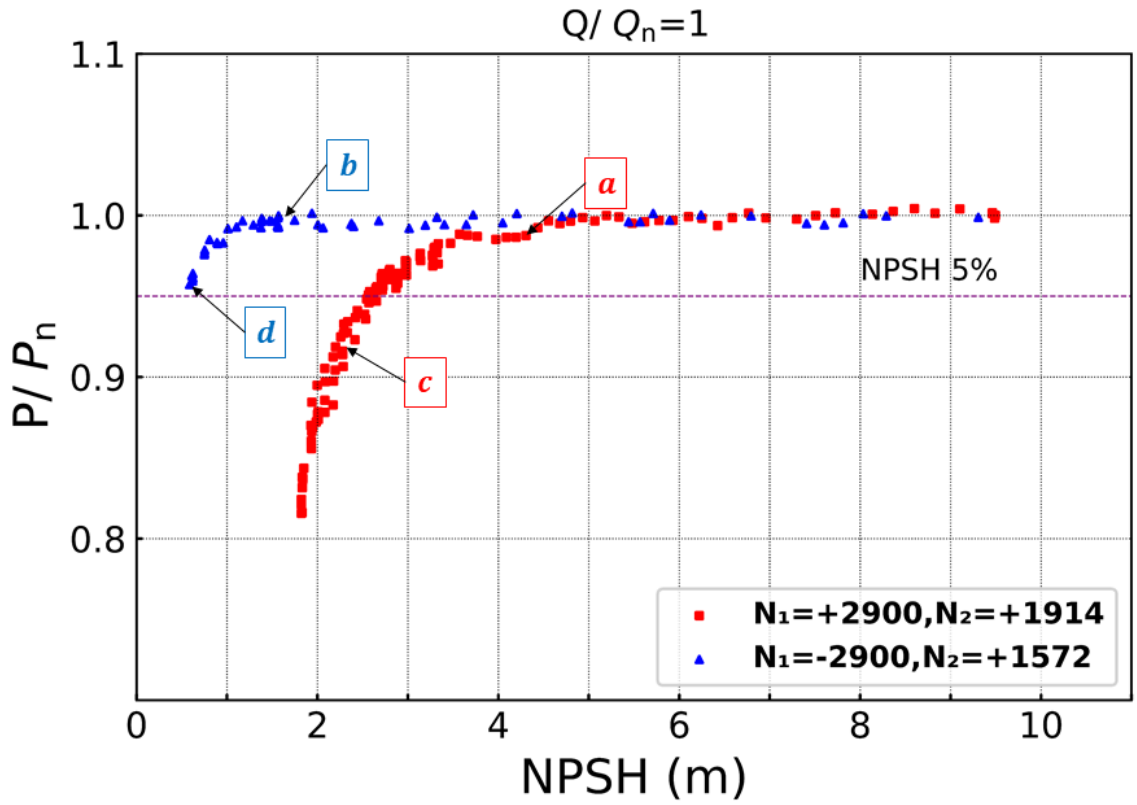

FIGURE 5.33 – Comparison of cavitation performance of pump for $\frac{Q}{Q_n} = 1$ and $N_1 = \pm 2900$ rpm

At point a for the co-rotation inducer, as shown in Figure 5.34a, both tip vortex cavitation and backflow cavitation are seen on the first inducer blade. At these higher speeds, the intensity of the backflow is greater than that of the vortex tip. Additionally, a weak and fluctuating hub vortex cavitation appears between the inducer and the impeller with a thin thickness. In contrast, in Figure 5.34b for the counter-rotation inducer, a lower $NPSH$ value is presented. The hub vortex intensity is noticeably increased, and its diameter closely matches the inducer inner diameter. The strength of the backflow vortex is also enhanced, and some tip leakage cavitation is observed at the edge of the first blade. When the system pressure is decreased to achieve a pressure drop of 5% in the pump, the cavi-

tation of the co-rotation inducer shows no marked change. Backflow cavitation and tip vortex are still evident on the first inducer blade. Additionally, the hub vortex between the inducer and the impeller is visible, as illustrated in Figure 5.34c, though its intensity has seen a minor increase. Conversely, for the counter-rotation inducer, the inducer is fully cavitated, with the cavitation extending to the third blade, covering its surface entirely. Yet, the intensity and force of the hub cavitation between the inducer and the impeller have diminished, accompanied by a reduction in its thickness.

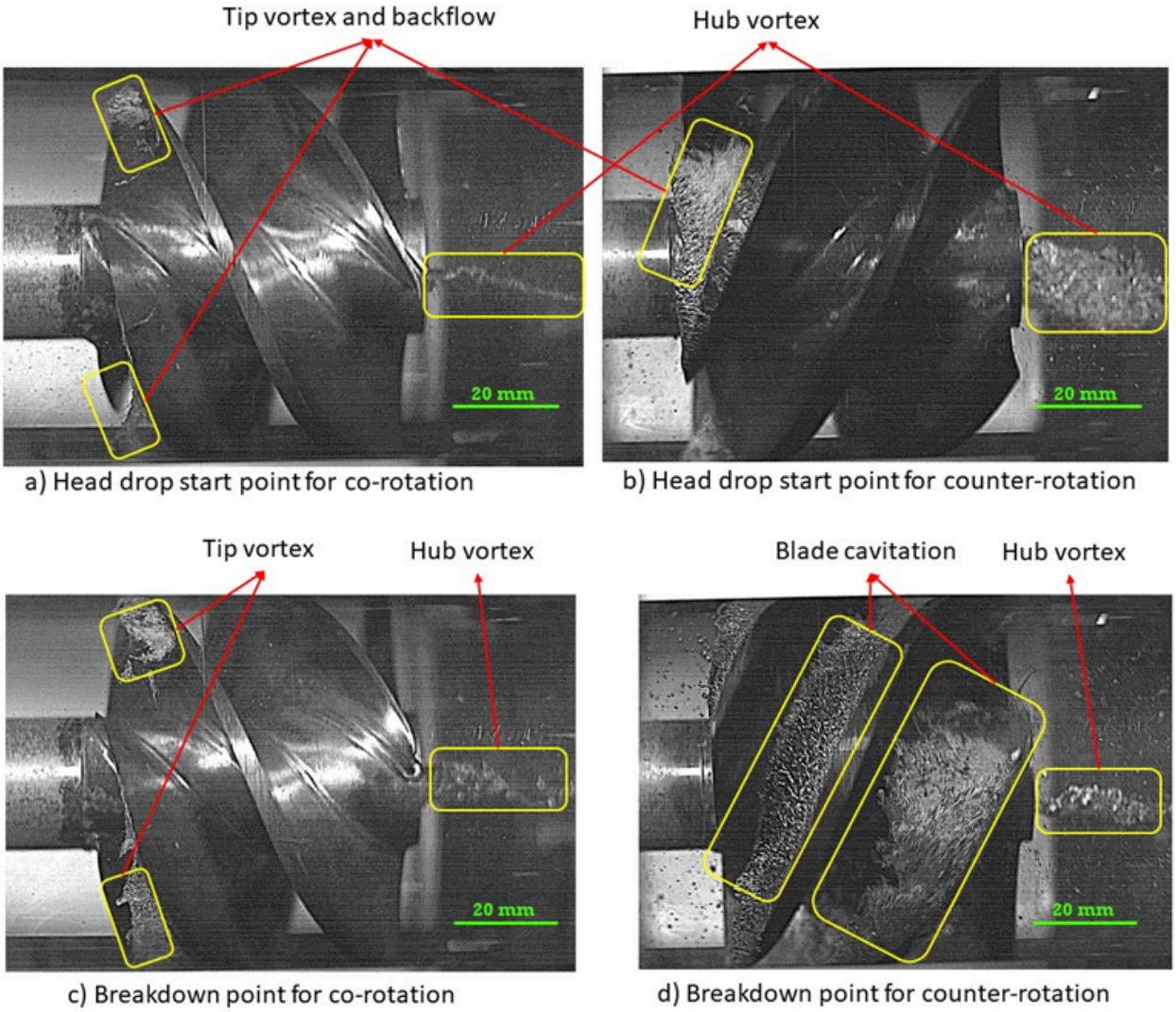

FIGURE 5.34 – Development of cavitation for $\frac{Q}{Q_n} = 1$ and $N_1 = \pm 2900$ rpm

5.4.3.3 High flow rate

At $\frac{Q}{Q_n} = 1.2$ and a speed of 2900 rpm, the most pronounced difference in pump cavitation performance between the co-rotation and counter-rotation modes is noted. By changing the inducer rotation direction, the $NPSH5\%$ value can be reduced from 4.9 m in the co-rotation mode to 1.53 m in the counter-rotation mode. This highlights the significant impact of the direction of rotation on the cavitation performance of the pump.

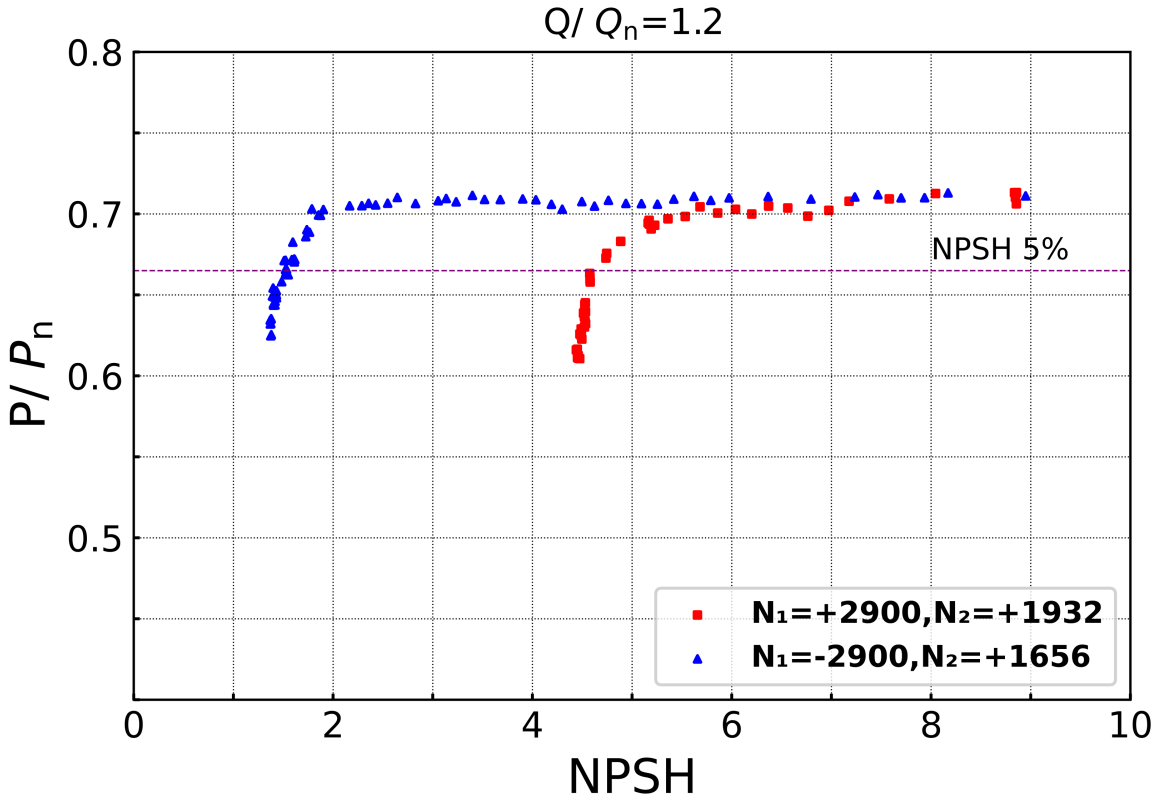

FIGURE 5.35 – Comparison of cavitation performance of pump for $\frac{Q}{Q_n} = 1.2$ and $N_1 = \pm 2900$ rpm for co-rotation and counter-rotation modes

5.4.3.4 NPSH5% for $N_1 = \pm 2900$ rpm

When the inducer speed is increased to 2900 rpm, it is evident that the difference in $NPSH5\%$ for the pump across varying flow rates is considerably greater than at lower speeds, as illustrated in Figure 5.36. Furthermore, as the flow rate rises at this speed, the difference in $NPSH5\%$ between the

co-rotation and counter-rotation modes becomes more pronounced. This emphasizes the enhancement in pump cavitation performance when employing a counter-rotation inducer.

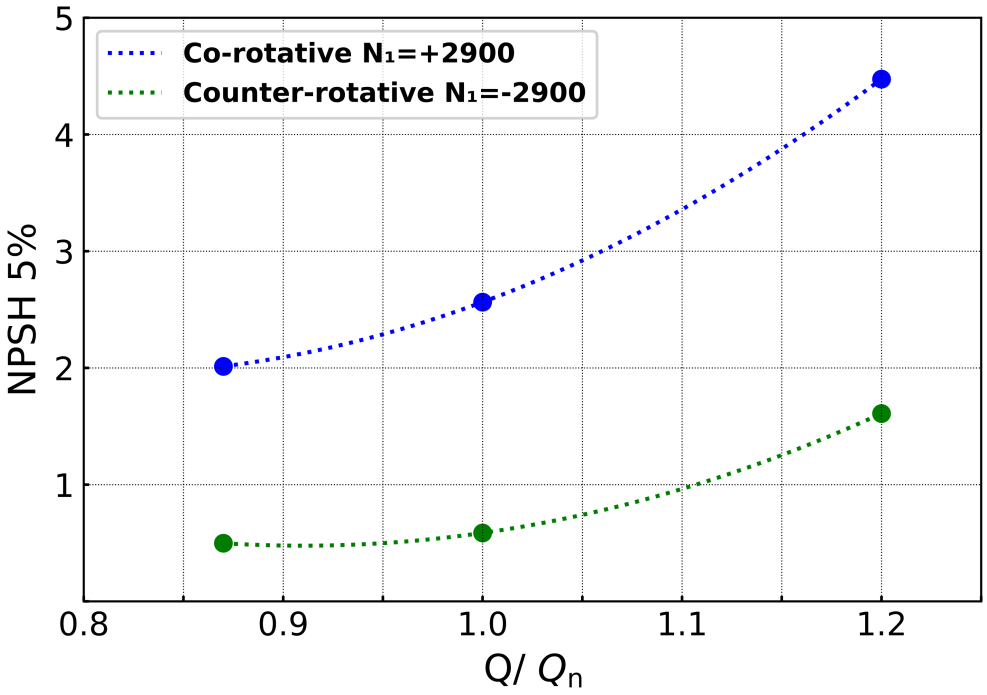

FIGURE 5.36 – NPSH5% for different flow rates and $N_1 = \pm 2900$ rpm

5.5 Cavitation instabilities

In the previous section, the influence of the rotation speed and direction of the inducer on pump cavitation performance was examined. The impact of the distance between the inducer and the impeller on pump cavitation was also investigated. In the following section, cavitation instability at two operating conditions will be investigated through the analysis of images captured by a high-speed camera. Cavitation is characterized as an unstable phenomenon, and variations in its type at different operational points of the pump are observed. In this section, images from a high-speed camera will be used for the study of the symmetry and asymmetry of cavitation within the pump at specific operational conditions. Analysis will also be conducted on the formation of the hub vortex cavitation between the two rotors at a particular point of pump operation.

5.5.1 Symmetric cavitation

In a situation of symmetric cavitation, the cavitation occurs uniformly across the blade surfaces. Figure 5.37 shows the cavitation within the pump when operating in counter-rotation mode at nominal flow rate and $N_1 = -2500$ rpm, when $NPSH = 1.4\,\text{m}$. The angle of rotation for the inducer is denoted as λ, which starts at zero degrees. The blades of the inducer are referred to as blade numbers 1, 2, and 3, moving from left to right. At ($\lambda = 0°$), cavitation becomes apparent on blade number 1. When the inducer turns 60 degrees ($\lambda = 60°$), cavitation is seen on blade number 3. After a 120-degree turn ($\lambda = 120°$) and also completing a full rotation ($\lambda = 180°$), the distribution of cavitation remains symmetric and consistently shows on the first blade.

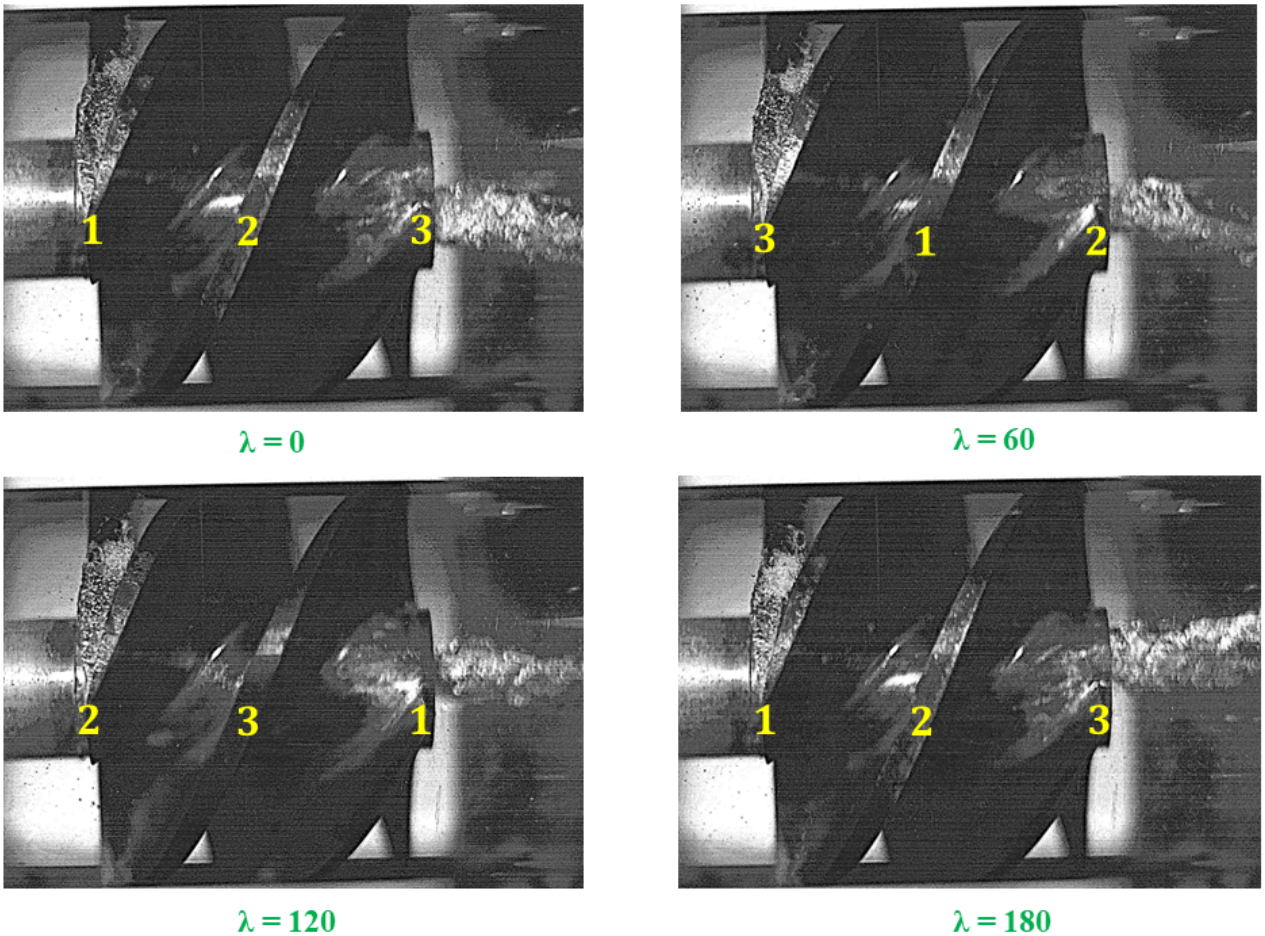

FIGURE 5.37 – Symmetric cavitation in inducer in one complete rotation for $L = 80\ mm$, $\frac{Q}{Q_n} = 1$, $N_1 = -2500$ rpm, $N_2 = 1716$ rpm and $NPSH = 1.4\,\text{m}$

5.5.2 Asymmetric cavitation

Figure 5.38 illustrates the variations in cavitation within the inducer at $N_1 = -2900$ rpm, operating in counter-rotation mode for $\frac{Q}{Q_n} = 0.87$ and $NPSH = 0.5\,\text{m}$ over the course of a full rotation. Unlike the case of symmetric cavitation, the distribution of cavitation on the blade surfaces is asymmetric in this case. At $\lambda = 0°$, blade 2 exhibits complete cavitation. When the inducer rotates 60 degrees ($\lambda = 60°$), blade 1 takes the position of blade 2, and considerably less cavitation is observed on its surface. Also, blade number 2, which has now moved to the position formerly occupied by blade number 3, also experiences cavitation, which was not the case earlier. After completing a full rotation, reaching $\lambda = 180°$, blade 2 again shows complete cavitation on its surface.

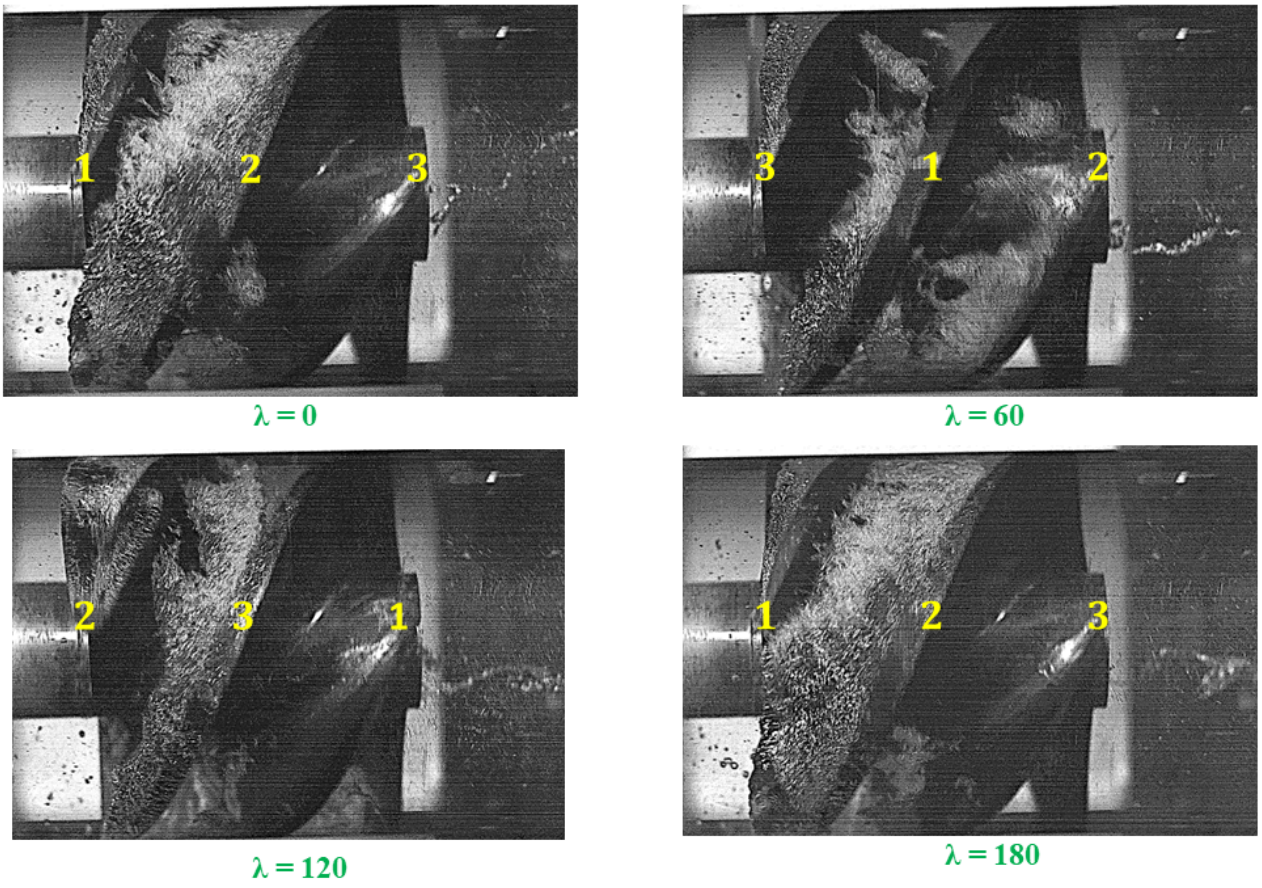

FIGURE 5.38 – Asymmetric cavitation in inducer in one complete rotation for $L = 80\ mm$, $\frac{Q}{Q_n} = 0.87$, $N_1 = -2900$ rpm, $N_2 = 1506$ rpm and $NPSH = 0.5\,\text{m}$

5.5.3 Hub vortex cavitation instability

In this section, a high-speed camera examines the evolution of the hub vortex cavitation at $\frac{Q}{Q_n} = 0.87$ and $N_1 = -2900$ rpm when the pressure drops by 5%. Figure 5.39 shows the development of the hub vortex between the inducer and the impeller. The hub vortex initially appears on the hub side of the impeller. The direction of this vortex opposes the rotation of the impeller but matches the rotation of the inducer. The vortex strengthens and connects with the inducer after 5.7 seconds. Its angle of rotation then decreases, and by 8.6 seconds, it becomes coaxial with both the inducer and impeller. The vortex starts to lose strength after this point and completely disappears by 19.9 seconds. The vortex starts at the impeller but is influenced by the presence of the inducer. This is why, even when the vortex is only attached to the impeller, it rotates in the direction of the inducer.

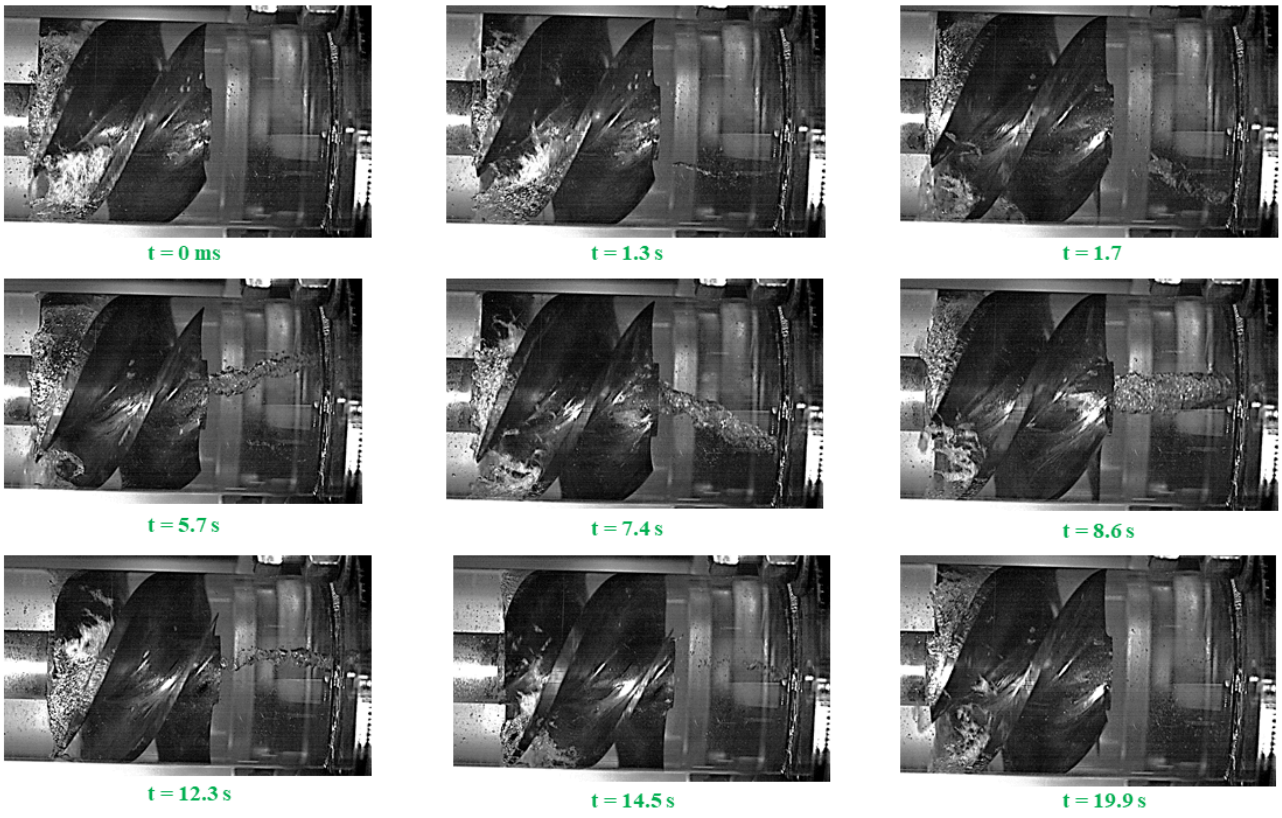

FIGURE 5.39 – Hub vortex cavitation instability for $L = 80\ mm$, $\frac{Q}{Q_n} = 0.87$, $N_1 = -2900$ rpm, $N_2 = 1506$ rpm at $NPSH5\%$.

The creation of this hub vortex results from a pressure difference between the inducer and the

impeller. Specifically, the area behind the inducer blades experiences a local increase in pressure, while the space behind the inducer hub is less affected. So as the fluid flows close to the impeller blades after passing through the inducer, it is influenced by the impeller's suction. Part of the flow sees a reduction in pressure, which results in the emergence of the hub vortex where the hub meets the impeller blade.

Thanks to the innovative design that allows the inducer and impeller to rotate independently in both co-rotation and counter-rotation modes, the impact of inducer speed on the characteristics and cavitation performance of a centrifugal pump is investigated in this chapter. The investigation of the characteristics of the pump in both counter-rotation and co-rotation modes, operating at the same rotational speed, demonstrated a significant pressure rise in the counter-rotation mode. The main reason of this pressure rise in counter-rotation mode is the decrease in tangential velocity of flow at the inlet of the impeller according to the Euler equation. This pressure rise allows the impeller to rotate at a lower speed to reach the same operating point as the co-rotation mode, which provides better cavitation performance for the counter-rotation mode compared to the co-rotation mode. Experimental results demonstrate the noticeable effect of the counter-rotation inducer on the cavitation performance of the pump across various flow rates. Studies for three different flow rates, including nominal flow rate, less than nominal flow rate, and more than nominal flow rate, demonstrate that the counter-rotation mode has better cavitation performance in all three flow rates. Image analysis of the variations and strength of the hub vortex between the inducer and impeller reveals that the vortex typically originates from the impeller and moves towards the inducer hub. When analyzing the hub vortex at NPSH = 6 m during the counter-rotation mode, it has been observed that the vortex frequently disconnects and reconnects to the inducer due to pressure variations. As the NPSH value decreases and cavitation in this region intensifies, the size of this hub vortex increases and it successfully establishes a connection to the inducer.

Chapitre 6

Conclusion

content

6.1 Conclusion

This research is set out to experimentally analyze the impact of separate rotation and the combined functioning of the inducer and impeller on the characteristics of the pump as well as its cavitation performance. To facilitate this investigation, a 6-blade closed centrifugal impeller and a 3-blade inducer were initially designed to ensure they could be coupled. A novel experimental test bench was developed for these experiments, uniquely built to independently rotate both the inducer and the impeller. Moreover, to study the impact of the distance between the inducer and the impeller on pump functionality, this bench was specifically designed to adjust their distances. By inverting the inducer angle of attack and adopting a counter-rotation design, the impact of the inducer's counter-rotation on the pump's performance was studied.

6.1.1 Inducer and impeller design

The impeller and inducer were designed using the MFT and 3D Turbo software, tools developed at the LIFSE Laboratory. Initially, the impeller was designed to have the desired characteristics. Following this, the inducer was designed in a way that its characteristics align with the impeller, ensuring a proper coupling between them. The geometric design of the impeller and inducer was then finalized using Ansys BladeGen software. For the next steps, Catia software was utilized to perfect the geometry of the inducer and impeller, helping in creating the final 3D model and design plans for both co-rotation and counter-rotation versions. The 6-blade closed centrifugal impeller has been manufactured using a stereolithography printer (SLA printer). To reduce weight and prevent shaft bending and vibration at high speeds, the inducer is made of aluminum 6062, given the long shaft used in the inducer section.

6.1.2 Experimental test bench design and numerical method

Following the design of the inducer and impeller, the next step was to create a test bench capable of independently rotating the two rotors. To achieve this, the test bench was split into two primary sections : one for the inducer and one for the impeller. The design process began with the impeller section. Here, an electric motor is employed to supply torque just like conventional pumps. This torque is then transferred to the impeller via a shaft. Mechanical seals were employed to ensure the shaft of the impeller remains sealed. To determine the right components, the rotation of the impeller was simulated using Star CCM+ software. This simulation helped in calculating the peak torque as well as the vertical and radial forces exerted on the shaft. Based on these findings, appropriate components, including mechanical seals and bearings, were chosen. A diffuser, fabricated using 3D printing technology, is utilized at the impeller outlet. Following the finalization of the impeller section's design, focus shifted to the design of the inducer section. This part was conceptualized in a way that, upon completion, it would easily integrate with the impeller section. To facilitate the rotation of the inducer, an independent electric motor was used. Given that the inducer is positioned before the impeller, and liquid can't flow directly into the test bench through a straightforward pipe, an elbow was incorporated for the system's input. Considering the potential impact of the elbow on the flow proceeding to the inducer and impeller, it was crucial to determine the optimal distance between the inducer and the inlet elbow. Similarly, because of the requirement for a long shaft in the design,

careful attention was given to determining the shaft's thickness and where to place its supports. This was done to prevent vibrations when the inducer runs at high speeds. The inducer shaft's design considers its unique positioning, where the mechanical seal isn't situated right after the inducer and isn't pressurized during its rotation. Hence, this seal is designed to be naturally under slight pressure, ensuring the inducer section remains sealed, especially during cavitation tests. The inducer is housed within a plexiglass tube, enabling image analysis. Different lengths of these plexiglass tubes allow for varying distances between the inducer and the impeller. For convenience in adjusting this distance, the entire inducer section is mounted on a slider. This setup simplifies the process, reducing the time and effort needed to modify both the inducer's position and its spacing relative to the impeller.

6.2 Experimental results

This research aims to study the impact of rotors rotating independently on the characteristics of the pump and its cavitation performance. To achieve this, experimental tests were conducted in two parts : the characteristic test and the cavitation test.

6.2.1 Effect of independent rotation of inducer on pump characteristics

The ability of the inducer to rotate independently offers flexibility in adjusting the pump's operational range based on requirements. Notably, when the inducer's speed is increased, there is a corresponding rise in the pump's generated pressure. However, these speed changes don't significantly impact the pump's efficiency. Hence, the pump's operational point can be adjusted by modifying its speed. The study highlighted that the use of a counter-rotating inducer significantly influences pump pressure. Remarkably, by changing the rotation direction of the inducer without increasing its speed, the pump pressure can be boosted considerably more than with speed enhancements in the co-rotation mode. Additionally, increasing the inducer's speed in the counter-rotation mode results in a more significant pressure increase than in the co-rotation setting. This increased pressure allows the impeller to function at a lower speed while achieving the equivalent pressure seen in the co-rotation mode. This reduced speed of the impeller plays a role in the improved pump cavitation performance observed in the counter-rotation approach.

6.2.2 Effect of independent rotation of inducer on pump cavitation

One primary objective of using an inducer is to enhance pump cavitation performance. Typically, the inducer reduces the pump's $NPSH$. The introduction of independent rotation technology in this study, aimed at exploring its influence on pump cavitation, highlights the significant impact of inducer speed and rotation on cavitation across various flow rates. By changing the direction of the inducer's rotation and adopting a counter-rotation approach, the pump's ability to handle cavitation is significantly enhanced. When flow rates are high, the pump's $NPSH$ decreases with increasing inducer speed, helping prevent premature cavitation. This is due to the coupling between the inducer and the impeller. By inverting the rotation and altering the fluid's tangential velocity as it exits the inducer in counter-rotation, there is an increase in the pressure produced by the impeller. This allows the impeller to operate at reduced speeds while maintaining the same pressure as when rotating in the same direction, thus pushing back the start of cavitation. Additionally, due to the separate rotation capabilities of the inducer and impeller, the impact of the distance between the rotors has been studied. The findings indicate that the distance has an important effect on the enhancing the pump's cavitation performance, particularly when they are positioned farther apart.

6.3 Perspective

In this section, potential future studies and tests that could build upon the current research are suggested. With the introduction of a novel test bench allowing for independent rotation of both the inducer and impeller, there is a wide opportunity for in-depth analysis of various parameters. Additionally, new measurement and analysis methods can be incorporated.

6.3.1 PIV measurements

Particle Image velocimetry or PIV is a strong optical method to better understand the phenomena occur in the fluid field. PIV is used to capture the flow pattern in all turbomachine systems. Both data measurement and flow pattern can be achieved by PIV method.
In the PIV method, the laser light is first irradiated, this light becomes a screen with the help of special lenses and illuminates the area inside the fluid. A fluid that contains particles that have been injected into a suitable concentration to determine its position. By taking two consecutive photos with

a digital camera and sending them to a computer, the photos are saved and then by comparing these two images, the amount of particle displacement is determined. In the simplest way, two components of flow velocity can be measured on an exposed screen.
With the integration of the PIV measurement technique into the updated test bench design, there is an enhanced capability to closely study the flow within the inducer as well as between the inducer and impeller. Furthermore, this setup provides insight into the impacts of both independent and counter-rotation mode on the flow patterns between the rotors.

6.3.2 Geometry optimization

The findings from this research are specific to the inducer and impeller that were designed. Future work can focus on optimizing rotor geometries by designing various inducers and impellers and conducting further experiments and research on them. Additionally, by adjusting variables such as rotation speed and the distance between the two rotors, the effects of these parameters beyond the current study scope can be explored.

6.3.3 CFD simulation of pump cavitation performance

In this thesis, the pump simulation was conducted in a non-cavitation state. Moving forward, by simulating the pump under cavitation conditions at diverse flow rates and rotational speeds, different forms of cavitation in the inducer and impeller can be explored. Through the use of simulation, insights into impeller cavitation can be observed, which cannot be seen in the experimental test bench. Additionally, this method allows us to compare and evaluate these simulated results with Experimental results.

6.3.4 Rim driven inducer and impeller

Introducing an independent rotation system for the inducer and impeller is an innovative approach to enhance pump cavitation, a topic thoroughly explored in this research. While constructing a test bench with dual shafts provides a broader range of parameters to study, it simultaneously poses practical application challenges because of the requirement of two shafts and the duplication of components like supports. To solve these challenges, rim drive technology could be implemented. By situating the motor around the blade, the necessity for shafts, supports, and elbows can be bypassed.

Bibliographie

[1] Y. A. Çengel et J. M. Cimbala, *Fluid mechanics : fundamentals and applications*, third edition éd. McGraw Hill, 2014.

[2] M. Schmirler et H. Netrebska, "The design of axial shaftless pump," vol. 143, p. 02104, 2017. [En ligne]. Disponible : http://www.epj-conferences.org/10.1051/epjconf/201714302104

[3] F. Feng, C. Geng, T. Guo, Q.-y. Huang et J. Hu, "Numerical simulation of cotra rotating propellers," dans *Proceedings of the 2017 International Conference on Manufacturing Engineering and Intelligent Materials (ICMEIM 2017)*. Atlantis Press, 2017. [En ligne]. Disponible : http://www.atlantis-press.com/php/paper-details.php?id=25874089

[4] E. Kravitz, "Analysis and experiments for contra-rotating propeller," 2011. [En ligne]. Disponible : https://api.semanticscholar.org/CorpusID:109442984

[5] T. Shigemitsu, A. Furukawa, S. Watanabe et O. Kusuo, "Air/water two-phase flow performance of contra-rotating axial flow pump and rotational speed control of rear rotor," 2005.

[6] H. Nouri, A. Danlos, F. Ravelet, F. Bakir et C. Sarraf, "Experimental study of the instationary flow between two ducted counter-rotating rotors," vol. 135, n°. 2, p. 022601, 2013-02-01. [En ligne]. Disponible : https://asmedigitalcollection.asme.org/gasturbinespower/article/doi/10.1115/1.4007756/373394/Experimental-Study-of-the-Instationary-Flow

[7] H. Ghassemi et M. Taherinasab, "Numerical calculations of the hydrodynamic performance of the contra-rotating propeller (CRP) for high speed vehicle," vol. 20, n°. 2, p. 13–20, 2013-04-01. [En ligne]. Disponible : https://content.sciendo.com/doi/10.2478/pomr-2013-0012

[8] J. Wang, F. Ravelet et F. Bakir, "Influence of design parameters on the global performances of low-speed counter-rotating axial-flow fans," dans *Volume 1B, Symposia : Fluid Machinery ; Fluid-Structure Interaction and Flow-Induced Noise in Industrial Applications ; Flow Applications*

in Aerospace ; Flow Manipulation and Active Control : Theory, Experiments and Implementation ; Multiscale Methods for Multiphase Flow ; Noninvasive Measurements in Single and Multiphase Flows. American Society of Mechanical Engineers, 2014-08-03, p. V01BT10A045. [En ligne]. Disponible : https://asmedigitalcollection.asme.org/FEDSM/proceedings/FEDSM2014/46223/Chicago,%20Illinois,%20USA/233165

[9] M. Ryu, L. Cho et J. Cho, "The effect of tip clearance on performance of a counter-rotating ducted fan in a VTOL UAV," vol. 60, n°. 1, p. 1–9, 2017. [En ligne]. Disponible : https://www.jstage.jst.go.jp/article/tjsass/60/1/60_T-15-38/_article

[10] S. N. Jung, T.-S. No et K.-W. Ryu, "Aerodynamic performance prediction of a 30kw counter-rotating wind turbine system," vol. 30, n°. 5, p. 631–644, 2005-04. [En ligne]. Disponible : https://linkinghub.elsevier.com/retrieve/pii/S0960148104002903

[11] V. A. Koehuan, Sugiyono et S. Kamal, "Investigation of counter-rotating wind turbine performance using computational fluid dynamics simulation," vol. 267, p. 012034, 2017-11. [En ligne]. Disponible : https://iopscience.iop.org/article/10.1088/1757-899X/267/1/012034

[12] Y. Chen, C. An, R. Zhang, Q. Fu et R. Zhu, "Research on Two-Way Contra-Rotating Axial-Flow Pump–Turbine with Various Blade Angles in Pump Mode," *Processes*, vol. 11, n°. 5, p. 1552, mai 2023. [En ligne]. Disponible : https://www.mdpi.com/2227-9717/11/5/1552

[13] D. Pundhir et P. Sharma, "A study of aerodynamic performance of a contra rotating axial compressor stage," vol. 42, n°. 3, p. 191–199, 1992-01-01. [En ligne]. Disponible : http://publications.drdo.gov.in/ojs/index.php/dsj/article/view/4381

[14] Y.-Y. Chen, B. Liu, Y. Xuan et X.-R. Xiang, "A study of speed ratio affecting the performance of a contra-rotating axial compressor," vol. 222, n°. 7, p. 985–991, 2008-07-01. [En ligne]. Disponible : http://journals.sagepub.com/doi/10.1243/09544100JAERO364

[15] V. T. Nguyen, A. Danlos, R. Paridaens et F. Bakir, "Study of the effect of the contra-rotating component on the performance of the centrifugal compressor," vol. 13, n°. 5, 2019.

[16] v. T. Nguyen, "Experimental study of the rotor-rotor aerodynamic interaction of a counter-rotating centrifugal compressor," Theses, HESAM Université, août 2020. [En ligne]. Disponible : https://theses.hal.science/tel-02967047

[17] A. Furukawa, T. Shigemitsu et S. Watanabe, “Performance test and flow measurement of contra-rotating axial flow pump,” vol. 16, n°. 1, p. 7–13, 2007-03. [En ligne]. Disponible : https://link.springer.com/10.1007/s11630-007-0007-4

[18] W. Xiuli, L. Bin, L. Yang, Z. Yan, Z. Rongsheng, L. Yun et F. Qiang, “Hydraulic optimization of two-way counter-rotating axial flow pump turbine,” vol. 8, p. 577232, 2020-11-23. [En ligne]. Disponible : https://www.frontiersin.org/articles/10.3389/fenrg.2020.577232/full

[19] I. Pavlenko, O. Kulikov, O. Ratushnyi, V. Ivanov, J. Pitel’ et V. Kondus, “Effect of Impeller Trimming on the Energy Efficiency of the Counter-Rotating Pumping Stage,” *Applied Sciences*, vol. 13, n°. 2, p. 761, janv. 2023. [En ligne]. Disponible : https://www.mdpi.com/2076-3417/13/2/761

[20] C. An, Y. Chen, R. Zhu, X. Wang, Y. Yang et J. Shi, “Internal Flow Phenomena of Two-Way Contra-Rotating Axial Flow Pump-Turbine in Pump Mode under Variable Speed,” *Journal of Applied Fluid Mechanics*, vol. 16, n°. 2, p. 285–297, févr. 2023. [En ligne]. Disponible : https://www.jafmonline.net/article_2140.html

[21] W. Han, Y. Liu, C. Gong, Y. Su, P. Guo, M. Su, F. Shi et Z. Wei, “Effect of tip clearance on performance of contra-rotating axial flow water-jet propulsion pump,” vol. 34, n°. 10, p. 2050094, 2020-04-10. [En ligne]. Disponible : https://www.worldscientific.com/doi/abs/10.1142/S0217984920500943

[22] D. Zhang, Y. Katayama, S. Watanabe, S.-I. Tsuda et A. Furukawa, “Numerical study on loss mechanism in rear rotor of contra-rotating axial flow pump,” vol. 13, n°. 1, p. 241–252, 2020-03-31. [En ligne]. Disponible : http://www.dbpia.co.kr/Journal/ArticleDetail/NODE09320017

[23] T. Kanemoto et S. Oba, “Proposition of unique pumping system with counter-rotating mechanism,” vol. 10, n°. 4, p. 233–240, 2004-07-01. [En ligne]. Disponible : http://www.informaworld.com/openurl?genre=article&doi=10.1080/10236210490447494&magic=crossref||D404A21C5BB053405B1A640AFFD44AE3

[24] L. Cao, S. Watanabe, T. Imanishi, H. Yoshimura et A. Furukawa, “Experimental analysis of flow structure in contra-rotating axial flow pump designed with different rotational speed concept,” vol. 22, n°. 4, p. 345–351, 2013-08. [En ligne]. Disponible : http://link.springer.com/10.1007/s11630-013-0634-x

[25] S. Brizzolara, D. Grassi et E. P. Tincani, “Design Method for Contra-Rotating Propellers for High-Speed Crafts : Revising the Original Lerbs Theory in a Modern Perspective,” *International Journal of Rotating Machinery*, vol. 2012, p. 1–18, 2012. [En ligne]. Disponible : http://www.hindawi.com/journals/ijrm/2012/408135/

[26] K.-S. Min, B.-J. Chang et H.-W. Seo, “Study on the Contra-Rotating Propeller system design and full-scale performance prediction method,” *International Journal of Naval Architecture and Ocean Engineering*, vol. 1, n°. 1, p. 29–38, sept. 2009. [En ligne]. Disponible : http://koreascience.or.kr/journal/view.jsp?kj=E1JSE6&py=2009&vnc=v1n1&sp=29

[27] A. Danlos, F. Ravelet, M. Solis et F. Bakir, “Numerical study of performance gains and suction capacity improvement obtained using a contra-rotating axial stage instead of a mono-rotor pump.”

[28] S. Momosaki, S. Usami, S. Watanabe et A. Furukawa, “Numerical simulation of internal flow in a contra-rotating axial flow pump,” *IOP Conference Series : Earth and Environmental Science*, vol. 12, p. 012046, août 2010. [En ligne]. Disponible : https://iopscience.iop.org/article/10.1088/1755-1315/12/1/012046

[29] S. Tosin, J. Friedrichs et A. Dreiss, “New Design Approach for a Highly Loaded Counter-Rotating Mixed-Flow Pump in Cavitation Conditions,” dans *www.euroturbo.eu//*. EUROPEAN TURBOMACHINERY SOCIETY, 2015, iSSN : 2410-4833. [En ligne]. Disponible : https://www.euroturbo.eu/publications/proceedings-papers/etc2015-199/

[30] S. Tosin, J. Friedrichs, R. Farooqi et A. Dreiss, “New Approach for Multi-Rotor Mixed-Flow Pump Design and Optimization,” dans *Volume 1A, Symposia : Advances in Fluids Engineering Education ; Turbomachinery Flow Predictions and Optimization ; Applications in CFD ; Bio-Inspired Fluid Mechanics ; Droplet-Surface Interactions ; CFD Verification and Validation ; Development and Applications of Immersed Boundary Methods ; DNS, LES, and Hybrid RANS/LES Methods*. Chicago, Illinois, USA : American Society of Mechanical Engineers, août 2014, p. V01AT02A007. [En ligne]. Disponible : https://asmedigitalcollection.asme.org/FEDSM/proceedings/FEDSM2014/46216/Chicago,%20Illinois,%20USA/232640

[31] S.-S. Hong, D.-J. Kim, J.-S. Kim, C.-H. Choi et J. Kim, “Study on inducer and impeller of a centrifugal pump for a rocket engine turbopump,” vol. 227, n°. 2, p. 311–319, 2013-02. [En ligne]. Disponible : http://journals.sagepub.com/doi/10.1177/0954406212449939

[32] A. Koishikawa, Y. Takeuchi et S. Ohta, *Development of advanced inducer pump for LMFBR.* Atomic Energy Society of Japan, 1992, INIS Reference Number : 24075425.

[33] Y. A. Semenov, A. Fujii et Y. Tsujimoto, "Rotating choke in cavitating turbopump inducer," vol. 126, n°. 1, p. 87–93, 2004-01-01. [En ligne]. Disponible : https://asmedigitalcollection.asme.org/fluidsengineering/article/126/1/87/445605/Rotating-Choke-in-Cavitating-Turbopump-Inducer

[34] M. Mansour, B. Wunderlich et D. Thévenin, "Effect of tip clearance gap and inducer on the transport of two-phase air-water flows by centrifugal pumps," vol. 99, p. 487–509, 2018-12. [En ligne]. Disponible : https://linkinghub.elsevier.com/retrieve/pii/S0894177718311877

[35] B. Y. Kang et S.-H. Kang, "Effect of the number of blades on the performance and cavitation instabilities of a turbopump inducer with an identical solidity," vol. 29, n°. 12, p. 5251–5256, 2015-12. [En ligne]. Disponible : http://link.springer.com/10.1007/s12206-015-1126-6

[36] I. Mejri, F. Bakir, R. Rey et T. Belamri, "Comparison of computational results obtained from a homogeneous cavitation model with experimental investigations of three inducers," vol. 128, n°. 6, p. 1308–1323, 2006-11-01. [En ligne]. Disponible : https://asmedigitalcollection.asme.org/fluidsengineering/article/128/6/1308/478069/Comparison-of-Computational-Results-Obtained-From

[37] M. El Samanody, A. Ghorab et M. A. F. Mostafa, "Investigations on the performance of centrifugal pumps in conjunction with inducers," vol. 5, n°. 1, p. 149–156, 2014-03. [En ligne]. Disponible : https://linkinghub.elsevier.com/retrieve/pii/S2090447913000671

[38] X. Guo, C. Jiang, H. Qian, Z. Zhu et C. Zhou, "Effect of tip clearance on the cavitation flow in a shunt blade inducer," vol. 15, n°. 17, p. 6330, 2022-08-30. [En ligne]. Disponible : https://www.mdpi.com/1996-1073/15/17/6330

[39] X. Guo, C. Jiang, H. Qian et Z. Zhu, "The influence of tip clearance on the performance of a high-speed inducer centrifugal pump under different flow rates conditions," vol. 11, n°. 1, p. 239, 2023-01-11. [En ligne]. Disponible : https://www.mdpi.com/2227-9717/11/1/239

[40] A. H. I. Aboelnil, S. A. F. Hawash et M. A. Hashim, "Effect of helical inducer usage on both performance and npsh for a centrifugal pump," vol. 36, n°. 1, p. 41–47, 2022-12-31. [En ligne]. Disponible : https://www.tandfonline.com/doi/full/10.1080/23570008.2022.2043524

[41] H. Quan, J. Cheng, Y. Guo, L. Kang et G. Peng, “Influence of screw centrifugal inducer on internal flow structure of vortex pump,” vol. 142, n°. 91203, 2020-06-08. [En ligne]. Disponible : https://doi.org/10.1115/1.4047229

[42] B. Yang, B. Li, H. Chen et Z. Liu, “Entropy production analysis for the clocking effect between inducer and impeller in a high-speed centrifugal pump,” vol. 233, n°. 15, p. 5302–5315, 2019-08. [En ligne]. Disponible : http://journals.sagepub.com/doi/10.1177/0954406219843946

[43] A. Mishra et P. Ghosh, “Predicting performance of axial pump inducer of LOX booster turbo-pump of staged combustion cycle based rocket engine using CFD,” vol. 101, p. 012180, 2015-12-18. [En ligne]. Disponible : https://iopscience.iop.org/article/10.1088/1757-899X/101/1/012180

[44] M. M. Shamsuddeen, S.-B. Ma, S. Kim, J.-H. Yoon, K.-H. Lee, C. Jung et J.-H. Kim, “Effect of an inducer-type guide vane on hydraulic losses at the inter-stage flow passage of a multistage centrifugal pump,” vol. 9, n°. 3, p. 526, 2021-03-15. [En ligne]. Disponible : https://www.mdpi.com/2227-9717/9/3/526

[45] B. Cui et C. Li, “Influence of axial matching between inducer and impeller on energy loss in high-speed centrifugal pump,” vol. 11, n°. 5, p. 940, 2023-04-27. [En ligne]. Disponible : https://www.mdpi.com/2077-1312/11/5/940

[46] L. d’Agostino, L. Torre, A. Cervone, G. Pace, D. Valentini et A. Pasini, “An introduction to cavitation in inducers and turbopumps,” dans *Cavitation Instabilities and Rotordynamic Effects in Turbopumps and Hydroturbines*, L. d’Agostino et M. V. Salvetti, édit. Springer International Publishing, 2017, vol. 575, p. 1–33, series Title : CISM International Centre for Mechanical Sciences. [En ligne]. Disponible : http://link.springer.com/10.1007/978-3-319-49719-8_1

[47] “Cavitation instabilities and rotordynamic effects in turbopumps and hydroturbines : Turbopump and inducer cavitation, experiments and design,” 2017. [En ligne]. Disponible : http://link.springer.com/10.1007/978-3-319-49719-8

[48] G. Mousmoulis, J. Anagnostopoulos et D. Papantonis, “A review of experimental detection methods of cavitation in centrifugal pumps and inducers,” vol. 12, n°. 1, p. 71–88, 2019-03-31. [En ligne]. Disponible : http://www.dbpia.co.kr/Journal/ArticleDetail/NODE08767204

[49] F. Avellan, “INTRODUCTION TO CAVITATION IN HYDRAULIC MACHINERY.”

[50] M. Binama, A. Muhirwa et E. Bisengimana, “Cavitation effects in centrifugal pumps- a review,” vol. 6, n°. 5, 2016.

[51] C. E. Brennen, *Hydrodynamics of Pumps*, 1er éd. Cambridge University Press, 2011-03-28. [En ligne]. Disponible : https://www.cambridge.org/core/product/identifier/9780511976728/type/book

[52] M. Bhatt et K. Mahesh, "Investigation of propeller cavitation using compressible large eddy simulations."

[53] J. Friedrichs et G. Kosyna, "Rotating Cavitation in a Centrifugal Pump Impeller of Low Specific Speed ," *Journal of Fluids Engineering*, vol. 124, no. 2, p. 356–362, 05 2002. [En ligne]. Disponible : https://doi.org/10.1115/1.1457451

[54] D. Kang, T. Watanabe, K. Yonezawa, H. Horiguchi, Y. Kawata et Y. Tsujimoto, "Inducer Design to Avoid Cavitation Instabilities," *AIP Conference Proceedings*, vol. 1225, no. 1, p. 433–446, 06 2010. [En ligne]. Disponible : https://doi.org/10.1063/1.3464890

[55] T. Watanabe, H. Sato, Y. Henmi, H. Horiguchi, Y. Kawata et Y. Tsujimoto, "Rotating Choke and Choked Surge in an Axial Pump Impeller."

[56] S. Hatano, D. Kang, S. Kagawa, M. Nohmi et K. Yokota, "Study of Cavitation Instabilities in Double-Suction Centrifugal Pump," *International Journal of Fluid Machinery and Systems*, vol. 7, no. 3, p. 94–100, sept. 2014. [En ligne]. Disponible : http://koreascience.or.kr/journal/view.jsp?kj=OCGKEU&py=2014&vnc=v7n3&sp=94

[57] G. D. Neill, R. L. Reuben, P. M. Sandford, E. R. Brown et J. A. Steel, "Detection of incipient cavitation in pumps using acoustic emission," *Proceedings of the Institution of Mechanical Engineers, Part E : Journal of Process Mechanical Engineering*, vol. 211, no. 4, p. 267–277, 1997. [En ligne]. Disponible : https://doi.org/10.1243/0954408971529737

[58] M. Chudina, "Noise as an indicator of cavitation in a centrifugal pump," *Acoustical Physics*, vol. 49, no. 4, p. 463–474, juill. 2003. [En ligne]. Disponible : http://link.springer.com/10.1134/1.1591303

[59] G. Dyson, D. Brown et L. Fayez, "Detection of Incipient Cavitation and the best Efficiency Point of a 2.2 MW Centrifugal Pump using Acoustic Emission."

[60] M. Fukaya, S. Ono et R. Udo, "Prediction of Cavitation Intensity in Pumps Based on Propagation Analysis of Bubble Collapse Pressure Using Multi-Point Vibration Acceleration Method," *International Journal of Fluid Machinery and Systems*, vol. 2, no. 2, p. 165–171, juin 2009. [En ligne]. Disponible : http://koreascience.or.kr/journal/view.jsp?kj=OCGKEU&py=2009&vnc=v2n2&sp=165

[61] T. Sato, T. Nagahara, K. Tanaka, M. Fuchiwaki, F. Shimizu et A. Inoue, "Vortex Cavitation from Baffle Plate and Pump Vibration in a Double-Suction Volute Pump," *International Journal of Fluid Machinery and Systems*, vol. 4, n°. 1, p. 76–83, mars 2011. [En ligne]. Disponible : http://koreascience.or.kr/journal/view.jsp?kj=OCGKEU&py=2011&vnc=v4n1&sp=76

[62] S. Farokhzad, "Vibration Based Fault Detection of Centrifugal Pump by Fast Fourier Transform and Adaptive Neuro-Fuzzy Inference System," *Journal of Mechanical Engineering and Technology*, p. 82–87, nov. 2013. [En ligne]. Disponible : http://www.bowenpublishing.com/jmet/paperInfo.aspx?PaperID=14438

[63] A. Baldassarre, M. De Lucia et P. Nesi, "Real-Time Detection of Cavitation for Hydraulic Turbomachines," *Real-Time Imaging*, vol. 4, n°. 6, p. 403–416, déc. 1998. [En ligne]. Disponible : https://linkinghub.elsevier.com/retrieve/pii/S1077201497901005

[64] M. Hofmann, B. Stoffel, J. Friedrichs et G. Kosyna, "SIMILARITIES AND GEOMETRICAL EFFECTS ON ROTATING CAVITATION IN TWO SCALED CENTRIFUGAL PUMPS."

[65] R. B. Medvitz, R. F. Kunz, D. A. Boger, J. W. Lindau, A. M. Yocum et L. L. Pauley, "Performance Analysis of Cavitating Flow in Centrifugal Pumps Using Multiphase CFD," *Journal of Fluids Engineering*, vol. 124, n°. 2, p. 377–383, juin 2002. [En ligne]. Disponible : https://asmedigitalcollection.asme.org/fluidsengineering/article/124/2/377/444533/Performance-Analysis-of-Cavitating-Flow-in

[66] X. Guo, Z. Zhu, B. Cui et Y. Li, "The rotating cavitation performance of a centrifugal pump with a splitter-bladed inducer under different rotational speed," vol. 32, n°. 3, p. 275–283, 2015-09-01, publisher : De Gruyter. [En ligne]. Disponible : https://www.degruyter.com/document/doi/10.1515/tjj-2014-0034/html

[67] Y.-y. Huan, Y.-y. Liu, X.-j. Li, Z.-c. Zhu, J.-t. Qu, L. Zhe et A.-d. Han, "Experimental and numerical investigations of cavitation evolution in a high-speed centrifugal pump with inducer," vol. 33, n°. 1, p. 140–149, 2021-02-01. [En ligne]. Disponible : https://doi.org/10.1007/s42241-021-0006-z

[68] O. Coutier-Delgosha, P. Morel, R. Fortes-Patella et J. Reboud, "Numerical simulation of turbopump inducer cavitating behavior," vol. 2005, n°. 2, p. 135–142, 2005. [En ligne]. Disponible : http://www.hindawi.com/journals/ijrm/2005/752538/abs/

[69] X. Guo, Z. Zhu, B. Cui et G. Shi, “Effects of the number of inducer blades on the anti-cavitation characteristics and external performance of a centrifugal pump,” vol. 30, n°. 7, p. 3173–3181, 2016-07. [En ligne]. Disponible : http://link.springer.com/10.1007/s12206-016-0510-1

[70] X.-m. Guo, Z.-c. Zhu, G.-p. Shi et Y. Huang, “Effects of rotational speeds on the performance of a centrifugal pump with a variable-pitch inducer,” vol. 29, n°. 5, p. 854–862, 2017-10. [En ligne]. Disponible : http://link.springer.com/10.1016/S1001-6058(16)60797-7

[71] T. Magne, R. Paridaens, S. Khelladi, F. Bakir, P. Tomov et L. Pora, “Experimental study of the hydraulic performances of two three-bladed inducers in water, water with dissolved CO2, and jet fuel,” vol. 142, n°. 11, p. 111210, 2020-11-01. [En ligne]. Disponible : https://asmedigitalcollection.asme.org/fluidsengineering/article/doi/10.1115/1.4048143/1086257/Experimental-Study-of-the-Hydraulic-Performances

[72] F. Bakir, R. Rey, A. Gerber, T. Belamri et B. Hutchinson, “Numerical and experimental investigations of the cavitating behavior of an inducer,” vol. 10, n°. 1, p. 15–25, 2004-01-01. [En ligne]. Disponible : http://www.informaworld.com/openurl?genre=article&doi=10.1080/10236210490258034&magic=crossref||D404A21C5BB053405B1A640AFFD44AE3

[73] Y. Fu, J. Xie, Y. Shen, G. Pace, D. Valentini, A. Pasini et L. D’Agostino, “Experimental and numerical study on cavitation performances of a turbopump with and without an inducer,” vol. 236, n°. 6, p. 1098–1111, 2022-05. [En ligne]. Disponible : http://journals.sagepub.com/doi/10.1177/09544100211027045

[74] C. Bi et J. Li, “Effect of radial height of helical static blade on the cavitation performance of inducer,” vol. 12, n°. 8, p. 3897, 2022-04-12. [En ligne]. Disponible : https://www.mdpi.com/2076-3417/12/8/3897

[75] Z. Xu, F. Kong, H. Zhang, K. Zhang, J. Wang et N. Qiu, “Research on visualization of inducer cavitation of high-speed centrifugal pump in low flow conditions,” vol. 9, n°. 11, p. 1240, 2021-11-08. [En ligne]. Disponible : https://www.mdpi.com/2077-1312/9/11/1240

[76] R. Campos-Amezcua, S. Khelladi, Z. Mazur-Czerwiec, F. Bakir, A. Campos-Amezcua et R. Rey, “Numerical and experimental study of cavitating flow through an axial inducer considering tip clearance,” p. 12.

[77] C. Kim, C.-H. Choi, S. Kim et J. Baek, "Numerical study on the effects of installing an inducer on a pump in a turbopump," vol. 235, n°. 8, p. 1877–1891, 2021-12. [En ligne]. Disponible : http://journals.sagepub.com/doi/10.1177/09576509211014984

[78] D. Wang, B. Gao, Y. Chen, Y. Pan, J. Luo, L. Liu, Q. Wei et L. Liu, "Effects of matching between the inducer and the impeller of a centrifugal pump on its cavitation performance," 2023.

[79] R. J. Moffat, "Describing the uncertainties in experimental results," vol. 1, n°. 1, p. 3–17, 1988-01. [En ligne]. Disponible : https://linkinghub.elsevier.com/retrieve/pii/089417778890043X

[80] H. W. Coleman et W. G. Steele, *Experimentation, validation, and uncertainty analysis for engineers*, fourth edition éd. Wiley, 2018.

[81] D. C. Baird et W. R. Hendee, "Experimentation : An introduction to measurement theory and experiment design," vol. 33, n°. 1, p. 64–64, 1965-01-01. [En ligne]. Disponible : https://pubs.aip.org/ajp/article/33/1/64/1038315/Experimentation-An-Introduction-to-Measurement

[82] J. Taylor, *An Introduction to Error Analysis : The Study of Uncertainties in Physical Measurements*, ser. ASMSU/Spartans.4.Spartans Textbook. University Science Books, 1997. [En ligne]. Disponible : https://books.google.fr/books?id=ypNnQgAACAAJ

[83] E. Dehnavi, M. Solis, A. Danlos, M. Kebdani et F. Bakir, "Improving the Performance of an Innovative Centrifugal Pump through the Independent Rotation of an Inducer and Centrifugal Impeller Speeds," *Energies*, vol. 16, n°. 17, p. 6321, août 2023. [En ligne]. Disponible : https://www.mdpi.com/1996-1073/16/17/6321

[84] E. Dehnavi, M. Kebdani, A. Danlos et F. Bakir, "Numerical analysis of Counter-Rotating Pump (CRP) including inducer and centrifugal impeller," dans *25e Congrès Français de Mécanique*, Nantes, France, août 2022. [En ligne]. Disponible : https://hal.science/hal-04281734

[85] F. White, *Fluid Mechanics*, ser. McGraw-Hill series in mechanical engineering. McGraw-Hill Higher Education, 2000. [En ligne]. Disponible : https://books.google.fr/books?id=L4hvAQAACAAJ

[86] E. Dehnavi, F. Bakir, A. Danlos et M. Kebdani, "Numerical Analysis of Distance Effect between Inducer and Centrifugal Impeller in Independent Rotational Turbopump in Co-rotating and Counter-rotating Mode," dans *ETC15, 15th European Turbomachinery conference : fluid dynamics and thermodynamics*. Budapest, Hungary : Euroturbo (European Turbomachinery Society), avr. 2023. [En ligne]. Disponible : https://hal.science/hal-04184150

[87] E. Dehnavi, A. Danlos, M. Solis, M. Kebdani et F. Bakir, “Study on the pump cavitation characteristic through novel independent rotation of inducer and centrifugal impeller in co-rotation and counter-rotation modes,” *Physics of Fluids*, vol. 36, n°. 1, p. 015120, 01 2024. [En ligne]. Disponible : https://doi.org/10.1063/5.0182731

Annexe A

List of Publications

Journal Articles

E. Dehnavi, A. Danlos, M. Solis, M. Kebdani, et F. Bakir, " Study on the pump cavitation characteristic through novel independent rotation of inducer and centrifugal impeller in co-rotation and counter-rotation modes ", Phys. Fluids, vol. 36, no 1, p. 015120, janv. 2024, doi : 10.1063/5.0182731. (Q1)

E. Dehnavi, M. Solis, A. Danlos, M. Kebdani, et F. Bakir, " Improving the Performance of an Innovative Centrifugal Pump through the Independent Rotation of an Inducer and Centrifugal Impeller Speeds ", Energies, vol. 16, no 17, p. 6321, août 2023, doi : 10.3390/en16176321. (Q1)

Conference Articles

E. Dehnavi, F. Bakir, A. Danlos, et M. Kebdani, " Numerical analysis of the distance effect between inducer and centrifugal impeller in independent rotational turbopump in co-rotating and counter-rotating mode ", présenté à 15th European Conference on Turbomachinery Fluid dynamics Thermodynamics, 2023, doi : 10.29008/ETC2023-203.

E. Dehnavi, M. Kebdani, A. Danlos, et F. Bakir, " Numerical analysis of Counter-Rotating Pump (CRP) including inducer and centrifugal impeller ", Nantes, France, août 2022, Consulté le : avr. 17, 2024. [En ligne]. Disponible sur : https ://hal.science/hal-04281734.

Annexe B

Titre de l'annexe B

B.1 Introduction

Les machines tournantes sont utilisées pour transférer de l'énergie entre la partie mécanique et le fluide de travail. Les machines tournantes peuvent être divisées en deux groupes principaux : le premier, qui absorbe l'énergie et produit un mouvement mécanique, tel que des pompes, des compresseurs, des ventilateurs. Le second produit de l'énergie (principalement électrique) en absorbant l'énergie mécanique du fluide de travail (qui peut être de la vapeur, du gaz ou de l'eau) [1]. La direction du flux peut classer les machines tournantes en machines axiales, centrifuges et à écoulement mixte. Les machines axiales peuvent fonctionner avec un débit plus élevé et une perte de pression plus faible, ce qui donne à ce type de machine la capacité de fonctionner comme des pompes, des turbines et des compresseurs à débit élevé [2]. Au cours des dernières décennies, les changements rapides dans la conception des turbomachines et le besoin de turbomachines plus efficaces et fiables sont la raison pour laquelle les scientifiques et les industries ont délaissé les hélices à pale unique conventionnelles et conçu des turbomachines contra-rotatives [3]. Les turbomachines contra-rotatives ont de nombreuses applications dans les industries. Ces machines comprennent deux rotors coaxiaux tournant en sens opposé, ce qui permet une conversion d'énergie plus importante, un encombrement réduit et de meilleures performances. Une partie de l'énergie cinétique rotationnelle du rotor amont est convertie en charge statique par le rotor aval. Cependant, le bruit généré par l'interaction des deux rotors et la complexité de la conception représentent les principaux inconvénients des turbomachines contra-rotatives [4]. Les études sur les pompes axiales contra-rotatives ont montré que l'utilisation d'un rotor aval à la place d'un stator contribue à améliorer le débit et le rendement total de la pompe axiale contra-rotative,

en particulier à faibles débits [5]. La distance entre les rotors a un effet majeur sur les performances locales et totales, et une augmentation de l'espacement axial relatif entre les deux rotors réduit les pics d'interaction rotorique près du rotor avant sans affecter significativement les performances globales [6].

Les turbomachines contra-rotatives sont composées de deux roues montées sur deux arbres coaxiaux , tournant en sens opposé. Bien qu'elles présentent des défis tels qu'une conception plus complexe et une masse plus importante due de la roue, elles offrent plusieurs avantages par rapport aux rotors simples. Le principal avantage des machines contra-rotatives est leur efficacité accrue, grâce à l'énergie récupérée par la roue aval. La roue aval capture une partie de l'énergie rotationnelle que la roue amontt transfère à l'eau, ce qui se traduit par une consommation de carburant réduite. De plus, le second rotor aide à stabiliser le couple du système, en particulier dans les situations nécessitant une grande stabilité. Le bruit est réduit grâce au champ de sillage constant en aval créé par les roues contra-rotatives [7]. Ryu et al.[9] ont étudié l'effet du jeu à l'extrémité des pales sur la performance du ventilateur caréné. Le ratio du jeu l'extrémité des pales du rotor aval par rapport au rotor amont varie de $1,80\%$ à $7,62\%$. Le coefficient de poussée diminue avec l'augmentation du jeu l'extrémité des pales du rotor amont en raison d'une fuite plus importante au niveau de l'extrémité des pales. En diminuant le jeu à l'extrémité des pales du rotor aval, le coefficient de poussée augmente. Le coefficient de puissance diminué également avec un jeu plus grand à la périphérie des pales en raison de l'effet de pertes visqueuse et de la perte de fuite aux bords. L'efficacité augmente en diminuant le jeu en périphérie des pales du rotor aval et elle diminuera en augmentant le jeu en périphérie des pales du rotor amont. Jung et al.[10] ont étudié les performances aérodynamiques d'une éolienne contra-rotative (CRWT) de 30 kW et les ont comparées à celles d'une éolienne conventionnelle. Les résultats indiquent que l'augmentation de la puissance est affectée par les caractéristiques de l'écoulement et par la rotation du premier rotor. La vitesse de l'écoulement au niveau du second rotor est faible lorsque le premier rotor est de la même taille que le second, ce qui entraîne une diminution de la puissance. De plus, la puissance de sortie est fortement liée à la distance entre les rotors.

L'étude des performances du compresseur centrifuge à contra-rotation (CRCC) a été réalisée par Nguyen et al.[16]. Quatre géométries différentes (CF1, CF2, CF3 et CF4), basées sur un rotor de référence, ont été mises à l'épreuve et les résultats indiquent que le CRCC présente un taux de compression plus élevé pour un débit inférieur au Point de Fonctionnement de Conception (PFC). Le taux

de compression augmente en accroissant le rapport de longueur (rapport entre la longueur au moyeu du premier rotor et la longueur du rotor de référence) ; cependant, l'efficacité diminue rapidement. En modifiant la vitesse du premier rotor à 130% du PFC, le taux de compression peut augmenter de 8,7%. Un diamètre plus grand à la sortie du premier rotor résulte en taux de compression plus élevé, produisant un flux d'énergie cinétique plus important dans le second rotor. Le taux de compression pour le compresseur de référence est de 1,29, alors que le taux de compression maximum est de 1,53.

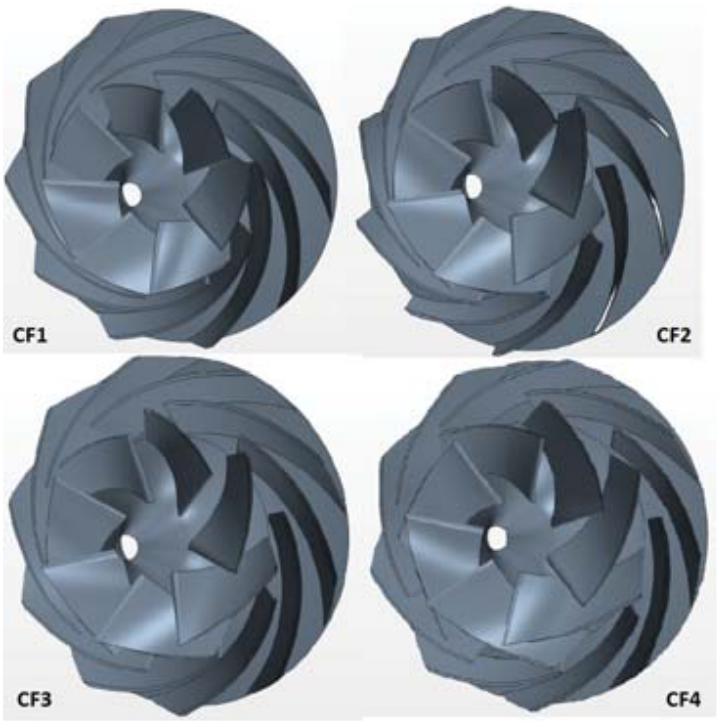

FIGURE B.1 – Configurations CF1,CF2,CF et CF4 du systéme de compression contra-rotatif[16]

Les performances instables et la consommation élevée d'énergie sont deux défis majeurs dans le fonctionnement des pompes. Augmenter l'efficacité et réduire l'instabilité peut se traduire par des économies d'énergie substantielles. L'utilisation de pompes à contra-rotatives (CRP) est récemment envisagée en raison de leur vitesse spécifique et de leur rendement plus élevés. Le concept de CRP consiste à remplacer un stator par une roue tournant dans le sens opposé. L'utilisation de pompes à contra-rotatives(CRP) dans un écoulement diphasique air/eau étudiée par Shigemitsu et al.[5] a montré une augmentation significative des performances et de l'efficacité en contrôlant la vitesse du

rotor aval. Une courbe de caractéristiques plus stable, une gamme de fonctionnement plus étendue avec des performances plus élevées et moins de cavitation sont quelques-uns des avantages des pompes contra-rotatives. Cependant, ce type de pompe présente également certains inconvénients, tels qu'un arbre d'entraînement double indépendant complexe. La conception du rotor aval est importante pour atteindre de meilleures performances et une efficacité accrue.

Les principaux paramètres caractéristiques de la pompe seront différents en changeant la distance entre les rotors.[18] En considérant l'épaisseur de la roue L comme référence, en augmentant la distance du rotor de zéro $D_L = 0$ jusqu'à $D_L = 2L$, la hauteur manométrique maximale et le rendement le plus élevé sont atteints lorsque la distance du rotor est égale à la largeur axiale de la roue $D_L = L$ (Figure B.2). En dépassant cette valeur, le rendement ne s'améliore pas et la hauteur manométrique diminue lentement. La vorticité au niveau du rotor secondaire est distribuée près de l'entrée du rotor, la zone à haute pression sur la face de travail de l'aube secondaire est plus petite que la zone à basse pression à l'arrière de l'aube. À mesure que la distance entre les rotors augmente, la zone à basse pression à l'arrière de l'aube diminue et la zone à haute pression sur la surface de travail augmente. Lorsque la distance entre les rotors est faible, il y a une forte vorticité sur le rotor secondaire et une interface dynamique plus importante de rotor contra-rotatif, ce qui résulte en une hauteur manométrique et un rendement plus faibles. cependant, en augmentant la distance entre les rotors au-delà de $D_L = 0$, ces paramètres diminueont également lentement.

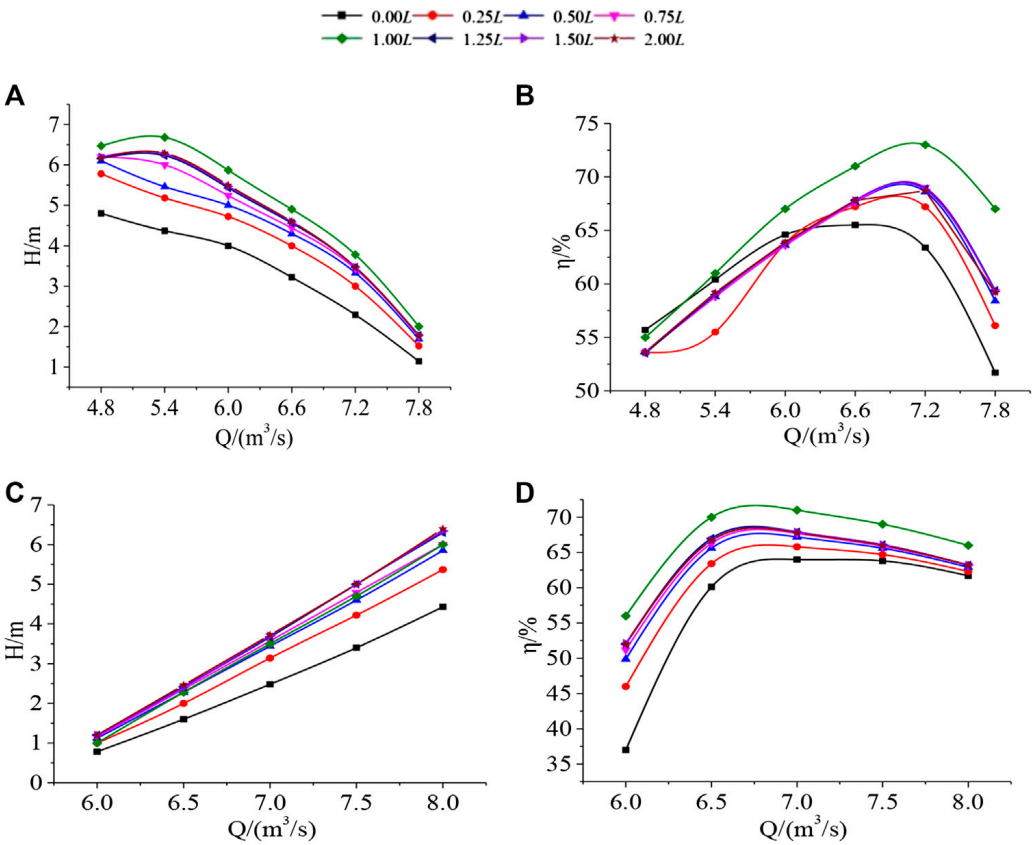

FIGURE B.2 – Courbes de performances de pompes et turbines avec différentes distances entre rotors (A) Hauteur de la pompe. (B) Efficacité de la pompe. (C) Courbes de hauteur de la turbine. (D) Courbes d'efficacité de la turbine.[18]

Trois modèles CRP avec une vitesse spécifique différente et deux méthodes d'évaluation des pertes ont été étudiés numériquement par Zhang et al.[22]. La vitesse du rotor avant est de 1500 et pour le rotor arrière, trois vitesses différentes sont considérées (1200 tr/min, 1300 tr/min et 1400 tr/min). La simulation a été réalisée avec Ansys CFX et les résultats ont montré que le rendement total est maximal avec la vitesse spécifique moyenne du rotor arrière. Bien que la zone de fortes pertes se produise au niveau du bord triangulaire en raison de la séparation au coin, une dissipation et des pertes plus importantes sont observées près de la paroi, en particulier dans la région de préphérie. Les pertes près du bord d'attaque de l'éxtrémité sont causées par l'interaction de la couche limite du carter, des rangées de pales et d'autres phénomènes. Cependant, les pertes près du vortex de fuite de l'extrémité peut être le résultat de l'effet de blocage causé par la vitesse spécifique plus élevée du rotor aval.
Pour améliorer la Hauteur Nette Positive d'Aspiration (NPSH) et prévenir la dégradation des perfor-

mances, un impulseur axial, connu sous le nom d'inducteur, est positionné devant la roue centrifuge primaire. L'inducteur peut soit être un composant intégré du rotor de la pompe, soit être positionné séparément sur l'arbre de la pompe en amont de la roue. L'objectif principal de la conception d'un inducteur est d'optimiser les capacités d'aspiration. Cependant, atteindre son efficacité maximale est limité par des aspects de sa conception structurelle. Cette configuration augmente efficacement la pression à l'entrée de la roue. L'objectif principal de la conception d'un inducteur est de s'assurer une marge de cavitation suffisante plutôt que de viser un rendement maximal. L'augmentation de la hauteur manométrique d'un inducteur doit être juste suffisante pour prévenir la cavitation dans la roue principal de la pompe[31], maintenant ainsi et optimisant les performances au point de fonctionnement nominal. Les impulseurs centrifuges équipés d'inducteurs sont utilisés dans diverses industries, y compris les industries nucléaire[32], aéronautique et maritime, ainsi que dans le pompage de propergol cryogénique[33]. Pour sélectionner un inducteur approprié à associer à la roue, il est essentiel de considérer l'efficacité des deux composants. L'inducteur doit avoir une efficacité optimale pour s'assurer que, lorsqu'il est intégré, la pompe centrifuge fonctionne également à son rendement maximal[37]. L'étude de l'impact du jeu à l'extrémité de l'inducteur à aubes de dérivation sur la pompe centrifuge à faibles débits souligne l'influence significative de ce paramètre sur la cavitation. La présence d'un jeu à en prépherié entraîne souvent une cavitation par fuite à la prépherié, et la cavitation est principalement observée à l'entrée des pales longues[38]. Le jeu en prépherié de l'inducteur a un impact significatif sur l'efficacité et la pression de la pompe centrifuge équipée d'un inducteur. À faibles débits, une augmentation du jeu à la pointe entraîne une augmentation du reflux et des fuites au niveau du jeu, résultant en une diminution de la pression et du rendement de la pompe. Cependant, à des débits élevés, un jeu à la pointe plus grand peut éliminer le flux bloqué, entraînant des améliorations de l'efficacité et de la pression de la pompe[39].

L'évolution de la cavitation dans les turbomachines commence généralement par l'apparition, caractérisée par une bulbe de séparation laminaire au niveau des bords d'attaque des extrémités des pales ou sous forme de cavitation dans le vortex de la pointe, puis progresse vers la cavitation des pales, une forme plus étendue qui peut apparaître sur une pale sur deux à certains moments, suivie par la cavitation développée marquée par des poches de cavitation plus grandes, oscillant périodiquement, et se conclut par une rupture de cavitation où poches de cavitation impactent grandement l'écoulement et réduisent l'efficacité de la turbomachine[47]. Dans la région d'entrée des pales, en raison de la faible

hauteur de pression d'aspiration combinée à une vitesse d'écoulement élevée, il peut y avoir une chute significative de la pression locale, tombant parfois en dessous de la pression de vapeur du liquide. Cette condition conduit à la vaporisation du liquide et à la formation et à la croissance subséquentes de poches de vapeur. Les poches de cavitation se déplacent ensuite en aval ou vers les parois de la roue dans des régions où la pression statique est supérieure à la pression de vapeur du fluide. Ces poches de cavitation s'effondrent rapidement, leur volume disparaît et le vide laissé derrière est immédiatement rempli par le liquide environnant, ce qui crée des microjets à grande vitesse. Ce processus génère des augmentations de pression localisées élevées, qui sont les principales causes des dommages par cavitation sur les surfaces de la roue et des pales[48].

Dans les pompes, la cavitation peut apparaître sous différentes formes (Figure B.3), principalement déterminées par le débit de la pompe et l'angle de la vitesse d'entrée d'écoulement au bord d'attaque de la pale. Ces éléments influencent de manière significative la distribution de la pression sur les surfaces des pales à l'entrée. La cavitation apparaît d'abord au bord d'attaque de la pale et à son extrémité, conduisant à une "cavitation du vortex de pointe (tip vortex cavitaiton)". Avec une légère réduction du nombre de cavitation, la cavitation à bulles voyageuses se développe sur les côtés aspiration des pales. Cela est également connu sous le nom de "cavitation à bulles (bubbles cavitation)". Ces cavités sont liées à un petit angle d'écoulement entrant et, en fonction de la conception de la roue, elles s'alignent avec la zone de pression la plus basse à l'entrée de la roue[49]. Une réduction plus poussée conduit à la fusion des bulles, résultant en une cavitation attachée sur le côté aspiration de la pale. Ceci est communément appelé "cavitation de pale (blade cavitation)" dans les pompes[50].

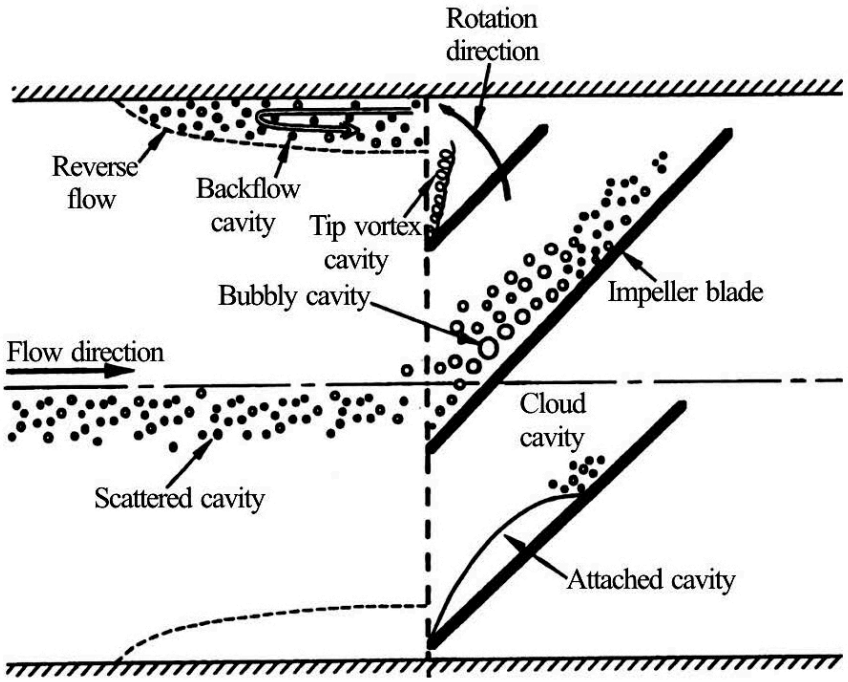

FIGURE B.3 – Different types de cavitation dans les pompes[51]

Coutier-Delgosha et al.[68] ont mené une analyse numérique pour étudier les caractéristiques d'un inducteur à quatre pales dans des conditions avec et sans cavitation. Guo et al.[69] ont démontré que le nombre de pales sur l'inducteur influence significativement la hauteur manométrique de la pompe et sa résistance à la cavitation. Selon leurs résultats expérimentaux, un inducteur à trois pales surpasse les inducteurs à deux ou quatre pales en termes d'efficacité, de pression et de résistance à la cavitation. Bakir et al.[72] ont réussi à développer un modèle de cavitation diphasique pour les inducteurs et l'ont validé par des tests expérimentaux. Leur modèle a montré un bon accord et une corrélation avec les résultats expérimentaux en termes de chute de pression et d'identification des poches de cavitation. L'inducteur, conçu avec trois pales, un diamètre extérieur de 235 mm, un jeu à la pointe de 0,4 mm, et une vitesse de rotation de 1450 tr/min, a démontré de solides performances dans des conditions de cavitation d'après les résultats expérimentaux. En raison des caractéristiques favorables de l'inducteur, une version plus petite de celui-ci a été utilisée dans cette thèse.

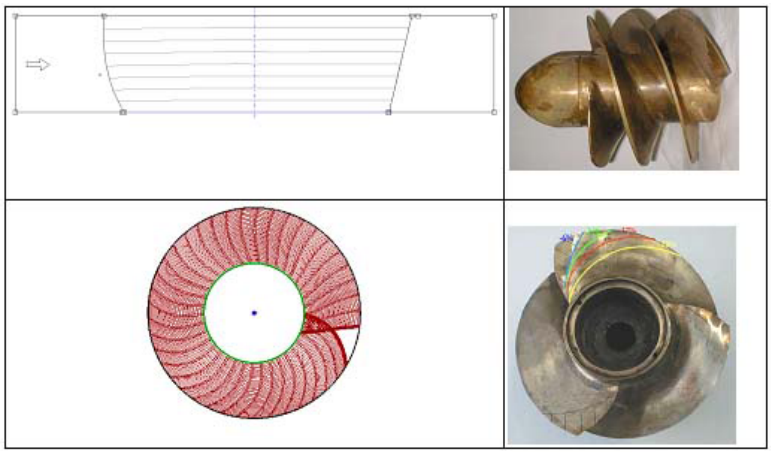

FIGURE B.4 – inducteur conçu par Bakir et al.[72]

Une étude expérimentale par visualisations menée par Xu et al.[75] sur un inducteur à haute vitesse a révélé le développement d'un vortex à l'entrée de l'inducteur, tournant à la moitié de la vitesse de l'inducteur. Le volume du vortex de recirculation diminue avec le débit et disparaît complètement pour des débits supérieurs à 30% du débit de conception. Campos-Amezcua et al.[76] ont étudié l'écoulement cavitant à travers un inducteur axial à deux pales, en considérant l'effet du jeu en périphérie. Sur la base de l'analyse de performance d'une pompe centrifuge avec des inducteurs à pas variable fonctionnant à différentes vitesses [39], il a été observé que la hauteur manométrique statique augmente avec la vitesse de rotation. Cependant, des vitesses de rotation plus élevées entraînent également une augmentation du NPSH, indiquant un risque plus élevé de cavitation dans la pompe.

Bien qu'il y ait eu beaucoup de recherches sur les turbomachines à rotation indépendante des rotors, telles que les ventilateurs, les turbines, les compresseurs et les pompes axiales, il existe peu de recherches sur les pompes centrifuges dotées à la fois d'inducteurs et de roues qui tournent indépendamment. Dans toutes les pompes précédemment étudiées dotées à la fois d'inducteurs et de roues, les deux composants ont partagent le même arbre. Cela signifie qu'ils ont toujours eu des vitesses de rotation et sens de rotation identiques. Cette thèse présente une approche novatrice en examinant une pompe centrifuge dans laquelle l'inducteur et la roue fonctionnent sur des arbres différents, leur permettant de tourner indépendamment. Cette configuration unique offre l'occasion d'étudier divers paramètres, tels que le rapport de vitesse de rotation entre l'inducteur et la roue et la direction de rotation de l'inducteur. De plus, avec intégration innovante d'un d'un systéme de dépelacement dans le banc d'essai expérimental, la recherche explore en outre la distance entre l'inducteur et la roue.

B.2 Matériels et méthodes

B.2.1 Introduction

Pour étudier une pompe capable de faire tourner l'inducteur et la roue indépendamment, la première étape consiste à concevoir un inducteur et une roue appropriés. Une fois les conceptions de l'inducteur et de la roue finalisées, l'étape suivante consiste à concevoir et à construire un banc d'essai expérimental novateur pouvant réaliser la rotation indépendante de ces deux rotors. Cette section explore les procédures de conception pour les roues, les inducteurs, et le banc d'essai expérimental. Ensuite, les procédures pour réaliser à la fois des tests sans cavitation et avec cavitation sont décrites. Après cela, la précision et la répétabilité des résultats du banc d'essai expérimental sont détaillées. Enfin, le processus de validation pour le test de similitudes de la pompe est fourni.

B.2.2 Conception de la roue et de l'inducteur

Le processus de conception d'une pompe commence par la création de la roue en fonction de certaines exigences. Cette section présente la méthodologie de conception de la roue, en mettant en évidence ses caractéristiques hydrodynamiques et physiques. Dans le cadre de cette recherche, une roue centrifuge fermée avec 6 pales a été développée. La conception préliminaire de la roue a été réalisée à l'aide des outils logiciels MFT et 3D Turbo, produits du *Laboratoire d'Ingénierie des Fluides et des Systèmes Énergétiques (LIFSE)*. La conception finale de la roue a été développée en utilisant le logiciel CATIA, qui a également aidé à produire son plan. En utilisant ce logiciel, le disque et la couronne ont été conçus pour assurer la compatibilité avec la roue. La conception de la roue est configurée pour un débit de $40\,\mathrm{m}^3/\mathrm{h}$ (Q_n) et une pression de $560\,\mathrm{mbar}$ (P_n) à son point nominal de fonctionement (BEP), avec une vitesse de rotation de $2000\,\mathrm{tr/min}$.

Le tableau B.1 présente les caractéristiques géométriques de la roue centrifuge. Les paramètres D_1, b_1, et β_1 correspondent respectivement au diamètre d'entrée des aubes, à la largeur d'entrée des aubes et à l'angle des aubes à l'entrée. De même, D_2, b_2, et β_2 correspondent respectivement au diamètre de sortie des aubes, à la largeur de sortie des aubes et à l'angle des aubes à la sortie.

TABLE B.1 – Caractéristiques géométriques de la roue centrifuge

Paramétres	Nombre de pales	D_1	b_1	β_1	D_2	b_2	β_2
Valeurs	6	67.6 mm	23.3 mm	68.9°	134.2 mm	17.6 mm	70°

La figure B.5 montre la roue centrifuge fermée à six pales, fabriquée à l'aide d'une imprimante stéréolithographique (imprimante SLA). Une imprimante SLA est un type spécifique d'imprimante 3D qui utilise la technique de stéréolithographie pour créer des objets tridimensionnels à partir de résine liquide. Dans ce cas, le procédé d'impression a utilisé de la résine standard noire, connue pour ses excellentes propriétés mécaniques et sa finition de surface de haute qualité, toutes deux cruciales pour assurer le bon fonctionnement de la roue. La méthode d'impression 3D a la capacité de produire des objets de géométrie complexe, tels que des roues, avec précision et une grande résistance en peu de temps.

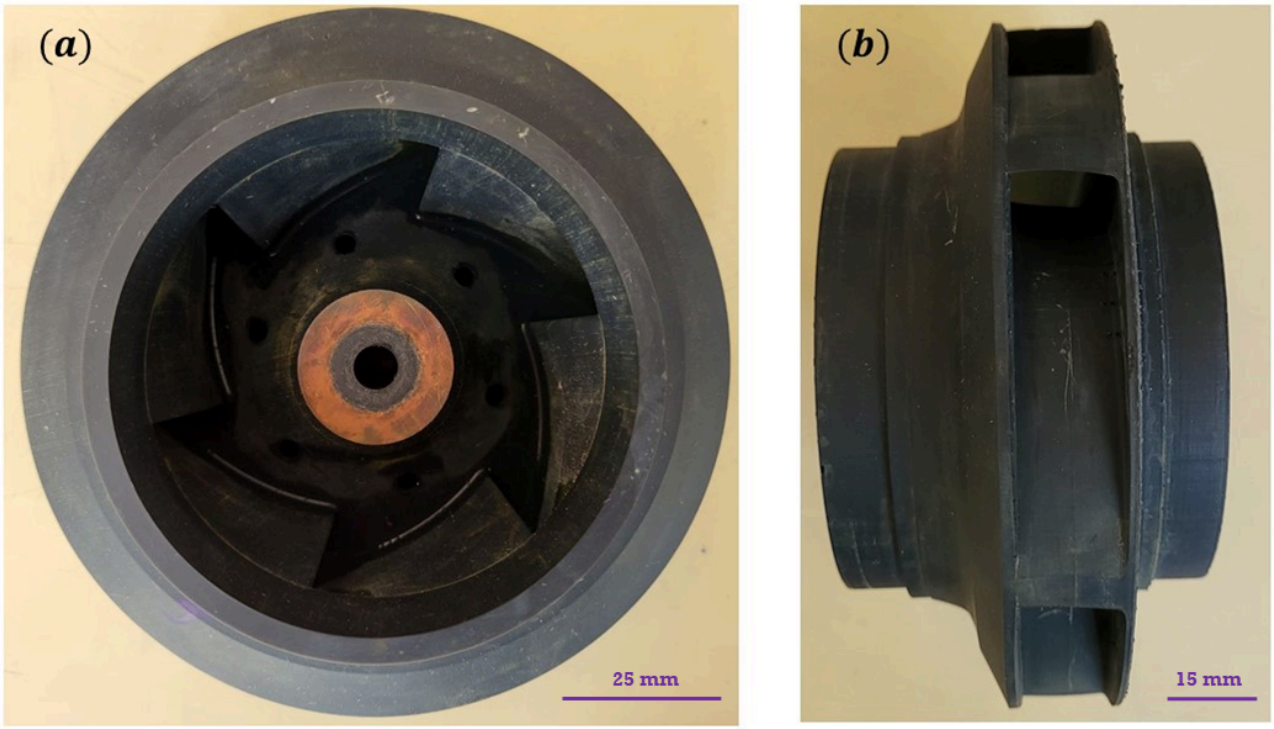

FIGURE B.5 – Vue de (a) face et (b) de coté de la roue centrifuge fabriqué par méthode SLA.

Après avoir complété la conception de la roue, il est nécessaire de concevoir l'inducteur afin de l'adapter aux caractéristiques de la roue. La conception de l'inducteur est dérivée des modifications apportées à l'inducteur discuté dans l'article de Bakir et al.[72]. Le tableau B.2 présente les caractéristiques géométriques de l'inducteur, où R_1, R_2, θ, S_h et S_t représentent respectivement le rayon interne, le rayon externe, l'angle de balayage, la solidité du moyeu et la solidité de la pointe de l'inducteur.

TABLE B.2 – Caractéristiques géométriques de l'inducteur

Paramétres	Nombre du pales	R_1	R_2	θ	S_h	S_t
Valeurs	3	12 mm	39 mm	62°	3.8	2.15

Pour adapter les caractéristiques de l'inducteur à celles de la roue centrifuge, l'inducteur est conçu pour atteindre son rendement optimal à un débit de 40 m^3/h (Q_n) lorsqu'il tourne à une vitesse de 2500 tr/min. Cela correspond au point nominal de fonctionnement. Le champ caractéristique de l'inducteur, ainsi que les détails concernant sa pression et son rendement, seront discutés dans le chapitre suivant.

Pour réaliser la rotation inversée de l'inducteur tout en conservant ses caractéristiques, seuls les angles des pales ont été inversés. En conséquence, les inducteurs co-rotatifs et contra-rotatifs présentent des caractéristiques de performance identiques. Une comparaison de ces deux types d'inducteurs, qui fonctionnent dans des directions opposées mais avec les mêmes caractéristiques de performance, peut être vue sur la Figure B.6.

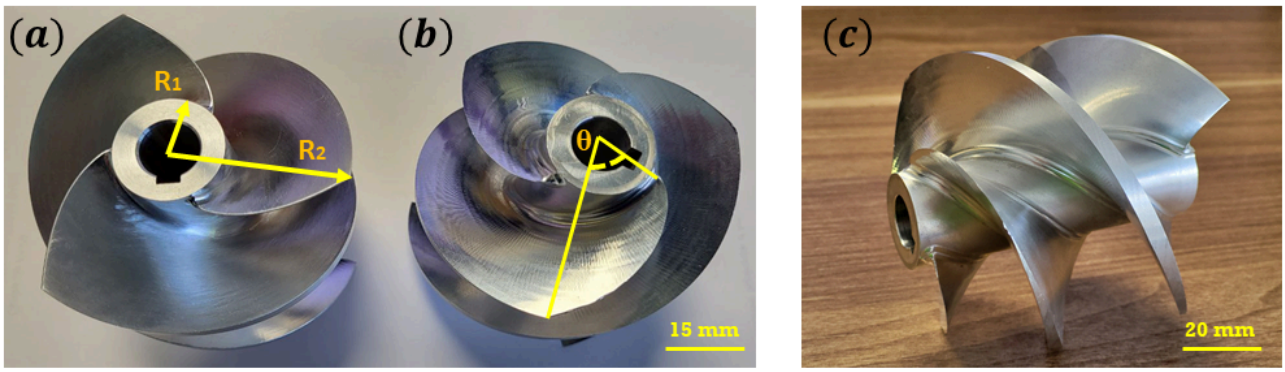

FIGURE B.6 – Vue de face (a) l'inducteur contra-rotatif et (b) l'inducteur co-rotatif inducteurs and (c) vue de coté du l'inducteur co-rotatif.

B.2.3 Description du banc d'essai

Après avoir finalisé la conception de la roue et de l'inducteur, un nouveau banc d'essai expérimental a été développé pour le système de pompe. Ce banc d'essai intègre des caractéristiques uniques qui permettent aux deux rotors d'être actionnés individuellement et d'être positionnés à des distances variables l'un de l'autre. L'ensemble du banc d'essai est divisé en deux sections principales : la section de la roue et la section de l'inducteur. Chacune d'entre elles a été conçue séparément avant d'être combinées pour former le banc d'essai complet (Figure B.7).

La section de la roue est une partie intégrante du système global. Cette section est alimentée par un moteur électrique Dietz de 30 kW, qui entraîne la roue pour tourner jusqu'à 20 000 tr/min. Le moteur, assure des performances constantes et efficaces. L'arbre est conçu pour se connecter directement à la roue, pour la maintenir la roue en place et assurer son fonctionnement sans heurt. Cet arbre est maintenu en position et soutenu par deux roulements. Chaque roulement joue un rôle unique : l'un a la capacité de supporter à la fois des charges radiales et axiales, assurant la stabilité de l'arbre pendant le fonctionnement. L'autre roulement, en bronze auto-lubrifiant, est apte à fonctionner dans l'eau, réduisant le besoin de maintenance constante et assurant la durée de vie du roulement.

En revanche, la section de l'inducteur, légèrement plus petite en échelle, est alimentée par un moteur ABB de 4 kW. Ce moteur est utilisé pour faire tourner l'inducteur jusqu'à 3000 tr/min. Tout comme la section de la roue, un arbre est utilisé ici pour entraîner l'inducteur. Cet arbre est également soutenu par deux roulements. Ces roulements reflètent les spécifications de ceux de la section de la roue, assurant l'uniformité dans la conception et la fonctionnalité. Assurer le scellage fin et les connexions entre les composants statiques sont réalisés à l'aide de joints toriques. Ces joints toriques sont personnalisés et calculés aux dimensions exactes de chaque pièce fixe pour assurer l'étanchéité du système. Pour les pièces rotatives, tant dans les sections de l'inducteur que de la roue, des joints mécaniques entrent en jeu sur les arbres. En général, avec une pression de fluide accrue, ces joints offrent une meilleure étanchéité. Cependant, dans ce système, l'inducteur est placé en amont de la roue, l'exposant au côté basse pression du système. Cette position unique fait de l'étanchéité pendant la rotation de l'inducteur un défi. Pour résoudre ce problème, un design innovant a été intégré : le joint mécanique reste légèrement pressurisé. Ce design offre une étanchéité supérieur et assure qu'il n'y a pas de fuite de la partie de scellage mécanique de l'inducteur mais provoque une consommation d'énergie plus élevée du moteur de l'inducteur, réduisant légèrement son efficacité. La force de rotation des moteurs est transmise aux arbres par des accouplements à ressort, qui ont la capacité de neutraliser un léger désalignement et une déviation angulaire.

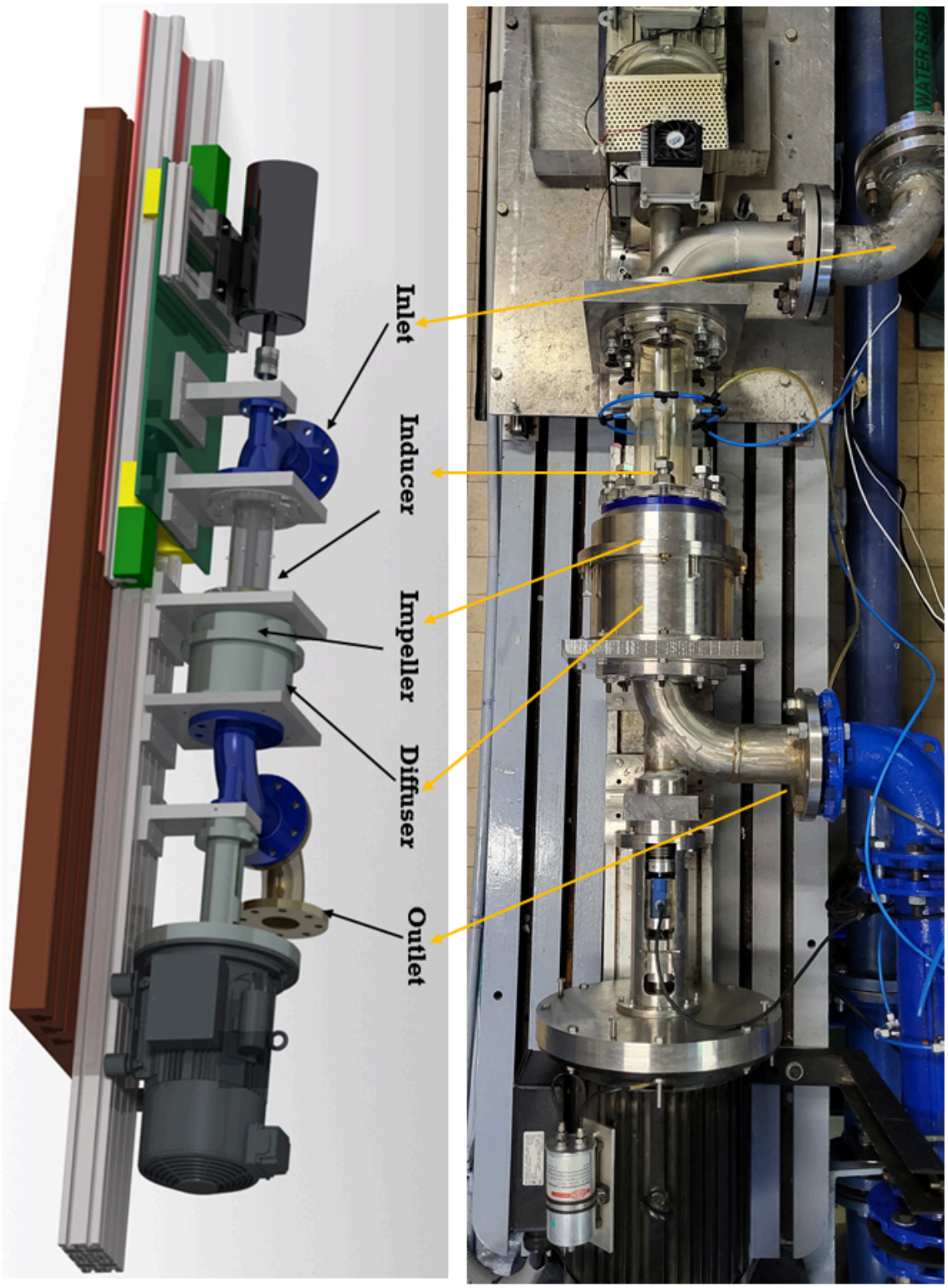

FIGURE B.7 – Schéma et photographie du banc d'essai expérimental conçu

Comme le montre la Figure B.8, le banc d'essai est conçu pour fonctionner dans un circuit fermé qui inclut un réservoir d'eau, une pompe à vide et un débitmètre. Le réservoir a un volume de 1000 litres et est équipé de deux manomètres pour mesurer la pression positive et négative. De plus, il y a une vanne d'entrée pour remplir le réservoir, une vanne connectée à l'air atmosphérique pour réguler la pression du système, et une vanne pour connecter la pompe à vide. Une pompe à vide Edward d'une capacité de pompage de 17,1 m^3/h a été utilisée pour réduire la pression du système, capable de la réduire jusqu'à 0,007 mbar. La Figure B.8 indique la direction de l'écoulement dans le système. Deux vannes sont situées à l'entrée et à la sortie pour réguler le débit et un débitmètre est installé en amont de la vanne de sortie pour mesurer le débit.

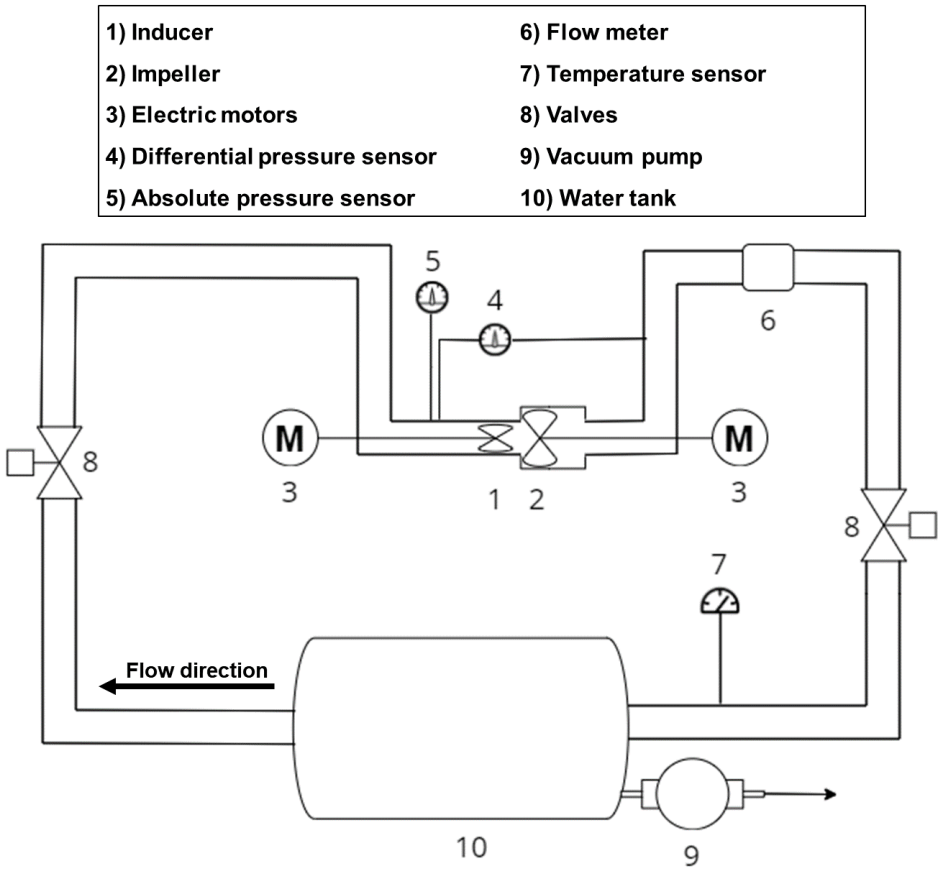

FIGURE B.8 – Banc d'éssai et circuit

B.3 Caractéristiques de la pompe en condition de non-cavitation

B.3.1 Caractéristiques de la roue et de l'inducteur

La Figure B.9 présente les caractéristiques une roue centrifuge tournant à 2000 tr/min ($N_2 = 2000$ tr/min). Le débit pour lequel la roue offre le rendement le plus élevé est appelé le débit nominal (Q_n). Pour normaliser les résultats, la pression correspondant à Q_n est également connue sous le nom de pression nominale (P_n), et tous les débits sont normalisés en les divisant par le débit nominal, tandis que toutes les pressions sont divisées par la pression nominale. $Q_n = 40$ m$^3/h$ et $P_n = 560$ mbar. De plus, le rendement maximal atteignable de la pompe est de 74%.

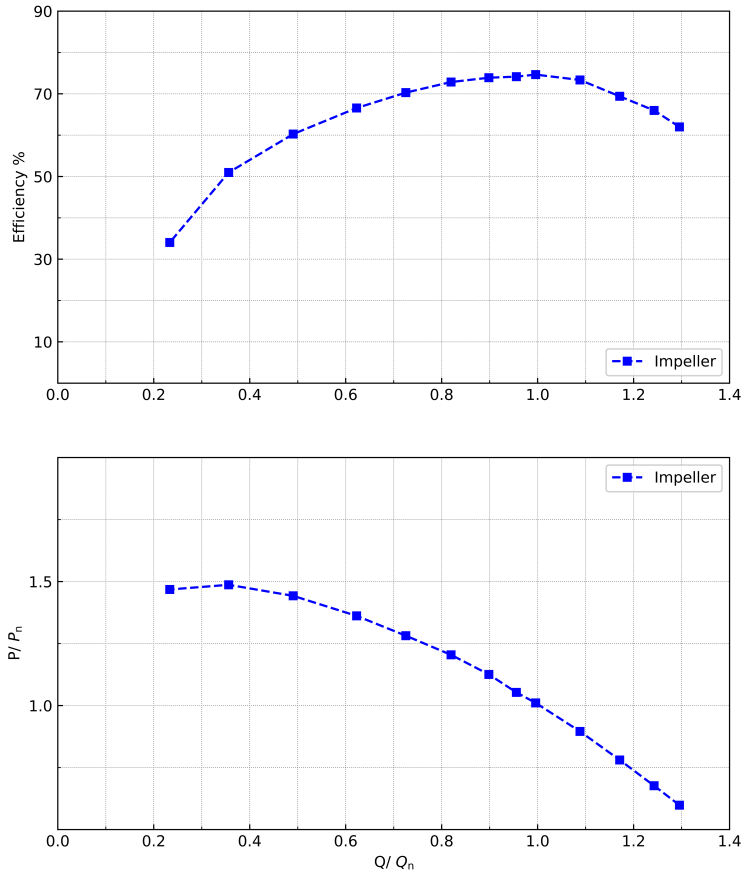

FIGURE B.9 – Résultats expérimentaux des caractéristique de la roue ($N_2 = 2000$ tr/min)

La Figure B.10 montre les caractéristiques de l'inducteur fonctionnant à une vitesse de 2500 tr/min ($N_1 = 2500$ tr/min). Le rendement maximal de l'inducteur, qui est significativement inférieur à celui

de la roue, est de 34%. La principale raison de cette baisse d'efficacité est la conception de l'inducteur, qui vise à prévenir la cavitation dans la roue. De plus, la forte compression du joint mécanique dans la section de l'inducteur contribue à la réduction de l'efficacité. En règle générale, les joints mécaniques utilisés pour sceller l'arbre sont positionnés en aval du rotor et sont comprimés par la pression de l'eau. Cependant, dans ce système particulier, en raison de la position de l'inducteur en amont de la roue principal, le joint mécanique subit une pression pardéfaut. En conséquence, cette disposition assure l'étanchéité du système mais diminue l'efficacité.

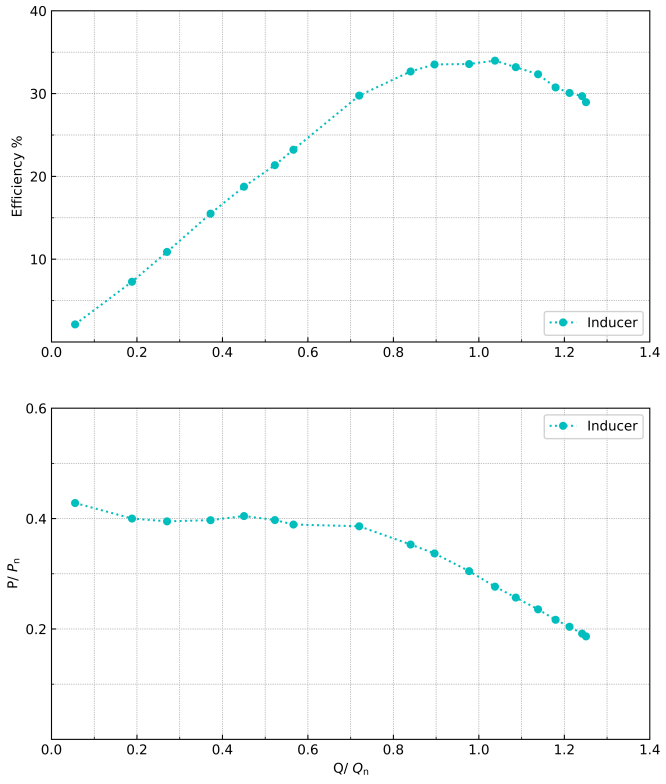

FIGURE B.10 – Résultats expérimentaux des caractéristique de l'inducteur ($N_1 = 2500$ tr/min)

B.3.1.1 Effet du rapport de vitesse

La Figure B.11 montre que la différence de pression entre $N_1 = 2900$ tr/min et $N_1 = 2000$ tr/min diminue avec des débits plus élevés. Néanmoins, il convient de noter que, malgré cette observation,

une augmentation de la vitesse de l'inducteur a toujours un impact positif sur la pression globale. La relation entre l'efficacité et la vitesse de l'inducteur indique que, bien que l'augmentation de la vitesse de l'inducteur augmente la pression, cela peut avoir un effet contradictoire sur l'efficacité. Dans la région de faible débit (LFR), l'efficacité est presque la même pour $N_1 = 2000$ tr/min et $N_1 = 2500$ tr/min, mais elle diminue pour $N_1 = 2900$ tr/min. À mesure que le débit s'approche du point nominal, l'efficacité de $N_1 = 2000$ tr/min et $N_1 = 2900$ tr/min devient similaire, tandis que $N_1 = 2500$ tr/min reste légèrement supérieure. Dans la région de débit élevé (HFR), il est clair que l'efficacité de $N_1 = 2900$ tr/min et $N_1 = 2500$ tr/min est supérieure à $N_1 = 2000$ tr/min.

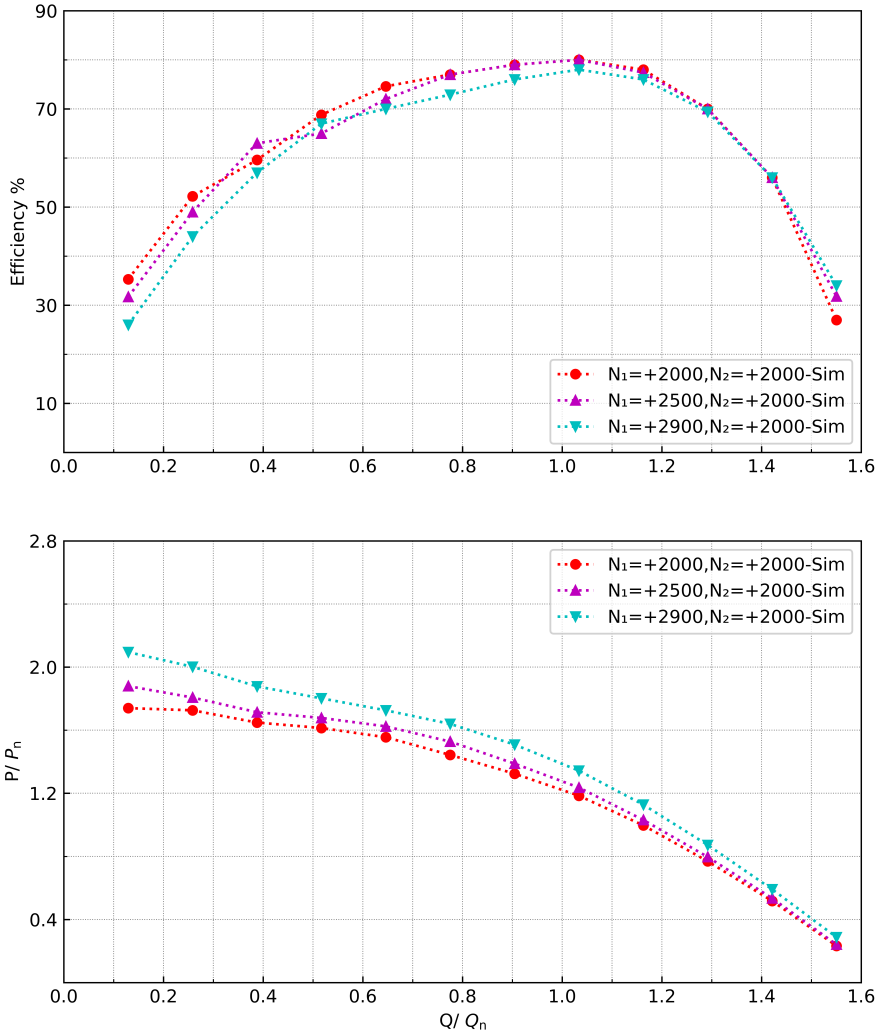

FIGURE B.11 – Caractéristique de la pompe avec différentes vitesses de rotation de l'inducteur (N_1) en co-rotation avec une valeur fixe de la vitesse de rotation de la roue ($N_2 = 2000$ tr/min)

La Figure B.12 montre l'influence de la vitesse de l'inducteur sur les caractéristiques de la pompe lorsqu'elle fonctionne en mode contra-rotatif. Les tendances observées en termes de variations d'efficacité et de pression avec les changements de débit sont similaires à celles observées en mode co-rotation. Cependant, il est évident que l'impact de la vitesse de l'inducteur sur la pression de la pompe est plus prononcé en mode contra-rotatif par rapport au mode co-rotation. Cet effet peut être constaté à partir de la différence significative dans les diagrammes de pression. Par exemple, au point nominal et pour $N_1 = -2900$ tr/min, le mode contra-rotatif génère une pression significativement plus élevée que la co-rotation, tout en maintenant la même efficacité. Dans la région HFR, la pression en mode contra-rotatif est toujours affectée par la vitesse de l'inducteur, contrairement au mode co-rotation. Cette différence provient de la pré-rotation inverse du fluide causée par la rotation inverse de l'inducteur en mode contra-rotatif.

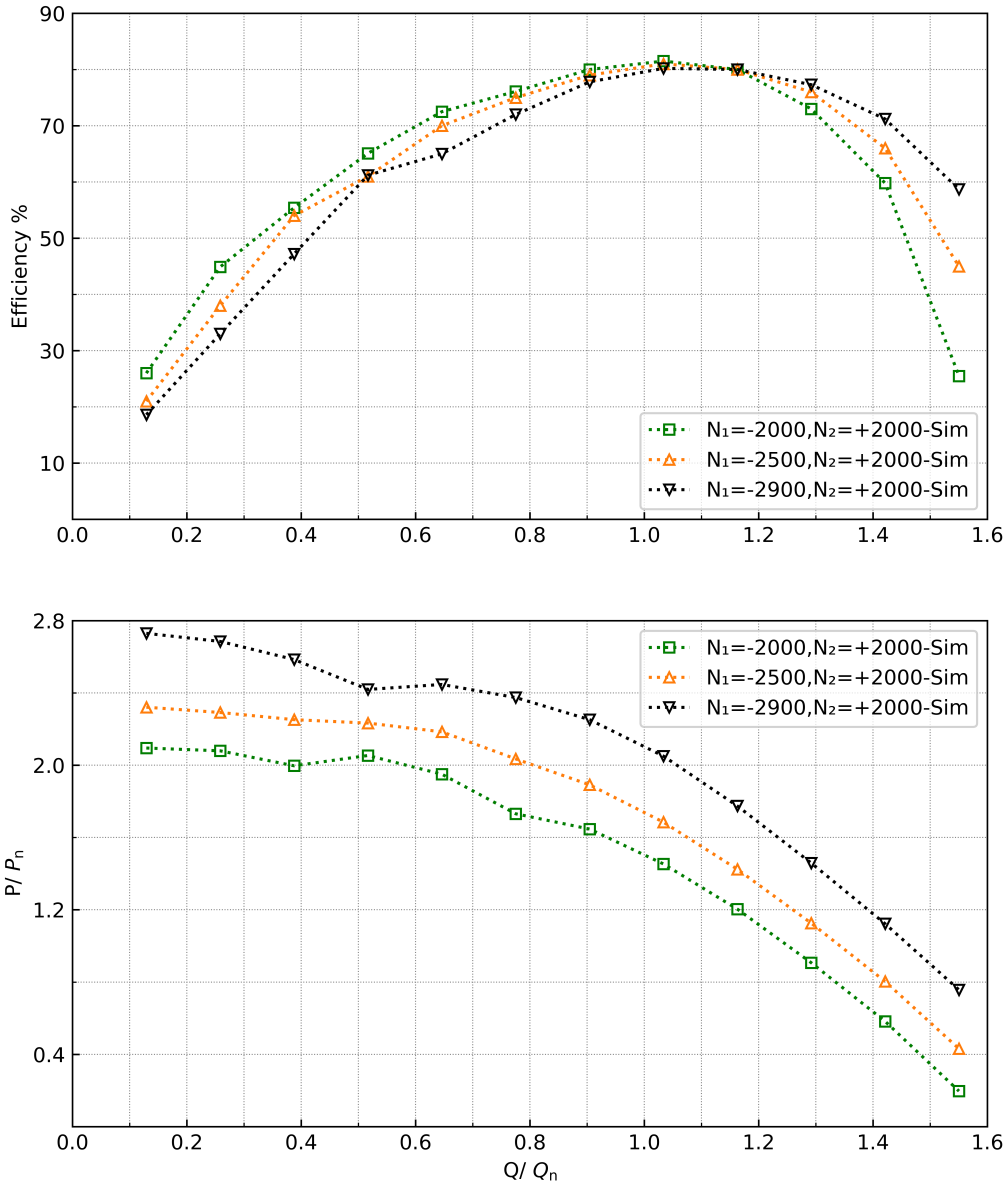

FIGURE B.12 – Caractéristique expérimantales de la pompe avec différentes vitesse de rotationde l'inducteur e contra-rotation avec $N_2 = +2000$ tr/min

B.3.1.2 Effet de la distance entre les rotors en condition de non cavitantes

L'analyse de l'impact des variations de la distance (L) entre l'inducteur et la roue sur les caractéristiques de la pompe montre un impact minimal à la fois sur la pression et sur l'efficacité de la pompe. La Figure B.13 illustre cela en montrant les résultats pour la pompe fonctionnant en mode contra-rotatif à une vitesse de 2000 tr/min, pour des distances de 20 mm et 80 mm entre les rotors.

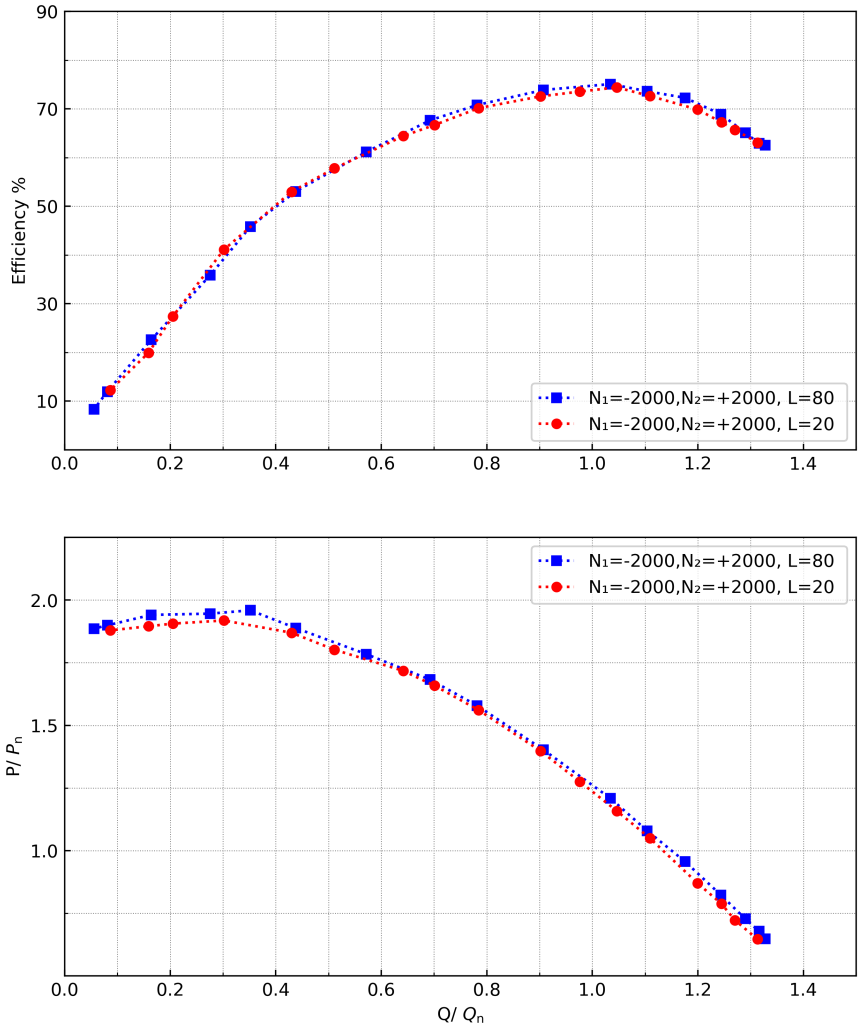

FIGURE B.13 – Effet de la distance entre l'inducteur et la roue ($L = 20$ mm, $L = 80$ mm) sur les caractéristique de la pompe en mode contra-rotatif ($N_1 = -2000$ tr/min, $N_2 = +2000$ tr/min)

B.3.2 Analyse CFD des caractéristiques de la pompe

Les résultats des simulations numériques de la pression et de l'efficacité de la pompe en co-rotation à différentes vitesses de l'inducteur sont illustrés dans la Figure B.14. Les données indiquent que lorsque la vitesse de l'inducteur est augmentée à 2500 tr/min, une légère augmentation de la pression est observée. Augmenter davantage la vitesse à 2900 tr/min entraîne une augmentation plus prononcée de la pression. Cette augmentation de la pression est particulièrement notable dans les régions de faible débit, avec des améliorations de la pression allant jusqu'à 30%. Cependant, à ce débit, il y a également une diminution de 10% de l'efficacité. Au débit nominal, l'augmentation de la vitesse de l'inducteur

entraîne une augmentation de la pression de la pompe, accompagnée d'une légère baisse de l'efficacité. À des débits élevés, l'augmentation de la vitesse de l'inducteur se traduit par plus de pression et d'efficacité ensemble.

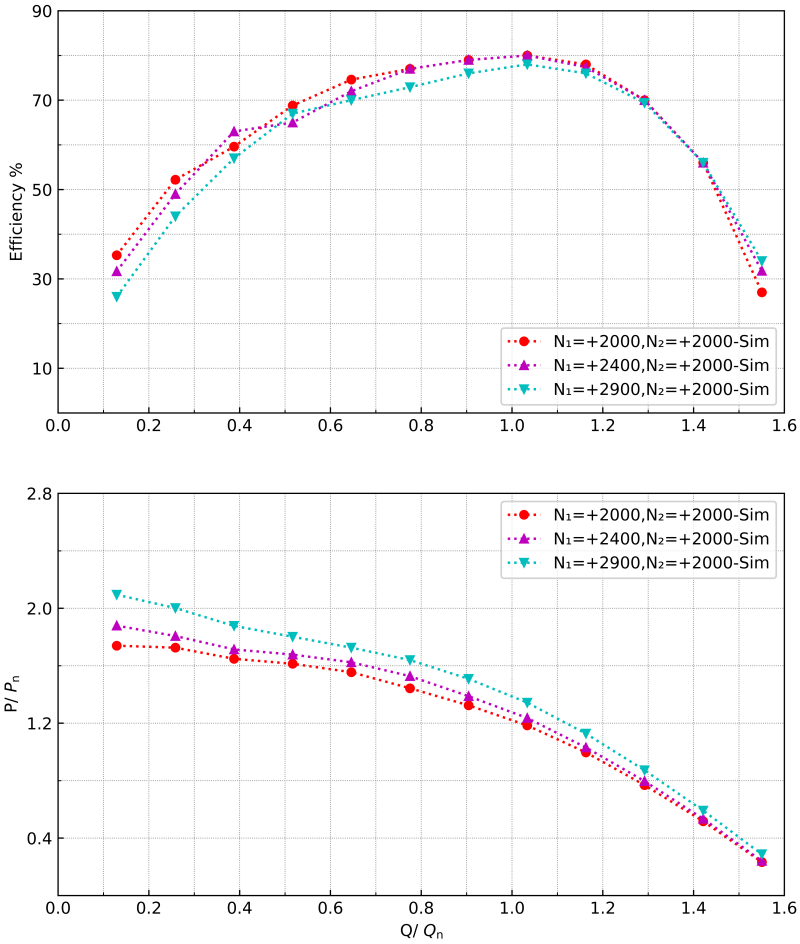

FIGURE B.14 – Caractéristique de la pompe obtenues par simulation numérique pour différentes vitesse du rotation de l'inducteur en co-rotation

La figure B.15 montre les résultats de la simulation concernant l'impact de l'augmentation de la vitesse de l'inducteur sur les caractéristiques de la pompe en contra-rotation. Il est évident qu'augmenter la vitesse de l'inducteur dans ce mode a une influence significative sur les caractéristiques de la pompe par rapport au mode co-rotatif. En conséquence, en augmentant la vitesse de l'inducteur à 2900 tr/min, le rapport de pression à $\frac{Q}{Q_n} = 1$ passe de $\frac{P}{P_n} = 1.5$ à plus de $\frac{P}{P_n} = 2.1$, ce qui est significativement plus élevé que la valeur du mode co-rotatif d'environ $\frac{P}{P_n} = 1.2$.

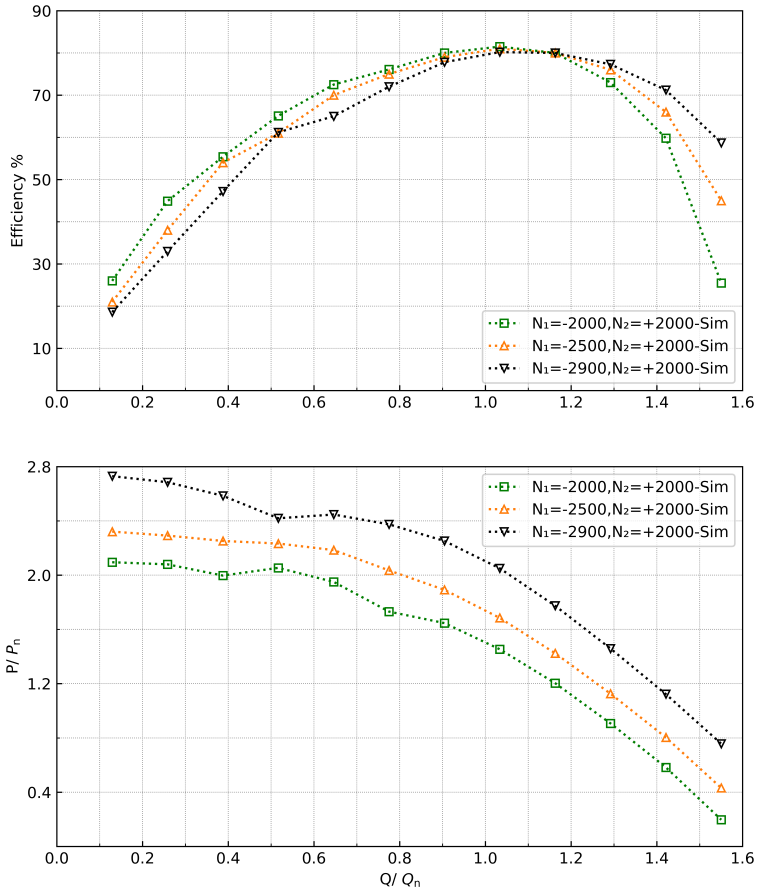

FIGURE B.15 – Caractérstique de la pompe obtenues par simulation numérique pour différentes vitesse de rotation de l'inducteur en contra-rotation.

La figure B.16 illustre la comparaison entre les résultats expérimentaux et numériques pour le mode contra-rotatif à $N_1 = -2500$ tr/min, $N_2 = +2000$ tr/min. Les résultats expérimentaux incluent à la fois les résultats des tests et les pertes mécaniques du système. Pour déterminer les pertes mécaniques résultant de composants tels que les roulements et les joints mécaniques, la roue et l'inducteur ont été retirés des arbres. Les arbres ont ensuite été tournés sans ces composants, et la consommation d'énergie de chaque section (inducteur et roue) a été mesurée. Cela a permis de calculer les pertes mécaniques causée par les roulements et les joints mécaniques dans le système. Les résultats expérimentaux et de simulation montrent une bonne corrélation, avec une différence d'environ 5%. Cette différence peut résulter de pertes supplémentaires dans le système expérimental, principalement la perte hydraulique. Les pertes hydrauliques est notable en raison de la présence de deux coudes à l'entrée et à la sortie de la pompe, ainsi que d'un support pour l'arbre de l'inducteur en amont. En raison du coût de calcul

élevé, la simulation ne prend pas en compte ces coudes et supports qui font partie du système. Par conséquent, une légère variation entre les résultats expérimentaux et les résultats de simulation est observée.

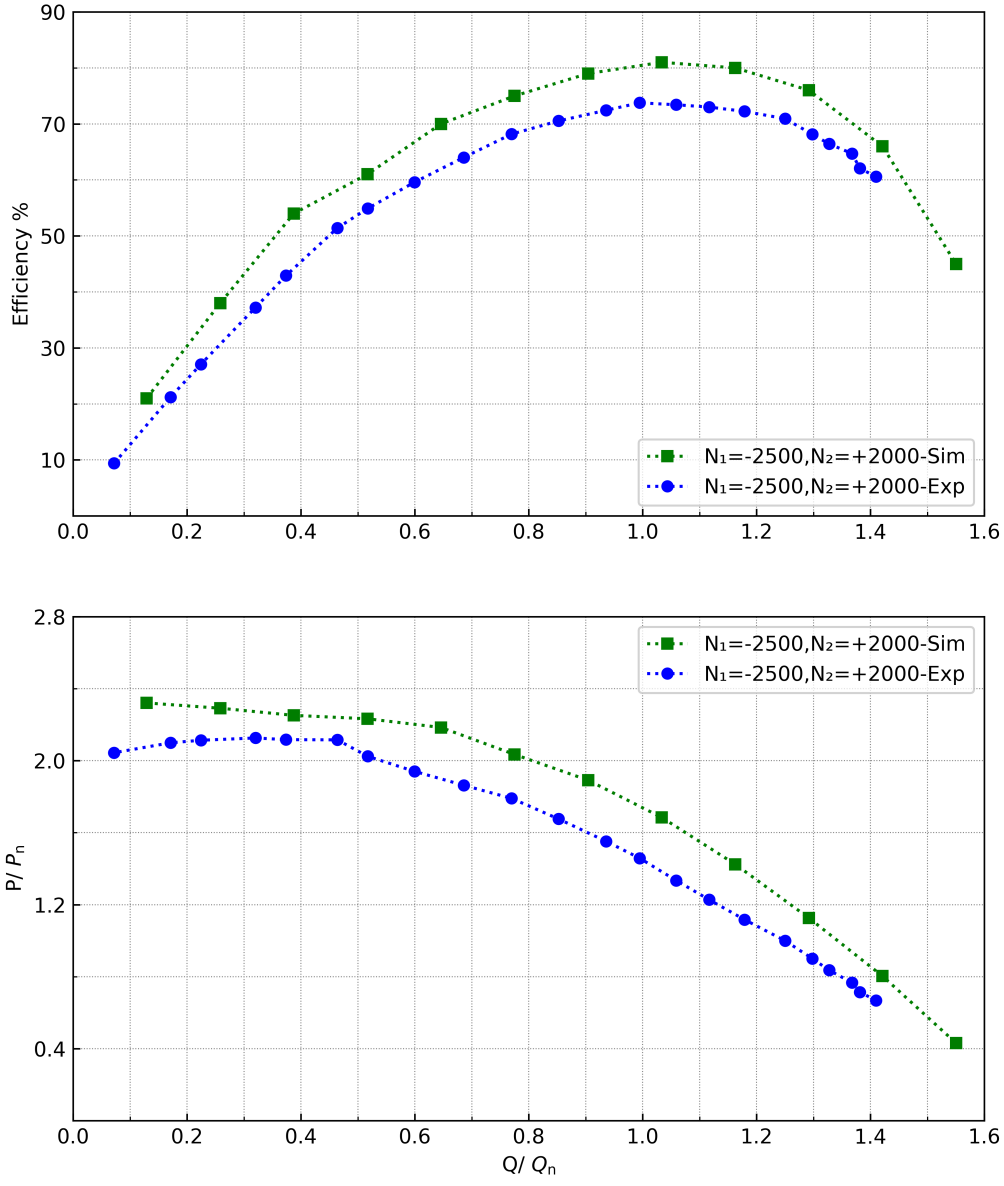

FIGURE B.16 – Résultats expérimentaux et numériques des caractéristique de la pompe en contra-rotation pour $N_1 = -2500$ tr/min, $N_2 = +2000$ tr/min

Dans la figure B.17, les triangles des vitesses pour les modes co-rotatif et contra-rotatif sont présentés. Le schéma représente divers paramètres : U représente la vitesse du rotor (soit la roue soit

l'inducteur) et est défini par $U = r\omega$ où r est la distance par rapport au centre de rotation et ω est la vitesse de rotation du rotor, V représente la vitesse absolue de l'écoulement et W représente la vitesse relative de l'écoulement.

Selon les équations d'Euler pour les turbomachines[85], la hauteur manométrique théorique H_{th} générée par la roue peut être déterminée en utilisant l'équation suivante :

$$H_{th} = \frac{U_4 V_{t4} - U_3 V_{t3}}{g} \tag{B.1}$$

où V_t représente la vitesse tangentielle de l'écoulement. L'écoulement sortant de l'inducteur est égal à l'écoulement entrant dans la roue, donc $V_{t2} = V_{t3}$ et en se basant sur le triangle des vitesses (Figure B.17), il est évident que dans le mode co-rotatif, U_3 et V_{t3} sont dans la même direction, résultant en une valeur positive pour $U_3 V_{t3}$, mais dans le mode contra-rotatif, la direction de V_{t3} est opposée à la direction de U_3 et l'équation ci-dessus devient l'équation suivante pour le mode contra-rotatif :

$$H_{th-CR} = \frac{U_4 V_{t4} + U_3 V_{t3}}{g} \tag{B.2}$$

Où H_{th-CR} représente la hauteur manométrique théorique de la pompe en mode contra-rotatif. La pression totale est plus élevée en mode contra-rotatif par rapport au mode co-rotatif.

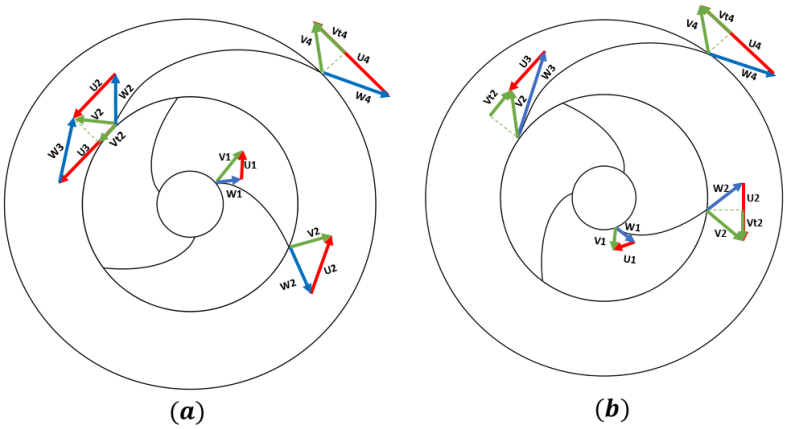

FIGURE B.17 – Triangle des vitesses pour (a) le mode co-rotatif et (b) le mode countra-rotatif.

B.4 Performances de cavitation de la pompe

La figure B.18 présente les performances de la pompe en termes de $NPSH$ pour trois points de fonctionnement spécifiés. On peut observer qu'à mesure que le débit augmente et que la pression de sortie de la pompe diminue, la cavitation se produit plus rapidement. Selon la figure B.18, $\frac{P}{P_n} = 0.7$, $\frac{P}{P_n} = 1$ et $\frac{P}{P_n} = 1.16$ correspondent respectivement à $\frac{Q}{Q_n} = 1.2$, $\frac{Q}{Q_n} = 1$ (débit nominal) et $\frac{Q}{Q_n} = 0.87$.

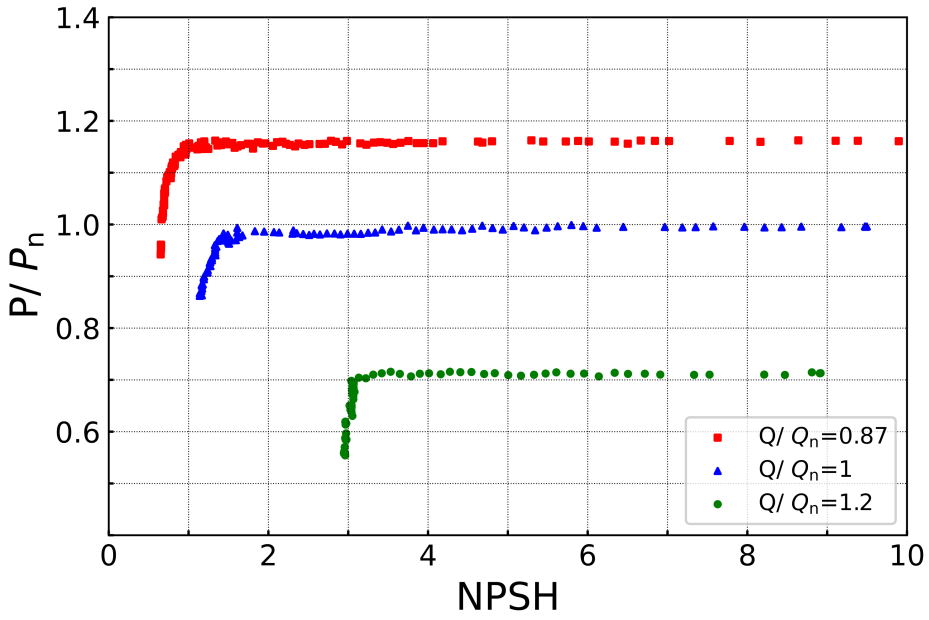

FIGURE B.18 – Performances de cavitation de la pompe pour différentes débits en co-rotation

B.4.1 Cavitation de l'inducteur et de la roue en mode co-rotatif

B.4.1.1 Effet du rapport de vitesse à $\frac{Q}{Q_n} = 0.87$

La figure B.19 illustre les performances de cavitation de la pompe lorsqu'elle fonctionne en mode co-rotatif, en présentant différentes vitesses d'inducteur. Comme on peut le voir, le changement de vitesse de l'inducteur affecte considérablement la cavitation de la pompe. Il est évident que la pompe subit une baisse de pression de 5% à $NPSH = 0.7\,\text{m}$ dans le cas où $N_1 = N_2 = 2000\,\text{tr/min}$ (points rouges). En augmentant la vitesse de l'inducteur à $2500\,\text{tr/min}$ (triangles bleus) et en réduisant la vitesse de la roue à $1994\,\text{tr/min}$ pour produire une pression similaire à l'état de $N_1 = N_2$, l'efficacité de la pompe contre la cavitation se réduit, de sorte qu'à $NPSH = 1.22\,\text{m}$, la pompe subit une baisse

de pression de 5%.

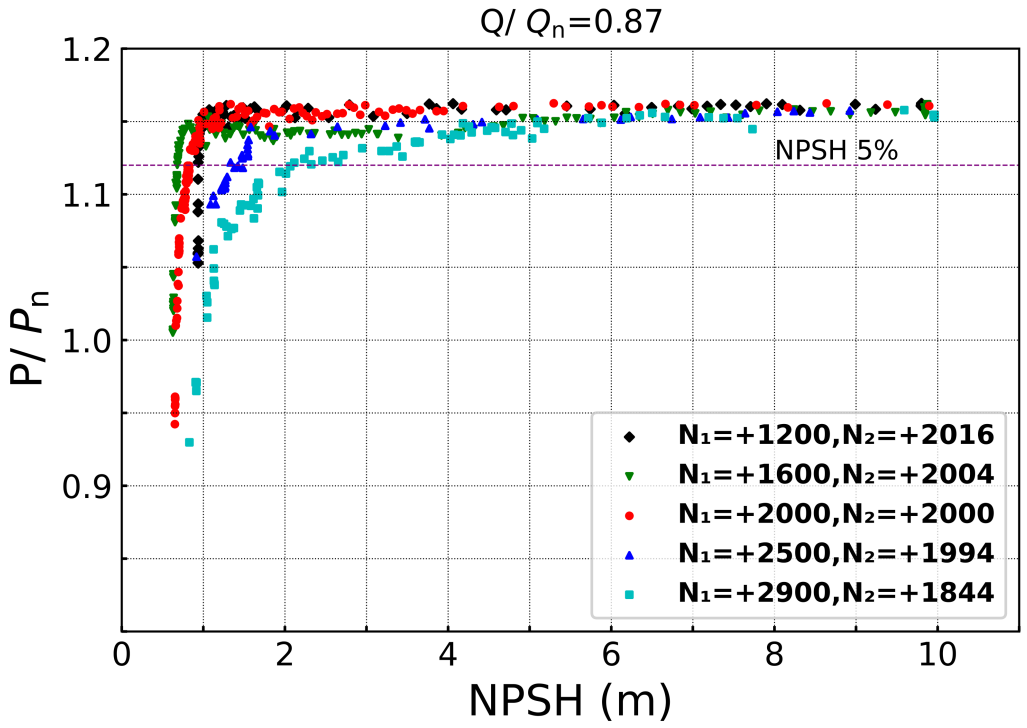

FIGURE B.19 – Performances de cavitation de la pompe par variation de la vitesse de l'inducteur en co-rotation pour $\frac{Q}{Q_n} = 0.87$

B.4.1.2 Effet du rapport de vitesses au débit nominal

Selon la Figure B.20, continuer à réduire la vitesse de l'inducteur à 2000 tr/min peut améliorer en douceur l'efficacité de la pompe contre la cavitation, provoquant une chute de pression de 5% à $NPSH = 1,25\,\text{m}$. Cependant, en abaissant davantage la vitesse de l'inducteur et en la ramenant à une vitesse inférieure à celle de la roue, ce processus s'inverse, provoquant une chute de pression de 5% à $NPSH = 1,35\,\text{m}$ pour une vitesse de 1600 tr/min. En mode co-rotatif, à des débits nominaux et élevés, une vitesse de 1200 tr/min pour l'inducteur a entraîné une baisse substantielle des performances de la pompe contre la cavitation. Par conséquent, cet état n'a pas fait l'objet d'investigations et d'analyses plus approfondies.

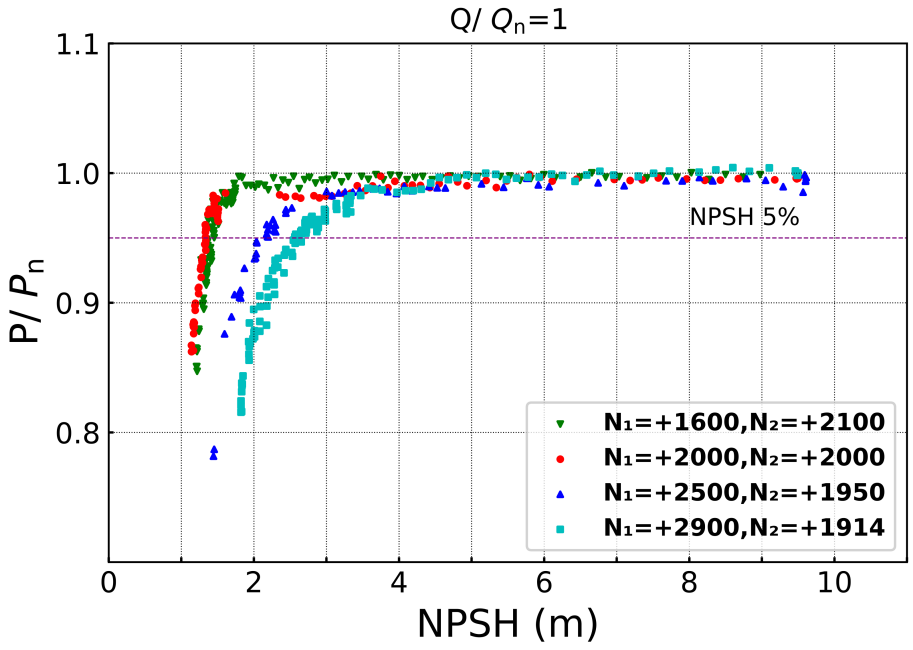

FIGURE B.20 – Performances de cavitation de la pompe par variation de la vitesse de l'inducteur en co-rotation pour $\frac{Q}{Q_n} = 1$

B.4.1.3 Effet du rapport de vitesses à $\frac{Q}{Q_n} = 1.2$

Par rapport aux deux débits précédents, l'impact des variations de vitesse de l'inducteur sur l'efficacité de la pompe contre la cavitation est nettement plus fort pour $\frac{Q}{Q_n} = 1.2$. Comme on peut le constater, la chute de pression pour l'inducteur à 1600 tr/min est rapide, et la pompe subit une chute de pression de 5% à $NPSH = 3.4\,\text{m}$. Cependant, l'efficacité contre la cavitation est améliorée en augmentant la vitesse de l'inducteur à 2000 tr/min dans la situation où l'inducteur et la roue tournent dans la même direction et à la même vitesse. Par conséquent, la chute de pression de 5% au sein de la pompe se produit à $NPSH = 2.96\,\text{m}$.

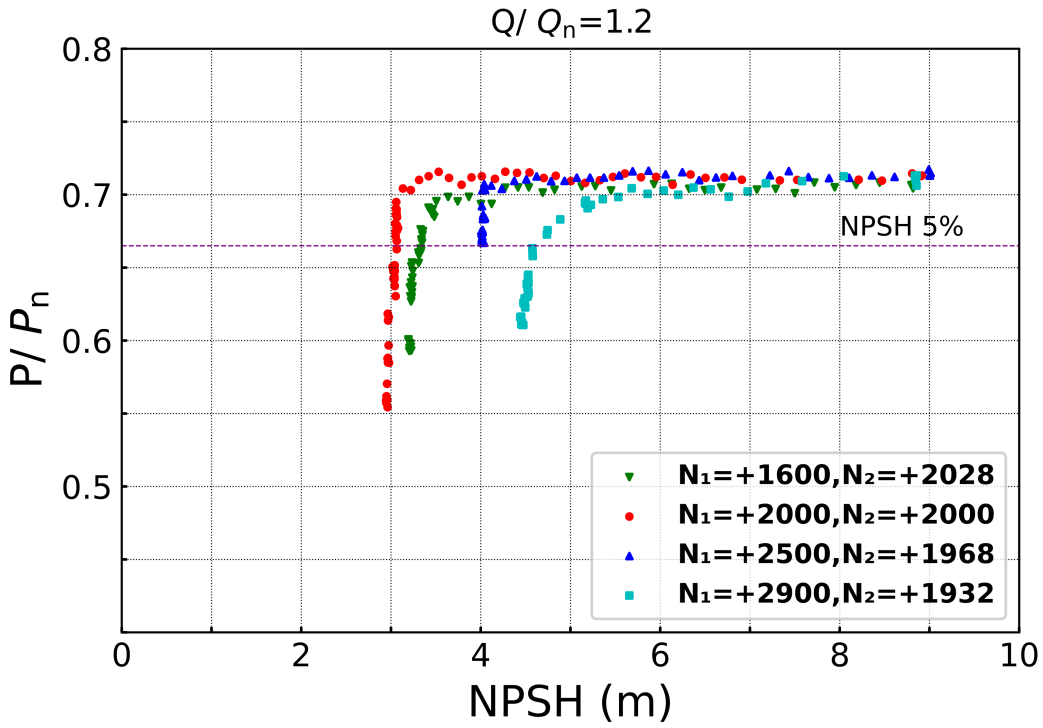

FIGURE B.21 – Performances de cavitation de la pompe par variation de la vitesse de l'inducteur en co-rotation pour $\frac{Q}{Q_n} = 1.2$

B.4.2 Cavitation de l'inducteur et de la roue en mode contra-rotatif

B.4.2.1 Effet du rapport de vitesses à $\frac{Q}{Q_n} = 0.87$

En observant la Figure B.22, il devient évident qu'à une vitesse de rotation de l'inducteur de 1200 tr/min, la pompe subit une diminution de 5% avec $NPSH = 0.83\,\text{m}$. De même, à la vitesse maximale de l'inducteur de 2900 tr/min, il y a une diminution de pression de 5% à $NPSH = 0.5\,\text{m}$. D'après la Figure B.22, les basses et hautes vitesses de l'inducteur améliorent l'efficacité de la pompe contre la cavitation. Entretemps, à des vitesses comme 1600, 2000 et 2500 tr/min, la chute de pression de 5% se produit autour de $NPSH = 0.35\,\text{m}$. De plus, la chute de pression locale à des vitesses de 1200 et 2900 tr/min commence à partir de $NPSH = 3\,\text{m}$.

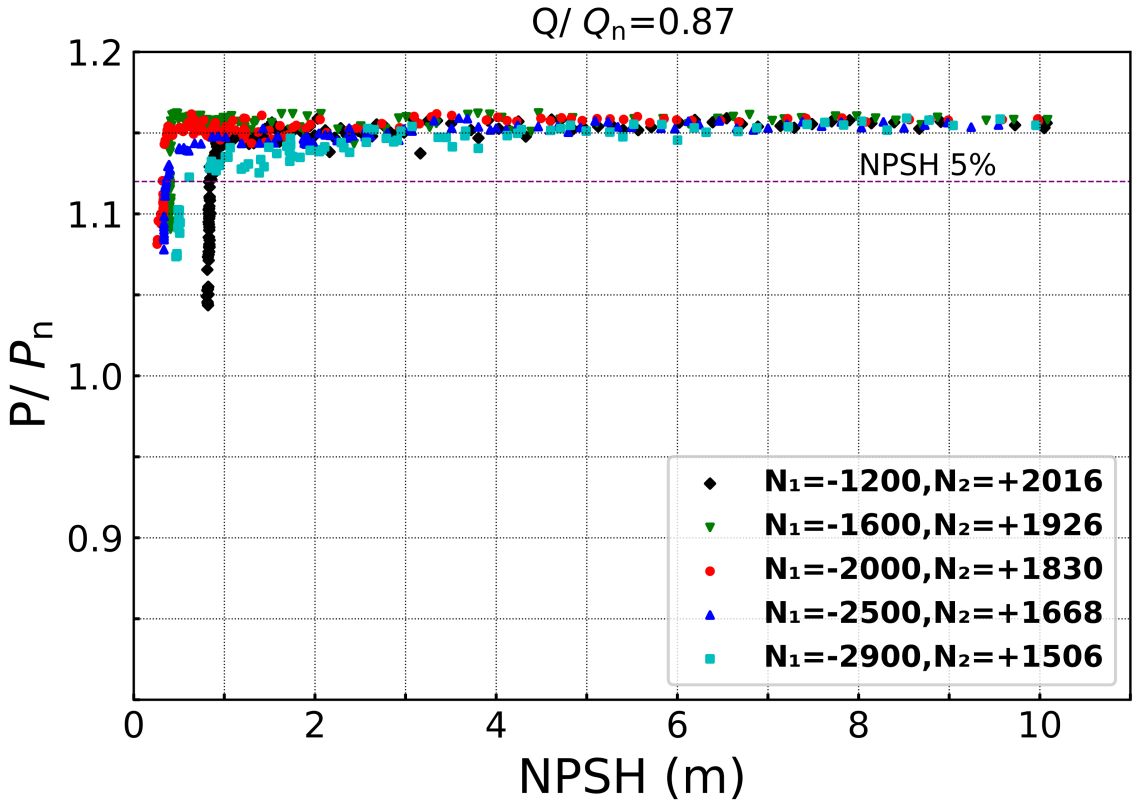

FIGURE B.22 – Performances de cavitation de la pompe par variation de la vitesse de l'inducteur en contra-rotation pour $\frac{Q}{Q_n} = 0.87$

B.4.2.2 Effet du rapport de vitesses au débit nominal

À mesure que le débit augmente pour atteindre le taux nominal, l'impact des variations de vitesse de l'inducteur sur la performance de la cavitation change, en particulier à des vitesses plus élevées. À une vitesse de l'inducteur de 2000 tr/min, on observe une chute de pression de 5% à $NPSH = 0.62\,\text{m}$. Lorsque la vitesse de l'inducteur est augmentée à 2500 tr/min, cette baisse de pression de 5% est observée à $NPSH = 0.52\,\text{m}$.

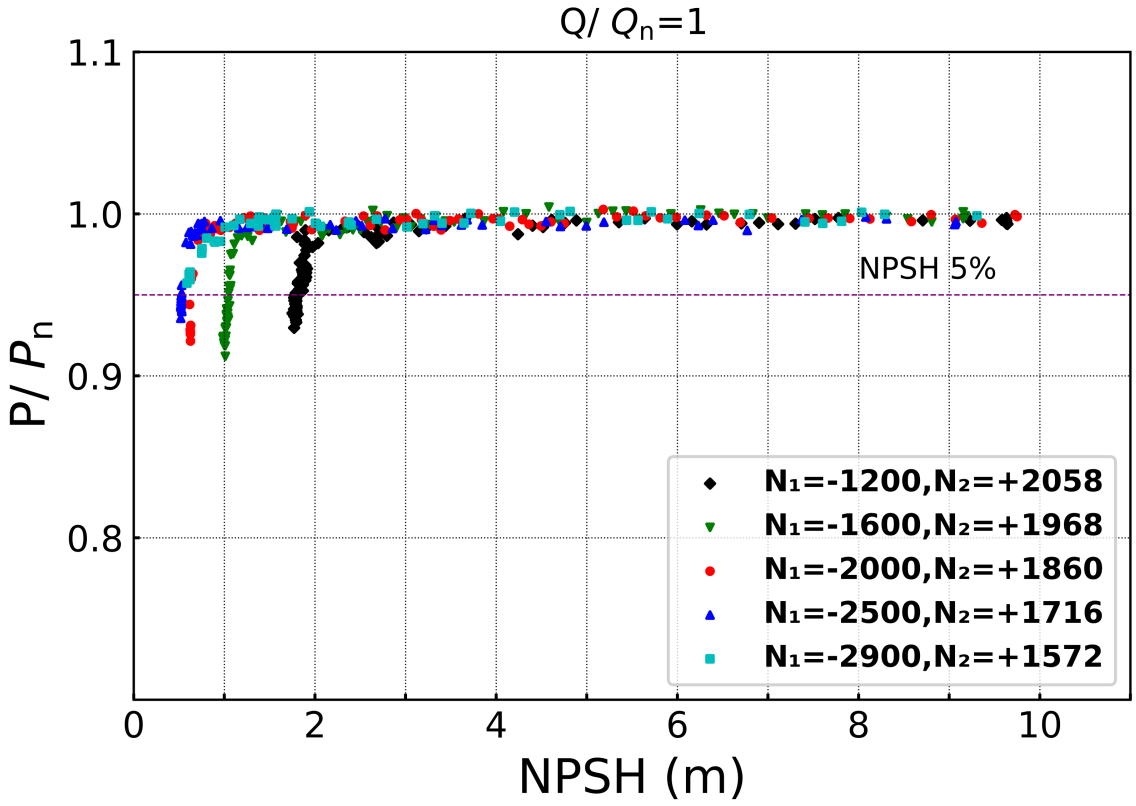

FIGURE B.23 – Performances de cavitation de la pompe par variation de la vitesse de l'inducteur en contra-rotation pour $\frac{Q}{Q_n} = 1$

B.4.2.3 Effet du rapport de vitesses à $\frac{Q}{Q_n} = 1.2$

La figure B.24 illustre comment les variations de la vitesse de rotation de l'inducteur influencent la performance de la cavitation de la pompe lorsqu'elle fonctionne en mode contra-rotatif à des débits élevés. Contrairement au paramétrage de co-rotation, l'augmentation de la vitesse de l'inducteur améliore de manière significative la performance de cavitation de la pompe. Lorsque l'inducteur tourne à 1200 tr/min, une chute de pression de 5% est observée à un $NPSH = 4.46\,\text{m}$. Cependant, lorsque la vitesse augmente à 1600 tr/min, cette valeur chute à 3.48 m. Il existe une corrélation positive notable entre la vitesse de l'inducteur et la performance de la cavitation : à 2000 tr/min, le $NPSH = 2.65\,\text{m}$, à 2500 tr/min, il est à 2.15, et remarquablement, à 2900 tr/min, la chute de pression de 5% correspond à un $NPSH = 1.53\,\text{m}$.

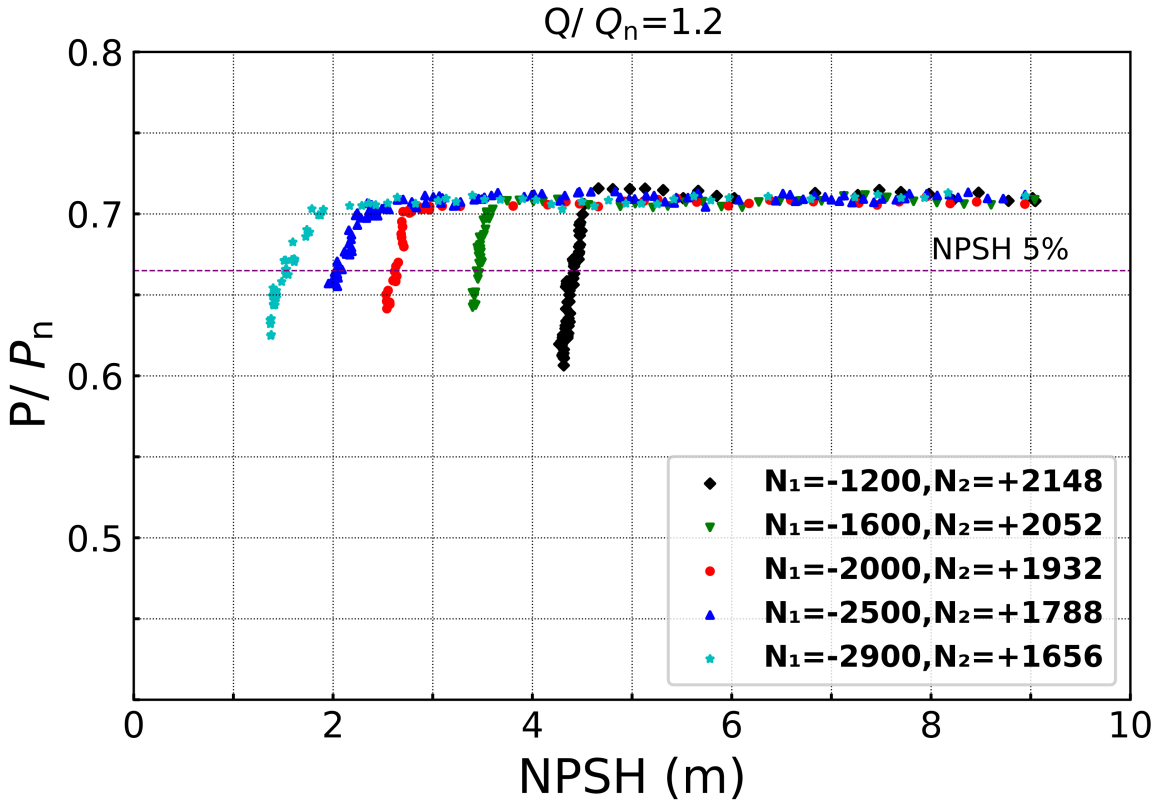

FIGURE B.24 – Performances de cavitation de la pompe par variation de la vitesse de l'inducteur en contra-rotation pour $\frac{Q}{Q_n} = 1.2$

B.4.3 Effet de la distance entre les rotors à faible débit et $N_1 = \pm 2000$ tr/min

Dans la présente section, l'impact de la distance entre l'inducteur et la roue de la pompe sur l'efficacité de cavitation de la pompe en mode contra-rotatif est exploré. Par conséquent, cet espacement est noté L, et est évalué à deux distances spécifiques : 20 mm et 80 mm.

La Figure B.25 présente les caractéristiques de cavitation de la pompe en contra-rotatif lorsque l'inducteur est positionné à 20 mm et 80 mm de la roue. Trois points spécifiques sont mis en évidence pour les courbes de co-rotation et de contra-rotation : les points a et b indiquant l'instabilité de la pression de la pompe, les points c et d indiquent la chute de pression de 5%, et les points e et f représentant le point de rupture.

La Figure B.25 indique que la performance de cavitation de la pompe est supérieure lorsque l'inducteur est positionné à 80 mm de la roue par rapport à une distance de 20 mm. À la distance de

20 mm, il y a une chute de pression de 5% à $NPSH = 0,55$ m. Cependant, lorsque l'écart entre l'inducteur et la roue est étendu à 80 mm, cette valeur tombe à 0,3 m.

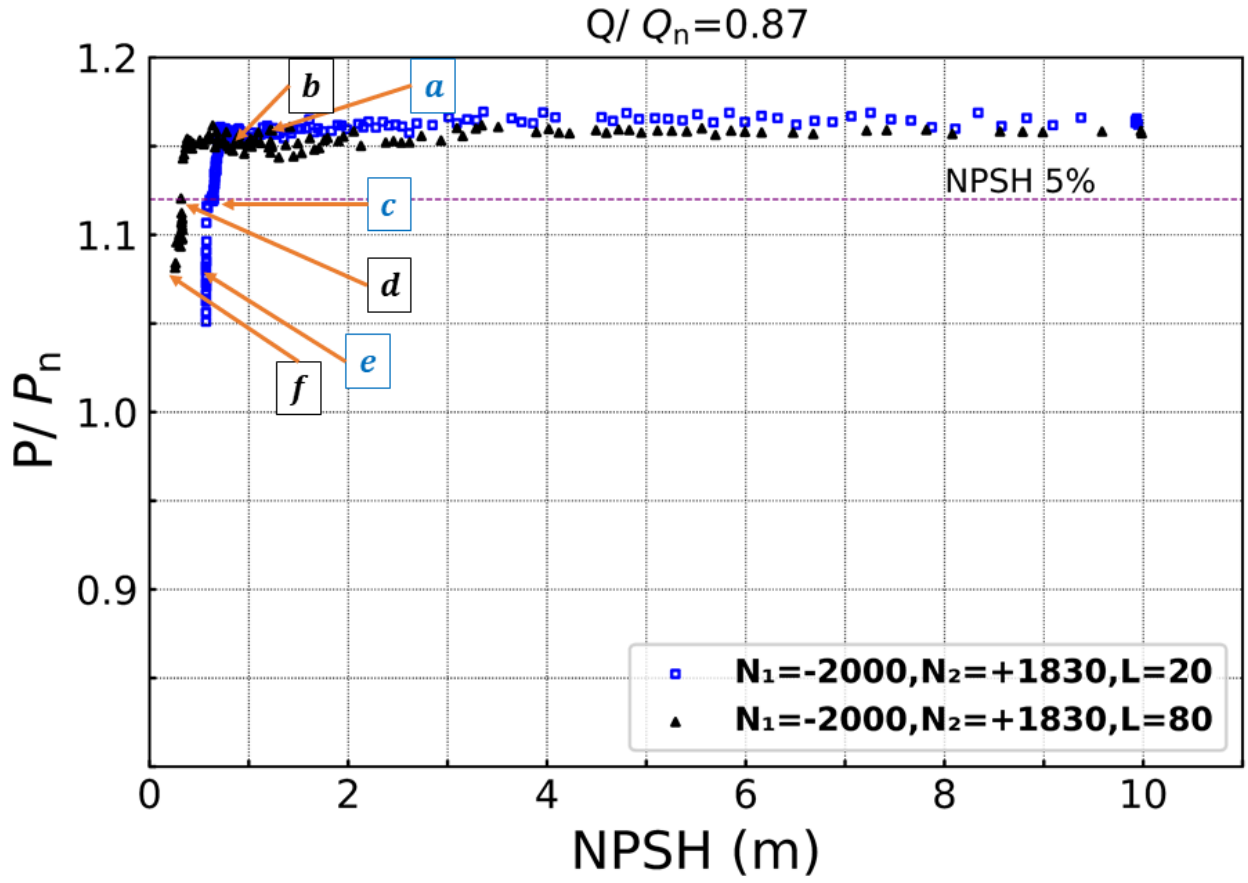

FIGURE B.25 – Performances de cavitation de la pompe pour $L = 20$ mm et $L = 80$ mm en contra-rotation pour $\frac{Q}{Q_n} = 0.87$ et $N_1 = -2000$ tr/min

La cavitation dans l'inducteur et entre l'inducteur et la roue a été étudiée à l'aide d'une caméra rapide. Les caractéristiques de la caméra ont été présentées précédemment, et deux écrans LED ont été utilisés de chaque côté du système pour générer l'exposition requise. Un écran LED blanc est également utilisé derrière l'inducteur pour réfléchir la lumière.

Dans la Figure B.26, la cavitation à l'intérieur de l'inducteur est analysée visuellement pour $L = 20$ mm et $L = 80$ mm, avec l'inducteur tournant à 2000 tr/min. Lorsque la pression à l'entrée de la pompe est diminuée, un long et étroit vortex d'extrémité est observé à l'arête de l'inducteur pour

$L = 20\,\text{mm}$ (figure B.26a). Cependant, lorsque L est augmenté à 80 mm, le vortex devient plus court et un peu plus large. De plus, un vortex de moyeu est détecté entre l'inducteur et la roue (figure B.26b). Ce vortex de moyeu présente des motifs de rotation doubles : il s'aligne avec la rotation de l'inducteur et tourne simultanément autour de son propre axe.

Dans la Figure B.26c, avec une chute de pression de 5% dans la pompe, l'expansion de la cavitation dans l'inducteur est illustrée. Ici, non seulement la première pale mais aussi la deuxième pale montrent des signes de cavitation. Un type de cavitation connu sous le nom de "fuite de cavitation" est noté, un phénomène résultant du différentiel de pression de part et d'autre des surfaces de la pale.

La Figure B.26d montre l'inducteur lorsqu'il est soumis à une chute de pression de 5%, mais avec l'inducteur positionné à 80 mm. Dans cette représentation, la cavitation semble s'être propagée sur la surface de la pale de l'inducteur. Le type de "fuite de cavitation" est à nouveau observé. De plus, le vortex de moyeu situé entre la roue et l'inducteur est nettement plus prononcé dans son épaisseur.

Lorsque la pression à l'entrée de la pompe est encore diminuée jusqu'au point de rupture, l'inducteur est entièrement cavitant. La Figure B.26e et la figure B.26f montrent les différentes formes de cavitation présentes dans l'inducteur lorsqu'il est positionné à 20 mm et 80 mm de la roue, respectivement. D'après les illustrations, il est évident qu'avec $L = 80\,\text{mm}$, le vortex de moyeu, qui se forme entre l'inducteur et la roue, s'est étendu. Cependant, à mesure qu'il se dilate, son intensité semble diminuer.

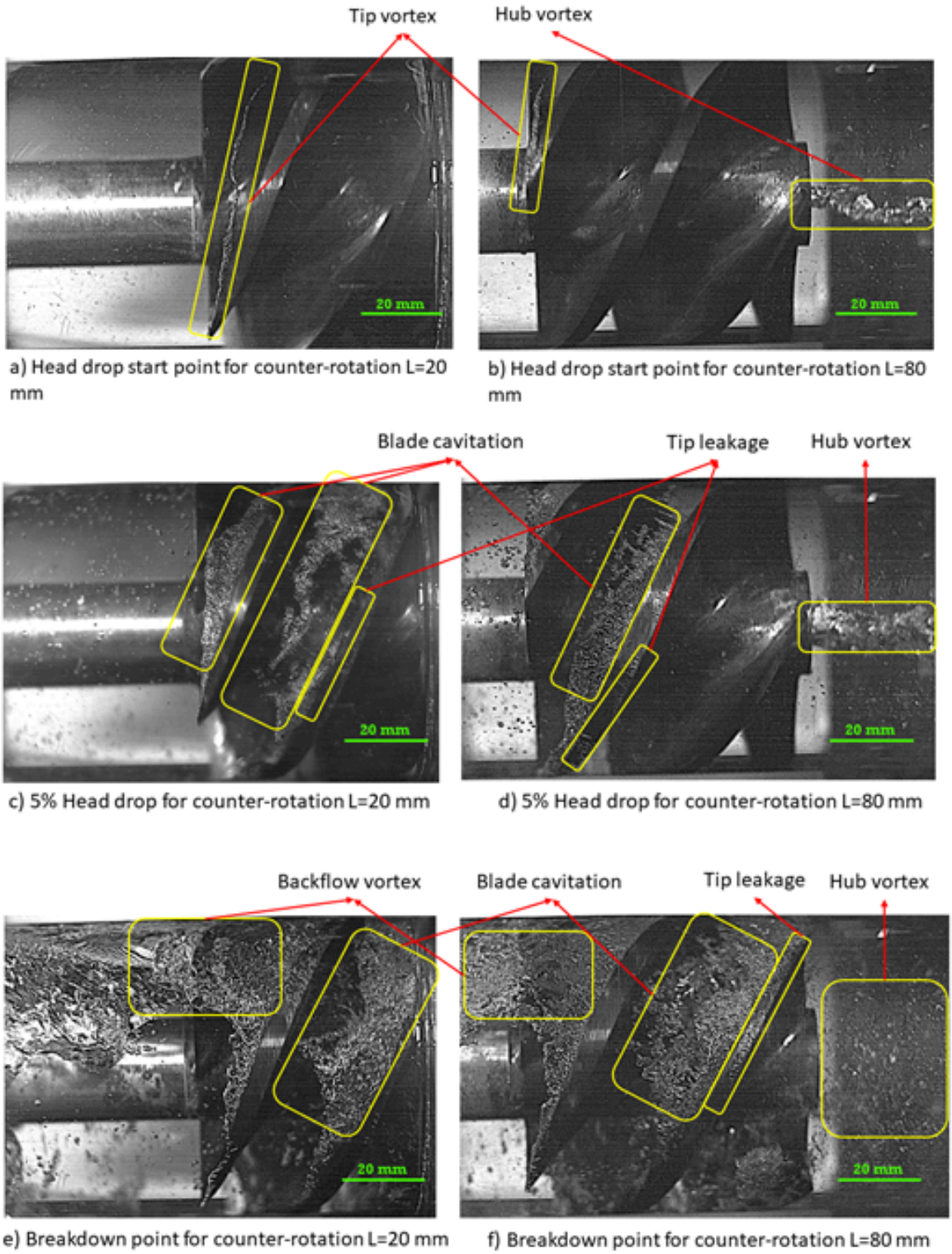

FIGURE B.26 – Développement de la cavitation pour $\frac{Q}{Q_n} = 0.87$ et $N_1 = -2000$ tr/min pour $L = 20$ mm et $L = 80$ mm

B.4.4 Comparaison des performances de cavitation en co-rotation et en contra-rotation

B.4.4.1 Débit nominal et $N_1 = \pm 2500$ tr/min

À débit nominal, une différence notable dans l'efficacité de la cavitation de la pompe apparaît lorsque l'inducteur tourne à 2500 tr/min à la fois en mode co-rotation et en contra-rotation. Plus précisément, en contra-rotation, une chute de pression de (5% est observée à $NPSH = 0.52$ m. En revanche, cette même chute de pression en co-rotation se produit à un $NPSH$ plus élevé, soit 2.18 m. En mode co-rotatif, il y a également des preuves d'une chute de pression locale. Cette diminution de la pression ne se produit pas soudainement, mais diminue avec une légère pente. Selon la Figure B.27, à ce débit et avec la vitesse de l'inducteur maintenue à 2500 tr/min, la roue tourne à 1950 tr/min en co-rotation et ralentit à 1716 tr/min en mode contra-rotatif. En contra-rotation, l'augmentation de la vitesse de l'inducteur tout en diminuant la vitesse de la roue améliore la performance de cavitation de la pompe. En revanche, en mode co-rotation, lorsque la vitesse de l'inducteur augmente, parce qu'il tourne dans le même sens que la roue, cela résulte en une vitesse de fluide plus élevée à l'entrée de la pale de la pompe. Cette vitesse accrue entraîne une diminution de la performance de cavitation de la pompe.

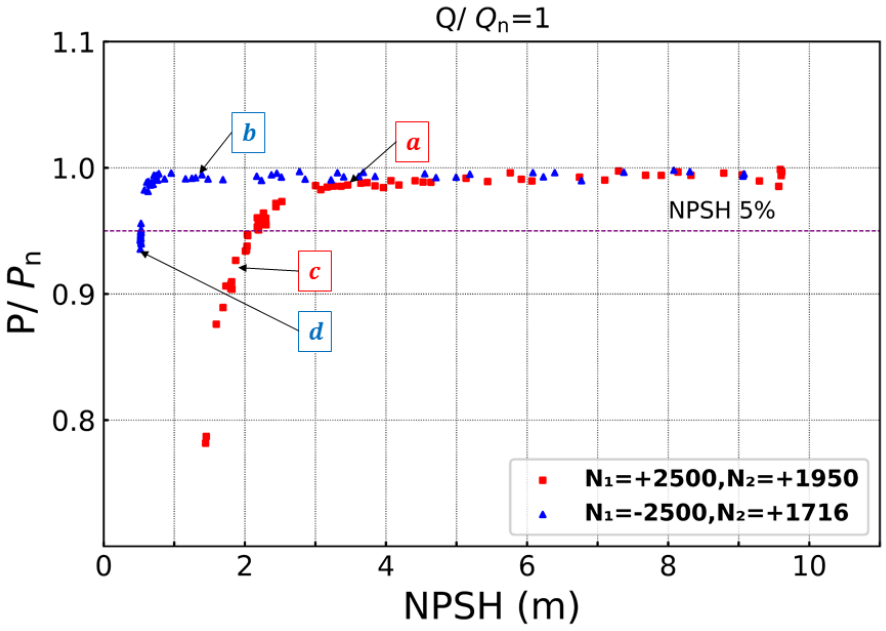

FIGURE B.27 – Comparaison des performances de cavitation de la pompe pour $\frac{Q}{Q_n} = 1$ et $N_1 = \pm 2500$ tr/min

Dans la Figure B.28, alors que la pression de la pompe commence à diminuer en co-rotation, un faible vortex de pointe est observé au bord de l'inducteur. Cela contraste avec le vortex de moyeu mince, mais très fluctuant, observé entre l'inducteur et la roue à faibles débits. Lorsque la pression à l'entrée tombe en dessous de 5% de la pression de la pompe, le vortex de pointe au bord de l'inducteur devient plus prononcé et s'élargit, tandis que le vortex de moyeu augmente en épaisseur. Cependant, sa relation angulaire avec l'axe de l'inducteur diminue, conduisant à moins de fluctuations.

Dans la Figure B.28b, au début de la chute de pression en mode contra-rotatif, un vortex de pointe plus prononcé apparaît, accompagné d'une fuite de pointe au bord de la première aube de l'inducteur. Un vortex de moyeu épais apparaît entre l'inducteur et la roue, sa taille étant comparable à celle du moyeu de l'inducteur. Cependant, sa fluctuation est faible et son angle par rapport à l'axe de l'inducteur et de la roue reste relativement faible. À mesure que la pression diminue (comme on le voit dans la Figure B.28d), l'inducteur subit une cavitation complète, s'étendant jusqu'à sa troisième aube et couvrant toutes les surfaces des aubes. Le vortex de moyeu entre l'inducteur et la roue devient plus fin, mais sa fluctuation et son angle par rapport à l'inducteur augmentent, ce qui signifie qu'il se rapproche des aubes de la roue , s'éloignant du centre de la roue . À mesure que le débit augmente et que la vitesse de l'inducteur reste constante, la vitesse de la roue augmente légèrement pour augmenter le débit. Cette augmentation de la vitesse de la roue entraîne une aspiration plus forte devant la roue et après l'inducteur. Cette zone de basse pression, en particulier entre le moyeu de l'inducteur et la roue , qui n'est pas affectée par la pression des aubes de l'inducteur, conduit à la création d'un vortex de moyeu plus fort par rapport au débit inférieur(Figure B.28b). Dans les sections suivantes, les changements dynamiques et les fluctuations de la cavitation au sein de l'inducteur et entre l'inducteur et la roue seront expliqués.

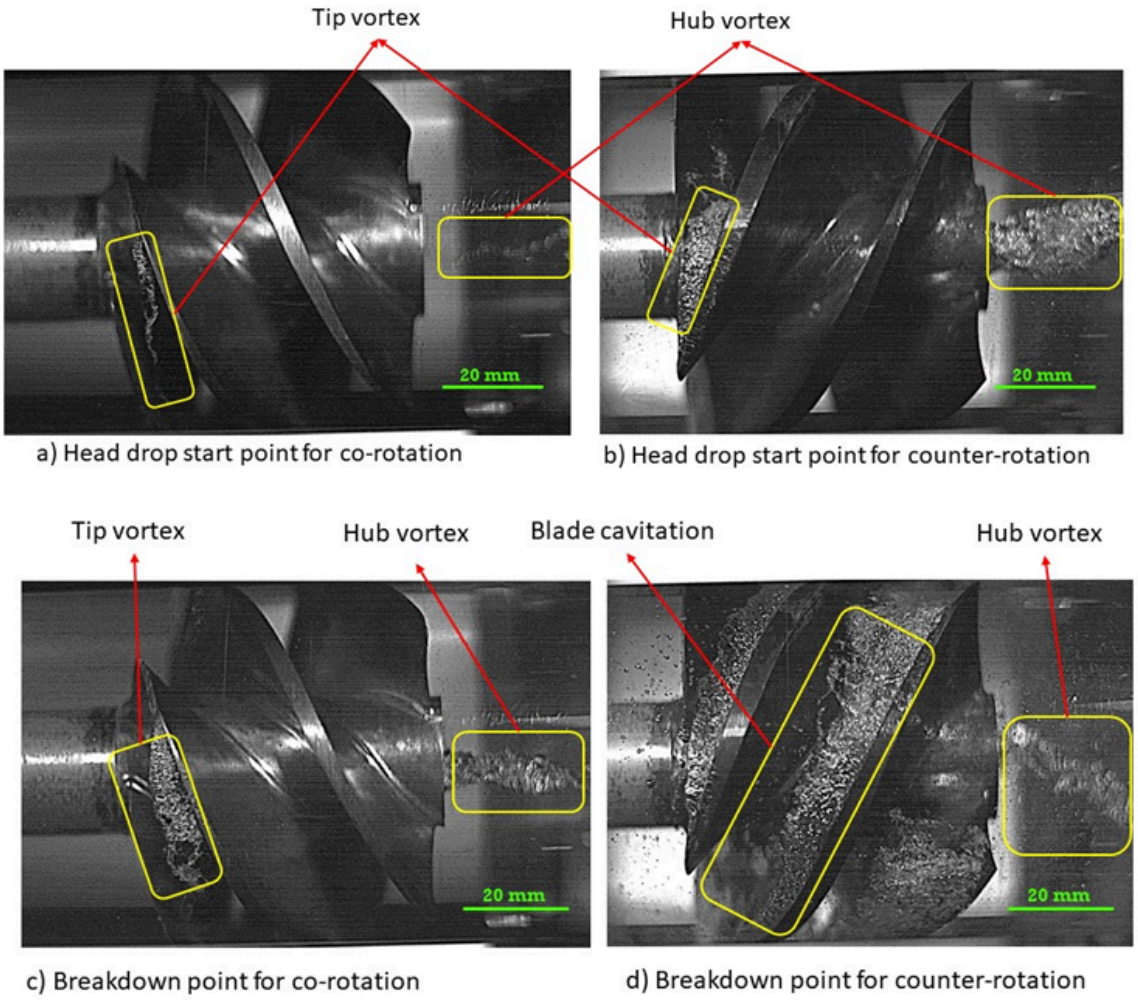

FIGURE B.28 – Dévelopement de la cavitation pour $\frac{Q}{Q_n} = 1$ et $N_1 = \pm 2500$ tr/min

B.5 Instabilités de cavitation

La cavitation est caractérisée comme un phénomène instable, et des variations dans son type à différents points de fonctionnement de la pompe sont observées. Dans cette section, des images d'une caméra rapide seront utilisées pour l'étude de la symétrie et de l'asymétrie de la cavitation à l'intérieur de la pompe dans des conditions opérationnelles spécifiques. Une analyse sera également menée sur la formation de la cavitation du vortex de moyeu entre les deux rotors à un point particulier de

fonctionnement de la pompe.

B.5.1 Cavitation symétrique

Dans une situation de cavitation symétrique, la cavitation se produit de manière uniforme sur les surfaces des aubes. La figure B.29 montre la cavitation à l'intérieur de la pompe lorsqu'elle fonctionne en contra-rotation à débit nominal et $N_1 = -2500\,\mathrm{tr/min}$, lorsque $NPSH = 1.4\,\mathrm{m}$. L'angle de rotation de l'inducteur est noté λ, et commence à zéro degré. Les aubes de l'inducteur sont désignées comme les aubes numéros 1, 2 et 3, de gauche à droite. À $\lambda = 0°$, la cavitation devient apparente sur l'aube numéro 1. Lorsque l'inducteur tourne de 60 degrés ($\lambda = 60°$), la cavitation est visible sur l'aube numéro 3. Après une rotation de 120 degrés ($\lambda = 120°$) et également après avoir effectué une rotation complète ($\lambda = 180°$), la distribution de la cavitation reste symétrique et constante sur la première aube.

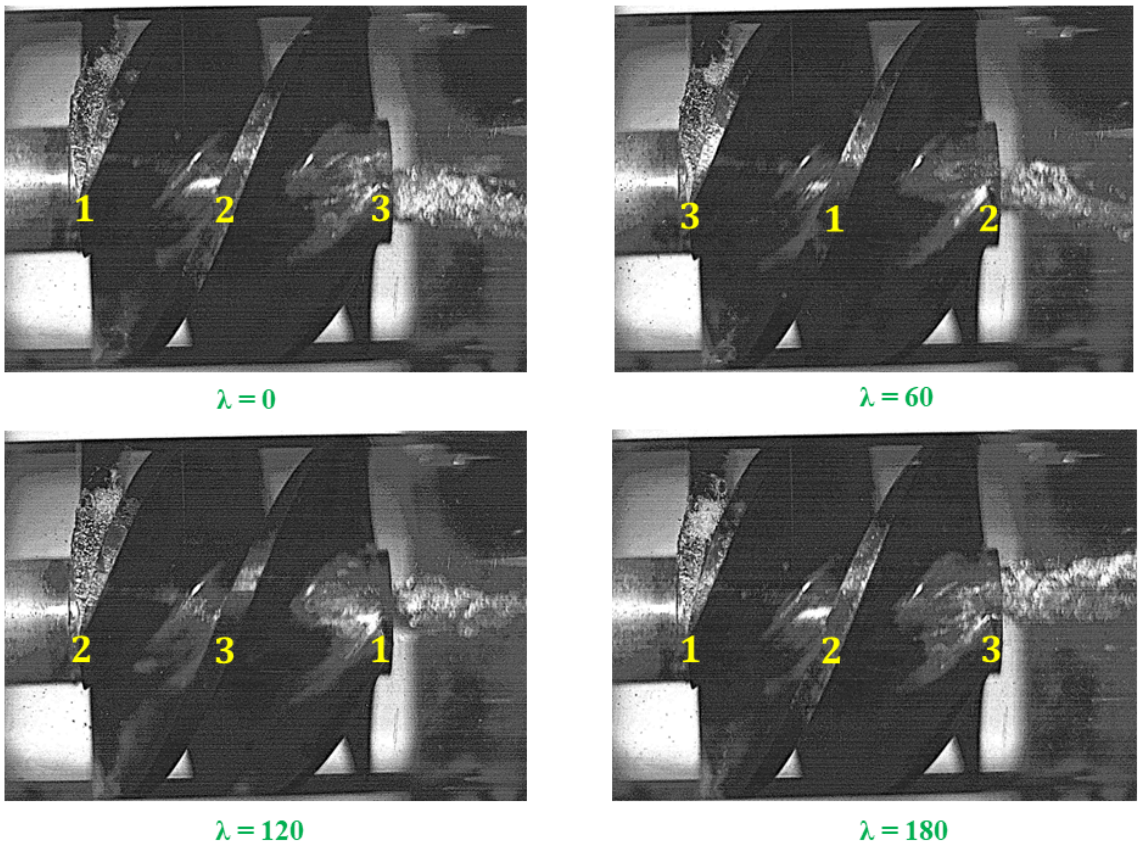

FIGURE B.29 – Cavitation symétrique dqns l'inducteur sur une rotation compéte pour $L = 80\ mm$, $\frac{Q}{Q_n} = 1$, $N_1 = -2500$ tr/min, $N_2 = 1716$ tr/min et $NPSH = 1.4\,\mathrm{m}$

B.5.2 Cavitation asymétrique

La figure B.30 illustre les variations de la cavitation à l'intérieur de l'inducteur à $N_1 = -2900\,\text{tr/min}$, fonctionnant en mode contra-rotatif pour $\frac{Q}{Q_n} = 0.87$ et $NPSH = 0.5\,\text{m}$ au cours d'une rotation complète. Contrairement au cas de la cavitation symétrique, la distribution de la cavitation sur les surfaces des aubes est asymétrique dans ce cas. À $\lambda = 0°$, l'aube 2 présente une cavitation complète. Lorsque l'inducteur tourne de 60 degrés ($\lambda = 60°$), l'aube 1 prend la position de l'aube 2, et une cavitation considérablement moindre est observée à sa surface. De plus, l'aube numéro 2, qui a maintenant bougé à la position précédemment occupée par l'aube numéro 3, subit également de la cavitation, ce qui n'était pas le cas auparavant. Après avoir effectué une rotation complète, atteignant $\lambda = 180°$, l'aube 2 montre à nouveau une cavitation complète à sa surface.

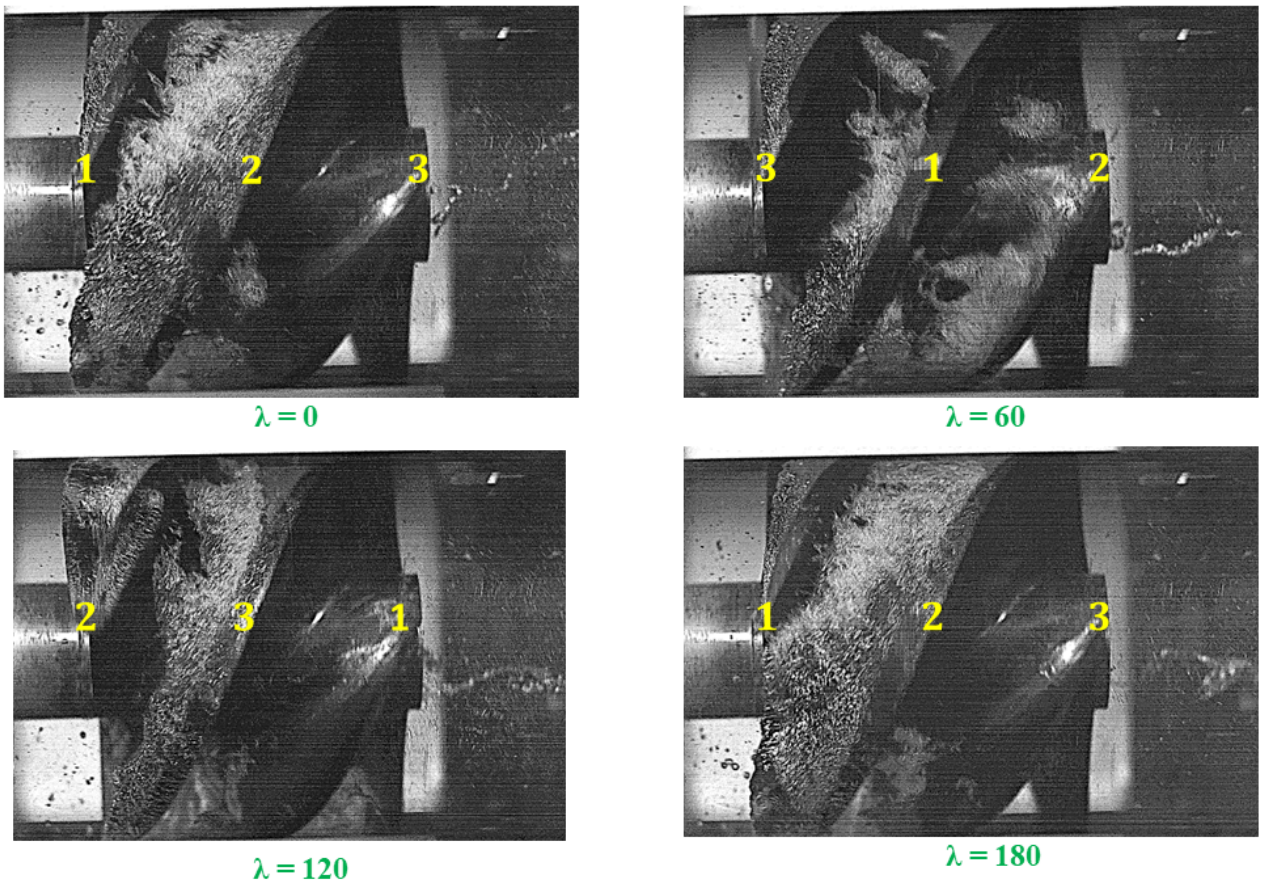

FIGURE B.30 – Cavitation asymétrique dans l-inducteur sur une rotation compléte pour $L = 80\ mm$, $\frac{Q}{Q_n} = 0.87$, $N_1 = -2900$ tr/min, $N_2 = 1506$ tr/min et $NPSH = 0.5\,\text{m}$

B.5.3 Instabilité de la cavitation du vortex du moyen

Dans cette section, une caméra rapide examine l'évolution de la cavitation du vortex de moyeu à $\frac{Q}{Q_n} = 0.87$ et $N_1 = -2900\,\text{tr/min}$ lorsque la pression chute de 5%. La figure B.31 montre le développement du vortex de moyeu entre l'inducteur et la roue. Le vortex de moyeu apparaît initialement du côté du moyeu de la roue. La direction de ce vortex est opposée à la rotation de la roue mais correspond à la rotation de l'inducteur. Le vortex se renforce et se connecte à l'inducteur après 5,7 secondes. Son angle de rotation diminue alors, et à 8,6 secondes, il devient coaxial avec à la fois l'inducteur et la roue. Le vortex commence à perdre de la force après ce point et disparaît complètement à 19,9 secondes. Le vortex commence au niveau de la roue mais est influencé par la présence de l'inducteur. C'est pourquoi, même lorsque le vortex est uniquement attaché à la roue, il tourne dans la direction de l'inducteur.

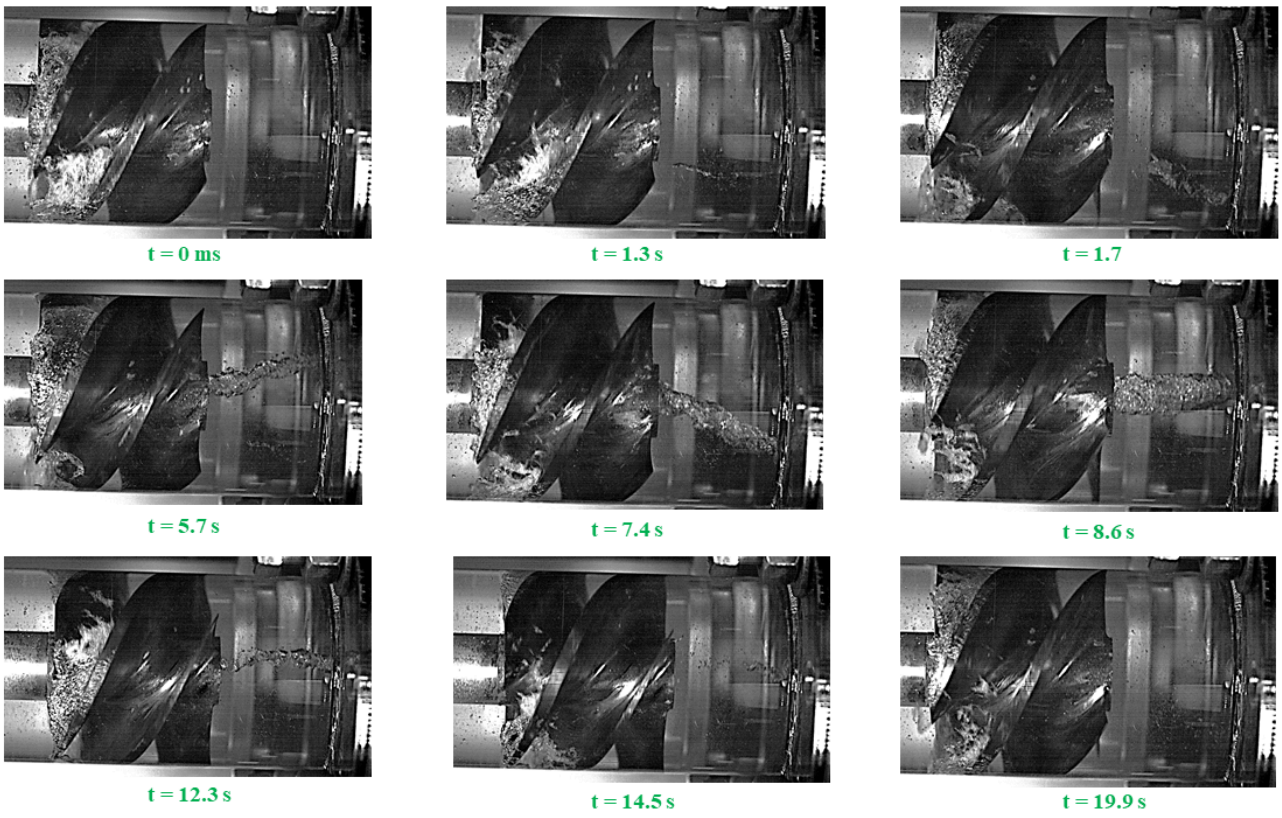

FIGURE B.31 – Instabilité de cavitation du vortex de moyen pour $L = 80\ mm$, $\frac{Q}{Q_n} = 0.87$, $N_1 = -2900$ tr/min, $N_2 = 1506$ tr/min à $NPSH5\%$.

La création de ce vortex de moyeu résulte d'une différence de pression entre l'inducteur et la roue. En particulier, la zone derrière les aubes de l'inducteur subit une augmentation locale de la pression, tandis que l'espace derrière le moyeu de l'inducteur est moins affecté. Ainsi, lorsque le fluide s'écoule près des aubes de la roue après avoir traversé l'inducteur, il est influencé par l'aspiration de la roue. Une partie de l'ecoulement subit une réduction de la pression, ce qui résulte en l'apparition du vortex de moyeu là où le moyeu rencontre l'aube de la roue.

B.6 Conclusion

Cette recherche a été mise en place pour analyser expérimentalement l'impact de la rotation séparée et du fonctionnement combiné de l'inducteur et de la roue sur les caractéristiques de la pompe ainsi que sur sa performance en termes de cavitation. Pour faciliter cette étude, une roue centrifuge fermée à 6 pales et un inducteur à 3 pales ont été initialement conçus pour s'assurer qu'ils pouvaient être accouplés. Un banc d'essai expérimental innovant a été développé pour ces expériences, conçu de manière unique pour faire tourner indépendamment à la fois l'inducteur et la roue. De plus, pour étudier l'impact de la distance entre l'inducteur et la roue sur le fonctionnement de la pompe, ce banc a été spécifiquement conçu pour ajuster leurs distances. En inversant l'angle d'attaque de l'inducteur et en adoptant une conception en contra-rotation, l'impact de la contra-rotation de l'inducteur sur la performance de la pompe a été étudié.

B.6.1 Conception de l'inducteur et de la roue

La roue et l'inducteur ont été conçus à l'aide des logiciels MFT et 3D Turbo, des outils développés au Laboratoire LIFSE. Initialement, la roue a été conçue pour avoir les caractéristiques désirées. Suite à cela, l'inducteur a été conçu de manière à ce que ses caractéristiques s'adaptent à celles de la roue, assurant ainsi un accouplement adéquat entre eux. La conception géométrique de la roue et de l'inducteur a ensuite été finalisée à l'aide du logiciel Ansys BladeGen. Pour les étapes suivantes, le logiciel Catia a été utilisé pour perfectionner la géométrie de l'inducteur et de la roue, aidant à créer le modèle 3D final et les plans de conception pour les versions en co-rotation et en contra-rotation. La roue centrifuge fermée à 6 pales a été fabriquée à l'aide d'une imprimante par stéréolithographie (imprimante SLA). Pour réduire le poids et éviter la flexion de l'arbre et les vibrations à haute vitesse, l'inducteur est fabriqué en aluminium 6062, compte tenu du long arbre utilisé dans la section de

l'inducteur.

B.6.2 Conception du banc d'essais expérimental et méthode numérique

Suite à la conception de l'inducteur et de la roue, l'étape suivante consistait à créer un banc d'essai capable de faire tourner indépendamment les deux rotors. Pour ce faire, le banc d'essai a été divisé en deux sections principales : une pour l'inducteur et une pour la roue. Le processus de conception a commencé par la section de la roue. Ici, un moteur électrique est utilisé pour fournir un couple, tout comme les pompes conventionnelles. Ce couple est ensuite transféré à la roue via un arbre. Des joints mécaniques ont été utilisés pour assurer l'étanchéité de l'arbre de la roue. Pour déterminer les composants appropriés, la rotation de la roue a été simulée à l'aide du logiciel Star CCM+. Cette simulation a aidé à calculer le couple maximal ainsi que les forces verticales et radiales exercées sur l'arbre. En fonction de ces résultats, les composants appropriés, y compris les joints mécaniques et les roulements, ont été choisis. Un diffuseur, fabriqué à l'aide de la technologie d'impression 3D, est utilisé à la sortie de la roue.

Suite à la finalisation de la conception de la section de la roue, l'attention s'est portée sur la conception de la section de l'inducteur. Cette partie a été conçue de manière à, une fois terminée, s'intégrer facilement à la section de la roue. Pour faciliter la rotation de l'inducteur, un moteur électrique indépendant a été utilisé. Étant donné que l'inducteur est positionné avant la roue, et que le liquide ne peut pas couler directement dans le banc d'essai via un tuyau simple, un coude a été incorporé à l'entrée du système. Considérant l'impact potentiel du coude sur le flux allant vers l'inducteur et la roue, il était crucial de déterminer la distance optimale entre l'inducteur et le coude d'entrée. De même, en raison de la nécessité d'un arbre long dans la conception, une attention particulière a été portée à la détermination de l'épaisseur de l'arbre et à l'emplacement de ses supports. Ceci a été fait pour éviter les vibrations lorsque l'inducteur tourne à grande vitesse. La conception de l'arbre de l'inducteur prend en compte son positionnement unique, où le joint mécanique n'est pas situé juste après l'inducteur et n'est pas pressurisé pendant sa rotation. Par conséquent, ce joint est conçu pour être naturellement sous une légère pression, assurant que la section de l'inducteur reste étanche, en particulier pendant les tests de cavitation. L'inducteur est logé dans un tube en plexiglas, permettant l'analyse d'images. Différentes longueurs de ces tubes en plexiglas permettent de varier les distances entre l'inducteur et la roue. Pour faciliter le réglage de cette distance, toute la section de l'inducteur est montée sur un

systéme de dépelacement à glissiéres. Cette configuration simplifie le processus, réduisant le temps et les efforts nécessaires pour modifier à la fois la position de l'inducteur et son espacement par rapport à la roue.

B.6.3 Résultats expérimentaux

Cette recherche a pour objectif d'étudier l'impact de la rotation indépendante des rotors sur les caractéristiques de la pompe et ses performances en matière de cavitation. Pour ce faire, des tests expérimentaux ont été menés en deux parties : le test de caractéristiques et le test de cavitation.

B.6.4 Effet de la rotation indépendante de l'inducteur sur les caractéristiques de la pompe

La capacité de l'inducteur à tourner indépendamment offre une flexibilité dans l'ajustement de la plage de fonctionnement de la pompe en fonction des besoins. Notamment, lorsque la vitesse de l'inducteur est augmentée, il y a une augmentation correspondante de la pression générée par la pompe. Cependant, ces changements de vitesse n'impactent pas de manière significative l'efficacité de la pompe. Par conséquent, le point de fonctionnement de la pompe peut être ajusté en modifiant sa vitesse. L'étude a souligné que l'utilisation d'un inducteur en contra-rotation influence considérablement la pression de la pompe. De manière remarquable, en changeant la direction de rotation de l'inducteur sans augmenter sa vitesse, la pression de la pompe peut être considérablement augmentée, bien plus qu'avec des améliorations de vitesse en mode de co-rotation. De plus, augmenter la vitesse de l'inducteur en mode de contra-rotation résulte en une augmentation de pression plus significative qu'en configuration de co-rotation. Cette pression accrue permet à l'impeller de fonctionner à une vitesse inférieure tout en atteignant la pression équivalente observée en de co-rotation. Cette vitesse réduite de l'impeller joue un rôle dans l'amélioration des performances de cavitation de la pompe observée avec l'approche en contra-rotation.

B.6.5 Effet de la rotation indépendante de l'inducteur sur la cavitation de la pompe

L'un des principaux objectifs de l'utilisation d'un inducteur dans les systèmes de pompage est d'améliorer la performance de la cavitation de la pompe. La performance de la cavitation est étroitement liée à la Hauteur Positive d'Aspiration Nette (NPSH) requise par la pompe. En général, un inducteur est utilisé pour réduire le NPSH requis, améliorant ainsi la résistance de la pompe à la

cavitation.

Dans cette étude, l'introduction de la capacité à faire tourner l'inducteur de manière indépendante a ouvert de nouvelles possibilités pour explorer son influence sur les caractéristiques de cavitation de la pompe. Les résultats des expériences ont démontré que tant la vitesse de l'inducteur que sa direction de rotation jouent un rôle crucial dsur la cavitation.

Ehsan DEHNAVI

Comportement hydrodynamique et cavitant d'une pompe innovante avec rotation indépendante de l'inducteur et de la roue centrifuge

Résumé : La technologie permettant aux rotors des turbomachines de tourner indépendamment, notamment dans des configurations en contre-rotation, a suscité l'intérêt de nombreux chercheurs et industries. L'étude de l'effet de cette technologie sur la turbine, le compresseur et les pompes axiales a montré son impact significatif sur les caractéristiques des turbomachines. Jusqu'à présent, aucune recherche n'a été menée sur l'effet de la rotation indépendante de l'inducteur et de la roue dans les pompes. Dans cette thèse, l'influence de la rotation indépendante de l'inducteur et de la roue sur les caractéristiques de la pompe a été étudiée pour la première fois, en utilisant à la fois des méthodes expérimentales et numériques. Pour atteindre cet objectif, la roue et l'inducteur en co-rotation et en contre-rotation ont été conçus pour une rotation indépendante. Les paramètres étudiés dans cette recherche sont la vitesse de rotation de l'inducteur, la distance entre l'inducteur et la roue, et la direction de rotation de l'inducteur.

Mots clés : Inducteur, Roue centrifuge, Rotation indépendante,Pompes contre-rotatives, Cavitation,

Abstract : Over the years, the technology that enables rotors in turbomachines to rotate independently, especially in counter-rotating configurations, has captured the interest of numerous researchers and industries. The study of the effect of this technology on the turbine, compressor and axial pumps has shown its important effect on the characteristics of the turbomachines. Until now, no research has been done on the effect of independent rotation of inducer and impeller in pumps. In this thesis, the influence of the independent rotation of the inducer and impeller on pump characteristics has been investigated for the first time, using both experimental and numerical methods. To meet this aim, the impeller and both co-rotation and counter-rotation inducer were designed for independent rotation. The parameters studied in this research are the rotational speed of the inducer, the distance between the inducer and the impeller, and the direction of the inducer rotation.

Keywords : Inducer, Centrifugal impeller, Independent rotation, Counter-rotating pumps, Pump performance, Cavitation, Numerical simulation.